THE UNIVERSITY *of* EDINBURGH

Inverting for Antarctic subglacial topography using variability in satellite remote-sensing observations of the ice surface

Helen Ockenden

The University of Edinburgh
School of GeoSciences

Thesis submitted for the degree of
Doctor of Philosophy

May 2024

Declaration

I declare that this thesis has been composed solely by myself and that it has not been submitted, in whole or in part, in any previous application for a degree. Except where stated otherwise by reference or acknowledgment, the work presented is entirely my own.

Helen Ockenden
May 2024

Acknowledgements

The work in this thesis was funded by the NERC E4 Doctoral Training Partnership at the University of Edinburgh, and supported by the Geophysical Habitat of Subglacial Thwaites (GHOST) project of the International Thwaites Glacier Collaboration (ITGC), both of which have been incredibly flexible with offering extra time and funding for research during the Covid-19 pandemic. I spent three months working as a field assistant for the British Antarctic Survey, and I am also grateful to have been the recipient of an Evans Family Postgraduate Fellowship which allowed me to spend three months visiting Dartmouth College.

I would first of all like to thank my supervisors, Rob Bingham, Dan Goldberg, and Andrew Curtis, for all the support you have offered me during my time in Edinburgh, and for sharing with me your enthusiasm for radioglaciology, ice-sheet modelling, and inverse theory. This thesis would never have come together in its current form without your thoughtful guidance, and skill in crafting a clear scientific narrative.

I was very fortunate throughout my PhD to be a part of the International Thwaites Glacier Collaboration, through which I have met many wonderful people, and travelled to some amazing places, in particular getting to spend three months in Antarctica with the GHOST team. I would like to thank Ted Scambos, David Vaughan and Rob Larter for fostering such a welcoming international community, with many opportunities for early career researchers to be involved from the very beginning. Within the GHOST project, Andy Smith, Sridhar Anandakrishnan and Alex Brisbourne have been tireless advocates despite the many delays.

The 2022/23 GHOST field season collecting ice-penetrating radar data on Thwaites Glacier, was undoubtedly one of the defining experiences of my PhD. Thank you to Ed King for teaching us how to use the DELORES radar system, and then coming back from retirement to teach us again two years later, and to Knut Christianson and Jonny Kingslake for engaging discussions in our many radar planning meetings. Particular thanks are due to Rebecca Pearce, for being the best room-mate, to Coen Hofstede, for teaching me to skate ski, and to Ronan Agnew and Emma Pearce for keeping the ski squad going, to Luke Glazzard and Louise Borthwick, for endless games of cribbage, to Andrew Hoffman, Nate Stevens and Amanda Willet, for running with me, sometimes dressed as ghosts, to Florian Koch, the star of the snow shovelling crew, to Catrin Thomas and Julie Baum, for all the early morning yoga, to Ole Zeising, for teaching me to take better photos, and to Elizabeth Case for art projects to make even stormy days better.

I have been lucky enough to work with many other inspiring glaciologists over the course of my PhD. Thank you especially to Mathieu Morlighem, Colin Meyer and Helen Seroussi who invited me to visit Dartmouth College, and to Danielle Mangini, Jessica Badgeley, Benji Getraer, Cheng Gong, Mansa Krishna, Joel Wilner and Kasia Warburton for welcoming me into the group, and showing me around Hanover. Emma Smith, Kiya Riverman and other ITGC colleagues answered my many questions about preparing for Antarctic fieldwork. Rebecca Schlegel and Felipe Napoleoni kindly shared their radio-glaciology expertise. Becky Sanderson has joined me in the pub at numerous conferences, and encourages me to continue working as a woman in glaciology.

I am also grateful to the many staff and students at the University of Edinburgh and in the Cryosphere research group for all the thought-provoking conversations, custard creams, and evenings in the Brass Monkey. I would like to thank Julien Bodart for teaching me the basics of radar processing, and encouraging my enthusiasm for apple sauce. Thanks also to the rotating cast of Lower Lewis and other darker, windowless offices, and particularly to Anthony Hoskins, Anya Towers, Aythya Young, Eliot Weir, Louis Kinnear, Marina Ruiz Sánchez-Oro, Milo Bischof, Morag Fotheringham, Nick Homer and Polly Thompson.

Away from the office, I would like to thank all my other friends, in Edinburgh and elsewhere, for taking me with you on your adventures and asking me about mine. Thank you to my parents, and to John and Annie, for always supporting me, and providing me with many excellent long lunches. And finally, thank you to Paul, who is always there for me, even when I am an ocean away.

Abstract

As global temperatures rise, melting of the Antarctic Ice Sheet will lead to increasing global sea levels, but we do not currently have good constraints on the speed of future sea-level rise. A lack of knowledge about the subglacial topography of the ice sheets is a key cause of this uncertainty, as small variations in subglacial topography can have a significant influence on the rates of ice loss in numerical ice-sheet models. Our current understanding of subglacial topography comes from airborne and ground-based geophysical observations, which are expensive and time consuming to collect, and there are very few regions where the 1-2 km resolution required by ice-sheet models is achieved. When interpolation methods such as kriging, mass conservation and flow-line diffusion are applied to fill the gaps, they can miss influential mesoscale (2-30 km) subglacial features.

In this thesis, I use a mathematical description of the relationship between surface and subglacial topography in flowing ice, alongside high-resolution observations of ice surface topography and velocities to invert for Antarctic subglacial topography and slipperiness. I develop a method for doing this which I term Ice Flow Perturbation Analysis (IFPA). Initially, I use synthetic models of subglacial topography to explore the range of landforms which can be resolved with this approach. I apply the IFPA method to Thwaites Glacier in West Antarctica in order to compare the results with high-resolution ice-penetrating radar measurements, and to select appropriate parameter values. I also apply the IFPA method to Pine Island Glacier in West Antarctica, and show that IFPA can resolve landforms which are not present in topographic maps which have interpolated between geophysical survey lines using flow-line diffusion. Finally, I use an updated version of the IFPA methodology to look at subglacial topography across the entire Antarctic continent. The new topography map reveals new features at the bed, and fills in the details for partially-surveyed features, providing an enriched understanding of the geometry and geomorphology of the subglacial landscape.

Overall, this thesis demonstrates the value of the Ice Flow Perturbation Analysis method for mapping the subglacial topography beneath ice sheets using high-resolution satellite datasets, particularly in regions which have not yet been the focus for geophysical surveying. I emphasise the utility of the IFPA map for studying subglacial geometry and interpreting landforms, and hope that future work will enable maps produced with IFPA to incorporate more of the existing geophysical observations. When applied alongside other methods which estimate ice thickness, bed topography maps from IFPA should lead to better-constrained projections of future sea-level rise.

Plain Language Summary

Rising global temperatures are leading to increased melting of the Antarctic ice sheets and causing global sea levels to rise. However, scientists are still very uncertain about exactly how quickly sea levels will rise, because there are still many parts of the Antarctic ice sheets which are poorly understood. One particularly important part of the ice sheets is the ice-bed interface, where ice sits on the underlying rocks or loose sediments. The topography of this interface controls where and how fast much of the ice flows into the ocean around the edges of Antarctica, and bumps in the ice-bed interface hundreds of kilometres away from the coastline can influence rates of ice loss. Our current understanding of subglacial topography comes from airborne and ground-based geophysical surveys, which are expensive and time-consuming to collect, and only cover a small fraction of the total area of Antarctica. Traditionally, simple statistical methods which do not incorporate the physics behind ice flow are used to fill in the gaps between these surveys in maps of subglacial topography. These simple statistical methods can miss important bumps and dips in the ice-bed interface.

In this thesis, I used mathematical equations describing the relationship between the subglacial topography and surface bumps and dips. I applied these equations to high-resolution satellite observations of the Antarctic Ice Sheet surface, and developed a method to produce maps of the subglacial topography, which I call Ice Flow Perturbation Analysis (IFPA). At Thwaites Glacier in West Antarctica, lots of ice-penetrating radar surveys have been carried out, and we have a good understanding of the subglacial topography from these surveys, which allowed me to calibrate some of the values required by the IFPA mapping method. At Pine Island Glacier in West Antarctica, comparing the results of the IFPA mapping method with radar surveys and maps using simple statistical methods allowed me to show that IFPA can resolve features which are not included in the simple statistical maps. Having validated the IFPA method in these regions with lots of scientific surveys, I then applied IFPA across the whole of Antarctica to produce a new map of Antarctic subglacial topography which is significantly more detailed than previous maps. The new map contains lots of new topographic features, such as a 400 km long subglacial canyon and new ridges in some subglacial mountain ranges. It also helps to fill in the details around features that have only been partially surveyed, and provides insight into the distribution of mountain ranges, fast-flowing glaciers and sediment-filled basins around Antarctica.

Overall, this thesis shows that the IFPA method can be used to map subglacial topography across Antarctica from high-resolution satellite datasets. It is particularly useful in regions which have not been intensively surveyed, of which there are many. In the future, the maps produced with this method will hopefully be used to inform the planning of geophysical surveying, and combined with more survey observations to improve the maps of Antarctic subglacial topography which are used to project future sea-level rise.

Data and code availability

Chapter 3: Inverting ice surface elevation and velocity for bed topography and slipperiness beneath Thwaites Glacier

The output data from the inversion is available on Zenodo (DOI: 10.5281/zenodo.5105687). The code for the inversion and plotting the figures is available on Zenodo (DOI: 10.5281/zenodo.5494600). The surface elevation data from REMA (Howat et al., 2019) and velocity data from ITS_LIVE (Gardner et al., 2018) used as inputs in the inversion are available freely online, as are the swath radar (Holschuh et al., 2020), airborne radar (Jordan and Robinson, 2021) and Bedmachine Antarctica (Morlighem et al., 2020) bed datasets to which the results of the inversion are compared.

Chapter 4: Ice-flow perturbation analysis: A method to estimate ice-sheet bed topography and conditions from surface datasets

The code used for IFPA over Pine Island Glacier is available on Github and Zenodo (DOI: 10.5281/zenodo.8085778). The data for plotting the figures in this article are available on Zenodo (DOI: 10.5281/zenodo.8085877). The surface elevation data from REMA (Howat et al., 2019), velocity data from ITS_LIVE (Gardner et al., 2018) and BedMachine Antarctica bed topography (Morlighem et al., 2020) datasets used are available online.

Chapter 5: Antarctic-wide subglacial topography

Chapter 5 is currently being prepared for publication. The Antarctic wide bed topography map produced will be made available online through the UK Polar Data Centre. The code used to apply IFPA over the whole of Antarctica will be made available on GitHub and Zenodo at the time of publication. The surface elevation data from REMA (Howat et al., 2019; Dong et al., 2022), velocity data from ITS_LIVE (Gardner et al., 2018) and bed topography data from BedMachine Antarctica v3 (Morlighem et al., 2020) used for this analysis are available online.

Table of contents

List of figures

Chapter 1

Introduction

1.1 Thesis motivations

Climate change induced by anthropogenic activity is already having serious impacts on the global population, and has the potential to have even more significant impacts in the future. One of the most concerning of these is the significant projected increase in global sea levels. Global atmospheric carbon dioxide concentrations during the Pliocene period (3 million years ago) were similar to today at around 400 ppm, but studies suggest that global sea levels were between 10 and 30 m higher (DeConto and Pollard, 2016). Rates of ice loss from the Antarctic ice sheets have increased over the last four decades, and we have already seen a total of 14 ± 2 mm of direct sea-level rise from melting Antarctic ice over this period (Rignot et al., 2019). The Antarctic ice sheets contain the equivalent of 57.9 m of global mean sea-level rise if entirely melted (Morlighem et al., 2020), and there is considerable uncertainty about how much and how quickly they will contribute to future sea-level rise (Scambos et al., 2017). The main motivation behind the work outlined in this thesis, as for much of Antarctic glaciology, is to reduce the uncertainty in projections of the future sea-level rise contribution from the Antarctic ice sheets.

Ice-sheet modelling studies persistently highlight the importance of the topography and rheology of the ice-bed interface in understanding future rates of ice loss (e.g. Gudmundsson 2003; Parizek et al. 2013; Kyrke-Smith et al. 2018; Koellner et al. 2019). Bed topography is particularly important for marine-terminating glaciers, such as Thwaites Glacier and Pine Island Glacier in West Antarctica, because they are vulnerable to the marine ice-sheet instability (Weertman, 1974; Hughes, 1981). Some direct measurements of bed topography have been obtained through geophysical surveying (Fretwell et al., 2013; Frémand et al., 2023). However, bed topography constrained by geophysical surveying at the resolutions required for ice-sheet modelling (Durand et al., 2011; McCormack et al., 2018) is rarely available, so projections of future ice-sheet behaviour have to rely on bed topographies interpolated in a variety of ways between these survey lines (Vaughan et al., 2006; Fretwell et al., 2013; Rignot et al., 2014; Millan et al., 2017; Morlighem et al., 2020).

A limited number of ice-penetrating radar surveys have been carried out with sub-ice-thickness line spacing (e.g. Rutford Ice Stream - King et al., 2016; Pine Island Glacier - Bingham et al., 2017; Thwaites Glacier - Holschuh et al., 2020). These studies all identified features important for ice flow which were not present in interpolated bed topography products. Most importantly for this thesis, they also identified topographic features with a similarity to the geometry of the ice surface above them. The relationship between bed topography and ice-surface topography has been explored in a range of theoretical studies (Gudmundsson, 2003; Raymond and Gudmundsson, 2005; Gudmundsson, 2008; Gudmundsson and Raymond, 2008; Raymond and Gudmundsson, 2009), but has rarely been applied to realistic settings, and primarily on 2D flowline data (Pralong and Gudmundsson, 2011; Ng et al., 2018; Igneczi et al., 2018), with limited applications on 3D topographic grids (Thorsteinsson et al., 2003; Crozier et al., 2018). This thesis aims to apply this theoretical bed-surface relationship to 3D topographic data across the Antarctic ice sheets.

1.2 Thesis aims

The overarching aim of this thesis is to explore ways in which variability in the surface topography and velocity of Antarctic ice can help us to learn about the conditions at the ice-bed interface. Previous work by Gudmundsson (2003, 2008) developed a theoretical framework for how variations in the ice-bed interface should be transferred to the ice surface, and this work (contextualised in Section 2.4.2) forms the basis for the approach taken here. There have been significant advances in the quality and resolution of satellite observations of the surface of Antarctica in the last 20 years, leading to datasets for all regions of Antarctica to which this theoretical framework can now be applied, in particular the Reference Elevation Model of Antarctica (Howat et al., 2019), and the NASA MEaSUREs ITS_LIVE project (Gardner et al., 2018) for surface velocities. This thesis therefore aims to develop and apply the earlier theoretical work to the high-resolution high-quality Antarctic-wide datasets of surface conditions that are now available, to provide new insights into the basal conditions.

1.3 Thesis organisation

The rest of this thesis is organised into six main chapters. Chapter 2 reviews the relevant scientific literature, and in particular the methods which have been used previously for studying Antarctic bed conditions through geophysical surveys and in regions without existing knowledge of the bed topography. This background chapter ends by posing three key research objectives, which are each then explored in one of the following three chapters.

Chapters 3, 4 and 5 make up the main body of original research contained within this thesis, and explore the development of the methodology of inverting basal conditions

from surface conditions, which I call Ice-Flow Perturbation Analysis, abbreviated as IFPA. These three chapters have been written for publication. Chapter 3 has been published in *The Cryosphere* (Ockenden et al., 2022), and Chapter 4 has been published in *Journal of Glaciology* (Ockenden et al., 2023). An adapted version of Chapter 5 is being prepared for publication.

Chapter 3 builds on previous work by Gudmundsson (2003, 2008) which developed a theoretical framework for how variations in the ice-bed interface should be transferred to the ice surface. The first part of Chapter 3 explains the mathematics of applying this forward modelling framework (bed -> surface) to the inverse problem (surface -> bed), and explores the capabilities of this inverse model in selected synthetic situations. The next part of the chapter then applies this inverse model across the main trunk of Thwaites Glacier, one of the fastest changing glaciers in West Antarctica. Selected patches of the ice-bed interface of Thwaites Glacier have been relatively well surveyed, and so provide a testing ground for tuning the parameters required for this inverse problem. The last part of the chapter discusses the importance of selecting the correct values for these parameters, and some of the problems which arise due to trade-offs between them.

Having presented in Chapter 3 a framework for the inverse problem, and established that it can be used to produce topographic maps which match the existing bed topography, Chapter 4 expands on this further. The inverse methodology is further developed to be applied to regions with different directions of ice flow. In order to assess the relative performance of IFPA compared to other techniques for studying the topography of the ice-bed interface, the technique is applied to Pine Island Glacier, where high resolution ice-penetrating radar measurements have been made which are not yet included in other bed topography maps. The final part of Chapter 4 explores how known topography from ice-penetrating radar can be used to map the 'slipperiness' of the ice-bed interface, an important parameter for ice-sheet modelling.

Following on from the conclusion that the IFPA methodology generally performs well at returning realistic bed topography, except in some specific circumstances, Chapter 5 applies this methodology to the whole Antarctic continent. A new map of Antarctic mesoscale bed topography is presented, and I explore a selection of the most notable novel landforms. A selection of quantitative metrics is calculated to allow an objective comparison of the new topographic map with topography from Bedmachine Antarctica (Morlighem et al., 2020), the existing best map of the interior of Antarctica. The final part of Chapter 5 explores how these quantitative metrics can be used, alongside a small set of selected training data, to classify Antarctic subglacial topography based on its geomorphological characteristics, and what this reveals about the nature of the bed beneath the Antarctic ice sheets.

Chapter 6 summarises the material covered in each of the previous chapters, and presents some new data which further supports their findings. The limitations of the Ice Flow Perturbation Analysis methodology are discussed, alongside opportunities for further

work to tackle these limitations and to address other interesting problems in glaciology. The thesis concludes in Chapter 7 with the main research findings.

Chapter 2

Background

2.1 Projecting sea-level rise with ice sheet models

2.1.1 Sea-level rise from melting Antarctic ice

The modern Antarctic Ice Sheet contains an ice volume equivalent to 57.9 m of global sea-level rise, of which 5.3 m is in the West Antarctic Ice Sheet and 52.2 m is in the East Antarctic Ice Sheet (Morlighem et al., 2020). Atmospheric and oceanic warming, driven by increasing anthropogenic carbon emissions, are causing these polar ice sheets to lose mass (Rignot et al., 2019). Ice loss due to accelerated flow has been observed across the whole Antarctic continent (Shepherd et al., 2012, 2019; Smith et al., 2020, Figure 2.1). Between 1992 and 2020, the Antarctic Ice Sheet lost 2670 gigatonnes of mass, which is equivalent to 7.4 mm of global mean sea-level rise (IMBIE, 2021).

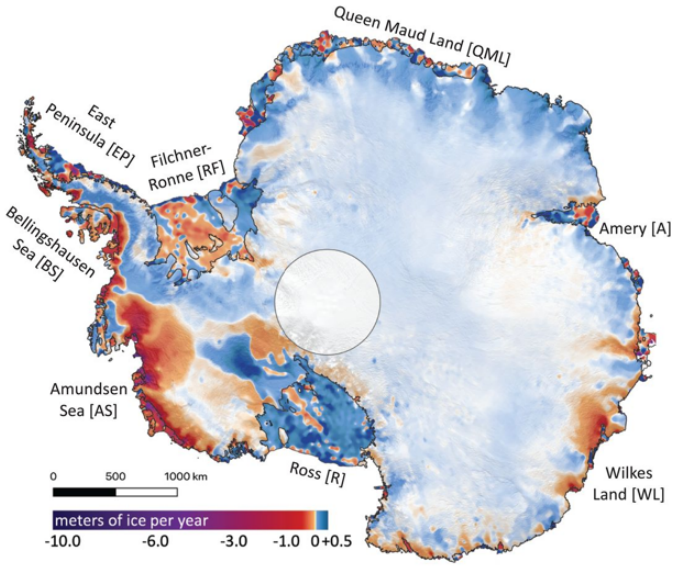

Fig. 2.1 Observed ice-mass loss across Antarctica between 2003 and 2019, from Smith et al. (2020).

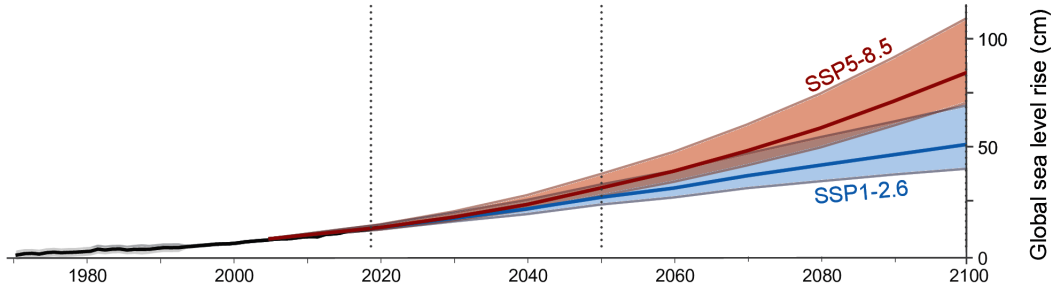

Fig. 2.2 Projected Global Sea level rise for the 21st century under different climate scenarios, from the IPCC AR6 report (Fox-Kemper et al., 2021). SSP1-2.6 is a low temperature scenario, where global temperatures rise on average between 1 and 2.6 degrees. SSP5-8.5 is a high temperature scenario, where global temperatures rise on average between 5 and 8.5 degrees. Although both scenarios agree relatively closely in 2050, by 2100 there is a significant range in the possible values of global sea level rise.

Although there is confidence that global temperatures will lead to mass loss from the global ice sheets, there is a lot of uncertainty in projections of global sea-level rise by 2100 and beyond (Ritz et al., 2015; Golledge et al., 2015; DeConto and Pollard, 2016; Edwards et al., 2019; Seroussi et al., 2020; Edwards et al., 2021). The Intergovernmental Panel on Climate Change AR6 on Ocean, Cryosphere and Sea Level Change states that sea levels are likely to rise by between 38 and 77 cm by 2100 (Fox-Kemper et al., 2021, Figure 2.2), although they identify poorly-understood glacial processes as a key cause for uncertainty in modelling Antarctic mass loss (Oppenheimer et al., 2019). As this chapter goes on to discuss, one of the key reasons for the poor understanding of glacial processes is that numerical ice-sheet models use basal boundary conditions which are still based on very sparse data for the shape and friction of the ice-bed interface.

2.1.2 Numerical ice sheet models

Fluid flow can be described physically by a set of partial differential equations known as the Navier-Stokes equations. For ice, and other very viscous fluids with a very small Reynolds number, the inertial terms in the Navier-Stokes equations can be neglected, giving a simplified set of equations known as the Stokes equations. Numerical methods are often used to model the behaviour and dynamics of ice sheets using these equations (Oerlemans, 1982; Huybrechts, 1990; Pattyn et al., 2012). Ice sheet models which use these equations and all nine principal stress components are known as full-Stokes models (Durand et al., 2009; Larour et al., 2012; Gagliardini et al., 2013). Modelling these for large systems over a useful time period requires significant computing power, and so most ice-sheet models use simplified forms of the full-Stokes equations (Gudmundsson, 1999; Hindmarsh, 2004).

After full-Stokes models, the next most complex are higher order Blatter-Pattyn type models, which use a vertical hydrostatic approximation and ignore vertical resistive stresses (Pattyn, 2003; Lipscomb et al., 2019). The Shallow Shelf Approximation (SSA) comes

from ignoring vertical shear, and is often applied to ice shelves, where basal shear is low (MacAyeal, 1989; Gudmundsson, 1999; Cornford et al., 2013). The simplest models use the Shallow Ice Approximation, which neglects longitudinal and transverse stress, and vertical stress gradients (Hutter, 2017). Some hybrid models use a mixture of these different approximations (Hulbe and MacAyeal, 1999; Bueler and Brown, 2009; Pollard and DeConto, 2009; Seroussi et al., 2012; Quiquet et al., 2018).

Ice-sheet models with more complex physics tend to have higher computational power requirements, as do models with a higher resolution. Typical model resolutions are between 5 and 15 km (Seroussi et al., 2020), which is not sufficient to resolve many local processes. In order to keep computational power requirements reasonable at the same time as resolving the regions where important processes are occurring, a variety of different gridding techniques have been developed. Initially nested grids were used (Pattyn et al., 2012), but adaptive mesh grids have become more popular (Larour et al., 2012; Cornford et al., 2013).

2.1.3 Causes of uncertainty in projections from ice-sheet models

Uncertainties in ice-sheet modelling arise for multiple reasons. Many models are calibrated by their ability to recreate past ice-sheet conditions, but limited palaeo-environmental observations and variable confidence in geological proxies mean that it is not always clear how these past ice-sheet conditions should be expressed (Gasson et al., 2015). Long term changes in ice-sheet topography due to geological activity may also mean that models require different boundary conditions for palaeo-ice sheets and modern day simulations (Paxman et al., 2019b, 2020).

Secondly, the external climatic conditions driving the behaviour of the ice sheets can be included in models in different ways. Typically, changes in ocean circulation, salinity, and temperature are parametrised in ice-sheet models through ocean melt rates and calving laws. Changes in atmospheric circulation, moisture and temperature are expressed through accumulation rates and the surface mass balance. Uncertainties can arise due to poor parameterisations which do not represent the real conditions. For example, many simulations (De Boer et al., 2015; DeConto and Pollard, 2016) use ocean temperature observations from ships to predict local ice-shelf melt rates, despite the fact that these measurements are often taken at significant distances from the ice shelf.

Even if the factors driving changes in ice sheet behaviour were known perfectly, there is still a lot of uncertainty around the physical processes occurring within ice sheets. Some processes, such as ice-cliff failure through the Marine Ice Cliff Instability, are highly controversial (DeConto and Pollard, 2016; Edwards et al., 2019), as they have not been observed in the modern day, but may help to reproduce palaeo-environmental conditions. Additionally, we do not have a good understanding of the material properties and rheology of the ice, as it is difficult to measure the temperature and viscosity of ice which is on average 2.1 km thick (Morlighem et al., 2020). Ice which has been subject to directional

pressures also behaves anisotropically, with a defined fabric that affects how it deforms. Although some observations of ice properties have been made on data from ice cores (Montagnat et al., 2014), these are drilled in slow moving stable ice which is likely to have different properties to faster flowing ice.

A significant contribute to uncertainty in projections of future sea level rise are the basal boundary conditions, which are very poorly constrained in current ice sheet models. In fact, the topography of the bed beneath the Antarctic ice sheet is the most poorly understand geographical surface in the inner solar system (Frémand et al., 2023). Bed rheology is a key part of understanding the way ice moves over the basal interface, and is influenced by both geology and hydrology. The rest of this introduction will explore our understanding of the bed **rheology** and **topography**. We begin by looking at how these factors are included in ice sheet models, and then explore what is known about the bed of Antarctica and whether this is sufficient for modelling ice sheet behaviour.

2.2 Bed rheology

2.2.1 Rheology in ice-sheet models

Ice-sheet models use parameterised sliding laws (Koellner et al., 2019; Woodard et al., 2021), which attempt to capture all the processes occurring at the bed. Hard-rock and soft sediments respond differently to the stresses of ice flow (Parizek et al., 2013), and exert friction on the flowing ice. The rheology of sediments also depends on the subglacial hydrology (MacKie et al., 2021). The majority of models use a very simple representation of the characteristics of the bed: a generalised power friction law where the basal shear stress, τ_b, varies with a slipperiness parameter C_m, the effective pressure at the ice bed interface N, the basal ice velocity u_b, and the stress exponent m. Effective pressure N is the difference between the pressure from the over-riding ice and the basal water pressure. For ice sliding over solid bedrock, Weertman style sliding laws are often used (Weertman, 1957), where effective pressure is neglected due to the assumption of a thin film of water which allows ice to slide, and with a stress exponent, m, of 2 to 3. However, Weertman sliding does not account for the effects of cavitation, where water underneath the ice affects basal drag. Lliboutry (1968) proposed that sliding laws should incorporate effective pressure to include this effect. If effective pressure is considered, a Coulomb friction law is obtained, where the basal shear stress, τ_b, eventually reaches a peak even if the basal ice velocity, u_b, increases further (Iken, 1981; Fowler, 1987; Schoof, 2005). Regularised Coulomb laws have been used in several models (Gagliardini et al., 2013; Nowicki et al., 2013; Leguy et al., 2014; Cornford et al., 2020), although with power law exponent ranging from $m = 1$ (linear-viscous behaviour, stress $\propto$ velocity) to $m = \infty$ (effectively plastic behaviour, stress is not proportional to velocity).

We still do not fully understand how to relate the slipperiness parameter C_m, the effective pressure N, and the stress exponent m, to measurable properties of the bed, such as sediment type and water availability. However, laboratory tests on sediment recovered from Whillans Ice Stream suggest that effectively plastic behaviour ($m \to \infty$) occurs beneath ice sheets resting on a weak sediment bed (Tulaczyk et al., 2000a,b). Gillet-Chaulet et al. (2016) found that a high value of the stress exponent ($m = 16$ to 20) produced a better match to modern day ice velocities at Pine Island Glacier than linear-viscous ($m = 1$) or slightly non-linear ($m = 3$) laws, most likely as a higher value of the stress exponent was a better representation of the physics of the underlying sediments. In general, higher values of m are normally utilised to represent sediments (Zoet and Iverson, 2020).

The influence of bed rheology on ice-sheet model projections

In many ice-sheet models, the evolution of the ice-sheet depends strongly on the basal friction law (Joughin et al., 2010; Brondex et al., 2019). Sun et al. (2020) explored the influence of the stress exponent, m, in models of Pine Island Glacier in West Antarctica. They concluded that when ice-shelf buttressing was reduced, models with higher values of m lost ice more quickly. However, this is not a universal finding, and other studies of Pine Island Glacier (Nias et al., 2018; Barnes and Gudmundsson, 2022), which also looked at the influence of the stress exponent on the future behaviour, have found that higher values of the stress exponent m do not necessarily result in increased mass loss. Nias et al. (2018) varied both the basal topography and stress exponent, and found that topography is at least as important as the stress exponent in determining the future behaviour of ice sheets.

Ice-sheet basal rheology is unlikely to be homogenous, and some studies have also looked at the effects of varying the sliding exponent across the glacier catchment. De Rydt et al. (2021) suggest that higher values of m are required in fast flowing areas to reproduce modern day ice velocities. In order to simulate the observed retreat since 1996 for Pine Island Glacier, Joughin et al. (2010) invoked a mixed sliding law with plastic behaviour in regions with abundant till, and non-linear viscous behaviour in regions of harder crystalline bedrock. Parizek et al. (2013) also found that mixed rheology beds can allow faster retreat than purely plastic or purely viscous beds. Koellner et al. (2019) studied the influence of a spatially variable sliding law on the retreat of Thwaites Glacier, and found that the behaviour of mixed beds does not necessarily lie between the end-member behaviours of viscous and plastic beds. Similarly to the work of Joughin et al. (2010), simulations with linear viscous beds had high rates of thinning near the grounding line, and simulations with plastic beds had thinning extending much further inland. For mixed-rheology beds, the stability of the grounding line was also found to depend on the variability of the bed topography. In one simulation, a change from a 10 km wavelength in topographical variability to a 8 km wavelength led to mass-loss and rapid glacier retreat.

Ice sheet models often incorporate subglacial hydrology into the basal sliding law through the effective pressure N (Pattyn, 1996). Effective pressure is thought to be high

in channelised hydrological systems, and low in distributed systems. Often hydrology is simplified by assuming distributed flow with the water pressure being equal to the ice overburden pressure (Paden et al., 2010; Goeller et al., 2013). Studies which have looked at the influence of water pressure on glacier evolution show that regions with low effective pressures are more sensitive to climatic forcing, and can change more quickly (Kazmierczak et al., 2022). Detailed knowledge of sediment geology and subglacial hydrology is therefore important for understanding how the Antarctic ice sheets will behave in the future, and needs to be coupled with an understanding of the bed topography (Nias et al., 2018).

2.2.2 Geology

Most of Antarctica is covered in ice, and rock exposure only accounts for 2% of the area of the entire continent (Craddock, 1982). The SCAR GeoMAP action group has mapped all the known samples from these exposed areas (Cox et al., 2023). In areas without rock exposure, geophysical techniques are used to study the geology. Different rock types have varying magnetic properties, and so magnetic sensors can be used to map out sub-surface faults, and igneous intrusions (Golynsky et al., 2018). Varying densities of different rock types means that gravity data, when combined with topography and magnetic data, can be used to study sediment distributions, igneous intrusions and large scale variations in the crustal thickness (Jordan et al., 2010, 2023). Seismic techniques use sound waves travelling through the rocks to map sub-surface faults and sedimentary layering. Typically, reflection seismic techniques are used to look at shallow structures (Brisbourne et al., 2017), and refraction seismic techniques are used to look at deeper structures in the crust and mantle (Baranov and Morelli, 2013).

Geological studies suggest that the Antarctic continent is divided into two parts by the Transantarctic Mountains. West Antarctica is traditionally considered to be an assemblage of accreted Cenozoic microcontinental terrains (Wörner, 1999), whereas East Antarctica is composed of several ancient continental cratons (Dalziel and Elliot, 1982). The West Antarctic Rift system is one of the largest zones of continental extension on Earth (Winberry and Anandakrishnan, 2004; Ferraccioli et al., 2007). Gravity surveys suggest rifting as recent as the Neogene has left a significantly thinned crust, with a minimum thickness of 19 km beneath the Pine Island Rift (Diehl et al., 2008; Jordan et al., 2010). The bedrock topography in West Antarctica is mostly below sea level (Lythe et al., 2001; Fretwell et al., 2013; Morlighem et al., 2020), and consists of several tectonic blocks (Dalziel and Elliot, 1982), including the Ross Sea and Ross Ice Shelf, Marie Byrd Land and the Bentley depression, the Ellsworth-Whitmore Mountains, the Antarctic Peninsula and the Filchner-Ronne Ice Shelf and Weddell Sea (Baranov and Morelli, 2013).

In contrast, East Antarctica is a much older continental shield that was part of Gondwana in the early Mesozoic, with mainly Precambrian basement rocks (Craddock, 1982). The large Archean Mawson craton makes up the central part of East Antarctica, and is

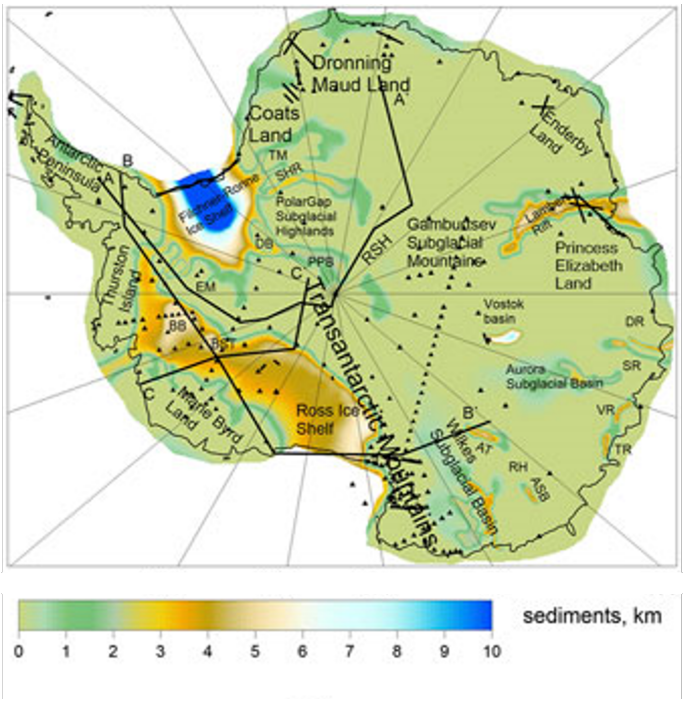

Fig. 2.3 The thickness of subglacial sediments across Antarctica, mapped using a combination of gravity, magnetic and seismic surveys. Figure adapted from Baranov et al. (2021).

surrounded by several younger orogenic belts (Groenewald et al., 1995). These mountain ranges include Dronning Maud Land, and the Gambertsev Subglacial Mountains, and are separated by rifts and large sedimentary basins, such as the Lambert Rift and Wilkes Subglacial Basin (Aitken et al., 2023). Numerical modelling simulations suggest that the majority of future ice retreat in East Antarctica will be focussed within these large sedimentary basins (Gasson et al., 2015; Golledge et al., 2015; DeConto and Pollard, 2016).

Sediment distribution

Since radar reflections do not penetrate the glacier bed, seismic surveys are the main way to study subglacial sediment distributions, and have been used to estimate the thickness of sedimentary basins across Antarctica. Baranov et al. (2021) combined broad scale magnetic and gravity data with many sediment thickness measurements from seismic surveys to map sediment cover across Antarctica (Figure 2.3).

Sediment cover in East Antarctica is relatively sparse, with seismic surveys across the South Pole, central parts of Dronning Maud Land and Enderby Land not finding any sediment cover (Bentley, 1974; Kanao et al., 2011). The deep subglacial valleys which flow into the Filchner-Ronne basin are thought to have 2-3 km thick sediment cover (Bamber et al., 2006; Shepherd et al., 2006). Sediment cover is also thought to be present in many East Antarctic basins, including the Astrolabe Basin (2-4 km, Aitken et al., 2014), the Aurora Subglacial Basin (1-3 km, Aitken et al., 2014; Scheinert et al., 2016), the

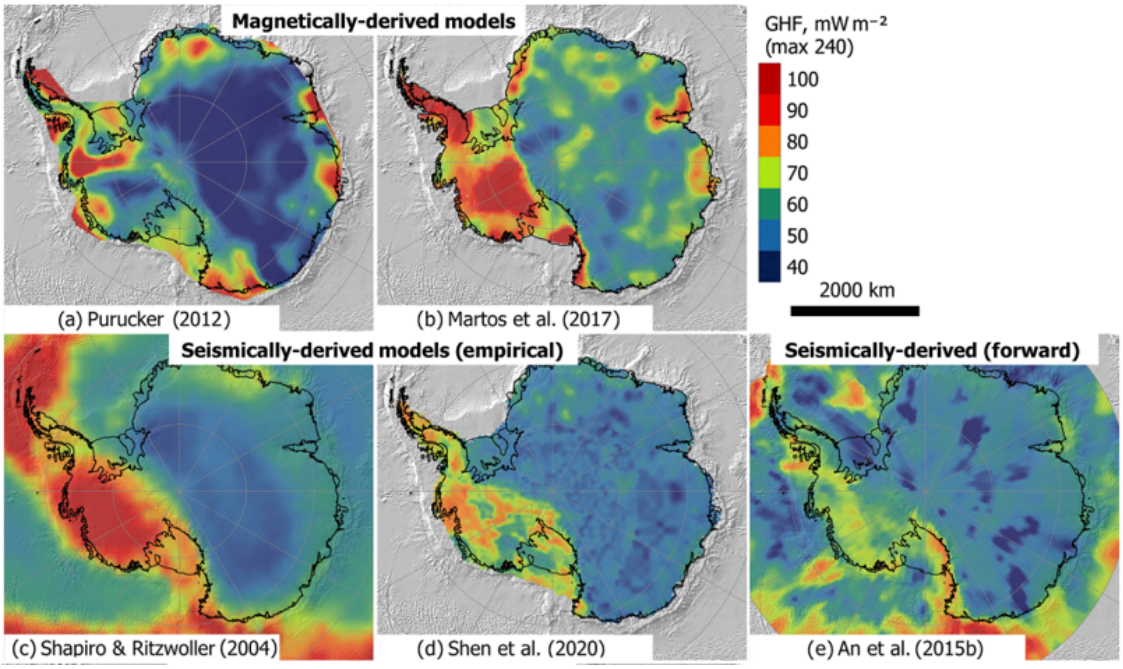

Fig. 2.4 Geothermal heat flux across Antarctica in mW m^{-2} from a variety of different models. Figure adapted from Burton-Johnson et al. (2020).

Wilkes Subglacial Basin (1-4 km, Ferraccioli et al., 2001; Frederick et al., 2016) and the Pensacola-Pole Basin (1-2 km, Bentley, 1974; Wannamaker et al., 2004; Paxman et al., 2019a). Some of the thickest sediment cover in East Antarctica may be in the Lake Vostok Basin, where seismic profiles suggest a thickness of up to 7 km.

In West Antarctica, sediment cover is primarily influenced by the West Antarctic Rift System, a series of deep rifted basins which have filled with sediments. Underneath the Ross Ice Shelf, sediment cover reaches 6 km in thickness (Bentley, 1974; Shen et al., 2018), and extends all the way to the Bentley Subglacial Trench in the Amundsen Sea sector, where the sedimentary thickness is suggested by seismic surveys to be 2-4 km thick (Bentley, 1974). For Pine Island Glacier, seismic observations suggest that there is a layer of glacial till across the whole glacier catchment, allowing rapid ice motion through bed deformation. This soft water-saturated sediment is present even on the topographic highs where it might have been expected to be eroded by glacial motion (Smith et al., 2013; Brisbourne et al., 2017). However, in other regions, seismic acoustic impedance suggests that there is discontinuous sediment cover (Muto et al., 2019b). Harder, more crystalline rock is thought to be present on the up-glacier (stoss) slopes of Thwaites Glacier, and softer, less consolidated sediments are observed on the down-glacier (lee) slopes. This variation in sediment types is expected to influence the ice motion. The thickest sediment cover in West Antarctic is in the centre of the Filchner-Ronne basin, where sediments may be more than 12 km deep (Hübscher et al., 1996; Leitchenkov and Kudryavtzev, 2000).

Geothermal heat flux

Geothermal heat can be generated by radioactive decay in rocks high in heat-producing elements, primarily felsic rocks in continental crust which are rich in uranium, thorium and potassium (Sandiford and McLaren, 2002). Since these rocks are unevenly distributed across Antarctica, they produce local and regional controls on subglacial geothermal heating. Geothermal heat flux is important for ice-sheet flow because it controls the distribution of frozen-to-the-bed basal ice (which must flow through internal deformation) and thawed basal ice (which is able to slide). Additionally, higher rates of basal melting increase subglacial water pressures and reduce basal slipperiness.

Analysis of gravity anomalies shows thinner continental crust within the West Antarctic Rift region (Damiani et al., 2014), which is linked to volcanism and elevated geothermal fluxes in West Antarctica. A few direct measurements of geothermal heat flux have been made in West Antarctica. At Siple Dome, which is not close to any known volcanic areas, a geothermal heat flux of 69 mW m^{-2} was observed (Engelhardt, 2004). Beneath Subglacial Lake Whillans, the heat flux has been measured as both 88 mW m^{-2} (Begeman et al., 2017) and 285 mW m^{-2} (Fisher et al., 2015), which may explain the abundance of subglacial lakes in the region. At the WAIS Divide core site, a geothermal heat flux of about 240 mW m^{-2} was estimated from measurements taken slightly above the bedrock (Clow et al., 2012), which was thought to be representative of the regional average.

In addition to these direct measurements in boreholes, Schroeder et al. (2014a) used radar measurements to estimate basal melting patterns beneath Thwaites Glacier, which can then be used to predict the minimum geothermal heat flux. From this analysis an average geothermal heat flux of 114 ± 10 mW m^{-2} was suggested for the main catchment, and elevated heat fluxes exceeding 200 mW m^{-2} in areas associated with rifting and volcanism. Helium isotope ratios in seawater sampled in the Pine Island Ice Shelf cavity provide geochemical evidence that beneath Pine Island Glacier, at least some melting is due to volcanic heating (Loose et al., 2018). Extremely high δ^3He ratios in the seawater suggest there is a significant volcanic geothermal heat flux, which is exerting a strong influence on basal melting and the subglacial hydrology.

For East Antarctica, which has a thicker and older crust, geothermal heat flux is thought to be lower on average than West Antarctica. Hondoh et al. (2002) found a geothermal heat flux of 59 mW m^{-2} from a borehole at Dome Fiji. At Law Dome, estimates of 72 mW m^{-2} (Mony et al., 2020) and 75 mW m^{-2} (Dahl-Jensen et al., 1999) have been made. However, few direct measurements have been made, and most geothermal heat flow models for East Antarctica use seismic or magnetic methods to infer ice bed heat flux (Burton-Johnson et al., 2020, Figure 2.4). Magnetic methods are used to calculate the depth at which ferromagnetic rocks lose their ability to maintain a magnetisation, and therefore calculate an isotherm and a surface heat flux (Purucker, 2013; Martos et al., 2017). Seismic methods look at the depth of the crust-mantle boundary, and calculate an isotherm and surface heat flux from that (An et al., 2015; Shen et al., 2020).

Although geothermal heat flux is a result of the crustal geology, the main way it influences the flow of the ice sheets is through increased basal melting when the temperature of the basal ice exceeds its pressure melting point. Geothermal heat flux is therefore often considered alongside the subglacial hydrology.

2.2.3 Subglacial hydrology

Subglacial water is primarily produced by melting at the base of the ice sheet, which occurs due to the insulating effect of thick ice, geothermal heat flux from the bed rock and frictional heating from rapid ice flow (Joughin et al., 2004, 2009). The presence and flow of water beneath the ice sheets influences ice flow in two main ways: by reducing basal friction which enables basal sliding, and by weakening till which enables bed deformation. Radar measurements can be used to identify subglacial water, because subglacial water produces stronger bed echoes than grounded ice (Schroeder et al., 2014b). Information about the subglacial environment can be extracted from the properties of reflected radar pulses.

Subglacial lakes

Subglacial lakes are particularly distinctive in radar data as they produce flat bright reflections, unlike the rough dim reflections produced by rock and sediments (Robin et al., 1969; Oswald and Robin, 1973). However, the majority of lakes in Antarctica have been identified from surface altimetry changes, connected to changes in subglacial water level as lakes fill and drain (Gray et al., 2005; Wingham et al., 2006; Fricker et al., 2016; Siegfried and Fricker, 2021). Various inventories of subglacial lakes have been made (Smith et al., 2009), with 379 lakes known about by 2012 (Wright and Siegert, 2012). Processing of large amounts of radar data since then, and improvements in satellite coverage have led to further discoveries. Analysis of radar survey data revealed the presence of 33 subglacial lakes in the Ellsworth Subglacial Highlands (Napoleoni et al., 2020). A recent inventory identified 675 subglacial lakes in Antarctica (Livingstone et al., 2022, Figure 2.5), although more are still being discovered (Yan et al., 2022).

There is some disagreement about the role that subglacial lake discharge may play on glacier dynamics. Satellite observations show strong localised changes in elevation over the central part of Thwaites Glacier between January 2013 and June 2014 (Smith et al., 2017), thought to be the drainage of four subglacial lakes. Although a large scale drainage event may be expected to led to a short-term increase in ice velocity, the discharge of these four subglacial lakes does not appear to have had a significant influence on the speed of Thwaites Glacier (Smith et al., 2017). However, temporary changes in glacier dynamics connected to subglacial lake drainage have been observed at Byrd Glacier (Stearns et al., 2008), Crane Glacier (Scambos et al., 2011) and Whillans Ice Stream (Fricker et al., 2016).

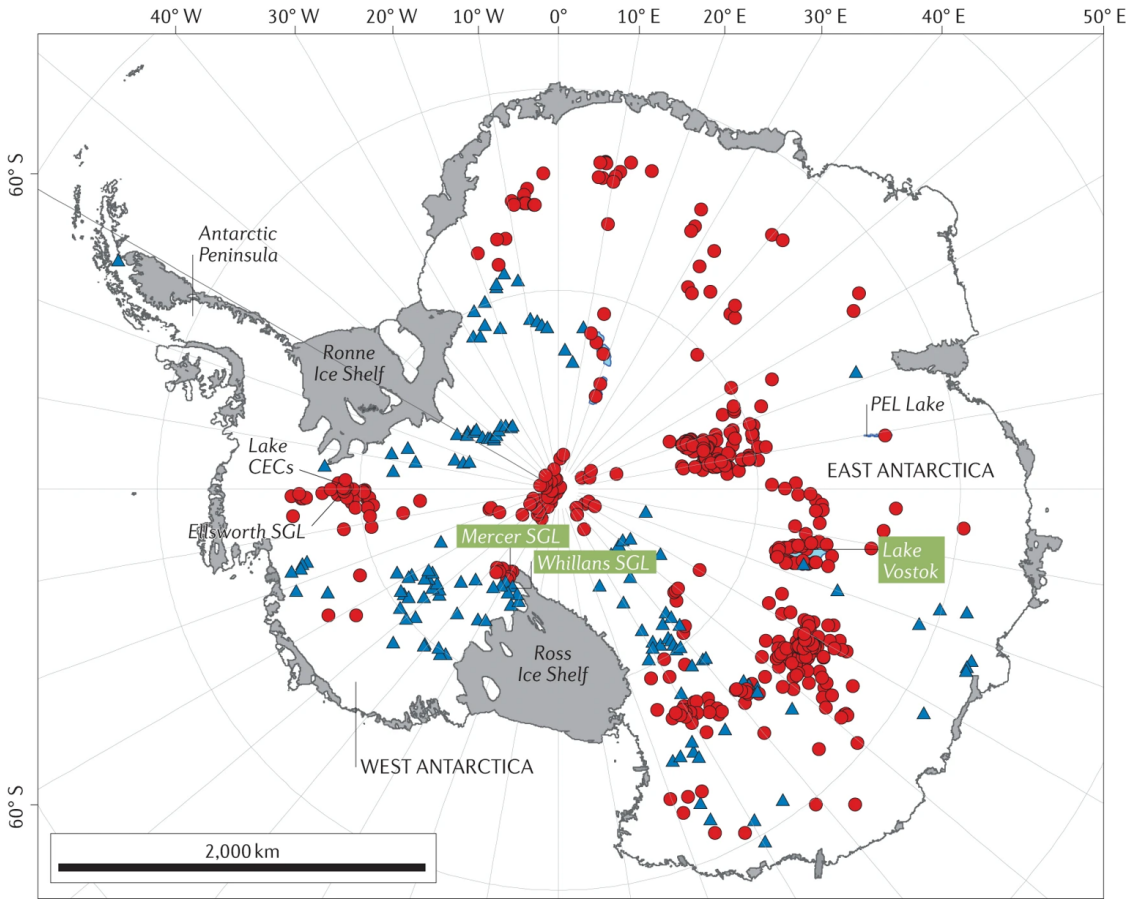

Fig. 2.5 The distribution of Antarctic subglacial lakes. Red dots represent stable subglacial lakes observed with ice-penetrating radar, whereas blue triangle represent lakes observed to fill and drain at least once in satellite records. Lakes labelled in green (Mercer subglacial lake, Whillans subglacial lake, and Lake Vostok) have been sampled. Figure from Livingstone et al. (2022).

It has been suggested that the reason for this variability may be due to differences in the subglacial hydrological drainage system. The main control on glacier speed is thought to be basal drag concentrated in high-stress regions (Joughin et al., 2009). Water flowing through a channelised drainage system would only be expected to influence a small area of these high-stress regions, so the response to subglacial lake drainage may suggest a channelised hydrological system at Thwaites Glacier (Smith et al., 2017), and more distributed hydrology at Byrd Glacier, Crane Glacier and Whillans Ice Stream (Fricker et al., 2016).

Hydrological drainage system

Aside from regions where subglacial water has pooled into lakes, there are very few observations of the ways in which water flows under the ice. Passive seismic techniques which are currently in development may allow us to map out the locations of subglacial "icequakes" caused by moving water (Kufner et al., 2021). Recently, the angular distribution

of energy in radar bed echoes (specularity) has been used to study the hydrological system (Schroeder et al., 2013; Young et al., 2016, 2017). The power and angular structure of radar echoes is related to the degree of scattering at the subglacial surface, and so contains information about the surface roughness (Wright and Siegert, 2011).

At Thwaites Glacier, high specularity is observed under the major tributaries and the main trunk upstream of a ridge in the bed (Schroeder et al., 2013). This high specularity suggests that there is a substantial volume of water ponded in distributed channels beneath the main glacier trunk, with the subglacial water bodies thought to have lengths of 15-75 m and widths of 0.5-5 m (Schroeder et al., 2014b). The specularity falls downstream of the ridge, which is thought to be due to a transition to a system of concentrated channels. Relatively high driving stresses are observed in the lower part of the glacier trunk, correlating with this transition to a channelized drainage system. It is therefore thought that the character of the basal water system may influence the flow and stability of Thwaites Glacier (Schroeder et al., 2013). Similar specularity studies to look at subglacial hydrological systems have been done on the Siple Coast, Byrd Glacier and Aurora Subglacial Basin (Young et al., 2016, 2017; Dow et al., 2020).

One of the main focusses of understanding subglacial hydrological pathways has been to look offshore at bathymetry from marine surveys, which has a much higher resolution. In formerly glaciated terrains, water drainage pathways are preserved as channelised landforms and other sedimentary landforms (Simkins et al., 2023). Channels eroded by the flow of subglacial water can be seem in offshore bathymetry from many places around Antarctica, including the Anvers-Hugo trough in the Antarctic Peninsula (Larter et al., 2019), the Amundsen Sea (Kirkham et al., 2020) and Marguerite Trough (Hogan et al., 2022), as well as in deglaciated terrains like the Dry Valleys (Ashmore and Bingham, 2014).

The huge incised channels, such as the Dry Valleys' Labyrinth system (Sugden et al., 2006), reach depths of greater than 300 m, and so require significant meltwater flow, thought to come from numerous episodic flood events due to the discharge of subglacial lakes over multiple glacial cycles (Kirkham et al., 2019). These landforms may therefore be more representative of enormous melting events connected to glacial floods and deglaciation, rather than the processes occurring underneath modern ice sheets (Lepp et al., 2022). However, comparisons between the dimensions of active modern subglacial lakes and the basins observed in Pine Island Bay suggest that modern systems do resemble this palaeo-ice-sheet drainage system (Nitsche et al., 2013), and so are likely to be channelised.

Groundwater

Most subglacial hydrology studies consider water at the base of the ice sheet, between the ice and the subglacial sediments, which are commonly assumed to be impermeable. High pore-water pressures in the subglacial sediments reduces their shear strength, allowing bed deformation and faster ice flow. If, contrary to assumptions, subglacial sediments are

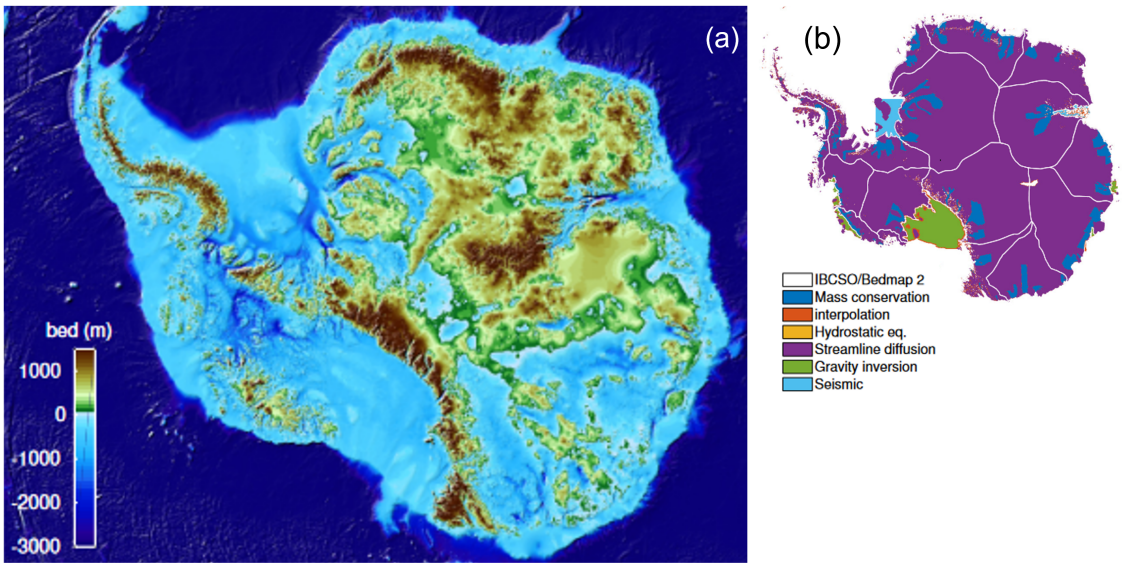

Fig. 2.6 (a) Antarctic bed topography elevation from the Bedmachine Antarctica digital elevation model. (b) Methodology used to calculate topography in each region. Figures from Morlighem et al. (2020).

not impermeable, then elevated pore-water pressures due to groundwater could have an important influence on ice flow (Siegert et al., 2018). As the West Antarctic Ice Sheet has decreased in volume since the Last Glacial Maximum, isostatic groundwater release is expected from subglacial sedimentary reservoirs.

Modelling of the Siple Coast Ice Streams suggests that groundwater in subglacial sedimentary basins makes up almost half of the water lubricating the base of the ice streams (Christoffersen et al., 2014). This numerical modelling also suggested that there are two key characteristics required for groundwater to influence ice stream flow: a deep basin of porous sedimentary rock, and a deformable subglacial till. Magnetotelluric and passive seismic surveys on Whillans Ice Stream suggest that the volume of groundwater present in subglacial sediments may be significantly higher than the volume of water in the classically considered subglacial system (Gustafson et al., 2022). There is currently very little observation data available, and further study of groundwater is required. A variety of geophysical techniques have been suggested to study the presence of groundwater beneath ice streams (Siegert et al., 2018; Chu, 2022; Killingbeck et al., 2022).

2.3 Bed topography

2.3.1 Topography in ice-sheet models

Modelling studies show that many aspects of the behaviour of the Antarctic ice sheets, including grounding-line retreat (Favier et al., 2014), subglacial hydrology (MacKie and Schroeder, 2020), basal melting (Timmermann et al., 2012) and surface undulations (De Rydt et al., 2013), are controlled by the topography of the ice-bed interface.

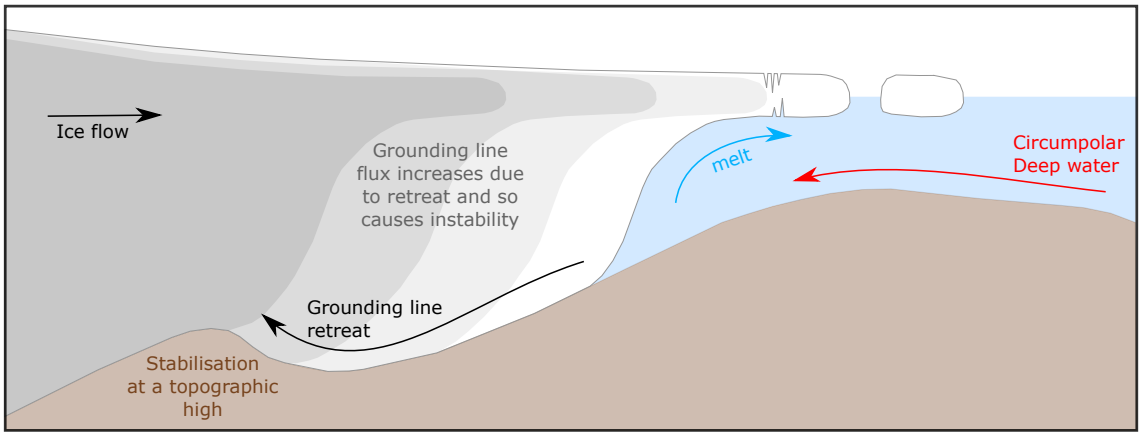

Fig. 2.7 A schematic diagram illustrating the Marine Ice Sheet Instability as explored in simple 2D models of ice-sheet behaviour.

The Marine Ice-Sheet Instability

In simple flowline models, marine-terminating glaciers are stable on prograde beds which get shallower inland and unstable on retrograde beds which deepen inland (Mercer, 1978; Weertman, 1974; Hughes, 1981; Schoof, 2007). This "Marine Ice Sheet Instability" arises due to a positive feedback which can be triggered by a small retreat in the grounding-line position. The rate of ice discharge over the grounding line (q_b) of a marine-terminating glacier is non-linearly proportional to the depth of ice at the grounding line (h_g), such that $q_b \propto (h_g)^a$, where the power law constant a is roughly 4 to 5 (Schoof, 2007). If the grounding line retreats slightly, the ice depth at the grounding line will increase, leading to an increase in the rate of ice loss. This drives further grounding-line retreat and ice loss, even if the initial driver of grounding-line retreat has ceased (Figure 2.7). In flowline models, the only way to stop this runaway retreat is stabilisation on a topographic high where the bed temporarily shallows inland (Parizek et al., 2013).

In more complex models, which account for the sideways effects of buttressing from ice-shelf friction and drag caused by the narrowing of the ice flow, it is sometimes possible to have a stable glacier on a retrograde slope (Goldberg and Heimbach, 2013; Gudmundsson, 2013). However, models which account for more components of the glacier system, such as variable snow accumulation rates and buoyancy, suggest that the stability of glaciers can not be generalised based on grounding-line geometry, but is specific to the individual configuration (Pegler, 2018; Sergienko, 2022).

Many of the glaciers in West Antarctica have retrograde beds (Vaughan et al., 2006; Holt et al., 2006; Fretwell et al., 2013; Morlighem et al., 2020, Figure 2.6), and are therefore potentially vulnerable to this marine ice-sheet instability. For glaciers in confined troughs, like Pine Island Glacier, buttressing may be enough to stabilise retreat even on a retrograde bed (Favier et al., 2014). Thwaites Glacier, however, lacks a confining trough and only has a small fractured ice shelf, so buttressing and back pressure are unlikely to be strong enough to stabilise the ice flow (Docquier et al., 2014; Joughin et al., 2014). The

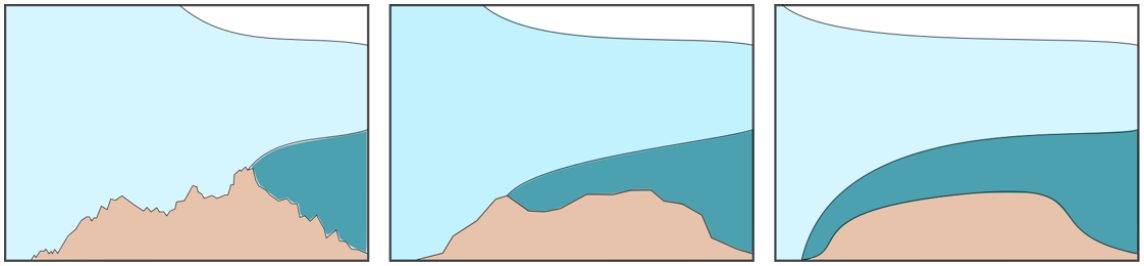

Fig. 2.8 A 2D schematic showing the influence of artificially smoothed bed topography on modelled ice sheet retreat over the next 1000 years, adapted from Figure 3 of Durand et al. (2011). From left to right, the topographic resolution used in the model was 1 km, 6 km and 20 km.

only way to stabilise Thwaites Glacier during retreat is therefore thought to be through the occupation of a topographic high (Parizek et al., 2013). An understanding of the specific conditions at each glacier, and in particular the geometry of the ice-bed interface, is required to understand how these glaciers will change in the future.

The influence of bed topography on ice-sheet model projections

Numerical modelling emphasises the importance of bed topography in influencing the future retreat of Antarctic glaciers (Nias et al., 2016; Yu et al., 2018; Nias et al., 2018; Koellner et al., 2019), especially for 3D full-Stokes models (Sergienko, 2022). Despite a general wish for more detailed topographic maps, there is not a community consensus of a desirable topographic resolution for ice-sheet modelling, only that it should be more detailed than current products (Le Brocq et al., 2010; Colleoni et al., 2018; Graham et al., 2017).

Most modelling studies which consider resolution requirements focus on the grounding line. In simulations of Thwaites Glacier with the BISICLES flow model, Nias et al. (2018) found that small topographic features at the grounding line could have a significant impact on the rate of ice thinning, with influence on the long term rate of sea-level rise. Subtle variations in the geometry near the grounding line triggered responses in the ice sheet that were felt hundreds of kilometres upstream. In addition, for both Pine Island and Thwaites Glacier, Nias et al. (2016) found that rougher beds produced lower rates of sea-level rise, supporting the need for high resolution topography maps. Durand et al. (2011) looked at the sensitivity of simulated glacier flow in models to the resolution of the bed topography, and compared the results of model runs with lower-resolution (1 to 20 km) smoothed topographies to the "true" results produced in simulations with a resolution of 200 m (Figure 2.8). They found that in order to reproduce the "true" results, and avoid erroneous initiation of the marine ice sheet instability in simulations, a minimum resolution of around 1 km is required for the bed topography in the region around the grounding line. However, this was a flowline model that did not account for the effects of buttressing and other lateral 3D support. Gladstone et al. (2012) agreed that 1 to 2 km of resolution is needed to

"accurately simulate grounding line positions", but Pattyn et al. (2013) found that sub km resolution is needed to fully simulate grounding zone migration of ice shelves and outlet glaciers.

Only a few modelling studies have considered resolution requirements further inland. Sun et al. (2014) studied the effect of bedrock uncertainty in the BISICLES ice-sheet model by adding random noise to the Bedmap2 dataset. They found that lower-frequency (larger spatial) features with a wavelength of 10s of kilometres had the largest influence on the retreat of the glacier, suggesting that small high frequency topographic features that are not detected by radar mapping are unlikely to have a significant influence on retreat rates. However, simulations with synthetic datasets which maintain the statistical properties of the glacier bed suggest that a bed resolution of 500 m may be required for simulating ice dynamics (McCormack et al., 2018). Castleman et al. (2022) suggest that in order to constrain uncertainty in sea-level rise to ± 2 cm in 200 years, a spatial resolution of 2 km and a vertical resolution of 8 m are required across the glacier catchment.

Small scale topography may also influence large scale ice flow in ways that are unresolved in many ice-sheet models. Short wavelength bed roughness can exert a frictional force against ice flow, influencing ice velocity (Bingham et al., 2017). Bed elevation also controls subglacial water routings (Siegert et al., 2005; Carter and Fricker, 2012). Kyrke-Smith et al. (2018) looked at the sensitivity of inversions for basal conditions to the bed topography, using high-resolution bed topography collected on Pine Island Glacier. They found that unresolved bed topography does not influence the overall basal slipperiness, but leads to overestimates in the basal shear stress (or skin drag) and underestimates in the topographic form drag. This division of form and skin drag may be particularly important in models which consider the time evolution of the basal conditions, as they would be expected to change independently. In the absence of detailed information about bed rheology, high resolution bed topography measurements may be able to capture some of these processes.

Glacial Isostatic Adjustment

Although unlikely to change small scale features, solid earth rebound and topographic uplift from glacier retreat could provide a negative feedback to slow the rate of mass loss (Adhikari et al., 2014). Ice loss reduces the weight of the ice sheet, de-compressing the solid earth and leading to bed uplift, which can slow retreat. In longer term modelling (centuries to millennia), these geodetic effects could lead to a significant (20 - 40 %) reduction in sea-level rise predictions, and they are thought to be particularly important for West Antarctica (Larour et al., 2019), where most of the ice streams are grounded below sea level. However, for retreat until 2100, this negative feedback is thought to have a negligible effect.

2.3.2 Mapping bed topography

Geophysical techniques including seismic surveys, airborne and ground-based ice-penetrating radar can be used to measure the bed topography. Ice is transparent to low frequency radio waves, and so they can travel through the ice sheet, reflecting back when they reach a contrast in the electrical properties of the material they encounter (Evans and Robin, 1966; Dowdeswell and Evans, 2004; Bingham and Siegert, 2007). The strongest reflection is generally at the ice-bed interface, although internal reflections thought to be from isochrones (surfaces of the same age) are also observed. Seismic waves can also travel through ice, and depending on the frequency they may penetrate into the bed, allowing a more detailed study of the properties of the sediment beneath the ice.

The earliest ice thickness measurements were obtained using seismic techniques, until radio echo sounding was developed in the 1960s (Schroeder et al., 2020). The first large scale airborne radar surveys of Antarctic were carried out in the late 1960s and 1970s by the Scott Polar Research Institute, the US National Science Foundation and the Technical University of Denmark (Robin, 1958). These were followed by a range of more regional targetted surveys. In 1983, 50% of Antarctica had at least one ice thickness observation within a 50 km grid cell (Drewry et al., 1982). The first subglacial topography map of the whole Antarctic continent, Bedmap (Lythe et al., 2001), combined all these field measurements to produce a digital elevation model at a 5 km resolution, although some regions did not contain any direct observations.

After another decade of data collection, Bedmap2 was released (Fretwell et al., 2013), and contained 25 million ice thickness measurements, more than twice as many as Bedmap. Bedmap 2 also covered a much greater area and incorporated regional surveys from areas like Pine Island Glacier (Vaughan et al., 2006), Thwaites Glacier (Holt et al., 2006), the Gambertsev Subglacial Mountains (Ferraccioli et al., 2011) and the Wilkes Subglacial Basin (Frederick et al., 2016). However, there were still many gaps exceeding 200km between measurements in some places (Pritchard, 2014).

The most recent compilation of Antarctic bed topography (or ice thickness) measurements is the Bedmap3 dataset (Frémand et al., 2023, Figure 2.9), which standardised and compiled all the existing survey data for the whole Antarctic region. In particular, the 'poles of ignorance' identified from Bedmap2 (Fretwell et al., 2013; Pritchard, 2014) have been surveyed, filling data gaps from important regions of East Antarctica. New data added in Bedmap3 include surveys from the South Pole (Jordan et al., 2018), the Pensocola Basin (Paxman et al., 2019a), Recovery Glacier (Forsberg et al., 2018), Dome Fuji (Karlsson et al., 2018; Tsutaki et al., 2022) and Princess Elizabeth Land (Cui et al., 2020b), as well as data collected by Operation IceBridge (MacGregor et al., 2021). The Bedmap3 compilation does not currently contain any information about the bed topography in the regions between these observations, although a gridded product is expected to be released in late 2024.

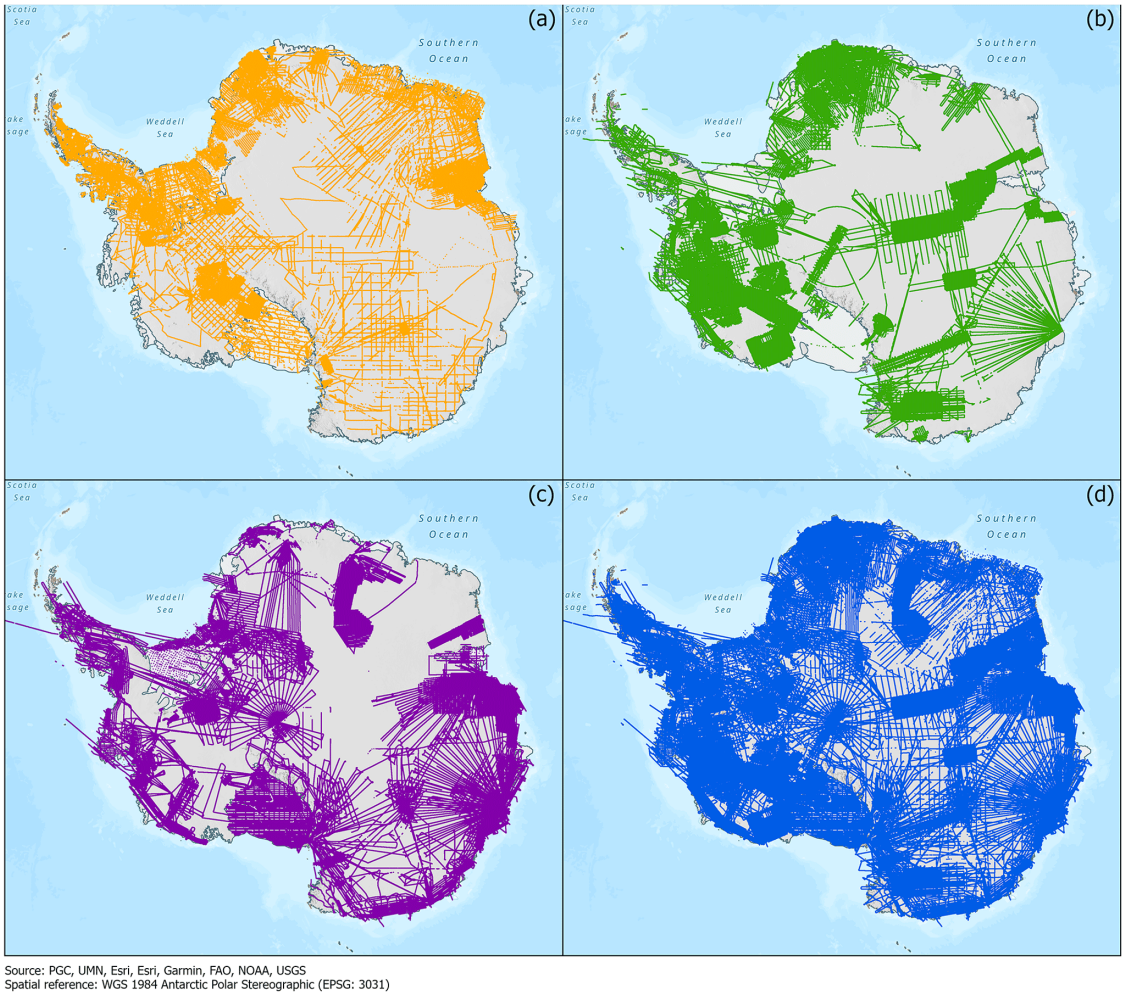

Fig. 2.9 Panels (a), (b) and (c) show the new data coverage added in the three progressive iterations of Bedmap 1, Bedmap 2, and Bedmap3. (d) Overall combined data coverage. Figure from Frémand et al. (2023).

Higher resolution surveys

Continent wide surveys, especially those flown on airborne platforms, often have a 10 km or greater spacing in more regions, with maybe a 2-5 km spacing between survey lines in areas deemed particularly important (Arnold et al., 2020). However, in some regions, higher resolution surveys with line spacing less than the ice thickness have been collected. These high resolution surveys have focussed on fast-moving ice streams such as Pine Island Glacier (Bingham et al., 2017), Rutford Ice Stream (King et al., 2009; Smith et al., 2012; King et al., 2016; Schlegel et al., 2022), Carson Inlet (King, 2011), and potential sites for ice core drilling such as WAIS Divide (Laird et al., 2009), Dome Fuji (Tsutaki et al., 2022), and Hercules Dome (Hoffman et al., 2023). The development of radar systems with multiple channel cross-track arrays has also allowed the development of swath processing, which increases the angle away from the vertical at which topography can be resolved. Swath processing has produced high resolution data for regions including Thwaites Glacier (Holschuh et al., 2020), and Hercules Dome (Hoffman et al., 2023).

How much does bed topography vary with time?

Little is known about the stability of ice-stream beds on the decadal timescales which are important for ice-sheet models, as very few repeat surveys of bed topography have been done. Seismic surveys carried out on Rutford Ice Stream in 1991, 1997 and 2004 show evidence of rapid landscape evolution (King et al., 2009). 6 m of sediment is thought to have eroded between 1991 and 1997, and a 10 m by 100 m drumlin was observed to appear between 1997 and 2004 (Smith et al., 2007, 2012). In contrast, repeat radar measurements taken on Pine Island Glacier between 2008 and 2013 show no significant change in the bed morphology (Davies et al., 2018). It has been suggested that this difference is due to the broad subglacial topography, as Rutford Ice Stream crosses a topographic ridge within the survey area whereas the Pine Island Glacier surveys were done in a flatter region. Seismic surveys on Pine Island Glacier also show a continuous deformable till layer beneath the glacier (Smith et al., 2013; Brisbourne et al., 2017), whereas Rutford Ice Stream is thought to be underlain by a mixture of hard rock and soft deformable sediments (Smith et al., 2015). The variability of bed topography may therefore also be linked to the local geology, but more repeat measurements are required to gain a better understanding of how bed topography evolves through time.

2.4 Bridging the gap between observations and model requirements

Ice-sheet modelling studies show that we need to know about bed topography at 500 m scales close to the grounding line (Durand et al., 2011; Gladstone et al., 2012; Pattyn et al., 2013), and 1-2 km resolution everywhere else (McCormack et al., 2018; Castleman et al., 2022). However, existing measurements of bed topography from ice-penetrating radar are often spaced out by 5 to 15 km. To fill in the gaps between direct geophysical observations, a variety of interpolation methods are used. These can be broadly grouped into spatial statistical methods, and inverse methods.

2.4.1 Spatial statistical methods

Classical interpolation

To estimate the value of a continuous spatial field from a limited set of sample data, the classic interpolation method used in geostatistics is kriging, or Gaussian process regression (Herzfeld et al., 1993). The Bedmap2 digital elevation model (Fretwell et al., 2013) utilised kriging through the ArcGIS Topogrid algorithm. Other simple interpolation methods include spline interpolation, which was used by Bedmap1 (Lythe et al., 2001) and early topography maps of Thwaites Glacier (Holt et al., 2006). However, these methods are very

sensitive to the density of sample data, and have high errors (up to ± 1 km) in regions with few observations where extrapolation is needed.

In addition, methods such as spline interpolation and kriging do not account for the anisotropy caused by directional ice flow, which means that in many regions ice thickness varies at shorter wavelengths across flow than along flow. Some interpolation methods such as streamline diffusion account for anisotropic ice thickness changes when interpolating between radar flowlines. Streamline diffusion is the main method used in the Bedmachine Antarctica digital elevation model in inland regions (Morlighem et al., 2020).

Statistical interpolation

Statistical interpolations can be used to produce ensembles of multiple different simulated bed topographies which maintain the key statistical properties of the data, and avoid the problem of over-smoothing. These techniques look at the statistical distribution of the roughness of the topography in areas which have been surveyed and reproduce this in more realistically rough topographies for areas with no data. Goff et al. (2014) used a conditional simulation and airborne data collected in 2004/05 to produce a realistic (but not necessarily correct) statistical map of the bed beneath Thwaites Glacier at 250 m resolution. Three main statistical characteristics were identified for the bed beneath Thwaites Glacier; a heterogeneous character (including lowlands/highlands), a channelised morphology and the general small scale roughness. Channels were resolved using an interpolation algorithm specifically designed for channels, and small scale roughness using an iterative fractal algorithm. Mackie and Schroeder (2019) and MacKie et al. (2020) expanded on this work by also accounting for the roughness in deglaciated regions where the nature of the bed is already known.

Graham et al. (2017) produced a 100 m resolution map of the bed for the whole of Antarctica using a different statistical method to account for regions of Antarctica where even a 15 km grid spacing is unavailable. The dataset produced does not agree with all available observations, but has similar statistical properties. Purely statistical approaches do not always produce beds which are physically plausible given glacier dynamics. For this reason, Guan et al. (2018) combined surface data sets and a glacier dynamics model in a Bayesian statistics approach to look at the bed topography along the central flowline of Thwaites Glacier. This approach has also been applied to the North West Greenland Ice Stream (Berliner et al., 2008). These statistically produced beds could in theory be used in ice-sheet modelling to explore the importance of small scale roughness for future glacier behaviour.

Neural networks

The growing availability of high performance computing means that neural networks are increasingly being applied to simulate statistically realistic topography, and being trained

on the existing high resolution bed topography (King et al., 2016; Bingham et al., 2017; Holschuh et al., 2020; Hoffman et al., 2023), as well as offshore bathymetry (Kirkham et al., 2019; Hogan et al., 2020) and deglaciated landscapes (Clark, 1993). Yin et al. (2022) used a non-stationary multiple point geostatistics method to map the bed topography of the Amundsen Sea Embayment.

Many of the techniques used by neural networks to study subglacial topography have their origins in image processing, such as inpainting, an artificial technique which mimics the ability of human vision to fill in gaps in images (Gavriil et al., 2019; Cai et al., 2023b). Leong and Horgan (2020) used another technique called super resolution to produce DeepBedMap, which has a 250 m resolution across the whole of Antarctica. This product has high bed-topography roughness, but also contains some unrealistic features which were artefacts of processing, and underestimates ice thickness in some regions. Cai et al. (2023a) expanded on this by using a multibranch network method to produce MB_DeepBedMap, which reduced the number of artefacts and included more realistic textures. However, due to difficulties in matching observation data and low objective accuracy, there are still improvements to be made before simulated beds from geostatical techniques can be widely applied.

2.4.2 Inverse methods

An alternative approach to statistical simulations of bed topography is to use a combination of knowledge about glaciological processes and observations of the ice surface to determine ice thickness through inverse methods (Van Pelt et al., 2013). Extensive satellite coverage means that far more is known about the surface of Antarctica than the bed, especially inland of the grounding line. Radar and laser altimetry, radar interferometry and optical imagery are all used to study properties of the ice-sheet surface including elevation and velocity. These surface data sets are vital for ice-sheet modelling, and are often used to invert for the conditions at the base of the ice sheet, which can not be observed by satellites and are therefore not available at such high resolutions. Many large scale ice-sheet models use satellite observations of surface velocities in fast-flowing areas to "invert" for basal friction or topography (Morlighem et al., 2010; Pollard and DeConto, 2012).

Mass Conservation

Bed topography and friction are often calculated by mass-conservation inversions of surface elevation and velocities (Morlighem et al., 2011, 2020). In regions where radar measurements are unavailable, these inversions maintain ice flux and divergence along the glacier using the integrated flow flux from the ice-surface velocities (Fig 2.10). Unlike purely statistical models, this technique produces ice thicknesses (and therefore basal topographies) which can be reproduced by ice flow models.

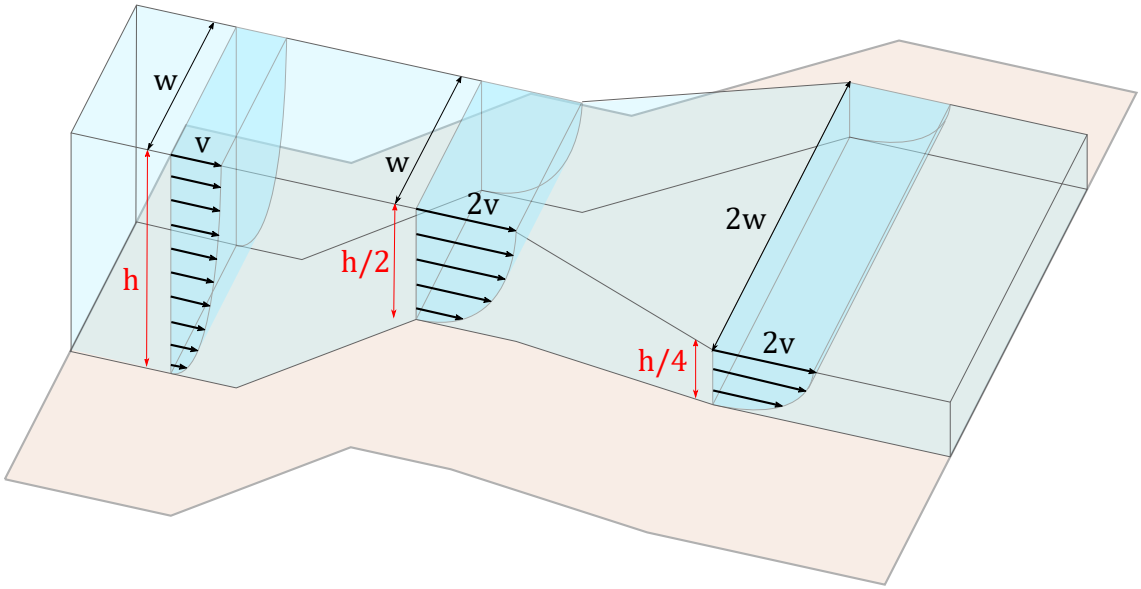

Fig. 2.10 A schematic diagram illustrating mass conservation techniques for a simple valley glacier. For a valley glacier with no tributaries mass conservation techniques assume that the volume flux of ice passing through flow gates on the glacier must be the same everywhere. Using the surface velocity (v) and Glen's flow law, an integrated ice velocity profile can be acquired, and combined with the surface dimensions (w), the relative ice thickness (h) at different locations can be calculated. If some radar measurements are available, these relative ice thicknesses can be converted to calculate the depth of the bed. In reality mass conservation algorithms are more complex as they also account for ice accumulation, surface elevation changes and the addition of ice from tributaries.

The most recent gridded map of bed topography everywhere beneath the Antarctic ice sheets is the BedMachine Antarctica dataset (Morlighem et al., 2020, Figure 2.6). This combines mass conservation techniques, gravity inversions and field observation to produce subglacial topography and ocean bathymetry on a 500 m grid resolution. However, BedMachine Antarctica (Morlighem et al., 2020) reports a vertical accuracy 30 to 60 m in well constrained regions, with vertical errors potentially exceeding 100 m in poorly constrained regions, so this still may not resolve small scale topography which is important for the ice flow.

Surface data

The transfer of variability in bed topography and slipperiness to the surface through ice flow is well known (De Rydt et al., 2013; Cooper et al., 2019b). This relationship was first described mathematically by Nye (1959), and has been developed by Budd (1970); Whillans and Johnsen (1983); Balise and Raymond (1985) and Reeh (1987). Gudmundsson (2003) and Gudmundsson (2008) built further on these early works with linear perturbation analysis, producing a set of analytical functions to describe the transfer of variability between bed topography and the ice surface across the frequency spectrum. Gudmundsson and Raymond (2008) looked at the accuracy of combining this spectral approach with

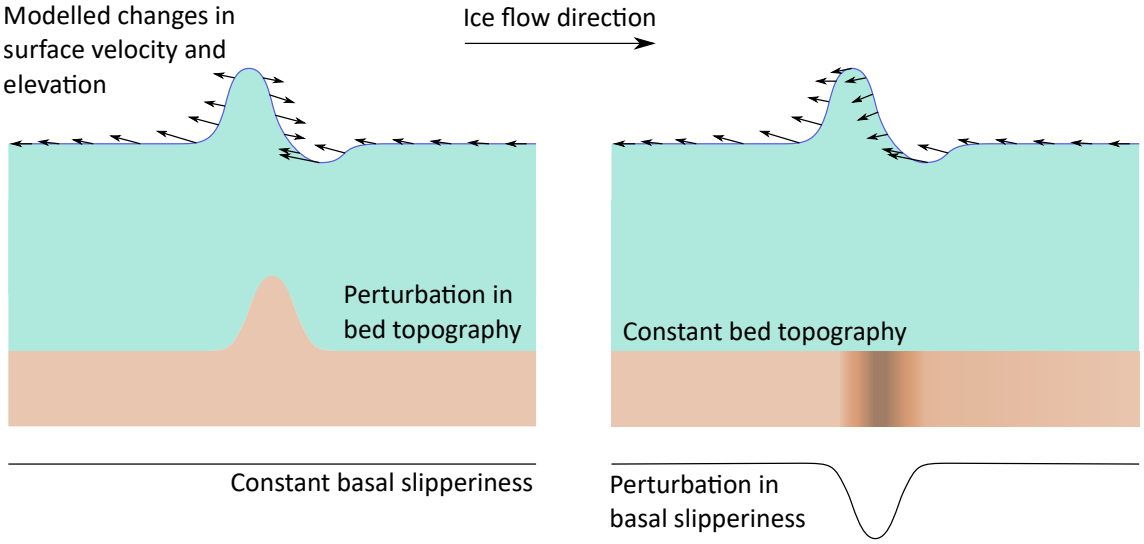

Fig. 2.11 A rough 2D schematic showing the changes induced in surface velocity and elevation by changes in basal topography and slipperiness, as modelled by Gudmundsson (2003). Although a bedrock bump may induce the same change in the surface as a decrease in basal slipperiness (a sticky patch), the observed changes in the velocity field allow these two different perturbations to be distinguished.

Bayesian statistics to take into account existing knowledge about the nature of the bed. Basal topography could be well resolved down to a scale similar to the ice thickness, but basal slipperiness was not as well resolved.

Gudmundsson (2013) modelled the expected variability in a glacier surface in response to variability in bed elevation and slipperiness (Figure 2.11). A positive Gaussian perturbation in basal topography (a bedrock bump) and a negative Gaussian perturbation in basal slipperiness (a sticky patch) both lead to changes in the surface velocity and topography. In both cases, ice thickness increases upstream of the disturbance and decreases downstream of the disturbance. However, for a change in basal slipperiness, the surface velocity changes are all in the same direction (opposite to the flow). For a change in topography, surface velocity changes are in different directions (opposite to the flow except above the perturbation). Since changes in bed topography and basal slipperiness lead to different responses in the surface, it should theoretically be possible to use the surface elevation and velocity to invert for both basal topography and slipperiness separately.

The transfer functions derived by Gudmundsson (2003) and Gudmundsson (2008) have been applied to flowlines at Rutford Ice Stream (Pralong and Gudmundsson, 2011; De Rydt et al., 2013) and in Greenland (Ng et al., 2018; Igneczi et al., 2018; Cooper et al., 2019b) to explore the bed topography. In regions with a higher basal slipperiness more topographic variability is transferred to the surface, as predicted by modelling. Topography with wavelength between 1 and 20 ice thicknesses is also observed most in the surface. Linear perturbation analysis has been applied to three-dimensional data to forward model ice-surface topography in western Greenland (Crozier et al., 2018), as part of a study looking at controls on supraglacial water routing. As an inverse method to study

basal topography, linear perturbation has only been applied to three-dimensional data at MacAyeal Ice Stream by Thorsteinsson et al. (2003). It was not applied more widely at the time due to the low availability of high-resolution surface observations.

2.5 Summary of key points and gaps in knowledge

The timing and extent of the behaviour in these models of the future evolution of glaciers in Antarctica varies significantly, due to the varying initial conditions and model physics used (e.g. Sun et al., 2014; Cornford et al., 2015; DeConto and Pollard, 2016; Yu et al., 2018). One of the greatest causes of uncertainty in projections of future sea-level rise in numerical models is the parameterisation of the basal boundary conditions, and in particular the bed topography and rheology.

82 million observations of the ice thickness of Antarctica have been made, primarily using ice-penetrating radar systems, and compiled in the Bedmap3 dataset (Frémand et al., 2023). In most regions, the gaps between survey lines are 5 - 15 km, but high resolution surveys have been carried out in some regions, and reveal a suite of interesting landforms such as MSGL, flutes, and crag-and-tail structures (Alley et al., 2021). Sensitivity studies suggest that, if we wish to understand the current and future behaviour of the Antarctic ice sheets, we need highly resolved (500 m around the grounding zone and 1-2 km inland) measurements of bed topography (McCormack et al., 2018; Castleman et al., 2022), and properties such as hydrology, geology, and sediment cover which influence bed rheology (Koellner et al., 2019).

Both statistical and inverse methods have been used to look at the basal conditions in regions of Antarctica where direct observations have not yet been made. Theoretical work has explored the relationship between the properties of the ice bed and surface (Gudmundsson, 2003, 2008, 2013). This methodology has been applied to 2D flowline data at Rutford Ice Stream (Pralong and Gudmundsson, 2011; De Rydt et al., 2013) and in Greenland (Ng et al., 2018; Igneczi et al., 2018; Cooper et al., 2019b), but only once to 3D data at MacAyeal Ice Stream (Thorsteinsson et al., 2003).

2.6 Research aims

The studies of basal conditions underneath the Antarctic ice sheets presented in this chapter demonstrate that significantly more information about the ice-bed interface is required to reduce the uncertainty in numerical model predictions, and therefore for policy makers to have greater confidence in projections of future sea-level rise. One way to achieve this is through targeted field campaigns, progressively filling gaps in radar sounding across the continental ice sheets. However, field campaigns are expensive and time consuming, and can only cover a limited area. Given the urgency of understanding future sea-level rise, additional approaches are required. The increase in capabilities of satellites focussed on

the polar regions means that we now have highly detailed maps of the surface elevation and velocity of the surface of the ice sheets, and provides an opportunity for inverse methods based on the properties of the ice surface which has not previously existed. This leads to three key research objectives for this thesis.

- **Thesis Objective 1 (Feasibility):** To assess whether inverse methods based on the transfer of perturbations in flowing ice can be applied to modern satellite datasets and utilised to study the ice-bed interface, through comparison with high-resolution ice-penetrating radar surveys.
- **Thesis Objective 2 (Utility):** To assess whether inverse methods based on the transfer of perturbations in flowing ice perform better than other methods for studying the ice-bed interface in regions without high-resolution ice-penetrating radar surveys.
- **Thesis Objective 3 (Extendibility)** To assess what inverse methods based on the transfer of perturbations in flowing ice and applied to modern satellite datasets can tell us about the ice-bed interface for the whole Antarctic continent, especially in areas with low density of geophysical survey data.

The following three chapters address these objectives through progressive applications to Thwaites Glacier in West Antarctica (Chapter 3), Pine Island Glacier in West Antarctica (Chapter 4) and the whole of Antarctica (Chapter 5). In Chapter 6 I synthesise these studies by considering how each of the objectives described above has been addressed throughout these chapters.

Chapter 3

Thwaites Glacier

A version of this chapter has been published in *The Cryosphere* as:
Ockenden, H., Bingham, R.G., Curtis, A., and Goldberg, D., 2022. Inverting ice surface elevation and velocity for bed topography and slipperiness beneath Thwaites Glacier. *The Cryosphere*, 16, 3867–3887. DOI: 10.5194/tc-16-3867-2022.

Author Contributions

RB, DG, AC and I developed the concept of the paper. DG advised on the use of the Gudmundsson 2008 equations; DG and I derived the steady state transfer functions. AC advised on the inversion methodology. I wrote the code, adapted the input data to the most useful form, and carried out the inversion. RB advised on the comparison to existing radar data. I wrote the main body of the text, but all authors contributed to the development of the final paper and associated figures.

3.1 Abstract

There is significant uncertainty over how ice sheets and glaciers will respond to rising global temperatures. Limited knowledge of the topography and rheology of ice-bed interface is a key cause of this uncertainty, as models show that small changes in the bed can have a large influence on predicted rates of ice loss. Most of our detailed knowledge of bed topography comes from airborne and ground-penetrating radar observations. However, these direct observations are not spaced closely enough to meet the requirements of ice-sheet models, so interpolation and inversion methods are used to fill in the gaps. Here we present the results of a new inversion of surface-elevation and velocity data over Thwaites Glacier, West Antarctica, for bed topography and slipperiness (i.e. the degree of basal slip for a given level of drag). The inversion is based on a steady-state linear perturbation analysis of the shallow-ice-stream equations. The method works by identifying disturbances to surface flow which are caused by obstacles or sticky patches in the bed, and can therefore be applied wherever the shallow-ice-stream equations hold and where surface data are

available, even where the ice thickness is not well known. We assess the performance of the inversion for topography with the available radar data. Although the topographic output from the inversion is less successful where the bed slopes steeply, it compares well with radar data from the central trunk of the glacier for medium wavelength features (5-50 km). This method could therefore be useful as either an independent test of other interpolation methods such as mass conservation and kriging. We do not have data to allow us to assess the success of the slipperiness results from our inversions, but we provide maps that may guide future seismic data collection across Thwaites Glacier. The methods presented here show significant promise for using high-resolution satellite datasets, calibrated by the sparser field datasets, to generate high resolution bed topography products across the ice sheets, and therefore contribute to reduced uncertainty in predictions of future sea-level rise.

3.2 Introduction

Predicting the rate at which marine sectors of the West Antarctic Ice sheet will retreat and contribute to globally rising sea levels is of increasing importance due to persistent climate forcing across the region over the last decades (Scambos et al., 2017; Turner et al., 2017). Ice-sheet modelling studies emphasise the role of bed topography and rheology in understanding future ice loss (Durand et al., 2011; Parizek et al., 2013; Sun et al., 2014; Nias et al., 2016, 2018; Kyrke-Smith et al., 2018; Yu et al., 2018; Koellner et al., 2019). Bed topography is particularly important for marine-terminating glaciers, such as Thwaites Glacier in West Antarctica, which are vulnerable to the marine ice-sheet instability (Weertman, 1974; Hughes, 1981; Schoof, 2007; Goldberg et al., 2009; Gudmundsson, 2013). However, bed topography constrained by geophysical surveying at the resolutions required for ice-sheet modelling (Durand et al., 2011; McCormack et al., 2018) is rarely available, so projections of future ice-sheet behaviour have to rely on bed topographies interpolated in a variety of ways between the direct measurements (Vaughan et al., 2006; Fretwell et al., 2013; Rignot et al., 2014; Millan et al., 2017; Morlighem et al., 2020). Over Thwaites Glacier, these interpolations have typically infilled areas of 15 by 15 km between aerogeophysical flight lines, but 15 km between observations is much coarser than the 1 to 2 km resolution which Durand et al. (2011) suggest is desirable.

Where ice-penetrating radar surveys have been undertaken with sub-ice-thickness line spacing (e.g. Rutford Ice Stream - King et al., 2016; Pine Island Glacier - Bingham et al., 2017; Thwaites Glacier - Holschuh et al., 2020), they clearly identify details which are important for studying future ice-sheet behaviour that are not present in the interpolated bed topography products. In particular, imaged signatures in the bed often show some similarity to the much subtler topography of the ice surface above them. Theoretical studies based on linear perturbation theory (Gudmundsson, 2003; Raymond and Gudmundsson, 2005; Gudmundsson, 2008; Gudmundsson and Raymond, 2008; Raymond and Gudmundsson,

2009) have explored the relationship between the bed and the surface. The resulting relations can be used to infer bed properties from those of the surface, but have only been applied to real settings a few times in Greenland (Ng et al., 2018; Igneczi et al., 2018; Crozier et al., 2018; Cooper et al., 2019b) and twice in Antarctica: on 2D surface data from MacAyeal Ice Stream (Thorsteinsson et al., 2003), and on a 1D flow line from Rutford Ice Stream (Pralong and Gudmundsson, 2011). Both Antarctic studies were undertaken in an era when surface elevation observations over Antarctica were of much lower quality and resolution than they are today.

Bed conditions such as geology, hydrology and sediment distribution also play a role in controlling ice flow and behaviour (Durand et al., 2011; Koellner et al., 2019), and are often poorly constrained. In many ice-sheet models, these bed conditions are combined into one parameter known as slipperiness, which is a measure of how easily the ice can slide over the topography (Rignot et al., 2011a). Some seismic lines have been collected on Thwaites Glacier (Muto et al., 2019a,b), allowing a brief glimpse into the sediment distribution. Over the whole glacier, however, there are very few direct measurements of bed conditions which can be combined into slipperiness.

In this paper we exploit the relatively new availability of high resolution surface elevation (REMA, $\sim$ 8 m, Howat et al., 2019) and velocity (NASA ITS_LIVE, $\sim$ 120 m resolution, Gardner et al., 2018) datasets. We apply linear-perturbation theories to explore bed topography and slipperiness across the Thwaites Glacier catchment. We use a steady-state version of the shallow-ice-stream equations presented by Gudmundsson (2008) and compare the topography output from the inversion to radar grids and flight lines to assess its performance.

3.3 Methodology

3.3.1 Derivation of the steady-state shallow-ice-stream transfer functions

Gudmundsson (2008) derived a set of transfer functions which describe the relationship between the time-variant Fourier transforms of bed topography ($\hat{b}$), bed slipperiness ($\hat{c}$), surface topography ($\hat{s}$) and horizontal components of surface velocity ($\hat{u}, \hat{v}$). For the purposes considered here, this derivation can be simplified by considering the steady state from the beginning, removing the need to do a Laplace transform. Other than this, the derivation largely follows that of Gudmundsson (2008), but for clarity we state key assumptions and results here.

Response of flow to basal topography perturbations

Following Gudmundsson (2008), and working in a coordinate system tilted forward in the x direction by the mean surface slope, α, we start with the shallow-ice-stream equations of

motion (MacAyeal, 1989),

$$\partial_x(4h\eta\,\partial_x u + 2h\eta\,\partial_y v) + \partial_y(h\eta(\partial_x v + \partial_y u)) - (u/c)^{1/m} = \rho g h \partial_x(s)\cos(\alpha) - \rho g h \sin(\alpha) \tag{3.1}$$

$$\partial_y(4h\eta\,\partial_y v + 2h\eta\,\partial_x u) + \partial_x(h\eta(\partial_y u + \partial_x v)) - (v/c)^{1/m} = \rho g h \partial_y(s)\cos(\alpha) \tag{3.2}$$

where u, v and w are the depth-independent velocity components in the x, y and z directions respectively, h is the ice thickness ($h = s - b$), η is the effective ice viscosity, c is the basal slipperiness, m is a sliding law parameter, ρ is the ice density, g is the acceleration due to gravity, s is the ice surface elevation, b is the ice bed elevation, and α is the mean ice surface slope in the x direction.

Assuming that ice is a linear viscous medium ($n = 1$) and that there is a non-linear sliding law ($m > 0$), then the shallow-ice-stream equations can be linearised and solved analytically. We consider the spatial response to a small perturbation in basal topography, b, linearising around a reference model ($\bar{h}, \bar{s}, \bar{b}, \bar{u}, \bar{v}, \bar{c}$) with $h = \bar{h} + \Delta h$, $s = \bar{s} + \Delta s$, $b = \bar{b} + \Delta b$, $u = \bar{u} + \Delta u$, $v = \Delta v$, $w = \Delta w$ and $c = \bar{c}$. The zero order solutions are spatially constant, representing uniform flow down an inclined plane.

We, however, are interested in the first order momentum balance equations

$$4\eta\bar{h}\partial^2_{xx}\Delta u + 3\eta\bar{h}\partial^2_{xy}\Delta v + \eta\bar{h}\partial^2_{yy}\Delta u - \gamma\Delta u = \rho g\bar{h}\cos\alpha\partial_x\Delta s - \rho g\sin\alpha\Delta h \tag{3.3}$$

$$4\eta\bar{h}\partial^2_{yy}\Delta v + 3\eta\bar{h}\partial^2_{xy}\Delta u + \eta\bar{h}\partial^2_{xx}\Delta v - \gamma\Delta v = \rho g\bar{h}\cos\alpha\partial_y\Delta s \tag{3.4}$$

Also to the first order, and importantly in the steady state, we have the upper and lower kinematic boundary conditions

$$\bar{u}\partial_x\Delta s - \Delta w(s) = 0 \tag{3.5}$$

$$\bar{u}\partial_x\Delta b - \Delta w(b) = 0 \tag{3.6}$$

Various points about the validity of the steady state assumption for Thwaites Glacier are raised in the discussion (Section 3.5).

All variables are then Fourier transformed with respect to the spatial variables x and y. Fourier transformed variables are denoted with a circumflex (ˆ). In the forward Fourier transform the wavenumbers in the x and y directions are denoted by k and l respectively. This Fourier transform gives

$$4\eta\bar{h}k^2\,\hat{u} + 3\eta\bar{h}kl\,\hat{v} + \eta\bar{h}l^2\,\hat{u} + \gamma\,\hat{u} = ik\rho g\bar{h}\cos(\alpha)\,\hat{s} + \rho g\sin(\alpha)\,\hat{h} \tag{3.7}$$

$$4\eta\bar{h}l^2\,\hat{v} + 3\eta\bar{h}kl\,\hat{u} + \eta\bar{h}k^2\,\hat{v} + \gamma\,\hat{v} = \rho g\bar{h}\cos(\alpha)il\,\hat{s} \tag{3.8}$$

$$\hat{w}(\bar{s}) = -i\bar{u}k\hat{s} \tag{3.9}$$

$$\hat{w}(\bar{b}) = -i\bar{u}k\hat{b} \tag{3.10}$$

where $\hat{h} = \hat{s} - \hat{b}$.

From depth integration of the Fourier-transformed incompressibility condition $w_z + u_x + v_y = 0$ we have

$$i\bar{h}(k\hat{u} + l\hat{v}) = \hat{w}(\bar{s}) - \hat{w}(\bar{b}) \tag{3.11}$$

which, along with the steady-state boundary conditions, yields

$$i\bar{h}(k\hat{u} + l\hat{v}) = -ik\bar{u}\hat{s} + ik\bar{u}\hat{b}. \tag{3.12}$$

Equations 3.7, 3.8 and 3.12 form a linear system of equations in $\hat{s}$, $\hat{u}$, $\hat{v}$ and $\hat{b}$ which can be solved algebraically (see Appendix 3.7.1), leading to the steady-state transfer functions

$$T_{sb}(k,l) = \frac{\hat{s}}{\hat{b}} = \frac{\mathrm{i}k\left(\bar{u}\xi + \tau_d\right)}{p\xi} \tag{3.13}$$

$$T_{ub}(k,l) = \frac{\hat{u}}{\hat{b}} = \frac{\tau_d \cot\alpha (l^2\tau_d - k^2\bar{u})}{\xi\nu p} \tag{3.14}$$

$$T_{vb}(k,l) = \frac{\hat{v}}{\hat{b}} = \frac{kl\tau_d \cot\alpha (\tau_d + \nu\bar{u})}{\xi\nu p} \tag{3.15}$$

which represent the ratio of the Fourier components of the surface to the Fourier components of the bed as a function of wave number. The following abbreviations are used for simplicity in the derivation: $\xi = \gamma + 4\bar{h}j^2\eta$, $\gamma = \frac{\tau_d^{1-m}}{m\bar{c}}$, $j^2 = k^2 + l^2$, $\tau_d = \rho g\bar{h}\sin\alpha$, $p = \frac{\mathrm{i}}{t_p} - \frac{1}{t_r}$, $\frac{1}{t_p} = k\left(\bar{u} + \frac{\tau_d}{\xi}\right)$, $\frac{1}{t_r} = \frac{j^2\tau_d\bar{h}\cot\alpha}{\xi}$, and $\nu = \gamma + \bar{h}j^2\eta$.

Response of flow to basal slipperiness perturbation

Starting once again with the shallow-ice-stream equations (Equations 3.1 and 3.2; MacAyeal, 1989), this time we consider the response to a small perturbation in basal slipperiness, c, linearising with $h = \bar{h} + \Delta h = \bar{h} + \Delta s$, $s = \bar{s} + \Delta s$, $b = \bar{b}$, $u = \bar{u} + \Delta u$, $v = \Delta v$, $w = \Delta w$ and $c = \bar{c}(1 + \Delta c)$ where Δc is the fractional slipperiness.

This gives the first order momentum balance equations

$$4\eta\bar{h}\partial_{xx}^2\Delta u + 3\eta\bar{h}\partial_{xy}^2\Delta v + \eta\bar{h}\partial_{yy}^2\Delta u - \gamma\Delta u = \rho g\bar{h}\cos\alpha\partial_x\Delta s - \rho g\sin\alpha\Delta s - \gamma\bar{u}\Delta c \tag{3.16}$$

$$4\eta\bar{h}\partial_{yy}^2\Delta v + 3\eta\bar{h}\partial_{xy}^2\Delta u + \eta\bar{h}\partial_{xx}^2\Delta v - \gamma\Delta v = \rho g\bar{h}\cos\alpha\partial_y\Delta s \tag{3.17}$$

Fourier transforming with respect to the spatial variables x and y gives:

$$4\eta\bar{h}k^2\hat{u} + 3\eta\bar{h}kl\hat{v} + \eta\bar{h}l^2\hat{u} + \gamma\hat{u} = \rho g\bar{h}\cos\alpha ik\hat{s} + \rho g\sin\alpha\hat{s} + \gamma\bar{u}\hat{c} \tag{3.18}$$

$$4\eta\bar{h}l^2\hat{v} + 3\eta\bar{h}kl\hat{u} + \eta\bar{h}k^2\hat{v} + \gamma\hat{v} = \rho g\bar{h}\cos\alpha il\hat{s} \tag{3.19}$$

As there is no bed topography perturbation, the steady-state boundary conditions become

$$i\bar{h}(k\hat{u}+l\hat{v}) = -ik\bar{u}\hat{s}. \tag{3.20}$$

Equations 3.18, 3.19 and 3.20 form a linear system of equations which can be solved using standard algebraic techniques (see Appendix 3.7.2), leading to the steady-state transfer functions

$$T_{sc}(k,l) = \frac{\hat{s}}{\hat{c}} = -\frac{\mathrm{i}k\bar{h}\bar{u}\gamma}{p\xi} \tag{3.21}$$

$$T_{uc}(k,l) = \frac{\hat{u}}{\hat{c}} = \frac{\gamma\bar{u}\Big((3\eta\bar{h}l^2+\nu)(ik\bar{u}) - l^2\tau_d\cot\alpha\bar{h}\Big)}{\xi\nu p} \tag{3.22}$$

$$T_{vc}(k,l) = \frac{\hat{v}}{\hat{c}} = \frac{kl\gamma\bar{u}\bar{h}\big(\tau_d\cot\alpha - 3i\eta\bar{u}k\big)}{\xi\nu p} \tag{3.23}$$

which represent the ratio of variability in the Fourier components of the surface to variability in the Fourier components of the slipperiness.

Note that the transfer functions T_{uc} and T_{vc} are not the same as the steady-state versions of the transfer functions published in Gudmundsson (2008), as there is a typographic error in their paper. However, when plotted graphically, they can be used to reproduce the figures in that paper.

Non-dimensionalisation

These transfer functions can also be considered in a non-dimensional form, allowing us to make more general statements about the behaviour of the system in terms of key variables, such as ice thickness as the characteristic length scale. For this purpose the same scalings as used in Gudmundsson (2003) and Gudmundsson (2008) are employed. All spatial scales are in units of mean ice thickness ($\bar{h}$), and stress components are in units of driving stress ($\tau_d = \rho g\bar{h}\sin\alpha$). Non-dimensional velocity components are in units of mean deformational velocity ($\bar{u}_d$) where

$$\bar{u}_d = \frac{\bar{h}\tau_d}{2\eta}. \tag{3.24}$$

The scale for slipperiness is given by $\bar{c}/\bar{C}$, where $\bar{c}$ is the mean dimensional slipperiness and $\bar{C}$ is the mean non-dimensional slipperiness. $\bar{C}$ depends on not only slipperiness but also viscosity and thickness (through its dependence on u_s and τ_d). From Gudmundsson (2008) we know that $\bar{c}/\bar{C} = \bar{u}_d/\tau_d^m$ and we also have $\bar{C} = \bar{u}_b/\bar{u}_d$. The ice surface velocity is the sum of the deformational velocity and the basal velocity, such that $\bar{u}_s = \bar{u}_d + \bar{u}_b$. With some simple algebra, we can therefore express the scale for slipperiness in terms of the surface velocity $\bar{u}_s$, which is a known quantity,

$$\frac{\bar{c}}{\bar{C}} = \frac{\bar{u}_s}{\tau_d^m(\bar{C}+1)}. \tag{3.25}$$

The non-dimensional form of the equations is obtained using the substitutions $\bar{c} \mapsto \bar{C}$, $\eta \mapsto 1/2$, $\bar{h} \mapsto 1$, $\bar{u} \mapsto \bar{C}$, $\gamma \mapsto (m\bar{C})^{-1}$, and $\tau_d = \rho g \bar{h} \sin\alpha \mapsto 1$. The non-dimensional transfer functions can be found in the supplementary information, and are also shown graphically there. Non-dimensionalised parameters are represented by capital letters (B, C, S, U, V, T_{SB}, T_{UB}, T_{VB}, T_{SC}, T_{UC} and T_{UV}).

3.3.2 The inverse problem

The non-dimensional transfer functions (T_{SB}, T_{UB}, T_{VB}, T_{SC}, T_{UC} and T_{VC}) describe the relationship between the Fourier transforms of non-dimensionalised bed topography ($\hat{B}$), bed slipperiness ($\hat{C}$), surface topography ($\hat{S}$) and surface velocity ($\hat{U}, \hat{V}$), as functions of the wavenumbers k and l. If the bed topography and slipperiness are known then surface topography and velocity components are given by the forward model:

$$\hat{S}(k,l) = T_{SB}(k,l)\,\hat{B}(k,l) + T_{SC}(k,l)\,\hat{C}(k,l) \tag{3.26}$$

$$\hat{U}(k,l) = T_{UB}(k,l)\,\hat{B}(k,l) + T_{UC}(k,l)\,\hat{C}(k,l) \tag{3.27}$$

$$\hat{V}(k,l) = T_{VB}(k,l)\,\hat{B}(k,l) + T_{VC}(k,l)\,\hat{C}(k,l) \tag{3.28}$$

For each set of wavenumbers in Fourier space (k and l) we have three known variables ($\hat{S}(k,l)$, $\hat{U}(k,l)$ and $\hat{V}(k,l)$) and two unknowns ($\hat{B}(k,l)$ and $\hat{C}(k,l)$), so the system is over-determined. We can therefore solve these equations independently for each wavenumber component of non-dimensional bed topography and slipperiness using a weighted least-squares inversion of equations 3.26, 3.27 and 3.28. Short-wavelength features and features aligned with ice flow are problematic because they cause flow disturbances in the ice which do not reach the surface in a measurable way, and so they can not be inverted from the surface data. We include a filtering parameter (p_{filt}) to remove these problematic wavelength components, such that increasing the filtering parameter (p_{filt}) removes progressively longer wavelength features. The filtering parameter p_{filt} is negative, so increases towards zero. This method was first used by Thorsteinsson et al. (2003) in their study of MacAyeal Ice Stream (formerly Ice Stream E). The equations which solve Equations 3.26, 3.27, 3.28 are therefore not repeated here in the main text, but are given in notation consistent with this paper in Appendix 3.7.3.

3.3.3 Synthetic tests

Synthetic tests allow us to explore which bed features can and can not be resolved using this inversion method. First we create a synthetic bed topography (b) and slipperiness (c) on a 50 km by 50 km grid, with a 120 m data spacing, purposely matching the data spacing of the ITSLIVE velocity product (Gardner et al., 2018). We subtract the mean bed elevation, slope and slipperiness so that the bed varies about 0, and taper the outer 5 km of the grid linearly to 0 at the edges. This reduces edge effects in the inversion,

because the Fourier transform requires a periodic domain. We tested a few other sensible tapering functions, including semi-sinusoids, but observed negligible differences in the inversion output when compared to the linear function. We then non-dimensionalise the tapered bed using the length scales given in Section 3.3.1, and Fourier transform to get $\hat{B}$ and $\hat{C}$. The non-dimensional surface elevation ($\hat{S}$) and the velocity components ($\hat{U}$, $\hat{V}$) are calculated using the forward model, and dimensionalised using the length scales given in Section 3.3.1. To simulate measurement errors in the real surface data, we add random noise to the generated surface (s, u, v). This noise is white noise with a Gaussian low pass filter applied in Fourier space to give it a non-random frequency distribution. We then taper, non-dimensionalise and Fourier transform the noise-added surface data. Finally, we invert for non-dimensional bed topography ($\hat{B}$) and slipperiness ($\hat{C}$) using the inversion procedure described in Section 3.3.2 and the supplementary information. After dimensionalisation, the inverted bed can be compared to the synthetic bed to study the behaviour of the inversion.

Parameter value choices

When running synthetic tests, several model parameters can be varied, in addition to the synthetic bed topography and slipperiness. Following Gudmundsson (2008) and Thorsteinsson et al. (2003) the sliding law constant was set to $m = 1$, and the filtering parameter (Equation 3.36) to $p_{filt} = -2$. The mean ice thickness $\bar{h}$, mean surface slope α and mean ice surface velocity $\bar{u}$ depend on the region studied, but for these synthetic tests are set at $\bar{h} = 2000$ m, $\alpha = 0.02$, $\bar{u} = 100\text{ms}^{-1}$, values thought to be appropriate for the Thwaites Glacier region (Gudmundsson, 2008; Howat et al., 2019; Morlighem et al., 2020; Gardner et al., 2018). After studying the results of the Thwaites Glacier inversion for a variety of values of $\bar{C}$, the non-dimensional mean slipperiness parameter which encompasses basal slipperiness alongside ice temperature and viscosity, we set to be $\bar{C} = 100$. When applied to Equation 3.25, these values give a dimensional mean slipperiness $\bar{c} = 2.7\text{ x}10^{-3}\text{ myr}^{-1}\text{Pa}^{-1}$. Since the non-dimensionalised velocity perturbations are expected to be around 10^0 in magnitude, and the non-dimensionalised surface elevations are expected to be around 10^{-3}, we set the weighting factors (Equation 3.35) to be $\Sigma_s = 0.001$, $\Sigma_u = 1$ and $\Sigma_v = 1$. This normalises the least-squares distance for each component of the system, and means the least-squares inversion should solve for all three factors equally.

Resolution of bed forms

A two-dimensional Fourier transform decomposes an image into a weighted sum of two-dimensional sinusoidal basis functions. For this reason, all of our synthetic tests used sinusoidal bed topographies and slipperiness, as these are the most illustrative of the capabilities of the inversion. Sinusoidal basis functions vary depending on three parameters: the wavenumbers in the x and y directions (k,l) and the weighting or amplitude of the

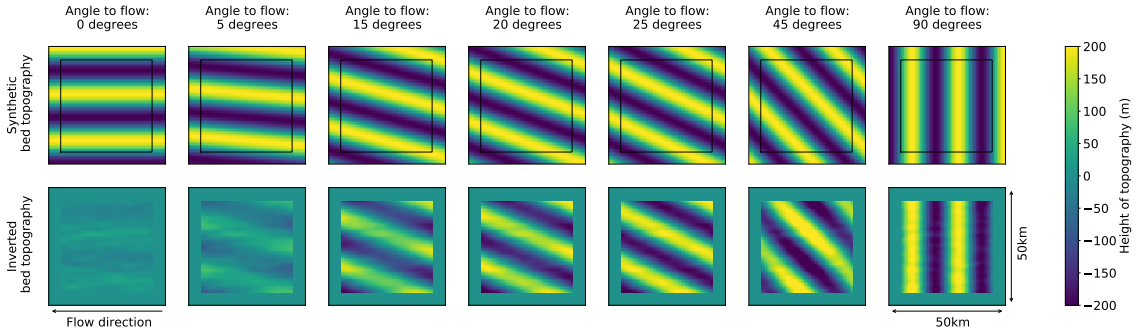

Fig. 3.1 The effect of orientation to flow direction on how well landforms (top row; created synthetically) can be resolved by the inversion. These tests are presented on a 50 km by 50 km grid, where in the inversion results (bottom row) the outer 5 km is greyed out to hide edge effects that will be neglected. In these simulations mean ice thickness $\bar{h}$ = 2000 m, mean slipperiness $\bar{C}$ = 100, surface slope α = 0.02, amplitude = 200 m, and wavelength λ= 20 km. Landforms at an angle of less than 15° to the ice flow direction are not well resolved because they fall in the null space of the inversion.

sinusoid. However, rather than considering wavenumbers, it is more intuitive to consider the horizontal wavelength, λ, and the angle of the sinusoidal crests to the direction of the flow (θ'), where $j^2 = l^2 + k^2$, $\lambda/\bar{h} = 2\pi/j$, $k = j\cos(\theta)$, $l = j\sin(\theta)$ and $\tan(\theta') = \cot(\theta)$.

Figures 3.1, 3.2 and 3.3 show how well bed topography and slipperiness can be resolved by the inversion when angle to flow, θ', wavelength, λ, and amplitude are varied. The amplitude of the noise added to the synthetically generated surface is $\pm$2 m for surface elevation and $\pm$15 m s^{-1} for velocity components as these are at the upper limit of the errors for REMA (Howat et al., 2019) and ITSLIVE (Gardner et al., 2018) in the Thwaites Glacier region.

These synthetic tests show that in this simple least-squares inversion, the bed can be well resolved if the angle to the flow is greater than 15 degrees, the wavelength is more than 2000 m and the amplitude is greater than 10 m for bed topography or 1 x10^{-4} myr^{-1}Pa^{-1} for variability in basal slipperiness. It is worth noting, however, that the resolution of wavelengths varies depending on the ice thickness, which is the non-dimensional scale factor for lengths. This means that the wavelength at which variations in bed topography and slipperiness should be resolvable is directly proportional to the ice thickness.

3.3.4 Applying the inversion to real data

We now turn our attention to the methodology used to apply the synthetically tested inversion to real data, using the Thwaites Glacier catchment as our example.

Our base data for surface elevation and velocity were, respectively, the REMA digital elevation model with 8 m resolution (Howat et al., 2019) and output from the NASA MEaSURES ITS-LIVE project with 120 m resolution (Gardner et al., 2018). Based on the latter, we therefore inverted for bed topography and slipperiness at 120 m resolution. An estimate of the ice thickness in each 50 km by 50 km region is obtained from a 50 km

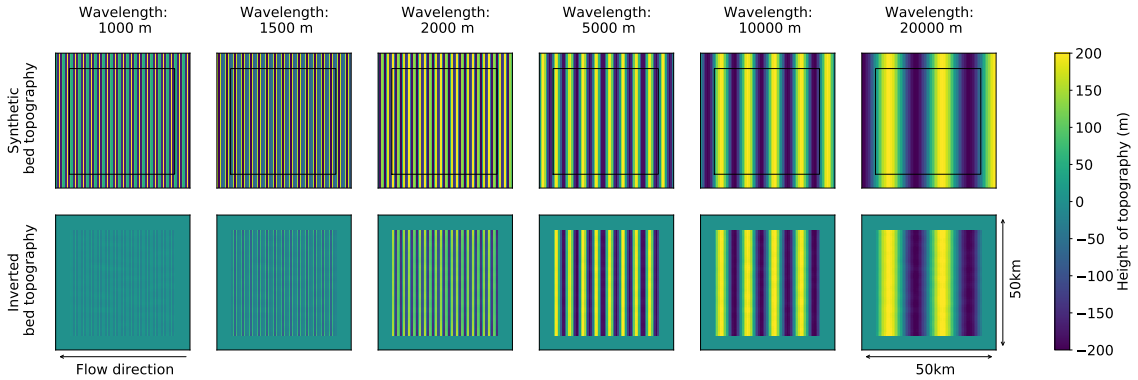

Fig. 3.2 The effect of wavelength on how well landforms (top row; created synthetically) can be resolved by the inversion. These tests are presented on a 50 km by 50 km grid, where in the inversion results (bottom row) the outer 5 km is greyed out to hide edge effects that will be neglected. In these simulations mean ice thickness $\bar{h} = 2000$ m, mean slipperiness $\bar{C} = 100$, surface slope $\alpha = 0.02$, amplitude = 200 m, and angle to flow $\theta' = 90°$. Landforms with a wavelength of less than 2 km (the simulated mean ice thickness) can not be well resolved.

averaged version of Bedmachine Antarctica ice thickness (Morlighem et al., 2020), and this is the only prior information about ice thickness used in the inversion. Within each grid where the inversion is applied, the surface elevation, s, has the mean least-squares fit slope removed and is non-dimensionalised (see scalings in Section 3.3.1) to give S, the non-dimensional variations about the mean. Ice flow is assumed to be parallel to the polar stereographic grid in the negative x direction across the whole of the main trunk of Thwaites Glacier, and so the ice-surface velocity components, u and v, have their respective means removed and are non-dimensionalised to give U and V, to which the least squares inversion described in Section 3.3.3 is applied.

In the synthetic tests discussed above, the inversion was run over a single 50 km by 50 km grid, with the outer 10 % of the grid discarded to reduce edge effects introduced during the Fourier transform. To look at the whole Thwaites catchment we could use a set of adjacent 50 km by 50 km grids, but instead we chose to use more densely distributed grids which overlap. For each grid point, we calculate 9 different (but overlapping) inverted beds and then the mean bed topography and standard deviation. The standard deviation is **not** a measure of the error, but since a key approximation in the physics is the linearisation, we interpret the standard deviation to be a measure of non-linearity. In each of the overlapping grids, we use a set of zero order parameters (such as average ice thickness), and because these zero-order parameters vary between the grids, the linearisation is different, and the resulting beds are also different. However, complex ice rheology and vertical or transverse stresses not considered by the shallow-ice-stream approximation could also have an impact. Figure 3.4a summarises this methodology. The bed topography and slipperiness results presented here are the grid-point by grid-point means of nine overlapping grids where each

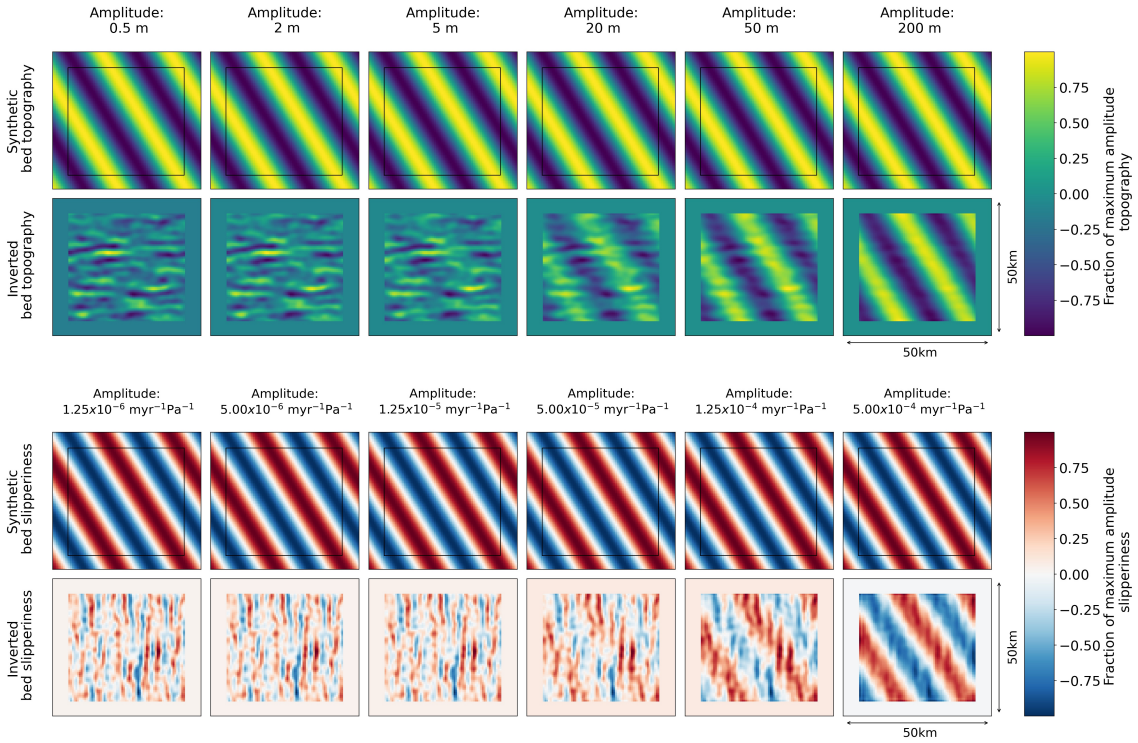

Fig. 3.3 The effect of amplitude on how well landforms and slipperiness (rows 1 and 3, respectively; created synthetically) can be resolved by the inversion. These tests are presented on a 50 km by 50 km grid, where in the inversion results (rows 2 and 4, respectively) the outer 5 km is greyed out to hide edge effects will should be neglected. In these simulations mean ice thickness $\bar{h} = 2000$ m, mean slipperiness $\bar{C} = 100$, surface slope $\alpha = 0.02$, wavelength $\lambda = 20$ km and angle to flow $\theta' = 120°$. The limiting factor on how well small amplitudes can be resolved is errors in the ice-surface data, which are simulated by adding noise to the synthetic surface generated from the synthetic bed. Noise is added with an amplitude of 2 m for the ice surface elevation (Howat et al., 2019), and an amplitude of 15 ms^{-1} for the ice surface velocity (Gardner et al., 2018). Bedforms with an amplitude of less than 10 m (0.01 $\bar{h}$), and slipperiness of less than around 1x10^{-4} m yr^{-1} Pa^{-1} (0.01 $\bar{C}$) are not well resolved.

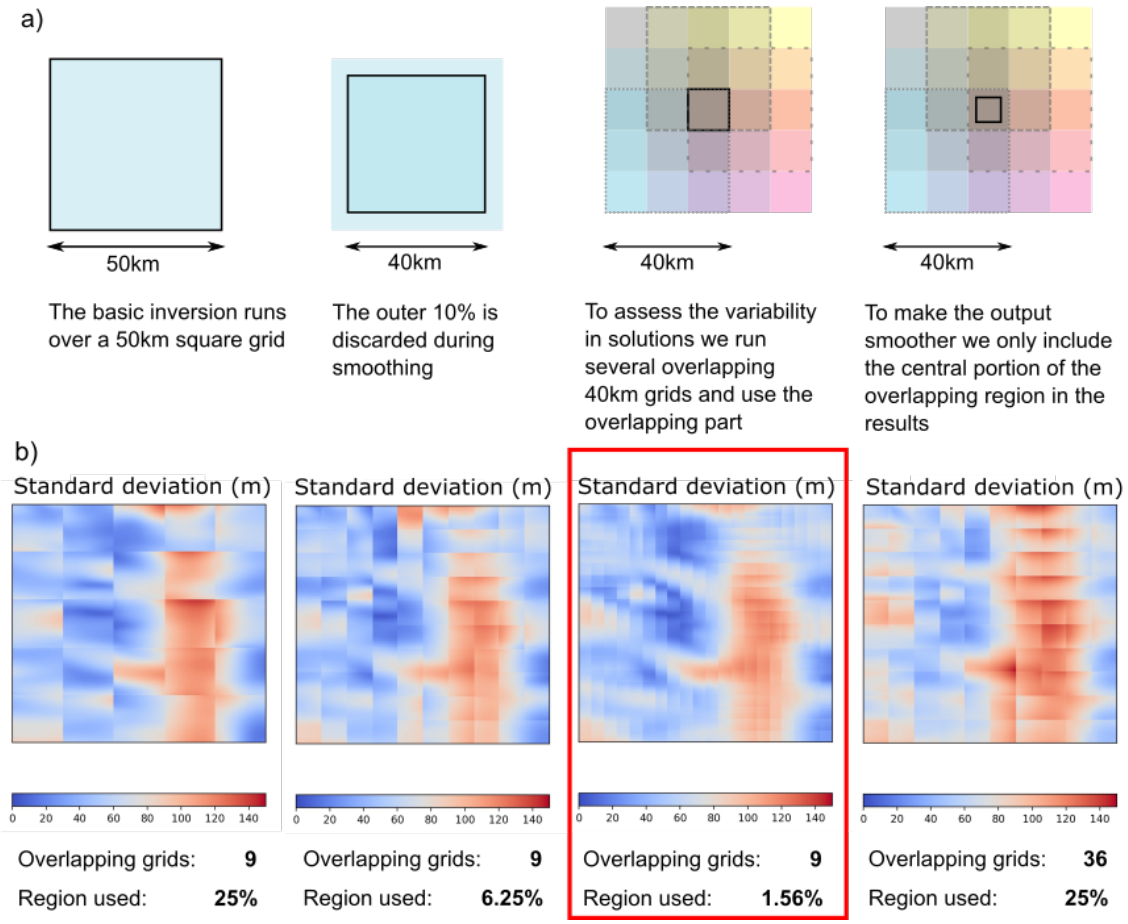

Fig. 3.4 a) Multiple overlapping grids are used in the inversion when applied to real data to allow the variability between solutions to be studied. b) The effect of changing the number of overlapping grids and the fraction of the overlapping central region used to calculate the standard deviation of bed topography from the inversion in a roughly 60 km by 60 km region.

overlapping region is 1.67 km by 1.67 km. These values were chosen following tests on a small region of the real data (Figure 3.4b).

When applied to real surface-elevation and velocity data, this method generates four products: the mean and standard deviation of bed topography and the mean and standard deviation of bed slipperiness. The standard deviation is **not** a measure of the error in the bed topography or bed slipperiness, and should not be interpreted as such.

3.4 Results for Thwaites Glacier

Figure 3.5 shows the bed conditions we inverted from REMA (Howat et al., 2019) and ITSLIVE (Gardner et al., 2018) over a 280 km by 160 km region of the main trunk of Thwaites Glacier.

The bed topography product from the inversion is shown in Figure 3.5b. On the basin scale, the main basal topographic features identified by the inversion are several

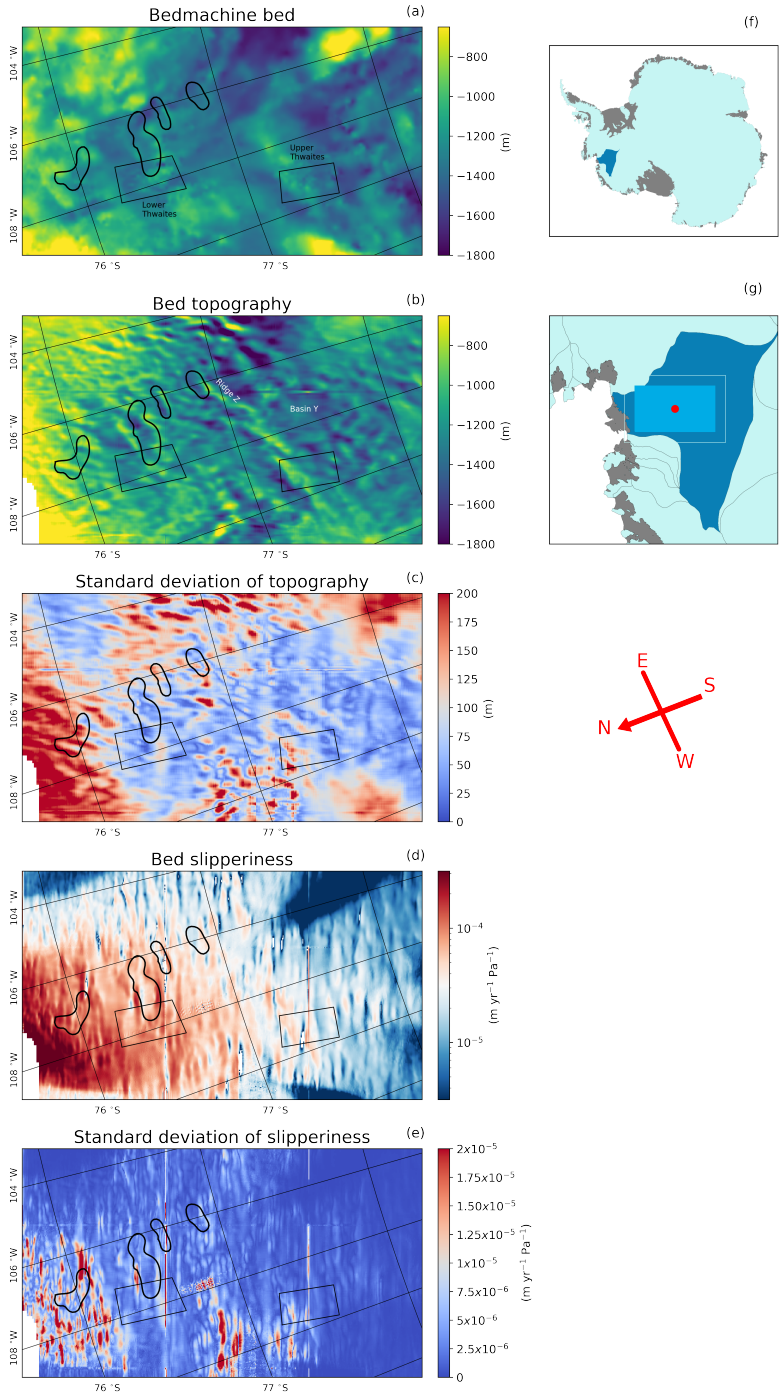

Fig. 3.5 Inversion outputs across a 160 km by 280 km region of Thwaites Glacier (location shown in panels f) and g)). The compass directions shown are accurate at the center of the region (red dot in panel g), but may vary by up to 10 degrees across the region due to the polar stereographic projection. a) Bed topography from BedMachine Antarctica (Morlighem et al., 2020), and b) bed topography, c) standard deviation of bed topography, d) bed slipperiness and e) standard deviation of bed slipperiness from our inversions of REMA (Howat et al., 2019) and ITSLIVE (Gardner et al., 2018) at 120 m resolution. Standard deviations are a measure of variability between overlapped patches and should **not** be inerpreted as a measure of the error in the bed topography or bed slipperiness. Black rectangles depict regions of pre-existing highly resolved bed topography (Holschuh et al., 2020) examined in Figure 3.6. The four subglacial lakes observed from surface altimetry changes by Smith et al. (2017) are also outlined in black.

sets of parallel ridges which are oriented perpendicular to the direction of ice flow, and smooth basins in between these ridges. The location of these ridges matches well with the BedMachine Antarctica bed (Figure 3.5a), particularly around the subglacial lakes, which appear to be between successive sets of ridges. The smoother topography in the basins between ridges is reflected in the inversion, particularly in the basin to the east of the Upper Thwaites region (Basin Y, Figure 3.5). Many smaller hills also match Bedmachine Antarctica, such as those at the upstream (south) end of the Upper Thwaites radar grid. However, the inversion also generates some notable features that are not present in the Bedmachine Antarctica bed, such as the north-eastern extent of the central ridge next to the most upstream subglacial lake (Ridge Z, Figure 3.5b).

The standard deviation of the bed topography (Figure 3.5c) represents the range in model outputs from overlapping grid squares which use different regions of the ice surface. As might be expected, this standard deviation is lower in the central trunk of the glacier where the topographic gradients are smaller. The standard deviation is higher at the edges of the glacier trunk where the gradient of the topography changes, and the shallow-ice-stream approximation breaks down. Standard deviation is also high in the north-west part of the inversion where some of the input surface is the surface of the floating ice shelf, which is subject to different physical processes than the grounded ice. The inversion does not produce results for the north-west corner as there are gaps in the input data where the surface sampled is not ice, but open ocean.

The bed slipperiness product from the inversion is shown in Figure 3.5d. The pattern in the slipperiness output is similar to the topography, with a dominant east to west lineation, although it is slightly difficult to make out due to the strong underlying slipperiness variation across the Thwaites Glacier region. This directional trend in slipperiness is also observed in the slipperiness output of other inversions in the Thwaites Glacier region (Barnes et al., 2021). There is less variability in slipperiness in the basins where the topography is smoother. In contrast the ridges have much more variable slipperiness. Like the standard deviation of bed topography, the standard deviation of bed slipperiness (Figure 3.5e) is highest around the edges of the central trunk where there are higher topographic gradients.

3.4.1 Comparison to radar data

In order to assess the success of the inversion, the bed topography output can be compared to existing radar data. Figure 3.6 shows a comparison between the inverted bed topography and bed topography sounded by swath radar at sub-ice thickness resolution across two 20 km by 40 km regions (Holschuh et al., 2020). The inverted bed shows a good match to the swath-radar-imaged bed at larger scales, picking out the locations of all the main hills and valleys. There is a better match for the Upper Thwaites region than the Lower Thwaites region, and the fact that the inversion detects the channel between the ridges in the downstream (left) part of Upper Thwaites is particularly encouraging.

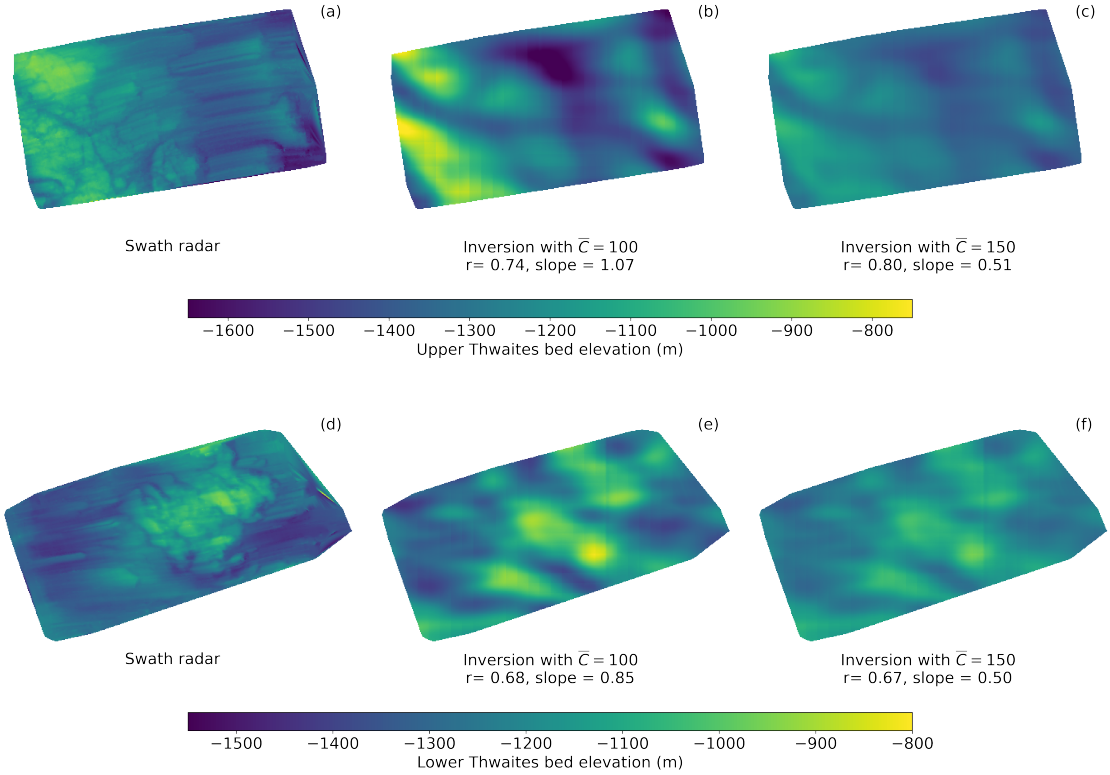

Fig. 3.6 a) Bed topography acquired at sub-ice-thickness resolution by swath radar (Holschuh et al., 2020); b) our inverted bed topography with mean non-dimensional slipperiness $\bar{C} = 100$; and c) our inverted bed topography with mean slipperiness $\bar{C} = 150$, for site labelled 'Upper Thwaites' in Figure 3.5a. d), e) and f) show equivalent products for site labelled 'Lower Thwaites' in Figure 3.5a. The results of a simple linear regression between the swath radar bed and the inverted bed are also given, with r being the regression coefficient and slope the gradient of the line of best fit. A slope of 1 means the amplitude of the inverted bed matches the amplitude of the swath radar bed.

We further compare the inverted bed topography with the bed topography sounded by swath-radar along ice flow (Figure 3.7) and across ice flow (Figure 3.8) by airborne radar over Thwaites Glacier in the 2019/2020 field season (Jordan and Robinson, 2021). Further comparisons to more radar flight lines collected in the same field season can be seen in the supplementary information. These figures also demonstrate that the inversion performs well in detecting the main hills and valleys, but also highlights that their amplitudes are not always resolved correctly. This is likely due to variability in the local mean slipperiness away from the imposed global value of non-dimensional slipperiness $\bar{C} = 100$. If a non-dimensional slipperiness $\bar{C} = 150$ is imposed (Figures 3.6, 3.7c, 3.8c) then the amplitudes of the inverted topography are reduced. Sometimes there is also an offset between the inverted and radar-sounded beds, caused by using a 50 km averaged version of the Bedmachine ice thickness as the inversion ice thickness, rather than more detailed prior information.

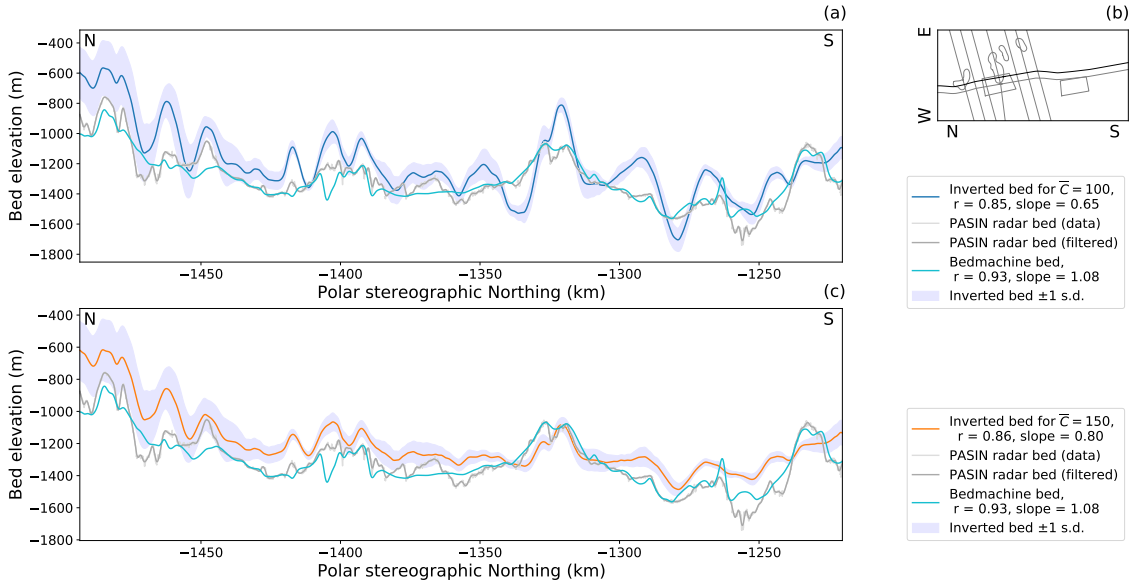

Fig. 3.7 a) Comparative plot of inverted bed topography with mean non-dimensional slipperiness $\bar{C} = 100$ with along-flow radar-sounded bed topography. Bed topography is given in three forms: as unfiltered bed picks from the 2019/20 airborne surveys (Jordan and Robinson, 2021); a version of the same filtered to 2 km wavelengths to be more representative of the detail we might expect to image in our inversion; and the bed profile extracted from BedMachine Antarctica (Morlighem et al., 2020). The envelope around the inverted bed topography shows plus or minus one standard deviation. Standard deviations are a measure of variability between overlapped patches and should **not** be inerpreted as a measure of the error in the bed topography or bed slipperiness. The correlation coefficients (r) and slopes given are the results of a linear regression between the inverted bed or the BedMachine Antarctica bed and the filtered radar bed. b) Profile location within the inverted grid. c) As for panel a) but with mean non-dimensional slipperiness $\bar{C} = 150$.

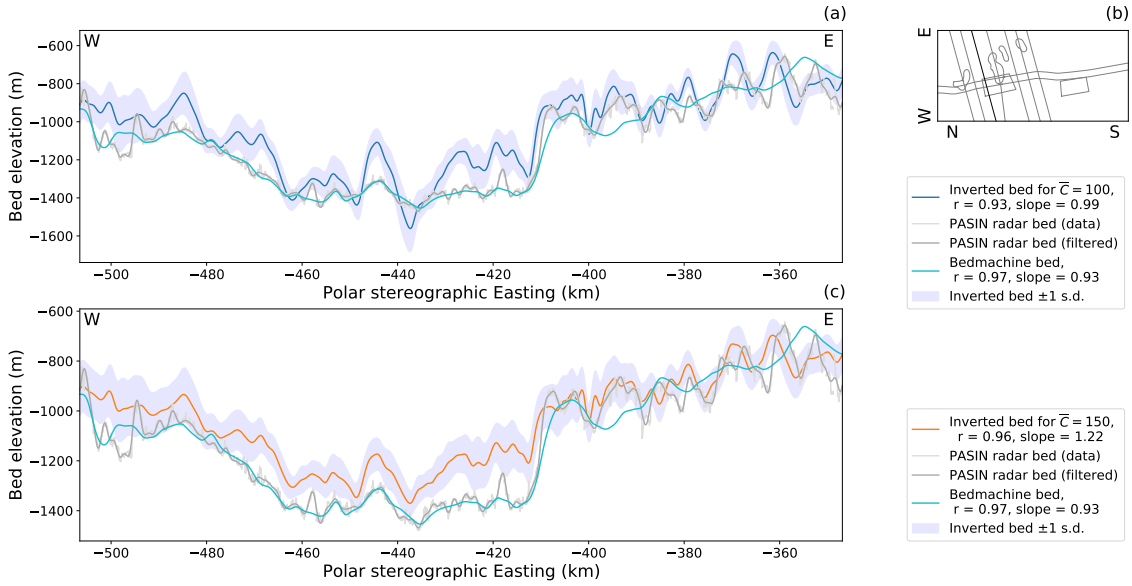

Fig. 3.8 Comparative plot of inverted bed topography with across flow radar-sounded bed topography. Key as for Figure 3.7.

3.5 Discussion

Our results demonstrate significant promise for being able to invert for bed topography across parts of Antarctica and other polar regions from surface elevation and velocity data sets. Comparisons with existing radar data available from Thwaites Glacier suggest that within the central trunk of the glacier the bed features identified by the inversion are normally in the correct locations, but are not always centred around the correct depth. These average depth differences are primarily due to the mean ice thickness used in the inversion, which is a 50 km averaged version of the Bedmachine Antarctica ice thickness (Morlighem et al., 2020). For regions where there are radar flight lines and grids, these radar observations could be used instead of the averaged ice thickness to ensure that the bed depth is correct. For regions where there are very few existing radar data, this method has the potential in the future to identify obstacles to flow which are significant enough to affect surface ice dynamics, even if there is uncertainty about the local or regional ice thickness. Additionally, the assumption of a mean uniform background state, applied here with this 50 km averaged ice thickness, does not represent the real conditions at Thwaites Glacier, where the long-wavelength background conditions are more variable. Ng et al. (2018) applied a non-uniform background state to look at the relationship between perturbations in the bed and the ice surface on flowlines from Columbia Glacier and Nordenskiöld Glacier, but this non-uniform background approach has not yet been extended to 3D data.

The regions where the inverted bed deviates significantly from the topography picked from radar surveys are of particular interest in assessing the potential of our inversion. Differences between inverted topography and radar lines are likely to be due to physical processes which are not encapsulated by the shallow-ice-stream approximation. One place in which the shallow-ice-stream approximation is known to break down is where the mean slope of the bedrock becomes too steep (Gudmundsson, 2003; Le Meur et al., 2004). The effect of this can be observed around the edges of the central trunk of the glacier, where the topographic slope is steep, and the match between the inverted bed and the radar lines is poor (Figure 3.5). Gudmundsson (2003) derived a full-system non-hydrostatic momentum balance version of the transfer function used in this work. The full-system approach does not rely on the shallow-ice-stream approximation, and should therefore perform better. Future work using this method is likely to incorporate these more complex equations.

A further consideration in comparing the inverted bed to real data is the steady-state assumption made when deriving the transfer functions. Without repeat radar measurements for Thwaites Glacier we can not be sure of the stability of the bed. If the bed beneath Thwaites Glacier is changing rapidly, as observed at Rutford Ice Stream (Smith et al., 2007) then the surface may not represent the current bed, but some long term average. However, observations at Pine Island Glacier (Brisbourne et al., 2017; Davies et al., 2018) suggest that the bed is not changing rapidly there, and it is possible that neighbouring Thwaites Glacier might be behaving similarly. Additionally, the erosion observed at Rutford Ice

Stream does not significantly change the shape of the topography on the wavelengths resolved by this inversion. If drumlins or mega-scale glaciation lineations (MSGL) were forming, we would not be able to detect them with this method, as landforms aligned to flow fall in the null space of the inversion.

The steady state assumption does not only apply to the bed but also to the ice surface. Ice surface lowering due to glacier thinning would also affect the steady state assumption, but since generally the ice surface lowers in a relatively uniform way, this would not have a significant effect on the first order variations in the ice surface, or the results of the model. More significant would be changes in the ice surface due to the filling and draining of subglacial lakes, but these changes are normally fairly localised, and would not propagate to the higher wavelength Fourier components. For Thwaites Glacier, the location of subglacial lakes is relatively well known (Smith et al., 2017; Hoffman et al., 2020; Malczyk et al., 2020), and we do predict troughs in these locations as expected. The ice surface also becomes more unstable closer to the grounding line, with increased crevassing which would affect the surface profile. However, since results in the region immediately adjacent to the grounding line are compromised by the different physics of the ice shelf anyway, this is not a significant concern. With these caveats, we therefore consider the steady-state assumption to be suitable for the purposes of this inversion.

If the steady state assumption is valid, then the age of the datasets used in the inversion is not important. However, input data from different years or decades could also affect the steady-state assumption. The main surface expressions of known bed features appear to be fairly similar between REMA (Howat et al., 2019) (2008-2018), and the earlier Bamber DEM (Bamber et al., 2009) (2003-2008), supporting the validity of the steady-state assumption for Thwaites Glacier. However, we also note that non-steady-state changes in the ice surface may be the reason for some of the features we observe (such as Ridge Z, Figure 3.5) in the inversion output which are not seen in the airborne flight lines.

Although we assume linear viscous ice here ($n = 1$), ice is generally accepted to flow with non-linear viscous behaviour ($n = 3$ to 4). In this case, the ice near the surface of the ice column has a higher effective viscosity than the ice at the base. Jóhannesson (1992) and Raymond and Gudmundsson (2005) showed that, over the range of wavelengths which have significant impacts on the ice-surface flow field, increasing viscosity means that the transfer of variability from the bed to the surface would generally increase. For the inverse problem, assuming $n = 1$ will therefore lead to an over-estimate in the amplitude of the bed topography, although this may be counteracted by the choice of the mean non-dimensional slipperiness parameter $\bar{C}$, which encompasses both basal slipperiness and ice viscosity.

As in any modelling study, it is important to explore the behaviour of the inversion when the parameters chosen are varied. In this inversion there are just four fixed parameters which are not derived from the input data: the sliding law exponent, m, the filtering parameter, p_{filt}, the weighting factor Σ_s and the mean slipperiness, $\bar{C}$. The filtering parameter p_{filt} controls which frequencies are suppressed in the inversion to avoid introducing singularities.

Higher values of p_{filt} (closer to 0), will filter out progressively longer wavelengths, and so a value of $p_{filt} = -2$ is chosen to filter out noisy short wavelengths, while maintaining realistic bed features. The weighting factor Σ_s controls the balance in the inversion between the surface elevation and surface velocity data, with smaller values of Σ_s weighting the inversion towards the surface data. Varying p_{filt} and Σ_s for the inversion of the real surface data confirms the choice of values from the synthetic tests ($p_{filt} = -2$, $\Sigma_s = 0.001$) as sensible values which return the best match with real bed data (Figures S3 and S4).

There is less certainty over what is the most suitable value for the non-dimensional mean slipperiness $\bar{C}$. Although we have some measurements of the bed properties of Thwaites glacier from seismic lines, gravity and magnetic inversions (Diehl, 2008; Jordan et al., 2010; Muto et al., 2019a), these are spatially limited and it is not currently clear how these properties combine into slipperiness at the bed (Kyrke-Smith et al., 2017). If $\bar{C}$ is higher, then the amplitude of bed variability in the inversion output falls. Given the geological variability likely to be associated with multiple rifted tectonic blocks (Dunham et al., 2020) and the sediments deposited in those rift basins (Muto et al., 2019a,b) it is unlikely that the mean slipperiness, $\bar{C}$, is the same across the whole region modelled here. Modelling studies which compare the results of different inversion procedures show that slipperiness may be quite variable across the Thwaites Glacier catchment (Barnes et al., 2021). In additional we note that the trend is quite different from features observed in the inverted topography, showing that the slipperiness map is not a result of linear trade-offs with topography in the inversion solution. The three dimensional radar grids (Holschuh et al., 2020) are both located within regions with more topographic variability, likely unlifted rift blocks. This may explain why a lower value of $\bar{C} = 100$ gives the best match in these regions, whereas a higher value of $\bar{C} = 150$ (more slippery) gives a better match for the radar lines which cover both lithologies. It may also be that the 3D grids, which contain both along and across flow variability, are more representative of the bed than the 2D radar lines. For this reason, the catchment scale bed topography presented in Figure 3.5 is from the inversion with $\bar{C} = 100$.

This uncertainty in $\bar{C}$ means that some prior radar information is useful in order to calibrate the inversion method to give the best results. However, changing $\bar{C}$ only alters the absolute magnitude of the topography and not its relative shape, so even if there is no prior information the inversion will still identify hills and troughs. More detailed analysis of seismic and gravity data alongside the results of the inversion could also reveal trends that could be useful when applying this technique elsewhere.

The high-resolution swath radar grids (Holschuh et al., 2020) presented here have already been included in Bedmachine Antarctica. Using the radar grids which are currently available, we can not therefore explore how well this inversion method performs compared to Bedmachine Antarctica (Morlighem et al., 2020) over a dense radar grid. Both techniques use ice surface elevation and velocity datasets. Bedmachine Antarctica uses these datasets and the principles of mass conservation (or streamline diffusion in slow moving areas)

to interpolate between detailed prior information on ice thickness from existing radar measurements. In contrast, the inversion method only requires an estimate of average ice thickness for each 50 km by 50 km grid and uses the linear perturbation theory described. This 50 km averaged ice thickness is subtracted from the ice surface to provide a reference bed to which the inversion adds perturbations. However, even if a single ice-thickness ($\bar{h}$) value is used for the entire catchment, then the inversion method will still identify the location of hills and troughs in the bed topography, although the amplitudes and absolute depths of these features may be affected. Since the mass conservation method used in Bedmachine assesses the ice flow through a series of flux gates ideally constrained by topography, it is much more reliant on good-quality, closely-spaced, ice thickness measurements from radar systems.

To explore the role that the 50 km averaged ice thickness plays in the results of the inversion, we computed a 50 km gridded version of the Bedmachine Antarctica ice thickness (Figure 3.9) and then carried out a new inversion over the Lower Thwaites region (where there is existing swath radar). In this alternate ice thickness input, each 50 by 50 km region contains only one ice thickness value, which is the average over that region. The results of this re-run (Figure 3.9) with reduced prior ice thickness information show the same short wavelength features as the results using the full ice thickness input, illustrating that the inversion method presented here is not unduly influenced by the ice thickness derived from Bedmachine Antarctica.

In figures 3.7 and 3.8, it appears that the method estimates shorter wavelength topography more accurately than longer wavelengths. We demonstrate this in Figure 3.10, which shows results after wavelengths greater than 50 km have been removed from all profiles. It is clear that the inversion identifies peaks and troughs in the bed, although the amplitude of these features is not always correct. Fourier components with a wavelength above 50 km mainly represent the prior ice thickness information supplied to the inversion, as this is the large scale zero-order topography to which the first-order perturbations from the inversion are added. The greater match between the results of the inversion at the PASIN data after this bandpass filter therefore provides further evidence that the ice thickness derived from Bedmachine Antarctica does not influence the key results from the inversion.

A comparison of the two methods over an area where radar data have not yet been incorporated into Bedmachine would allow an assessment of the reliability of the two techniques, and identification of any artificial bed features introduced by each. Since the two radar grids presented (Holschuh et al., 2020) were included in the derivation of BedMachine Antarctica, no independent test is possible until more radar grids are collected.

3.6 Conclusions

We present the method and results of an inversion of ice surface elevation and velocity for bed topography and slipperiness in the Thwaites Glacier region. Our method builds on the

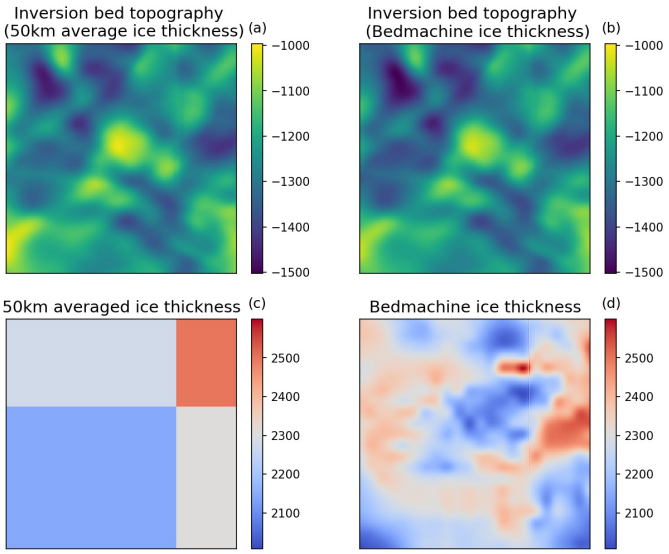

Fig. 3.9 The effect of ice thickness resolution on the results of the inversion in the Lower Thwaites region, as explored in Figure 3.6. a) Inversion bed topography when the low resolution (50 km average) ice thickness values shown in c) are used, b) Inversion bed topography when the full resolution (120m) ice thickness values from Bedmachine Antarctica (Morlighem et al., 2020) (d) are used.

.

method used by Thorsteinsson et al. (2003) in their study of MacAyeal Ice Stream, but is based on a steady-state linear perturbation analysis of the shallow-ice-stream equations (MacAyeal, 1989; Gudmundsson, 2003). Synthetic tests show that this method can resolve variability in bed topography and slipperiness on wavelengths greater than one ice thickness, and at amplitudes of more than 10 m for topography (or 0.01 $\bar{h}$) or 1 x10^{-4} myr^{-1}Pa^{-1} for slipperiness (or 0.01 $\bar{C}$), as long as the variability is not aligned to the ice flow direction. Comparison of the results of the inversion with radar grids and flight lines suggests that the inversion correctly identifies most short (< 50 km horizontal) wavelength features in the bed, with the correlation coefficient of a linear regression between the inverted bed and the radar bed as high as $r = 0.93$ along some flight lines. This method works best in the central trunk of the glacier, where the gradient of the long wavelength topography is low and relatively constant. Mismatches between the inverted bed topography and radar measurements are probably due to one of three factors: an incorrect ice thickness for that region, an unusually sticky or slippery bed, or physical processes not accounted for by the steady-state linearised shallow-ice-stream approximation. Future work, including incorporating more local prior ice thickness data from radar measurements, and the non-hydrostatic transfer functions from Gudmundsson (2003), may help to reduce these mismatches. Overall, the inversion provides an additional tool for studying landforms in the bed beneath glaciers which have a significant impact on ice flow. It will be particularly useful in ice streams where radar flight lines are sparse and standard interpolation techniques struggle, potentially reducing uncertainties in modelling the future behaviour of those regions and their contributions to global sea level rise.

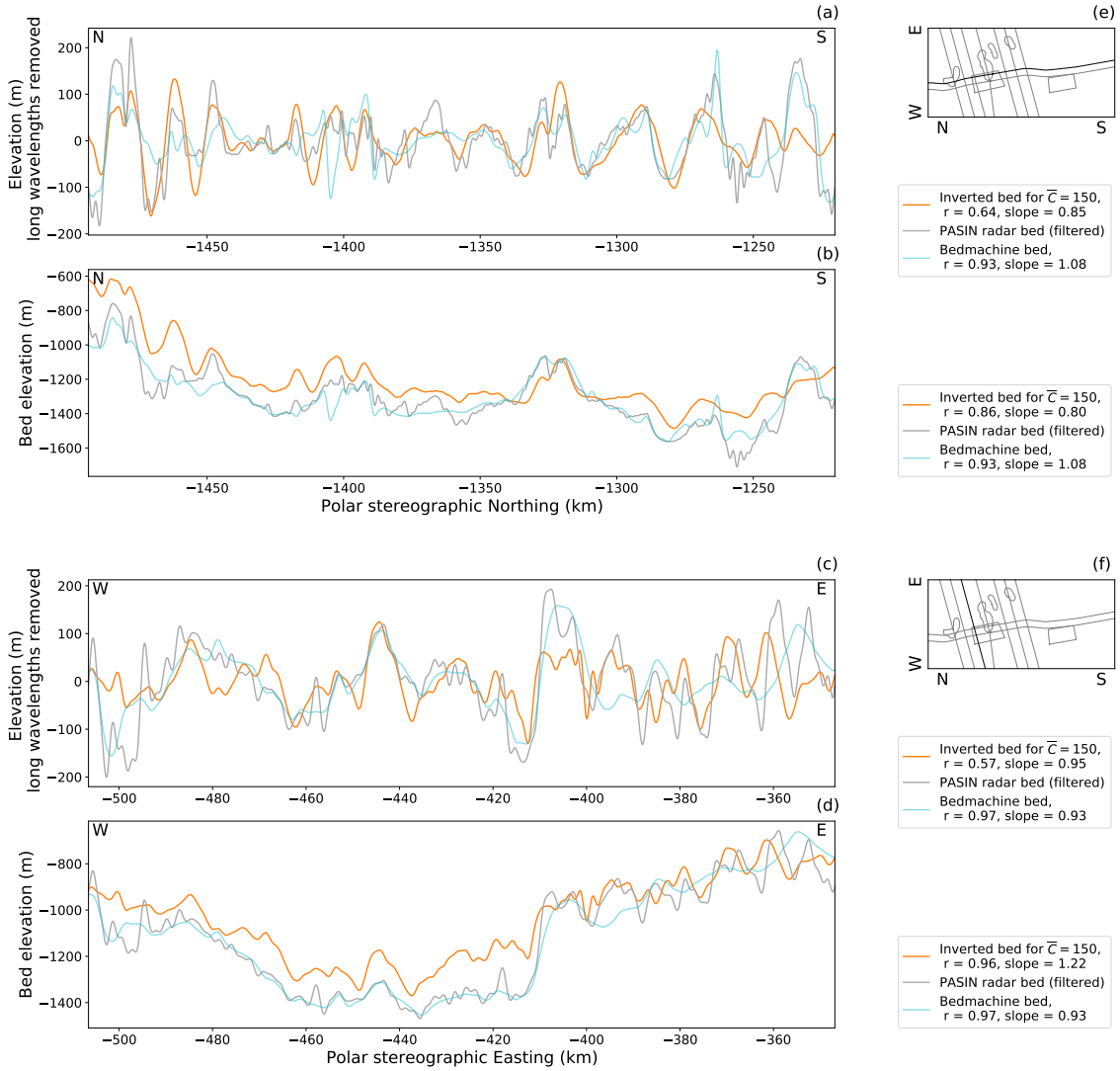

Fig. 3.10 The results of the inversion (orange) compared to PASIN radar flight lines (grey) and Bedmachine Antarctica (light blue) for an along flow profile and an across flow profile (locations shown in panels e) and f) respectively). Panels b) and d) show the bed profiles. Panels a) and c) show the results with any Fourier components between 40 and 50 km in wavelength progressively damped with a half cosine filter, and any Fourier components over 50 km in wavelength removed.

3.7 Appendices

3.7.1 Appendix A: Derivation of transfer functions from a topography perturbation

Starting from the shallow-ice-stream equations, linearising around a small perturbation in bed topography, and taking the fourier transform of the first order equations we have

$$4\eta\bar{h}k^2\hat{u} + 3\eta\bar{h}kl\hat{v} + \eta\bar{h}l^2\hat{u} + \gamma\hat{u} = \rho g\bar{h}\cos\alpha ik\hat{s} + \rho g\sin\alpha\hat{h} \quad \text{(Eq. 3.7)}$$

$$4\eta\bar{h}l^2\hat{v} + 3\eta\bar{h}kl\hat{u} + \eta\bar{h}k^2\hat{v} + \gamma\hat{v} = \rho g\bar{h}\cos\alpha il\hat{s} \quad \text{(Eq. 3.8)}$$

$$i\bar{h}(k\hat{u} + l\hat{v}) = -ik\bar{u}\hat{s} + ik\bar{u}\hat{b} \quad \text{(Eq. 3.12)}$$

Equations 3.7, 3.8 and 3.12 form a linear system of equations in $\hat{s}$, $\hat{u}$, $\hat{v}$ and $\hat{b}$ which can be solved algebraically using standard techniques:

$$\begin{bmatrix} (3\eta\bar{h}k^2 + \nu) & (3\eta\bar{h}kl) \\ (3\eta\bar{h}kl) & (3\eta\bar{h}l^2 + \nu) \end{bmatrix} \begin{bmatrix} \hat{u} \\ \hat{v} \end{bmatrix} = \begin{bmatrix} \left(ik\tau_d\cot\alpha + \frac{\tau_d}{\bar{h}}\right)\hat{s} - \frac{\tau_d}{\bar{h}}\hat{b} \\ il\tau_d\cot\alpha\hat{s} \end{bmatrix}$$

The determinant of the left-hand side of these equations:

$$\begin{aligned} &\left(3\eta\bar{h}k^2 + \nu\right)\left(3\eta\bar{h}l^2 + \nu\right) - \left(3\eta\bar{h}kl\right)\left(3\eta\bar{h}kl\right) \\ =&9\eta^2\bar{h}^2k^2l^2 + 3\eta\bar{h}l^2\nu + 3\eta\bar{h}k^2\nu + \nu^2 - 9\eta^2\bar{h}^2k^2l^2 \\ =&3\eta\bar{h}j^2\nu + \left(\bar{h}\eta j^2 + \gamma\right)\nu \\ =&\left(4\bar{h}\eta j^2 + \gamma\right)\nu \\ =&\xi\nu \end{aligned}$$

where the following abbreviations have been used to make the algebra clearer to follow: $\nu = \bar{h}\eta j^2 + \gamma$, $j^2 = l^2 + k^2$, and $\xi = 4\bar{h}\eta j^2 + \gamma$.

$$\begin{bmatrix} \hat{u} \\ \hat{v} \end{bmatrix} = \frac{1}{\xi\nu}\begin{bmatrix} (3\eta\bar{h}l^2 + \nu) & (-3\eta\bar{h}kl) \\ (-3\eta\bar{h}kl) & (3\eta\bar{h}k^2 + \nu) \end{bmatrix} \begin{bmatrix} \left(ik\tau_d\cot\alpha + \frac{\tau_d}{\bar{h}}\right)\hat{s} - \frac{\tau_d}{\bar{h}}\hat{b} \\ il\tau_d\cot\alpha\hat{s} \end{bmatrix}$$

Therefore we have:

$$\hat{u} = \frac{1}{\xi\nu}\left((3\eta\bar{h}l^2 + \nu)\left(\left(ik\tau_d\cot\alpha + \frac{\tau_d}{\bar{h}}\right)\hat{s} - \frac{\tau_d}{\bar{h}}\hat{b}\right) + (-3\eta\bar{h}kl)(il\tau_d\cot\alpha\hat{s})\right)$$

$$\hat{v} = \frac{1}{\xi\nu}\left((-3\eta\bar{h}kl)\left(\left(ik\tau_d\cot\alpha + \frac{\tau_d}{\bar{h}}\right)\hat{s} - \frac{\tau_d}{\bar{h}}\hat{b}\right) + (3\eta\bar{h}k^2 + \nu)(il\tau_d\cot\alpha\hat{s})\right)$$

which simplifies to:

$$\hat{u} = \frac{1}{\xi \nu \bar{h}} \left(3\eta \bar{h} l^2 \tau_d \hat{s} - 3\eta \bar{h} l^2 \tau_d \hat{b} + ik\nu \bar{h} \tau_d \cot\alpha \hat{s} + \tau_d \nu \hat{s} - \tau_d \nu \hat{b} \right) \tag{3.29}$$

$$\hat{v} = \frac{1}{\xi \nu \bar{h}} \left(-3\eta \bar{h} kl \tau_d \hat{s} + 3\eta \bar{h} kl \tau_d \hat{b} + i\bar{h} l \nu \tau_d \cot\alpha \hat{s} \right) \tag{3.30}$$

We then have:

$$\begin{aligned} i\bar{h}\big(k\hat{u} + l\hat{v}\big) &= \frac{i}{\xi \nu} \Bigg(k(3\eta \bar{h} l^2 \tau_d \hat{s} - 3\eta \bar{h} l^2 \tau_d \hat{b} + ik\nu \bar{h} \tau_d \cot\alpha \hat{s} + \tau_d \nu \hat{s} - \tau_d \nu \hat{b}) \\ &\qquad + l(-3\eta \bar{h} kl \tau_d \hat{s} + 3\eta \bar{h} kl \tau_d \hat{b} + i\bar{h} l \nu \tau_d \cot\alpha \hat{s}) \Bigg) \\ &= \frac{i}{\xi \nu} \left(ik^2 \nu \bar{h} \tau_d \cot\alpha \hat{s} + k\tau_d \nu \hat{s} - k\tau_d \nu \hat{b} + i\bar{h} l^2 \nu \tau_d \cot\alpha \hat{s} \right) \\ &= \frac{1}{\xi} \left(-j^2 \bar{h} \tau_d \cot\alpha \hat{s} + ik\tau_d \hat{s} - ik\tau_d \hat{b} \right) \end{aligned}$$

In the steady state, the kinematic boundary condition is

$$\begin{aligned} i\bar{h}(k\hat{u} + l\hat{v}) &= \hat{w}(s) - \hat{w}(b) \\ &= -i\bar{u}k\hat{s} + i\bar{u}k\hat{b} \end{aligned}$$

Substituting the expression from above:

$$\frac{1}{\xi} \left(-j^2 \bar{h} \tau_d \cot\alpha \hat{s} + ik\tau_d \hat{s} - ik\tau_d \hat{b} \right) = -i\bar{u}k\hat{s} + i\bar{u}k\hat{b}$$

Rearranging

$$\begin{aligned} \left(i\bar{u}k + \frac{ik\tau_d}{\xi} - \frac{j^2 \bar{h} \tau_d \cot\alpha}{\xi} \right) \hat{s} &= \frac{1}{\xi} \big(ik\tau_d + ik\bar{u}\xi \big) \hat{b} \\ \left(ik\big(\bar{u} + \frac{\tau_d}{\xi}\big) - \frac{j^2 \bar{h} \tau_d \cot\alpha}{\xi} \right) \hat{s} &= \frac{1}{\xi} \big(ik(\tau_d + \bar{u}\xi) \big) \hat{b} \\ \xi p \hat{s} &= ik\big(\tau_d + \bar{u}\xi\big) \hat{b} \end{aligned}$$

In agreement with Gudmundsson (2008), this leads to the steady-state transfer function

$$T_{sb}(k,l,t) = \frac{\hat{s}}{\hat{b}} = \frac{\mathrm{i}k\big(\bar{u}\xi + \tau_d\big)}{p\xi} \tag{Eq. 3.13}$$

Expanding the expression for $\hat{u}$:

$$\hat{u} = \frac{1}{\xi\nu\bar{h}}\left(3\eta\bar{h}l^2\tau_d\hat{s} - 3\eta\bar{h}l^2\tau_d\hat{b} + ik\nu\bar{h}\tau_d\cot\alpha\hat{s} + \tau_d\nu\hat{s} - \tau_d\nu\hat{b}\right) \qquad \text{(3.29 revisited)}$$

$$= \frac{\tau_d}{\xi\nu\bar{h}}\left(\bar{h}\nu(ik\cot\alpha)\hat{s} + (3\eta\bar{h}l^2+\nu)\hat{s} - (3\eta\bar{h}l^2+\nu)\hat{b}\right)$$

$$= \frac{\tau_d}{\xi\nu\bar{h}}\left(\bar{h}\nu(ik\cot\alpha)\Big(\frac{\mathrm{i}k\big(\bar{u}\xi+\tau_d\big)}{p\xi}\Big)\hat{b} + (3\eta\bar{h}l^2+\nu)\Big(\frac{\mathrm{i}k\big(\bar{u}\xi+\tau_d\big)}{p\xi}\Big)\hat{b} - (3\eta\bar{h}l^2+\nu)\hat{b}\right)$$

$$= \frac{\tau_d}{\xi\nu\bar{h}p\xi}\left(\bar{h}\nu(ik\cot\alpha)\Big(\mathrm{i}k\big(\bar{u}\xi+\tau_d\big)\Big) + (3\eta\bar{h}l^2+\nu)\Big(\mathrm{i}k\big(\bar{u}\xi+\tau_d\big)\Big) - (3\eta\bar{h}l^2+\nu)p\xi\right)\hat{b}$$

$$= \frac{\tau_d}{\xi\nu\bar{h}p\xi}\left(\bar{h}\nu(ik\cot\alpha)\Big(\mathrm{i}k\big(\bar{u}\xi+\tau_d\big)\Big) + (3\eta\bar{h}l^2+\nu)\Big(\mathrm{i}k\big(\bar{u}\xi+\tau_d\big)\Big)\right.$$
$$\left. - (3\eta\bar{h}l^2+\nu)\big(ik(\bar{u}\xi+\tau_d) - j^2\tau_d\bar{h}\cot\alpha\big)\right)\hat{b}$$

$$= \frac{\tau_d}{\xi\nu\bar{h}p\xi}\left(\bar{h}\nu(ik\cot\alpha)\Big(\mathrm{i}k\big(\bar{u}\xi+\tau_d\big)\Big) - (3\eta\bar{h}l^2+\nu)\big(-j^2\tau_d\bar{h}\cot\alpha\big)\right)\hat{b}$$

$$= \frac{\tau_d\cot\alpha}{\xi\nu p\xi}\left(-k^2\nu\bar{u}\xi - \nu k^2\tau_d + 3\eta\bar{h}j^2l^2\tau_d + \nu j^2\tau_d\right)\hat{b}$$

$$= \frac{\tau_d\cot\alpha}{\xi\nu p\xi}\left(3\eta\bar{h}j^2l^2\tau_d + \nu l^2\tau_d - k^2\bar{u}\xi\right)\hat{b}$$

$$= \frac{\tau_d\cot\alpha}{\xi\nu p\xi}\left(\xi l^2\tau_d - k^2\bar{u}\xi\right)\hat{b}$$

$$\hat{u} = \frac{\tau_d\cot\alpha}{\xi\nu p}\left(l^2\tau_d - k^2\bar{u}\right)\hat{b}$$

remembering that $\xi = 4\eta\bar{h}j^2 + \nu$.

In agreement with Gudmundsson (2008), this leads to the steady-state transfer function:

$$T_{ub}(k,l,t) = \frac{\hat{u}}{\hat{b}} = \frac{\tau_d\cot\alpha(l^2\tau_d - k^2\bar{u})}{\xi\nu p} \qquad \text{(Eq. 3.14)}$$

Expanding the expression for $\hat{v}$:

$$\begin{aligned}
\hat{v} &= \frac{1}{\xi\nu\bar{h}}\Big(-3\eta\bar{h}kl\tau_d\hat{s}+3\eta\bar{h}kl\tau_d\hat{b}+i\bar{h}l\nu\tau_d\cot\alpha\hat{s}\Big)\\
&= \frac{\tau_d l}{\xi\nu}\Big(-3\eta k\Big(\frac{\mathrm{i}k\big(\bar{u}\xi+\tau_d\big)}{p\xi}\Big)\hat{b}+3\eta k\hat{b}+i\nu\cot\alpha\Big(\frac{\mathrm{i}k\big(\bar{u}\xi+\tau_d\big)}{p\xi}\Big)\hat{b}\Big)\\
&= \frac{\tau_d l}{\xi\nu p\xi}\Big(-3\eta k\Big(\mathrm{i}k\big(\bar{u}\xi+\tau_d\big)\Big)+3\eta kp\xi+i\nu\cot\alpha\Big(\mathrm{i}k\big(\bar{u}\xi+\tau_d\big)\Big)\Big)\hat{b}\\
&= \frac{\tau_d l}{\xi\nu p\xi}\Big(-3\eta k\Big(\mathrm{i}k\big(\bar{u}\xi+\tau_d\big)\Big)+3\eta k\Big(ik(\bar{u}\xi+\tau_d)-j^2\tau_d\bar{h}\cot\alpha\Big)+i\nu\cot\alpha\Big(\mathrm{i}k\big(\bar{u}\xi+\tau_d\big)\Big)\Big)\hat{b}\\
&= \frac{\tau_d lk}{\xi\nu p\xi}\Big(+3\eta\Big(-j^2\tau_d\bar{h}\cot\alpha\Big)-\nu\cot\alpha\big(\bar{u}\xi+\tau_d\big)\Big)\hat{b}\\
&= -\frac{\tau_d lk\cot\alpha}{\xi\nu p\xi}\Big(-(3\eta\bar{h}j^2+\nu)\tau_d-\nu\bar{u}\xi\Big)\hat{b}\\
\hat{v} &= \frac{\tau_d lk\cot\alpha}{\xi\nu p}\Big(\tau_d+\nu\bar{u}\Big)\hat{b}
\end{aligned}$$

remembering that $\xi = 4\eta\bar{h}j^2+\nu$.

In agreement with Gudmundsson (2008), this leads to the steady-state transfer function:

$$T_{vb}(k,l,t) = \frac{\hat{v}}{\hat{b}} = \frac{kl\tau_d\cot\alpha(\tau_d+\nu\bar{u})}{\xi\nu p} \qquad \text{(Eq. 3.15)}$$

3.7.2 Appendix B: Derivation of transfer functions from a slipperiness perturbation

Starting once again with the shallow-ice-stream equations MacAyeal, 1989), this time we consider the response to a small perturbation in basal slipperiness, linearising and taking the fourier transform to give

$$4\eta\bar{h}k^2\hat{u}+3\eta\bar{h}kl\hat{v}+\eta\bar{h}l^2\hat{u}+\gamma\hat{u} = \rho g\bar{h}\cos\alpha ik\hat{s}+\rho g\sin\alpha\hat{s}+\gamma\bar{u}\hat{c} \qquad \text{(Eq. 3.18)}$$

$$4\eta\bar{h}l^2\hat{v}+3\eta\bar{h}kl\hat{u}+\eta\bar{h}k^2\hat{v}+\gamma\hat{v} = \rho g\bar{h}\cos\alpha il\hat{s} \qquad \text{(Eq. 3.19)}$$

$$i\bar{h}(k\hat{u}+l\hat{v}) = -ik\bar{u}\hat{s}. \qquad \text{(Eq. 3.20)}$$

Equations 3.18, 3.19 and 3.20 form a linear system of equations which can be solved using standard algebraic techniques:

$$\begin{bmatrix} (3\eta\bar{h}k^2+\nu) & (3\eta\bar{h}kl) \\ (3\eta\bar{h}kl) & (3\eta\bar{h}l^2+\nu) \end{bmatrix} \begin{bmatrix} \hat{u} \\ \hat{v} \end{bmatrix} = \begin{bmatrix} \left(ik\tau_d\cot\alpha + \frac{\tau_d}{h}\right)\hat{s} + \gamma\bar{u}\hat{c} \\ il\tau_d\cot\alpha\hat{s} \end{bmatrix}$$

The determinant of the left-hand side:

$$\begin{aligned} &\left(3\eta\bar{h}k^2+\nu\right)\left(3\eta\bar{h}l^2+\nu\right) - \left(3\eta\bar{h}kl\right)\left(3\eta\bar{h}kl\right) \\ =&9\eta^2\bar{h}^2k^2l^2 + 3\eta\bar{h}l^2\nu + 3\eta\bar{h}k^2\nu + \nu^2 - 9\eta^2\bar{h}^2k^2l^2 \\ =&3\eta\bar{h}j^2\nu + \left(\bar{h}\eta j^2+\gamma\right)\nu \\ =&\left(4\bar{h}\eta j^2+\gamma\right)\nu \\ =&\xi\nu \end{aligned}$$

where the following abbreviations have been used to make the algebra easier to follow: $j^2 = l^2 + k^2$, $\xi = 4\bar{h}\eta j^2 + \gamma$ and $\nu = \bar{h}\eta j^2 + \gamma$.

$$\begin{bmatrix} \hat{u} \\ \hat{v} \end{bmatrix} = \frac{1}{\xi\nu} \begin{bmatrix} (3\eta\bar{h}l^2+\nu) & (-3\eta\bar{h}kl) \\ (-3\eta\bar{h}kl) & (3\eta\bar{h}k^2+\nu) \end{bmatrix} \begin{bmatrix} \left(ik\tau_d\cot\alpha + \frac{\tau_d}{h}\right)\hat{s} + \gamma\bar{u}\hat{c} \\ il\tau_d\cot\alpha\hat{s} \end{bmatrix}$$

Therefore we have:

$$\hat{u} = \frac{1}{\xi\nu}\left((3\eta\bar{h}l^2+\nu)\left(\left(ik\tau_d\cot\alpha + \frac{\tau_d}{h}\right)\hat{s} + \gamma\bar{u}\hat{c}\right) + (-3\eta\bar{h}kl)(il\tau_d\cot\alpha\hat{s})\right)$$

$$\hat{v} = \frac{1}{\xi\nu}\left((-3\eta\bar{h}kl)\left(\left(ik\tau_d\cot\alpha + \frac{\tau_d}{h}\right)\hat{s} + \gamma\bar{u}\hat{c}\right) + (3\eta\bar{h}k^2+\nu)(il\tau_d\cot\alpha\hat{s})\right)$$

Which simplifies to:

$$\hat{u} = \frac{1}{\xi\nu}\left(\left(3\eta l^2\tau_d + \nu ik\tau_d\cot\alpha + \frac{\nu\tau_d}{\bar{h}}\right)\hat{s} + \left(3\eta\bar{h}l^2+\nu\right)\gamma\bar{u}\hat{c}\right) \tag{3.31}$$

$$\hat{v} = \frac{1}{\xi\nu}\left(-3\eta kl\tau_d\hat{s} + \nu il\tau_d\cot\alpha\hat{s} - 3\eta\bar{h}kl\gamma\bar{u}\hat{c}\right) \tag{3.32}$$

We then have:

$$
\begin{aligned}
i\bar{h}\big(k\hat{u}+l\hat{v}\big) &= \frac{i\bar{h}}{\xi\nu}\left(k\left(\left(3\eta l^2\tau_d+\nu ik\tau_d\cot\alpha+\frac{\nu\tau_d}{\bar{h}}\right)\hat{s}+\left(3\eta\bar{h}l^2+\nu\right)\gamma\bar{u}\hat{c}\right)\right.\\
&\qquad\left.+l\left(-3\eta kl\tau_d\hat{s}+\nu il\tau_d\cot\alpha\hat{s}-3\eta\bar{h}kl\gamma\bar{u}\hat{c}\right)\right)\\
&= \frac{i\bar{h}}{\xi\nu}\left(k\left(\left(\nu ik\tau_d\cot\alpha+\frac{\nu\tau_d}{\bar{h}}\right)\hat{s}+\nu\gamma\bar{u}\hat{c}\right)+l\left(\nu il\tau_d\cot\alpha\hat{s}\right)\right)\\
&= \frac{i\bar{h}}{\xi}\left(ik^2\tau_d\cot\alpha\hat{s}+\frac{k\tau_d}{\bar{h}}\hat{s}+k\gamma\bar{u}\hat{c}+il^2\tau_d\cot\alpha\hat{s}\right)\\
&= \frac{i}{\xi}\left(i\bar{h}j^2\tau_d\cot\alpha\hat{s}+k\tau_d\hat{s}+k\bar{h}\gamma\bar{u}\hat{c}\right)
\end{aligned}
$$

At steady state $\hat{s}_t = 0$, so we have the boundary condition:

$$
\begin{aligned}
-ik\bar{u}\hat{s} &= i\bar{h}(k\hat{u}+l\hat{v}).\\
&= \frac{i}{\xi}\left(ihj^2\tau_d\cot\alpha\hat{s}+k\tau_d\hat{s}+k\bar{h}\gamma\bar{u}\hat{c}\right)\\
-ik\bar{h}\gamma\bar{u}\hat{c} &= -hj^2\tau_d\cot\alpha\hat{s}+ik\tau_d\hat{s}+ik\bar{u}\xi\hat{s}\\
\frac{1}{\xi}\big(-ik\bar{h}\gamma\bar{u}\big)\hat{c} &= \left(-\frac{hj^2\tau_d\cot\alpha}{\xi}+ik\big(\frac{\tau_d}{\xi}+\bar{u}\big)\right)\hat{s}
\end{aligned}
$$

$$
\begin{aligned}
\frac{1}{\xi}\big(-ik\bar{h}\gamma\bar{u}\big)\hat{c} &= \left(-\frac{1}{t_r}+\frac{i}{t_p}\right)\hat{s}\\
\big(-ik\bar{h}\gamma\bar{u}\big)\hat{c} &= \xi p\hat{s}
\end{aligned}
$$

In agreement with Gudmundsson (2008) this leads to the steady-state transfer function:

$$
T_{sc}(k,l,t) = \frac{\hat{s}(k,l,t)}{\hat{c}(k,l)} = -\frac{\mathrm{i}k\bar{h}\bar{u}\gamma}{p\xi} \qquad \text{(Eq. 3.21)}
$$

Expanding the expression for $\hat{u}$ (Eq 3.31):

$$\begin{aligned}
\hat{u} &= \frac{1}{\xi\nu}\left(\left(3\eta l^2\tau_d + \nu ik\tau_d\cot\alpha + \frac{\nu\tau_d}{\bar{h}}\right)\hat{s} + \left(3\eta\bar{h}l^2+\nu\right)\gamma\bar{u}\hat{c}\right)\\
&= \frac{1}{\xi\nu}\left(\left(3\eta l^2\tau_d + \nu ik\tau_d\cot\alpha + \frac{\nu\tau_d}{\bar{h}}\right)\left(-\frac{ik\bar{h}\bar{u}\gamma}{p\xi}\right)\hat{c} + \left(3\eta\bar{h}l^2+\nu\right)\gamma\bar{u}\hat{c}\right)\\
&= \frac{\gamma\bar{u}}{\xi\nu p\xi}\left(\left(3\eta\bar{h}l^2\tau_d + \nu i\bar{h}k\tau_d\cot\alpha + \nu\tau_d\right)\left(-ik\right) + \left(3\eta\bar{h}l^2+\nu\right)p\xi\right)\hat{c}\\
&= \frac{\gamma\bar{u}}{\xi\nu p\xi}\left(\left(3\eta\bar{h}l^2\tau_d + \nu i\bar{h}k\tau_d\cot\alpha + \nu\tau_d\right)\left(-ik\right)\right.\\
&\qquad\left. + \left(3\eta\bar{h}l^2+\nu\right)\left(ik(\bar{u}\xi+\tau_d) - j^2\tau_d\bar{h}\cot\alpha\right)\right)\hat{c}\\
&= \frac{\gamma\bar{u}}{\xi\nu p\xi}\left(\nu k^2\tau_d\cot\alpha\bar{h} + 3\eta\bar{h}l^2 ik\bar{u}\xi - 3\eta\bar{h}l^2 j^2\tau_d\bar{h}\cot\alpha + \nu ik\bar{u}\xi - \nu j^2\tau_d\bar{h}\cot\alpha\right)\hat{c}\\
&= \frac{\gamma\bar{u}}{\xi\nu p\xi}\left(-\nu l^2\tau_d\cot\alpha\bar{h} - 3\eta\bar{h}l^2 j^2\tau_d\bar{h}\cot\alpha + 3\eta\bar{h}l^2 ik\bar{u}\xi + \nu ik\bar{u}\xi\right)\hat{c}\\
&= \frac{\gamma\bar{u}}{\xi\nu p\xi}\left(-\left(3\eta\bar{h}j^2+\nu\right)l^2\tau_d\cot\alpha\bar{h} + \left(3\eta\bar{h}l^2+\nu\right)\left(ik\bar{u}\right)\xi\right)\hat{c}\\
\hat{u} &= \frac{\gamma\bar{u}}{\xi\nu p}\left(-l^2\tau_d\cot\alpha\bar{h} + \left(3\eta\bar{h}l^2+\nu\right)\left(ik\bar{u}\right)\right)\hat{c}
\end{aligned}$$

remembering that $\xi = 4\eta\bar{h}j^2 + \nu$, leads to the steady-state transfer function:

$$T_{uc}(k,l,t) = \frac{\hat{u}}{\hat{c}} = \frac{\gamma\bar{u}\left((3\eta\bar{h}l^2+\nu)(ik\bar{u}) - l^2\tau_d\cot\alpha\bar{h}\right)}{\xi\nu p} \qquad \text{(Eq. 3.22)}$$

which is not as stated by Gudmundsson (2008).

Expanding the expression for $\hat{v}$ (Eq 3.32):

$$\begin{aligned}
\hat{v} &= \frac{1}{\xi\nu}\left(-3\eta kl\tau_d\hat{s} + \nu il\tau_d\cot\alpha\hat{s} - 3\eta\bar{h}kl\gamma\bar{u}\hat{c}\right) \\
&= \frac{1}{\xi\nu}\left(-3\eta kl\tau_d\left(-\frac{\mathrm{i}k\bar{h}\bar{u}\gamma}{p\xi}\right)\hat{c} + \nu il\tau_d\cot\alpha\left(-\frac{\mathrm{i}k\bar{h}\bar{u}\gamma}{p\xi}\right)\hat{c} - 3\eta\bar{h}kl\gamma\bar{u}\hat{c}\right) \\
&= \frac{kl\gamma\bar{u}\bar{h}}{\xi\nu p\xi}\left(3i\eta k\tau_d + \nu\tau_d\cot\alpha - 3\eta p\xi\right)\hat{c} \\
&= \frac{kl\gamma\bar{u}\bar{h}}{\xi\nu p\xi}\left(3i\eta k\tau_d + \nu\tau_d\cot\alpha - 3\eta\left(ik(\bar{u}\xi+\tau_d) - j^2\tau_d\bar{h}\cot\alpha\right)\right)\hat{c} \\
&= \frac{kl\gamma\bar{u}\bar{h}}{\xi\nu p\xi}\left(\nu\tau_d\cot\alpha - 3\eta ik\bar{u}\xi + 3\eta j^2\tau_d\bar{h}\cot\alpha\right)\hat{c} \\
&= \frac{kl\gamma\bar{u}\bar{h}}{\xi\nu p\xi}\left((3\eta j^2\bar{h}+\nu)\tau_d\cot\alpha - 3i\eta\bar{u}k\xi\right)\hat{c} \\
\hat{v} &= \frac{kl\gamma\bar{u}\bar{h}}{\xi\nu p}\left(\tau_d\cot\alpha - 3i\eta\bar{u}k\right)\hat{c}
\end{aligned}$$

remembering that $\xi = 4\eta\bar{h}j^2 + \nu$, leads to the steady-state transfer function:

$$T_{vc}(k,l,t) = \frac{\hat{v}}{\hat{c}} = \frac{kl\gamma\bar{u}\bar{h}\left(\tau_d\cot\alpha - 3i\eta\bar{u}k\right)}{\xi\nu p} \qquad \text{(Eq. 3.23)}$$

which is also not as stated by Gudmundsson (2008).

3.7.3 Appendix C: The inverse problem

The transfer functions (T_{sb}, T_{ub}, T_{vb}, T_{sc}, T_{uc} and T_{vc}) describe the relationship between the Fourier transforms of bed topography ($\hat{b}$), bed slipperiness ($\hat{c}$), surface topography ($\hat{s}$) and surface velocity ($\hat{u},\hat{v}$). If the bed topography and slipperiness are known then surface topography and velocity components are given by the forward model:

$$\hat{s} = T_{sb}\hat{b} + T_{sc}\hat{c} \qquad \text{(Eq. 3.26)}$$

$$\hat{u} = T_{ub}\hat{b} + T_{uc}\hat{c} \qquad \text{(Eq. 3.27)}$$

$$\hat{v} = T_{vb}\hat{b} + T_{vc}\hat{c} \qquad \text{(Eq. 3.28)}$$

Non-dimensionalised this gives:

$$\hat{S} = T_{SB}\hat{B} + T_{SC}\hat{C} \qquad \text{(Eq. 3.26 non-dimensionalised)}$$

$$\hat{U} = T_{UB}\hat{B} + T_{UC}\hat{C} \qquad \text{(Eq. 3.27 non-dimensionalised)}$$

$$\hat{V} = T_{VB}\hat{B} + T_{VC}\hat{C} \qquad \text{(Eq. 3.28 non-dimensionalised)}$$

Since the system is over-determined, we can use a weighted least squares inversion of equations 3.26, 3.27 and 3.28 to find the bed topography and slipperiness which are the most consistent with the ice surface. This is the same method used by Thorsteinsson et al. (2003) in their study of MacAyeal Ice Stream (formerly Ice Stream E), but is reproduced here in notation consistent with the rest of the equations we present.

In matrix form we have the forward model:

$$\mathbf{Y} = \mathbf{G}\mathbf{X} \tag{3.33}$$

where $\mathbf{Y} = \begin{bmatrix} \hat{S} \\ \hat{U} \\ \hat{V} \end{bmatrix}$, $\mathbf{G} = \begin{bmatrix} T_{SB} & T_{SC} \\ T_{UB} & T_{UC} \\ T_{VB} & T_{VC} \end{bmatrix}$, $\mathbf{X} = \begin{bmatrix} \hat{B} \\ \hat{C} \end{bmatrix}$ and $\mathbf{E} = \begin{bmatrix} \Sigma_S^{-2} & 0 & 0 \\ 0 & \Sigma_U^{-2} & 0 \\ 0 & 0 & \Sigma_V^{-2} \end{bmatrix}$

A least squares inversion gives:

$$\mathbf{X} = \left(\mathbf{G}^H\mathbf{E}\mathbf{G}\right)^{-1}\mathbf{G}^H\mathbf{E}\mathbf{Y}$$

$$\begin{bmatrix} \hat{B} \\ \hat{C} \end{bmatrix} = \left(\begin{bmatrix} T_{SB}^* & T_{UB}^* & T_{VB}^* \\ T_{SC}^* & T_{UC}^* & T_{VC}^* \end{bmatrix} \begin{bmatrix} \Sigma_S^{-2} & 0 & 0 \\ 0 & \Sigma_U^{-2} & 0 \\ 0 & 0 & \Sigma_V^{-2} \end{bmatrix} \begin{bmatrix} T_{SB} & T_{SC} \\ T_{UB} & T_{UC} \\ T_{VB} & T_{VC} \end{bmatrix} \right)^{-1} \tag{3.34}$$

$$\begin{bmatrix} T_{SB}^* & T_{UB}^* & T_{VB}^* \\ T_{SC}^* & T_{UC}^* & T_{VC}^* \end{bmatrix} \begin{bmatrix} \Sigma_S^{-2} & 0 & 0 \\ 0 & \Sigma_U^{-2} & 0 \\ 0 & 0 & \Sigma_V^{-2} \end{bmatrix} \begin{bmatrix} \hat{S} \\ \hat{U} \\ \hat{V} \end{bmatrix}$$

where ^{H} is the Hermitian transpose and * is the complex conjugate.

For compactness we define the following:

$K = T_{SB}^* T_{SC}/\Sigma_S^2 + T_{UB}^* T_{UC}/\Sigma_U^2 + T_{VB}^* T_{VC}/\Sigma_V^2$

$L = T_{SB}^* T_{SB}/\Sigma_S^2 + T_{UB}^* T_{UB}/\Sigma_U^2 + T_{VB}^* T_{VB}/\Sigma_V^2$

$M = T_{SC}^* T_{SC}/\Sigma_S^2 + T_{UC}^* T_{UC}/\Sigma_U^2 + T_{VC}^* T_{VC}/\Sigma_V^2$

$Y_b = \hat{S}T_{SB}^*/\Sigma_S^2 + \hat{U}T_{UB}^*/\Sigma_U^2 + \hat{V}T_{VB}^*/\Sigma_V^2$

$Y_c = \hat{S}T_{SC}^*/\Sigma_S^2 + \hat{U}T_{UC}^*/\Sigma_U^2 + \hat{V}T_{VC}^*/\Sigma_V^2$

The least squares solution is then:

$$\begin{bmatrix} \hat{B} \\ \hat{C} \end{bmatrix} = \begin{bmatrix} L & K \\ K^* & M \end{bmatrix}^{-1} \begin{bmatrix} Y_b \\ Y_c \end{bmatrix} = \frac{1}{LM - KK^*} \begin{bmatrix} M & -K \\ -K^* & L \end{bmatrix} \begin{bmatrix} Y_b \\ Y_c \end{bmatrix} \tag{3.35}$$

This inversion is problematic where $LM - KK^*$ is small or zero, which is for small wavelengths (when k and l are large) or for topography or slipperiness perturbations which are aligned in the direction of ice flow (k = 0). Short wavelengths bed features and features aligned with ice flow are problematic because they cause flow disturbances in the ice which do not reach the surface in a measurable way. They can therefore not be inverted from the surface data.

To avoid this problem with an ill-conditioned inverse, Thorsteinsson et al. (2003) use a truncated version of $L'M' - KK^*$ as a filter, F to remove problematic wavelengths. Their filter is

$$F = \begin{cases} (LM - KK^*)/P, & \text{if } (LM - KK^*) \leq P \\ 1, & \text{if } (LM - KK^*) > P \end{cases}$$

where

$$P = \max\{\left(|LM - KK^*|\right) \bar{C}^{(p_{filt})}\}, \tag{3.36}$$

and $p_{filt} \leq 0$. This filter allows through all wavelengths where $LM - KK*$ is larger than P, but gradually filters out other smaller wavelengths. Smaller values of P give more detail, but may over-fit the surface data due to errors. Larger values of P under-fit the data and may leave out features actually represented by the data.

The filtered least squares solution is then:

$$\begin{bmatrix} \hat{B} \\ \hat{C} \end{bmatrix} = \frac{F}{LM - KK^*} \begin{bmatrix} M & -K \\ -K^* & L \end{bmatrix} \begin{bmatrix} Y_b \\ Y_c \end{bmatrix} \tag{3.37}$$

3.8 Supplementary material

3.8.1 Non-dimensionalisation

The form of these transfer functions can be simplified by considering them in a non-dimensional form. For this purpose the same scalings as used in Gudmundsson (2003) and Gudmundsson (2008) are employed.

All spatial scales are in units of mean ice thickness ($\bar{h}$), and stress components in units of driving stress (τ_d).

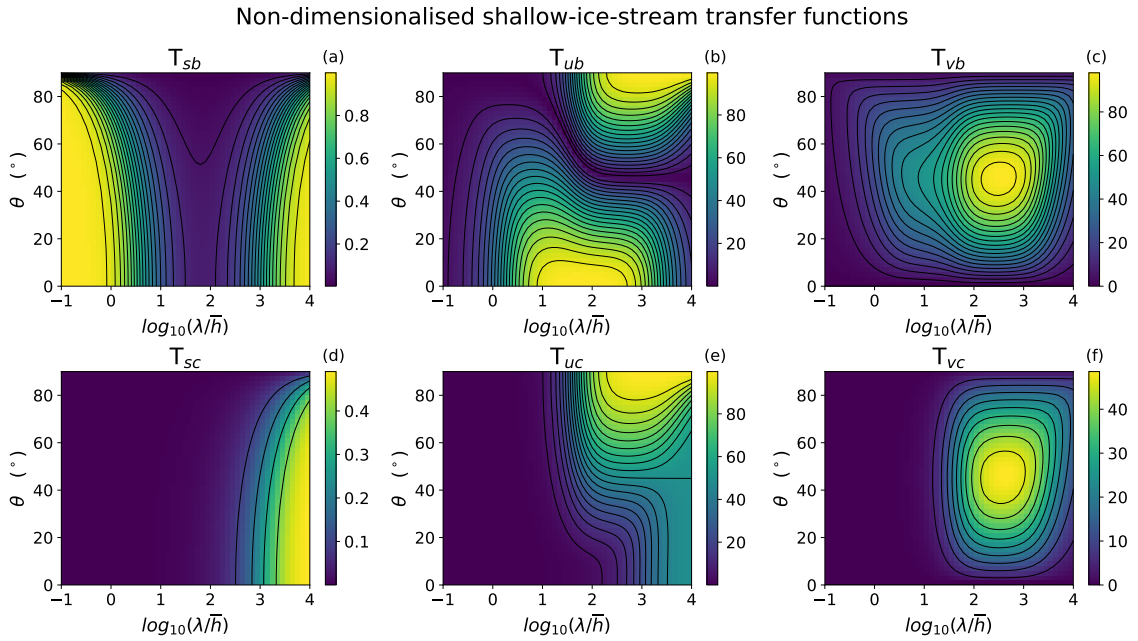

Fig. 3.11 Panels (a), (b) and (c) show the magnitude of the complex non-dimensional shallow-ice-stream transfer functions T_{SB}, T_{UB} and T_{VB} between non-dimensional bed topography B and surface topography S; along flow velocity U; and across flow velocity V, respectively. Panels (d), (e) and (f) show the magnitude of the complex non-dimensional shallow-ice-stream transfer functions T_{SC}, T_{UC} and T_{VC} between non-dimensional bed slipperiness C and surface topography S; along flow velocity U; and across flow velocity V, respectively. All transfer functions are calculated for mean slipperiness $\bar{C} = 100$, sliding law constant $m = 1$, and mean surface slope $\alpha = 0.002$. The angle θ is the angle between the x axis and the wave vector (k,l). This is also the angle between the x axis and a vector perpendicular to the crests of the sinusoidal perturbations, such that $\theta = 90$ for landforms aligned with the ice flow and $\theta = 0$ for landforms perpendicular to the ice flow. λ is the wavelength of variability and is non-dimensionalised in terms of $\bar{h}$, the mean ice thickness, such that $\log_{10}(\lambda/\bar{h}) = 1$ means that $\lambda = 10\bar{h}$. $T_{sb} = 0.1$ means that variability in the surface topography will have one tenth of the amplitude of variability in the bed topography at that angle and wavelength. Similar figures can be seen in Gudmundsson (2008) with $\bar{C} = 99$.

The non-dimensional form of the equations is obtained using the substitutions $\bar{c} \mapsto \bar{C}$, $\eta \mapsto 1/2$, $\bar{h} \mapsto 1$, $\bar{u} \mapsto \bar{C}$, $k \mapsto k$, $l \mapsto l$, $\gamma \mapsto (m\bar{C})^{-1}$, and $\tau_d = \rho g \bar{h} \sin\alpha \mapsto 1$.

Using these substitution leads to the non-dimensionalised transfer functions, shown in Figure 3.11:

$$T_{SB}(k,l) = \frac{k\Big(1+m\big(2j^2\bar{C}+1\big)\Big)}{k+m\Big(k+2kj^2\bar{C}+\mathrm{i}j^2\cot\alpha\Big)} \quad \text{(13 non-dimensionalised)}$$

$$T_{UB}(k,l) = \frac{-\mathrm{i}\cot\alpha\Big(l^2m-k^2\big(1+0.5j^2m\bar{C}\big)\Big)}{\Big(k+m\big(k+2kj^2\bar{C}+\mathrm{i}j^2\cot\alpha\big)\Big)\Big((m\bar{C})^{-1}+0.5j^2\Big)} \quad \text{(14 non-dimensionalised)}$$

$$T_{VB}(k,l) = \frac{\mathrm{i}kl\Big(1+0.5j^2mC+m\Big)\cot\alpha}{\Big(k+m\big(k+2kj^2\bar{C}+\mathrm{i}j^2\cot\alpha\big)\Big)\Big((m\bar{C})^{-1}+0.5j^2\Big)} \quad \text{(15 non-dimensionalised)}$$

$$T_{SC}(k,l) = \frac{k}{k+m\Big(k+2kj^2\bar{C}+\mathrm{i}j^2\cot\alpha\Big)} \quad \text{(21 non-dimensionalised)}$$

$$T_{UC}(k,l) = \frac{\bar{C}\Big(3kl^2m\bar{C}+2k+kj^2m\bar{C}+2il^2\cot\alpha m\Big)}{\Big(k+m\big(k+2kj^2\bar{C}+\mathrm{i}j^2\cot\alpha\big)\Big)\Big(2+j^2m\bar{C}\Big)} \quad \text{(22 non-dimensionalised)}$$

$$T_{VC}(k,l) = \frac{-klm\bar{C}\Big(2i\cot\alpha+3k\bar{C}\Big)}{\Big(k+m\big(k+2kj^2\bar{C}+\mathrm{i}j^2\cot\alpha\big)\Big)\Big(2+j^2m\bar{C}\Big)} \quad \text{(23 non-dimensionalised)}$$

3.8.2 Additional airborne-radar flight lines

There are 9 airborne radar flight lines from the 2019/2020 field season which cross the region of Thwaites Glacier where the inversion procedure was carried out. 2 of these are presented in the main body of the text, and the remaining 7 are presented here.

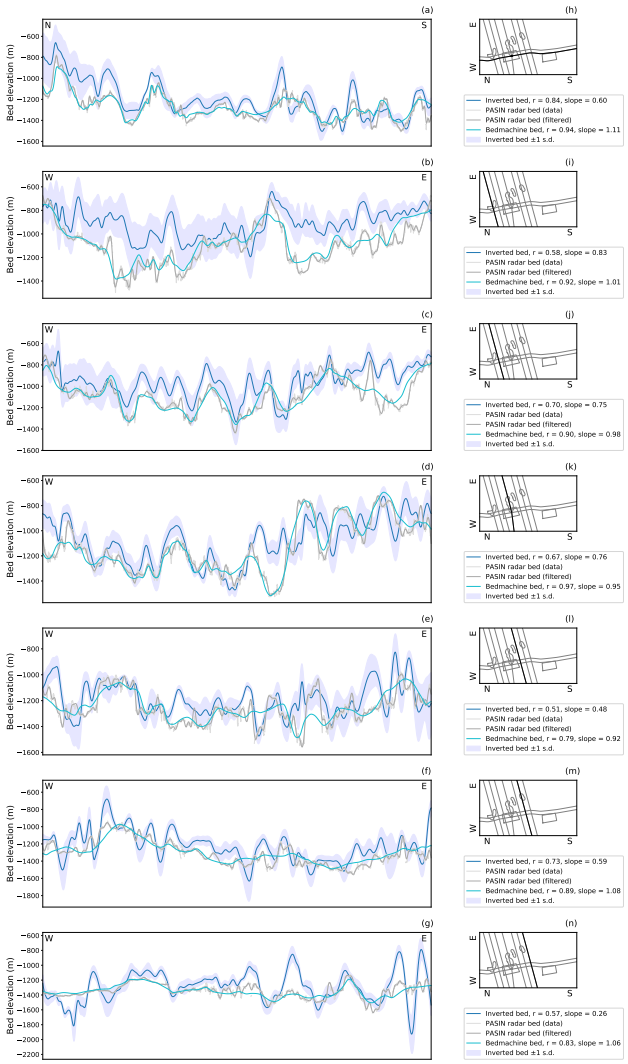

Fig. 3.12 a) to g) Comparative plots of inverted bed topography with mean non-dimensional slipperiness $\bar{C} = 100$ with along flow radar-sounded bed topography. Bed topography is given as unfiltered bed picks from the 2019/20 airborne surveys; a version of the same filtered to 2 km wavelengths to be more representative of the detail we might expect to image in our inversion; and the bed profile extracted from BedMachine Antarctica (Morlighem et al., 2020). The envelope around the inverted bed topography shows plus or minus one standard deviation. The correlation coefficients (r) and slopes given are the results of a linear regression between the inverted bed or the BedMachine Antarctica bed and the filtered radar bed. h) to n) Profile locations within the inverted grid.

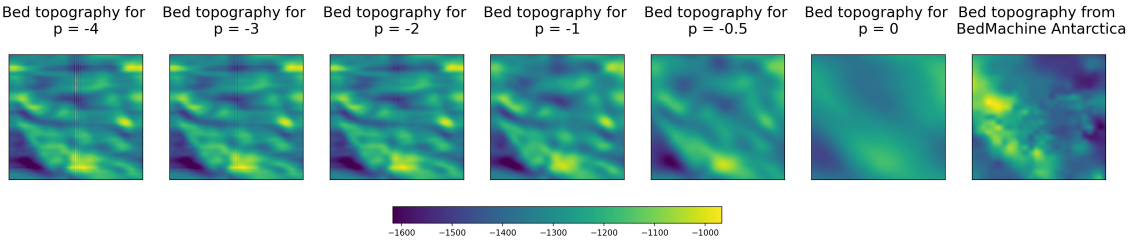

Fig. 3.13 Bed topography results of the inversion for the Upper Thwaites region (see Figure 6 for location) with a variety of values of p_{filt}. Increasing p filters out increasingly long wavelengths, and so a value of $p_{filt} = -2$ is chosen to filter out noisy short wavelengths, while maintaining realistic bed features, as compared to Bedmachine Antarctica (Morlighem et al., 2020).

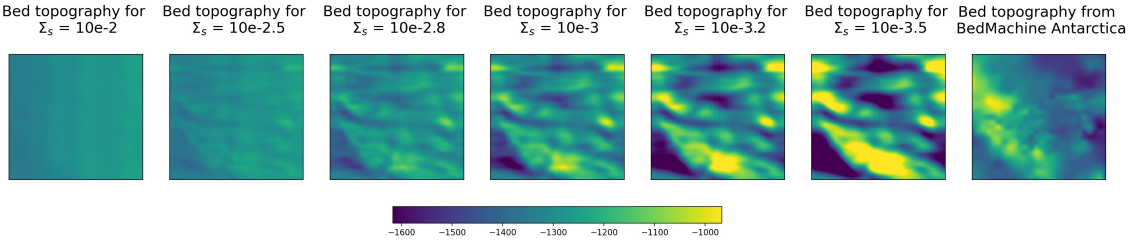

Fig. 3.14 Bed topography results of the inversion for the Upper Thwaites region (see Figure 6 for location) with a variety of values of Σ_s. The weighting factor Σ_s controls the balance in the least squares inversion between the surface elevation and surface velocity data, with smaller values of Σ_s weighting the inversion towards the surface elevation. A value of Σ_s = 0.001 is chosen to produce realistic amplitude bed features, as compared to Bedmachine Antarctica (Morlighem et al., 2020).

3.8.3 Parameter values

Figures 3.13 and 3.14 show the results from the inversion when carried out for the Upper Thwaites Glacier region with a range of values for the filtering parameter p_{filt} and the weighting factor Σ_s. These tests confirm the value choices from the synthetic tests ($p_{filt} = -2$, $\Sigma_s = 0.001$).

Chapter 4

Pine Island Glacier

A version of this chapter has been published in *Journal of Glaciology* as:
Ockenden, H., Bingham, R., Curtis, A., and Goldberg, D., 2023. Ice-flow perturbation analysis: A method to estimate ice-sheet bed topography and conditions from surface datasets. *Journal of Glaciology*, 1-10. DOI: 10.1017/jog.2023.50

Author Contributions

The concept of the paper was developed by HO, RB, DG and AC. The python code was developed and updated by HO, and applied to data from Pine Island Glacier. RB advised on the comparison to existing radar data, and DG on the methods for inverting for bed slipperiness. I wrote the main body of the text, but all authors contributed to the development of the final paper and associated figures.

4.1 Abstract

One of the largest contributors to uncertainty in predictions of sea-level rise from ice-sheet models is a lack of knowledge about the bed topography beneath ice sheets. Bed topography maps are normally made by interpolating between linear radar surveys using methods that include kriging, mass conservation and flowline diffusion, all of which may miss influential mesoscale (2-30 km) bedforms. Previous works have explored an Ice-Flow Perturbation Analysis (IFPA) approach for estimating bed topography using the surface expression of these mesoscale bedforms. Using regions of Pine Island Glacier that have been intensively surveyed by ice-penetrating radar as test sites, and a refined IFPA methodology, we find that IFPA detects bedforms capable of influencing ice flow which are not represented in Bedmachine Antarctica and other interpolated bed products. We further explore the ability of IFPA to estimate relative bed slipperiness, finding higher slipperiness in the main trunk and tributaries. Alongside other methods which estimate ice thickness, bed topography maps from IFPA have the potential to constrain projections of future sea-level rise, especially where radar data are sparse.

4.2 Introduction

Detailed knowledge of bed topography beneath ice sheets is an important input for modelling future ice-sheet behaviour and its contribution to sea-level rise. Direct measurements of bed topography have been made by radar sounding, but typically do not provide the density of coverage required by ice-sheet models. Traditionally, in slower-flowing ice, interpolation methods such as kriging and plate splines have been used to fill in the gaps (Fretwell et al., 2013), but these methods often have large uncertainties in regions where radar lines are sparse. In fast-flowing ice near the grounding line, the physical principle of mass conservation has been used to fill in the gaps (Morlighem et al., 2020). In many other upstream regions of Antarctica, a more complex interpolation method, flowline diffusion, has exploited the ice-surface flow direction to constrain the bed topography (Morlighem et al., 2020). However, the topography products from interpolation methods may miss mesoscale subglacial topography which is important for ice flow but which does not intersect radar survey lines. It is well known that variability in bed topography and basal slipperiness is transferred to the surface by ice flow (e.g. De Rydt et al., 2013; Crozier et al., 2018; Cooper et al., 2019b). High-resolution observations of ice-surface elevation may therefore provide an alternative route for recovering subglacial topography, even in regions with sparse radar coverage.

The relationship between surface and bed topography was first described mathematically by Nye (1959), and developed further by Budd (1970); Whillans and Johnsen (1983); Balise and Raymond (1985) and Reeh (1987). Gudmundsson (2003) and Gudmundsson (2008) built on these early works using a linearized perturbation analysis to provide analytical functions that describe the transfer of variability between bed topography and the ice surface. These transfer functions have been applied in 2D to bed topography on flowlines at Rutford Ice Stream (De Rydt et al., 2013) and in Greenland (Ng et al., 2018; Igneczi et al., 2018).

For three dimensions, this linear perturbation analysis approach was first applied to MacAyeal Ice Stream by Thorsteinsson et al. (2003) but, due to the low availability of high-resolution surface topography and velocity measurements at the time, it was not applied more widely. We recently built upon these foundations to apply an updated version of this methodology to modern satellite datasets across Thwaites Glacier (Chapter 3), and we call this methodology Ice-Flow Perturbation Analysis (IFPA). Here, we present a more efficient version of the code which now also accounts for variation in ice-flow direction, and implements a full-Stokes version of the analytical functions describing the transfer of variability between bed topography and the ice surface, rather than the shallow-ice-stream approximation version used previously. In Chapter 3, ice flow was assumed to be parallel to the polar stereographic grid in the negative x direction across the whole of the main trunk of Thwaites Glacier. Although this is a passable approximation for that region, it is obviously inappropriate for other regions of Antarctica, and so in this

paper's more advanced iteration of the IFPA code ice-flow direction is allowed to vary independently in each subdomain. Ice flow which is not aligned to the polar stereographic grid is accounted for by interpolating the ice surface data onto a grid aligned to the mean ice velocity, running the analysis, and then interpolating back to the polar stereographic grid. We apply IFPA to invert for subglacial topography and slipperiness at Pine Island Glacier. We selected this region for both its overall scientific significance and because within the catchment there exist several high-resolution radar surveys of bed topography (Bingham et al., 2017) which were not included in Bedmachine Antarctica (Morlighem et al., 2020) and hence provide independent sites for testing the success of our inversions. We therefore use these high-resolution radar surveys to assess the performance of IFPA relative to current interpolated products. We also produce broad-scale estimates of the variability in relative basal slipperiness across the glacier trunk, which potentially inform values of basal slipperiness to be applied when using this method in other regions of Antarctica.

4.3 Methodology

4.3.1 Ice-Flow Perturbation Analysis (IFPA)

The IFPA method is based on the observation that perturbations in the bed topography and basal slipperiness beneath flowing ice create variability in the ice-surface topography and velocity. Perturbations in bed topography and perturbations in basal slipperiness have different effects on the ice surface velocity and elevation, and so they can be resolved separately without mixing effects (Gudmundsson and Raymond, 2008). Gudmundsson (2003) and Gudmundsson (2008) considered the physics of such perturbations in an ice slab with constant viscosity and isotropic rheology, and derived a mathematical framework for understanding the relationship between the bed and the ice surface. This forms the basis for the work that we present here.

As in Chapter 3, section 3, we consider the steady-state spatial variability of the ice-surface elevation s, ice-surface velocity parallel to flow u and perpendicular to flow v, bed topography b, and basal slipperiness c, as functions of the spatial coordinates x and y. We denote the Fourier transforms of these with a circumflex ˆ, such that:

$$\hat{s}(k,l) = \int_{-\infty}^{\infty}\int_{-\infty}^{\infty} s(x,y)e^{-2\pi ikx}e^{-2\pi ily}dxdy, \tag{4.1}$$

where k and l are wavenumbers in the direction of flow (x) and perpendicular to the flow (y), respectively. So that we can make more general statements about the behaviour of the system in terms of variables such as ice thickness, we non-dimensionalise these parameters, and denote the non-dimensionalised quantities with a capital letter (see Section 2.1.3).

For ice in a planar slab aligned in the direction of ice flow, the non-dimensionalised Fourier transforms of perturbations in ice-surface elevation and velocity can be calculated from the non-dimensionalised Fourier transforms of perturbations in bed topography and basal slipperiness:

$$\Delta\hat{S}(k,l) = T_{SB}(k,l)\,\Delta\hat{B}(k,l) + T_{SC}(k,l)\,\Delta\hat{C}(k,l), \tag{4.2}$$

$$\Delta\hat{U}(k,l) = T_{UB}(k,l)\,\Delta\hat{B}(k,l) + T_{UC}(k,l)\,\Delta\hat{C}(k,l), \tag{4.3}$$

$$\Delta\hat{V}(k,l) = T_{VB}(k,l)\,\Delta\hat{B}(k,l) + T_{VC}(k,l)\,\Delta\hat{C}(k,l), \tag{4.4}$$

where T_{SB}, T_{SC}, T_{UB}, T_{UC}, T_{VB}, T_{VC} are wavenumber-specific, non-dimensional transfer functions that describe the amplitude ratio of perturbations in the bed properties relative to the ice surface properties, and which vary with angle of surface slope α, sliding law parameter m, and mean non-dimensional bed slipperiness $\bar{C}$. Depending on whether full-Stokes flow (Gudmundsson, 2003) or the shallow-ice-stream approximation (Gudmundsson, 2008) are considered, these transfer functions take different functional forms. Both sets of equations are set out in the Supplementary Information, and the code provided can be run with either. Due to their more complex functional form, the full-Stokes transfer functions take approximately twice as long to run.

Equations 4.2, 4.3 and 4.4 form an over-determined system of three known variables which can be solved using a weighted least-squares inversion (see Thorsteinsson et al., 2003, Section 3 and Chapter 3, Appendix C). The least-squares inversion runs over a defined grid where the parameters which influence the transfer functions (mean ice thickness $\bar{h}$, angle of slope α, sliding law parameter m, and mean bed slipperiness $\bar{c}$) should be approximately constant. As in Chapter 3, the mean ice thickness, $\bar{h}$, is obtained from a 50 km averaged version of BedMachine Antarctica ice thickness (Morlighem et al., 2020), and we use $m = 1$. In order to apply the method across a large area over which these parameters are variable, we run the model on overlapping 25 km by 25 km patches, and allow these patches to have different parameters. Each grid point in the larger area is included in nine overlapping patches, and the final elevation included in the results is the weighted mean of these nine values, with a weighting factor based on the position in the overlapping patch. This weighted smoothing reduces the number of overlapping patches required to remove most edge effects, which means that the code runs more efficiently compared to the iteration method used in Chapter 3.

4.3.2 Assessing method performance through comparison to radar surveys

IFPA produces maps of variations in both bed topography and basal slipperiness. However, since there are no direct observations of bed slipperiness (which is a parameter representing many components of hydrology, geology and sedimentology that cannot be independently

constrained), we focus on the bed topography component of these results to test the performance of IFPA. We compare our results with ice-penetrating radar surveys of the bed topography at seven sites in Pine Island Glacier surveyed in 2010 and 2013/14 (Bingham et al., 2017). These surveys acquired data with a 500 m line spacing between ice-flow-orthogonal survey tracks, and an along-track sounding interval of 4-6 m, over regions of 20 by 40 km (2010 survey) and 10 by 15 km (all six 2013/14 surveys). Further details of acquisition and processing are detailed in Bingham et al. (2017). These radar soundings were not processed in time for inclusion in BedMap2 (Fretwell et al., 2013) or Bedmachine Antarctica v1 (Morlighem et al., 2020), and so provide an opportunity to assess the performance of IFPA in emulating directly-measured and previously interpolated bed topography.

We used IFPA to invert surface elevation from REMA v1 (Howat et al., 2019) (100 m tiles, with interpolation to fill small gaps) and surface velocities from ITS_LIVE (Gardner et al., 2018) (450 m spatial resolution, velocity composite from 1995 - 2016). This produced bed topography and slipperiness across the main trunk of Pine Island Glacier. IFPA performance is assessed by comparison with the directly-surveyed bed topography sounded by the ice-penetrating radar, and with bed topography from Bedmachine Antarctica that, for all of these sites, was derived with flowline diffusion (Morlighem et al., 2020).

4.3.3 Exploring the role of the tuneable slipperiness parameter $\bar{C}$

The amplitude of variations in the topography on the surface of flowing ice sheets depends not only on the bed topography, but also on conditions at the base including the basal-ice and subglacial rheology, hydrology and till availability. These "basal conditions" are poorly mapped beneath the Antarctic ice sheets but are collectively represented in IFPA by a mean non-dimensional slipperiness parameter, $\bar{C}$. Here, building from Chapter 3 and Kyrke-Smith et al. (2017), we use $\bar{C}$ as a tuneable parameter to constrain the amplitude of the topography, and explore optimal values for basal slipperiness across different parts of the glacier. We therefore ran the model with respective mean-slipperiness values of $\bar{C} = 25, 50, 75, 100, 150$ and 200.

In order to evaluate the best value of mean non-dimensional slipperiness $\bar{C}$, we compare the bed topography across Pine Island Glacier from IFPA to a) 3D ice-penetrating radar-sounded bed topography acquired in 2013/14 and b) 2D airborne-radar-sounded bed topography acquired in 2004/05 (Vaughan et al., 2006; Jordan and Robinson, 2021). Because, mathematically, IFPA cannot resolve features aligned to the ice-flow direction ($k = 0$), we only examine results for radar lines oriented at an angle of less than 10 degrees to flow. These lines primarily sound across-flow features which should be resolved.

4.4 Results

4.4.1 Full-Stokes vs shallow-ice-stream approximation

Figure 4.1 shows a comparison of the bed topography from the IFPA model when run with the full-Stokes transfer functions and the shallow-ice-stream transfer functions, with all other parameters kept constant between the two model runs. We know from Gudmundsson (2008) that, compared to the full-Stokes equations, the shallow-ice-stream approximation underestimates variability in bed topography for wavelengths less than about 10 ice thicknesses (roughly 20 km in this case) when inverting from the ice surface. We can see in Figure 4.1 that the full-Stokes transfer functions generally produce higher amplitude topography, in agreement with the theory. Gudmundsson (2008) also shows that this underestimation depends on the ice surface slope, and the basal slip ratio, which is most likely why the differences in amplitude are higher closer to the grounding line. Since meso-scale (2-30 km) bedforms are some of the features which we are most interested to estimate with this method, the rest of the results presented in this paper use the full-Stokes transfer functions from Gudmundsson (2003).

4.4.2 Modelled bed topography

Figure 4.2 shows the bed topography derived from IFPA, compared with bed topography directly surveyed with radar and modelled from flowline diffusion in Bedmachine Antarctica. The results show that IFPA is successful in resolving medium-wavelength features which are not resolved by the flowline diffusion method. This is illustrated by the 5 km-wide subglacial hill in the centre of Site iSTARt1 (Fig. 4.2a) which is not present at all in Bedmachine Antarctica, the subglacial hill at the southwestern corner of Site iSTARt6 (Fig. 4.2b), and the 10 km-wide valley running from south to north (right to left) in the centre of Site iSTARt9 (Fig. 4.2c).

For features in the bed to make an impression on the ice surface, they need to have a wavelength which is at least equivalent to the thickness of the ice, which in the Pine Island region is around 2 km. Step functions have both long and short wavelength components, which means that sharp transitions in bed topography occurring over less than 2 km, such as the 400 m high cliff at Site iSTARt7 (Fig. 4.2d), tend to become more smoothed in the bed topography produced by IFPA, although they are still present. Smaller-scale features (or spikes) with no long-wavelength component, such as the subglacial hillocks in the western (lower in page) part of Site iSTARit (Fig. 4.2e), are completely smoothed out. Ice flow in Site iSTARit (Fig. 4.2e) is very slow, which also reduces transmission of basal variability to the ice surface. Synthetic tests (Chapter 3, Gudmundsson, 2003, 2008) show that these small-scale spikes and bumps are features which are not large enough to make an impression on the ice surface, and will only have a local influence on basal ice flow.

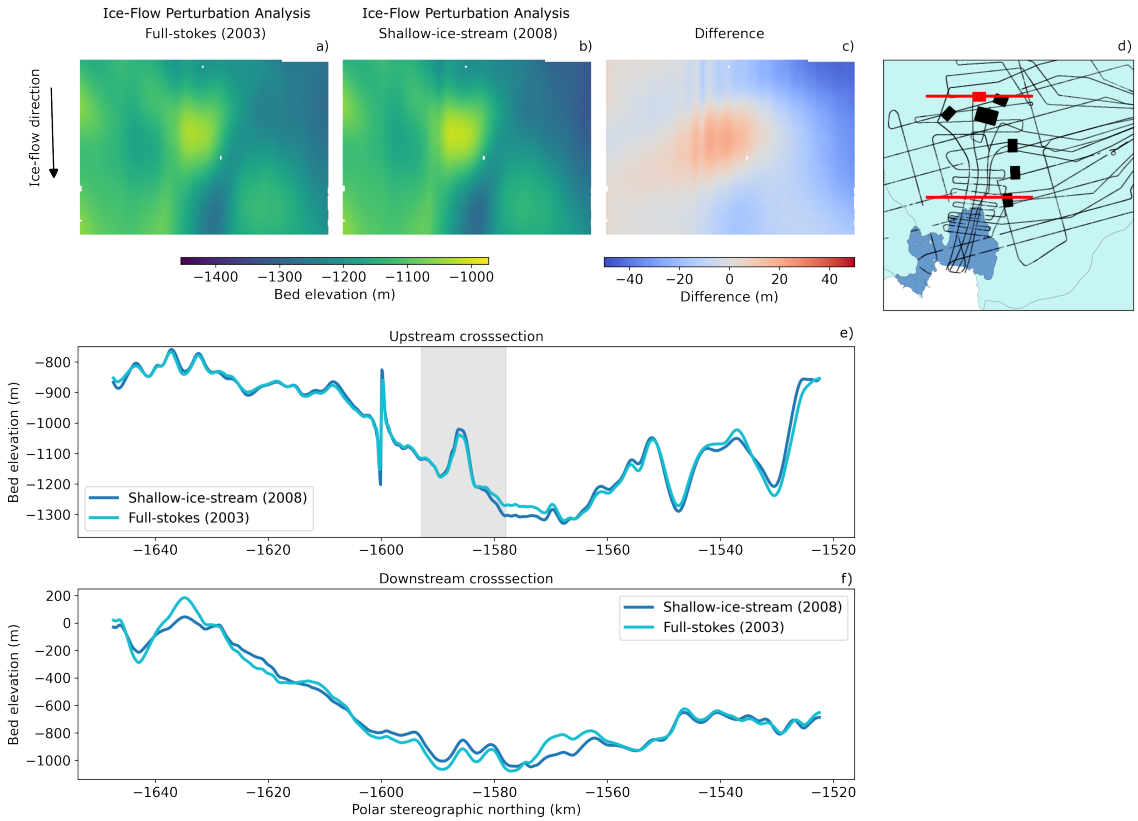

Fig. 4.1 A comparison of bed topography produced from Ice-Flow Perturbation Analysis (IFPA) with the full-Stokes transfer functions from Gudmundsson (2003) and the shallow-ice-stream transfer functions from Gudmundsson (2008) for a 3D topographic patch (Site iSTARt1), and two linear cross sections. Mean non-dimensional slipperiness, $\bar{C} = 100$. d) Location figure marking patches of 3-D topography surveyed at high resolution with ice-penetrating radar in 2013/14 (Bingham et al., 2017) black rectangles, with the patch in panels a-c coloured red), and airborne-radar profiles acquired in 2004/05 ((Vaughan et al., 2006) black lines, with red lines marking profiles in panels e and f). Panel e) shows the comparison for the upstream cross-section, and panel f) shows the comparison for the downstream cross section. The grey highlighted section of panel e) marks the profile's transition across Site iSTARt1. Spikes at -1600 km in panel e) result from an artefact of the transition between tiles of the REMA data, which could be avoided by using a continuous surface elevation product.

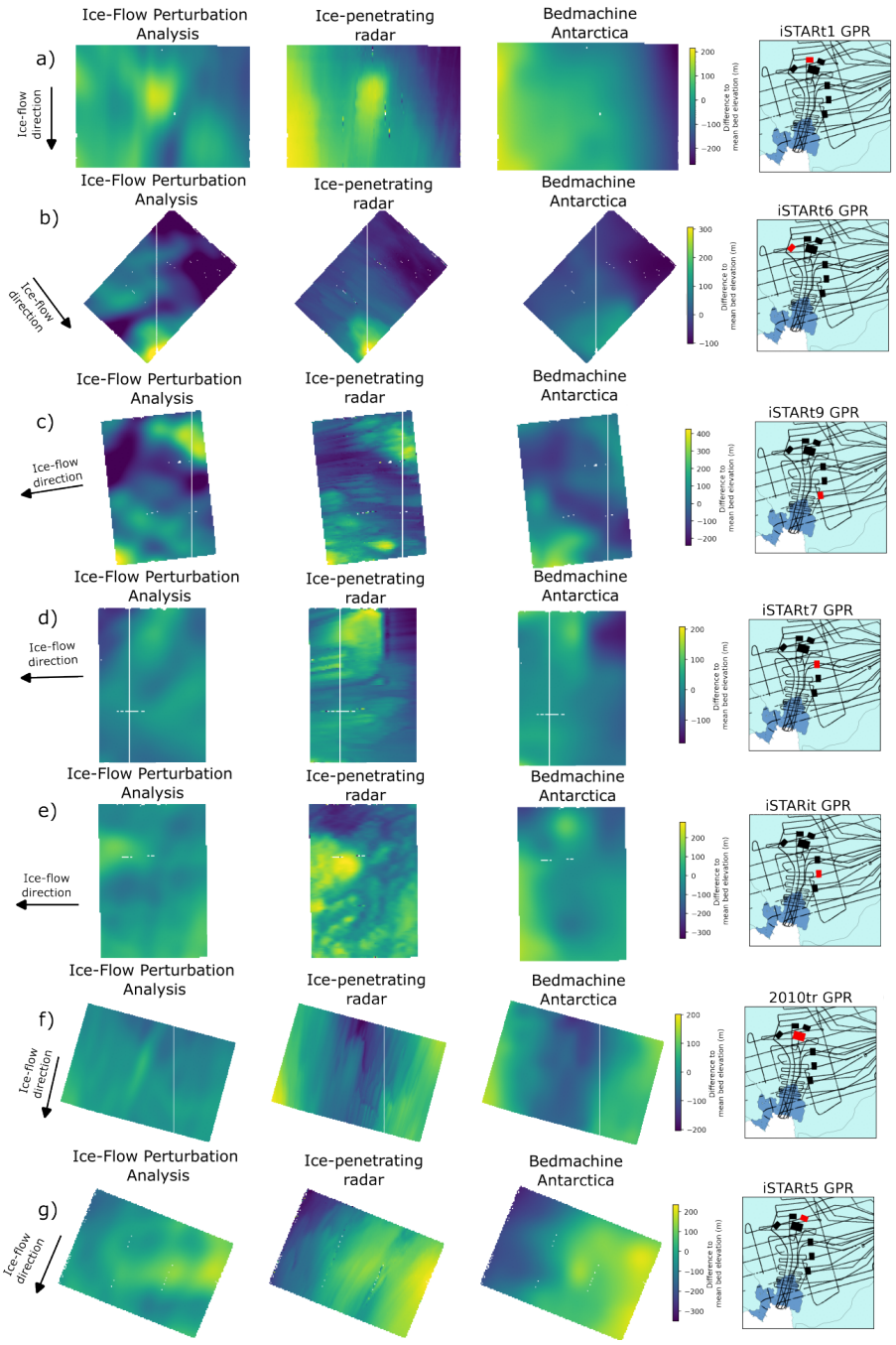

Fig. 4.2 A comparison of bed topography from IFPA, ice-penetrating radar, and BedMachine Antarctica flowline-diffusion interpolation for seven regions of Pine Island Glacier. a) iSTARt1, b) iSTARt6, c) iSTARt9, d) iSTARt7, e) iSTARit, f) 2010tr, and g) iSTARt5. IFPA plots are for the best fit value of $\bar{C}$, as shown in Figure 4.3. ($\bar{C} = 75, 50, 25, 150, 5, 200, 100$ from top to bottom). Survey-site locations are shown in red in the rightmost column.

Synthetic experiments have shown that for features in the bed to make an impression on the ice surface, they should be aligned in a direction offset from the flow direction by at least 10 degrees (Chapter 3). Landforms with wavenumber combinations which correspond to features aligned to flow (k = 0) are not resolved, as they fall into the null space of the inversion. We therefore do not expect flow-parallel features, such as the mega-scale glacial lineations observed at Site 2010tr (Fig. 4.2f), to be resolved in the bed topography produced by IFPA, although there is a wider flow-parallel feature through this site in the IFPA topography. Features with a combination of different orientations, such as the lineated north-south ridge at Site iSTARt5 (Fig. 4.2g), can be partly identified. The deeper groove on the south (right) side of the ridge is not resolved, as it is aligned with the ice flow ($k = 0$). However, the crest of the ridge (top right to bottom left) is picked out well, as it is at an angle of around 45° to the ice flow.

4.4.3 Basal slipperiness

Figure 4.3 shows bed-topography cross-sections from the 2010-2014 ice-penetrating radar sites, and the comparison with the modelled bed topography with different values of the mean non-dimensional slipperiness, $\bar{C}$. For each site, we visually judge the best-fit value of mean non-dimensional slipperiness, $\bar{C}$, to be the result with the most similar amplitude to the ice-penetrating-radar-sounded bed at the maximum point of the most distinct hill or trough in the cross-section, and label this on each cross-section.

For Site iSTARt1 (Fig 4.3a) and Site 2010tr (Fig 4.3f), there is a clear best fit across the main hill feature. For Site iSTARt6 (Fig 4.3b) we use the hill which goes off the side of the patch as the calibration feature. For some lines (e.g. Figs. 4.3c, 4.3d) we can not resolve all the small scale variability and so we compare to the broader-scale topographic shapes. For Site iSTARt5 (Fig 4.3g) the topography does not have any particularly distinct features, and so we use the mean non-dimensional slipperiness value of $\bar{C} = 100$. For Site iSTARit (Fig 4.3e) none of the model runs can reproduce the amplitude of the hill in the centre of the transect. For the purposes of mapping variability, we suggest an extremely low slipperiness of $\bar{C} = 5$, but in reality the slow flow of ice in this patch probably means that the ice surface does not fully reflect the bed in this region and so IFPA can not resolve the bed topography.

Figure 4.4 shows the bed-topography cross sections from selected airborne radar profiles, and the topography produced when the IFPA method is applied with different values of the mean non-dimensional slipperiness $\bar{C}$. Some of these profiles (Figs. 4.4c, 4.4e, 4.4g, 4.4i, 4.4j, 4.4k, 4.4i, 4.4m, 4.4n, and 4.4q) closely fit the radar-sounded bed topography such that the selection of the mean non-dimensional slipperiness $\bar{C}$ is straightforward. For two profiles (Figs. 4.4a and 4.4f), the positions of the amplitude maxima are not the same in the airborne radar and the inverted bed topography, but we pick the maximum amplitude of the inverted topography which lines up best. For the rest of the selected airborne-radar profiles, (Figs 4.4b, 4.4d, 4.4h, 4.4o, 4.4p, 4.4r), the

overall amplitude of the topography is correct but some of the shorter-scale features are not resolved.

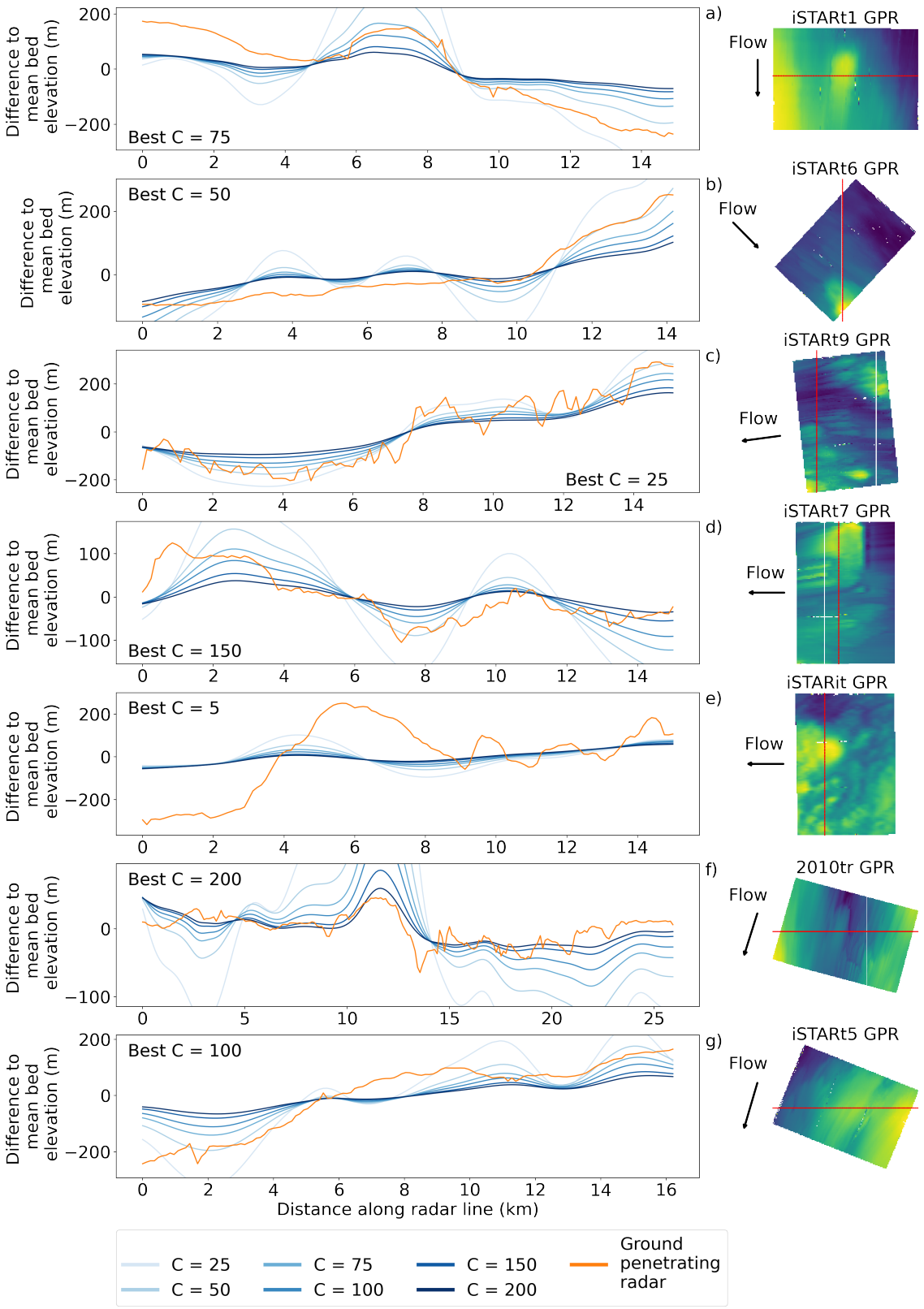

(Caption on next page.)

Fig. 4.3 Cross-sections across the main topographic features in each of the radar-survey sites: a) iSTARt1 (10 by 15 km), b) iSTARt6 (10 by 15 km), c) iSTARt9 (10 by 15 km), d) iSTARt7 (10 by 15 km), e) iSTARit (10 by 15 km), f) 2010tr (20 by 40 km), and g) iSTARt5 (10 by 15 km). The amplitudes of the IFPA results are shown for different values of the mean non-dimensional slipperiness parameter $\bar{C}$ in graduated shades of blue, and the ice-penetrating radar results in orange. Cross-section profile locations are marked red over the radar-sounded topographic maps. White lines are data gaps which arise due to interpolation. Comparison between the radar surveys and different model runs allows for an assessment of the best-fit mean non-dimensional slipperiness at each site (shown in the bottom-left), and therefore slipperiness variability across the Pine Island Glacier region.

Putting together the best-fit values for each cross-section leads to a map of mean non-dimensional slipperiness, $\bar{C}$, (Figure 4.5) across the main trunk of Pine Island Glacier. The dimensional slipperiness, $\bar{c}$, is shown in Figure 4.5b, but this is mostly dominated by the velocity (which is a component in the dimensionalisation, Figure 4.5d) and so does not necessarily show localised variability as well as the non-dimensional slipperiness (Figure 4.5c).

4.5 Discussion

4.5.1 Assessing IFPA performance through comparison to radar surveys

The overall performance of IFPA as applied to the radar-sounded topography on Pine Island Glacier for this paper is consistent with our understanding of IFPA from synthetic tests (Chapter 3). Mathematically we do not expect to be able to resolve features aligned to ice flow (k = 0) or smaller horizontal extent than the ice thickness, and indeed we do not. Features which do not fall into either of these two categories are, however, resolved well, and in a number of locations represent topography that is not resolved in the interpolated bed topography from Bedmachine Antarctica (e.g. Fig 4.2a).

For all of the sites discussed in this paper, Bedmachine Antarctica uses a method termed "flowline diffusion" to interpolate bed topography. Flowline diffusion is an anistropic interpolation method "not based on physics" (Morlighem et al., 2020, SI pg6) which allows more variability across flow than along flow, thereby preserving features aligned with the ice-flow direction ($k = 0$). Interpolation occurs between radar lines, which are often spaced more than 5 km apart. There is no allowance for features which are not aligned to flow, and which do not cross one of these radar lines, and so we would not expect flowline diffusion, and hence Bedmachine Antarctica, to be able to detect features such as the subglacial hills in Site iSTARt1 and Site iSTARt6 (Fig 4.2a and Fig 4.2b), or the valley in Site iSTARt9 (Fig 4.2c). IFPA therefore offers the potential to improve our knowledge of

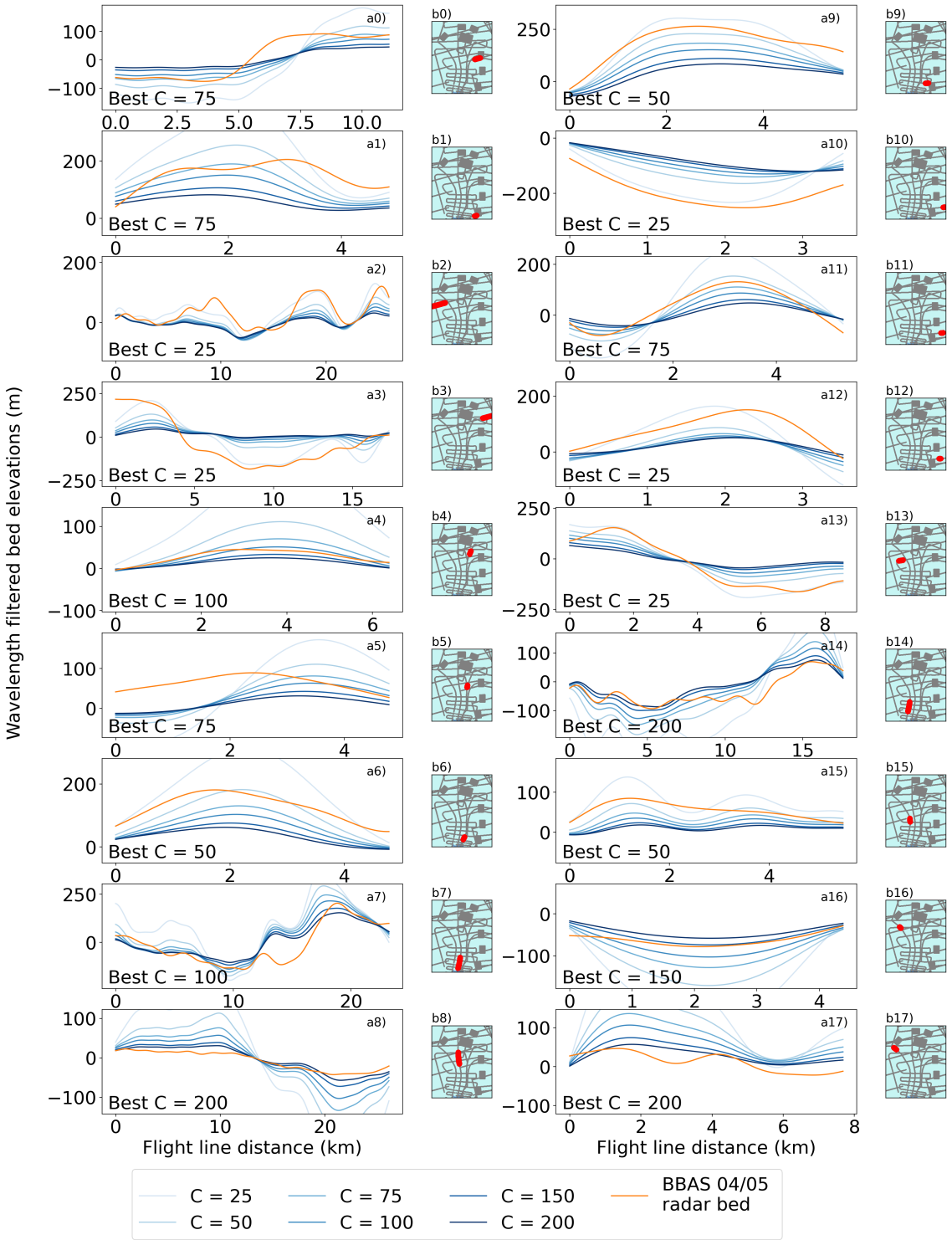

Fig. 4.4 Bed topography profiles (with wavelengths > 50 km removed) from selected airborne-radar profiles which are at angles of no more than 10 degrees to flow and contain distinct bedforms (panels a) - r)). The radar bed pick is shown in orange and the IFPA beds for different values of the mean non-dimensional slipperiness parameter $\bar{C}$ are in graduated shades of blue. Profile locations are shown in red on the inset maps.

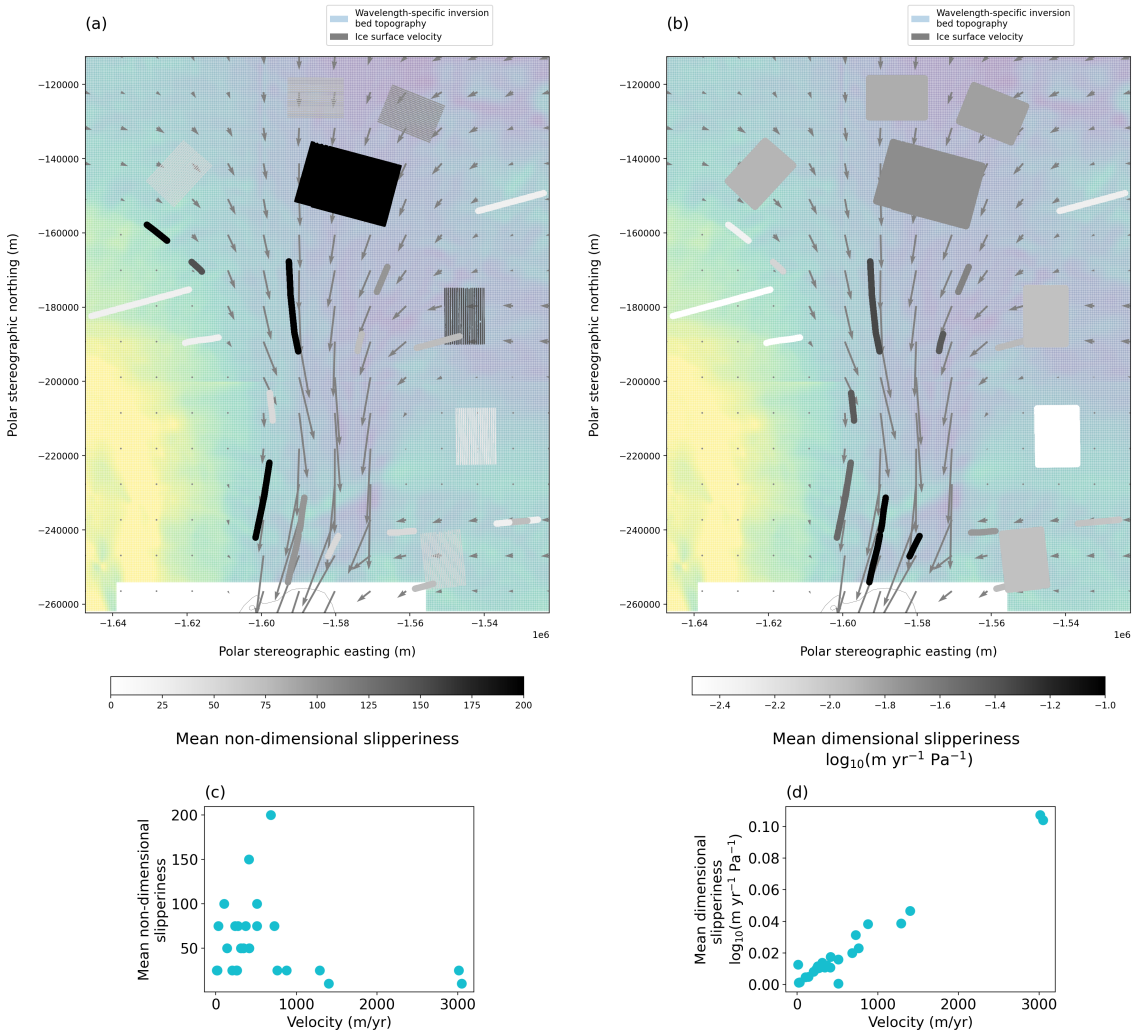

Fig. 4.5 The best-fit mean non-dimensional slipperiness across Pine Island Glacier, as calculated by comparing the amplitude of landforms observed in radar measurements to those from IFPA, with bed topography and ice-surface velocity shown in the background. Both the airborne radar lines and ice-penetrating radar grids are shown. a) Non-dimensional slipperiness, b) dimensional slipperiness (note that this mostly varies with velocity). Higher slipperiness is observed in the main trunk and tributaries. Due to the mathematical inability of IFPA to resolve landforms aligned to flow ($k = 0$), only radar lines aligned to flow (which cross landforms at an angle to flow) have been used. Panels c) and d) show the relationship between ice velocity and mean non-dimensional slipperiness (c) and mean dimensional slipperiness (d) respectively.

bed topography in parts of Antarctica where features exist between radar survey lines and have an expression in the ice surface.

4.5.2 Exploring the role of the tuneable slipperiness parameter $\bar{C}$

In this work we have also explored how we can use existing radar-sounded bed topography to explore the role of the mean non-dimensional slipperiness parameter, $\bar{C}$, and its effects on the amplitude of the topography. Typically, basal slipperiness is modelled by inverting surface observations with a fixed bed topography (Morlighem et al., 2010). Nias et al. (2016) adopt an iterative approach starting with BedMap2 to produce topography and friction maps for the Amundsen Bay Embayment. Some models invert for slipperiness and topography together, but these have not been applied to Pine Island Glacier. If there are errors in the bed topography, these then propagate into the slipperiness estimate. Kyrke-Smith et al. (2017) showed that including high-resolution topography can reduce the modelled basal slipperiness, as it changes the way basal drag is partitioned in these inversions. The total basal friction is partitioned between form drag (caused by topography) and skin drag (caused by other basal properties), so more knowledge about topography can increase the modelled contribution from form drag, but decrease the modelled skin drag contribution, which is what the basal slipperiness parameter represents. Modelled slipperinesses which use the bed topography from BedMap2 (Morlighem et al., 2010; De Rydt et al., 2013; Kyrke-Smith et al., 2017) or Bedmachine Antarctica (Barnes et al., 2021) are likely to overestimate the contribution from skin drag, and may falsely attribute this to bed properties such as water content or till distributions. The method which we apply here to map the basal slipperiness only uses direct observations of topography rather than interpolated topography, and therefore avoids this issue. It does require accurate bed measurements to be available in the local area for calibration, but topographic measurements from other tributaries to the same glacier, or nearby glaciers should be sufficient, as long as the geology is thought to be similar.

Figure 4.5 depicts a general trend for higher slipperiness in the main trunk of the glacier, and lower slipperiness in the higher topographic regions between the tributaries. A higher slipperiness means lower friction for sliding, and we propose that this is likely to be due to higher erosion rates and a thicker sediment layer in the main glacial trough, such as at Site 2010tr (Fig 4.3f) and some of the airborne survey lines (eg Fig 4.4h and Fig 4.4n). Lower slipperiness means more friction against sliding, and we suggest this is likely to be due to more exposed bedrock on the higher topography, for example at Site iSTARt9 (Fig 4.3c), and the airborne-radar profiles shown in Figure 4.4b and Figure 4.4c. As well as agreeing with other modelled basal-slipperiness studies (Morlighem et al., 2010; De Rydt et al., 2013; Kyrke-Smith et al., 2017; Barnes et al., 2021), this is what we would expect in an active glacial environment, where the motion of the ice erodes glacial till. The till is removed from the higher topography exposing the bedrock, and accumulates in glacial troughs, where it can lubricate ice flow. Seismic studies from Pine Island Glacier (Smith

et al., 2013; Brisbourne et al., 2017; Davies et al., 2018) and offshore work in Pine Island Bay (Nitsche et al., 2013; Muto et al., 2016) also support this picture of a mixed subglacial environment with abundant till and some exposed bedrock.

4.5.3 Applying Ice-Flow Perturbation Analysis to other regions of Antarctica

We have found that there is considerable variation in the values of IFPA-inferred mean slipperiness which match best with the existing bed topography across Pine Island, but this variability appears to be linked with broad-scale topographic patterns. Bingham et al. (2017) showed that there was a first-order relationship between bed topography and ice flow across Pine Island Glacier, pointing to the principal importance of form drag. Seismic surveys (Smith et al., 2013; Brisbourne et al., 2017) support these findings and have suggested that there is a connection between topography, the distribution of glacial tills and sliding patterns. A relationship between bed-sliding properties and topography has also been observed on Thwaites Glacier (Muto et al., 2019b,a; Clyne et al., 2020). Due to the spread of best-fit mean non-dimensional slipperiness values, we propose that a spatially-variable mean non-dimensional slipperiness parameter, $\bar{C}$, should be used when applying IFPA to other regions of Antarctica. Ideally a local constraint on the variations in $\bar{C}$ should be used, but since there are relatively few areas with such high density radar surveys to use for this calibration in other regions, we propose applying values of $\bar{C}$ = 150 in glacial troughs and $\bar{C}$ = 50 in rougher areas in between. This may lead to a slight overestimate of topography in troughs and an underestimate between them, but should account for some of the difference in sliding mechanics, and produce more realistic bed topography overall.

Additionally, as $\bar{C}$ represents the ratio between the mean basal-sliding velocity and the mean internal-deformation velocity (Gudmundsson, 2008), it may be possible to calculate suitable values of $\bar{C}$ using other observations. Information about the thermal and mechanical properties of the ice can be used to calculate the deformational velocity, and alongside the surface velocities (Rignot et al., 2011b), this may help to determine the most suitable values of $\bar{C}$ to apply in other regions of Antarctica.

When considering the regions of Antarctica where IFPA might be useful, it is important to consider the known weaknesses of the method. In regions of extremely slow flowing ice, such as Site iSTARit (Fig 4.3e), even extremely low values of the mean non-dimensional slipperiness can not match the existing bed topography. The IFPA method assumes that the ice surface is in steady state with the bed, but we suggest that this mismatch may be due to the slow transfer of the topographic variability from the bed to the surface. Although these slow flowing regions are not terribly important in contemporary ice dynamics, they may become important in the future as regions of faster flow expand further inland from the current coastline. More intriguingly, however, they may also give a hint of how palaeo-

ice-dynamics could have been different. Analysis of the relationship between englacial stratigraphy and both the 'true' radar topography and the modelled IFPA topography in these regions has the potential to further illuminate past variations in ice flow patterns.

Analysis of englacial stratigraphy alongside perturbations in the ice flow may also inform us about the viscosity distribution in ice sheets. Although we assume linear viscous ice for IFPA (flow law constant $n = 1$), observations suggest that viscosity is not constant through the ice column ($n = 3$ to 4). This would lead to non-uniform transfer of perturbations from the bed to the surface, which may be visible in regions where englacial layers can be seen throughout the ice column and especially at depth. Additionally, as higher values of n lead to stronger surface expressions of features (Jóhannesson, 1992; Raymond and Gudmundsson, 2005), assuming $n = 1$ may over-estimate the amplitude of the bed topography. However, the choice of the mean non-dimensional slipperiness may reduce this effect, as the most suitable value of $\bar{C}$ depends on both basal slipperiness and ice viscosity.

Another issue with IFPA is that we require a continuous 50 km by 50 km patch which can be approximated by flow in an inclined slab, in order to invert the surface elevation and velocity fields. This means that we can not apply the method too close to the grounding line, as floating ice behaves with different physics to grounded ice. However, in fast flowing ice close to the grounding line where dense radar observations are available, Bedmachine Antarctica uses the mass conservation method, which takes into account variation in surface elevation (Morlighem et al., 2020) and is therefore less likely to miss mesoscale landforms than the flowline diffusion method which is used further inland. Requiring flow which can be approximated by slab flow also means that IFPA is likely to struggle in regions where the ice is not fully covering the topography at the 50 km scale, such as in the Antarctic Peninsula. It is possible to reduce the size of the patch, which may increase the utility of the method in smaller glaciers, as long as the ice thickness is much less than the width between confining walls so that the flow can be approximated by an inclined slab. Additionally, the application of an non-uniform background state, as has previously been applied to flowlines from Columbia Glacier and Nordenskiöld Glacier (Ng et al., 2018), could improve the long-wavelength background conditions applied in the model, and account for converging and diverging flow in addition to non-slab flow. Generally though, we believe that the IFPA method will be of most use in inland regions with continuous ice cover.

IFPA tells us about variations in the bed relative to the mean elevation, but does not tell us about the absolute ice thickness. To demonstrate the potential of the method, and to ensure that we present an independent test of IFPA and Bedmachine Antarctica, we have used a single ice-thickness value for each 50 km by 50 km region in the Pine Island Glacier catchment. However, to improve the utility of the IFPA bed-topography product, we could incorporate more of the measured radar bed topography which is included in Bedmachine Antarctica, potentially using the error estimate which accompanies Bedmachine Antarctica.

The strength of flowline-diffusion is the ability to interpolate along flow landforms, which is one of the known weaknesses of IFPA. A combined product which includes both the flow-oriented landforms from Bedmachine Antarctica and the flow-orthogonal landforms from IFPA would represent a powerful baseline for the next generation of ice-sheet models, for which the representation of basal roughness and traction is so crucial (e.g., Durand et al., 2011; Kyrke-Smith et al., 2018; Nias et al., 2018).

4.6 Conclusions

Building on the work of Gudmundsson (2003); Gudmundsson and Raymond (2008) and Thorsteinsson et al. (2003), and our recent application of IFPA on Thwaites Glacier (Chapter 3), we have produced maps of the bed topography beneath Pine Island Glacier, West Antarctica, by inverting from satellite-derived surface ice properties and varying values of basal slipperiness. We use transfer functions for IFPA based on the full-Stokes equations rather than the shallow-ice-stream approximation. A comparison of the inverted topography with directly sounded topography from ice-penetrating radar and the bed interpolated using flowline diffusion in Bedmachine Antarctica shows that our application of Ice-Flow Perturbation Analysis (IFPA) is able to capture topographic features which could never be resolved by flowline diffusion. Since flowline diffusion is the main method used by Bedmachine Antarctica in the inland regions of Antarctica, IFPA offers the potential to enhance our understanding of bed topography across much of the continent.

We also used the trade-off between mean non-dimensional slipperiness $\bar{C}$, and topographic amplitude in the IFPA method to explore trends in slipperiness across the main trunk and tributaries of Pine Island Glacier. We found higher slipperiness (or lower basal friction) in the main glacial trough and lower slipperiness (or higher basal friction) on the elevated topography between tributaries; this trend agrees with observations from seismic surveys. Matching the radar topography with IFPA requires a range of values of the mean non-dimensional slipperiness parameter. When applying IFPA in other regions of Antarctica we would ideally use local radar observations for calibrating $\bar{C}$, but in areas with sparsely distributed radar measurements we suggest applying a variable mean non-dimensional slipperiness of $\bar{C} = 150$ in fast-flowing glacial troughs and $\bar{C} = 50$ in slower-moving highlands.

4.7 Supplementary information

4.7.1 Non-dimensionalised transfer functions

For ice in a planar slab aligned in the direction of ice flow, the non-dimensionalised Fourier transforms of perturbations in ice surface elevation, ($\hat{S}$), and velocity, ($\hat{U}$, $\hat{V}$), can be calculated from the non-dimensionalised Fourier transforms of perturbations in bed

topography, ($\hat{B}$), and basal slipperiness, ($\hat{C}$):

$$\hat{S}(k,l) = T_{SB}(k,l)\,\hat{B}(k,l) + T_{SC}(k,l)\,\hat{C}(k,l), \tag{4.5}$$

$$\hat{U}(k,l) = T_{UB}(k,l)\,\hat{B}(k,l) + T_{UC}(k,l)\,\hat{C}(k,l), \tag{4.6}$$

$$\hat{V}(k,l) = T_{VB}(k,l)\,\hat{B}(k,l) + T_{VC}(k,l)\,\hat{C}(k,l), \tag{4.7}$$

where T_{SB}, T_{SC}, T_{UB}, T_{UC}, T_{VB}, T_{VC} are wavenumber specific non-dimensional transfer functions which describe the amplitude ratio of perturbations in the bed properties relative to the ice surface properties, and which vary with the wavenumbers k and l, angle of slope, α, sliding law parameter, m, and mean non-dimensionalised bed slipperiness, $\bar{C}$.

Depending on whether full-Stokes flow (Gudmundsson, 2003) or the shallow-ice-stream approximation (Gudmundsson, 2008) are considered, these transfer functions take different functional forms, where $j^2 = k^2 + l^2$.

For the shallow-ice-stream approximation (Gudmundsson, 2008):

$$T_{SB}(k,l) = \frac{k\Big(1 + m\big(2j^2\bar{C} + 1\big)\Big)}{k + m\Big(k + 2kj^2\bar{C} + \mathrm{i}j^2\cot\alpha\Big)}, \tag{4.8}$$

$$T_{UB}(k,l) = \frac{-\mathrm{i}\cot\alpha\Big(l^2 m - k^2\big(1 + 0.5j^2 m\bar{C}\big)\Big)}{\Big(k + m\big(k + 2kj^2\bar{C} + \mathrm{i}j^2\cot\alpha\big)\Big)\Big((m\bar{C})^{-1} + 0.5j^2\Big)}, \tag{4.9}$$

$$T_{VB}(k,l) = \frac{\mathrm{i}kl\Big(1 + 0.5j^2 mC + m\Big)\,\cot\alpha}{\Big(k + m\big(k + 2kj^2\bar{C} + \mathrm{i}j^2\cot\alpha\big)\Big)\Big((m\bar{C})^{-1} + 0.5j^2\Big)}, \tag{4.10}$$

$$T_{SC}(k,l) = \frac{k}{k + m\Big(k + 2kj^2\bar{C} + \mathrm{i}j^2\cot\alpha\Big)}, \tag{4.11}$$

$$T_{UC}(k,l) = \frac{\bar{C}\Big(3kl^2 m\bar{C} + 2k + kj^2 m\bar{C} + 2il^2\cot\alpha m\Big)}{\Big(k + m\big(k + 2kj^2\bar{C} + \mathrm{i}j^2\cot\alpha\big)\Big)\Big(2 + j^2 m\bar{C}\Big)}, \tag{4.12}$$

$$T_{VC}(k,l) = \frac{-klm\bar{C}\Big(2i\cot\alpha + 3k\bar{C}\Big)}{\Big(k + m\big(k + 2kj^2\bar{C} + \mathrm{i}j^2\cot\alpha\big)\Big)\Big(2 + j^2 m\bar{C}\Big)}. \tag{4.13}$$

For full-Stokes flow (Gudmundsson, 2003):

$$T_{SB,num}(k,l) = jk\Big((1+\bar{C})\big(\bar{C}j\sinh(j)+\cosh(j)\big)+\cosh(j)\big(1+\bar{C}+\bar{C}^2j^2\big)\Big), \quad (4.14)$$

$$T_{surf,den}(k,l) = jk(1+\bar{C})\Big(\cosh(j)\big(\bar{C}j\sinh(j)+\cosh(j)\big)+1+j^2\big(1+\bar{C}\big)\Big) \quad (4.15)$$

$$+i\cot(\alpha)\Big(\big(Cj\sinh(j)+\cosh(j)\big)\sinh(j)-j\Big), \quad (4.16)$$

$$T_{SB}(k,l) = \frac{T_{SB,num}(k,l)}{T_{surf,den}(k,l)}, \quad (4.17)$$

$$
\begin{aligned}
T_{UB,num}(k,l) = &\Bigg(\sinh^2(j)\Big(j^2\cot(\alpha)\sinh(j)\cosh(j)\Big(\bar{C}\big(2-k^2(\bar{C}^2j^2+4+\bar{C})\big)+4\Big)\\
&+ik\Big(j^4\bar{C}\Big(3\bar{C}k^2(1+\bar{C})-4\Big)+2\Big(j^2\big(k^2(4\bar{C}+2+\bar{C}^2)+4+4\bar{C}\big)-2k^2(1+\bar{C})\Big)\\
&\quad+j^3\Big(\bar{C}^3j^2\big(k^2(1+\bar{C})+2\big)+\bar{C}k^2\big(5\bar{C}+4\big)+2\big(3\bar{C}-2\big)\big(1+\bar{C}\big)\Big)-4k^2j\bar{C}(1+\bar{C})\Big)\\
&+j\cot(\alpha)\Big(\big(-3\bar{C}^2k^2+2\bar{C}(2+\bar{C})\big)j^2-k^2(2+\bar{C})^2\Big)\Big)-2j^3\cot(\alpha)\Big(\bar{C}^2k^2+\bar{C}+2\Big)\\
&+2ikj\Big(j^2\Big(k^2\big(5\bar{C}^2+6\bar{C}+2\big)-4-4\bar{C}\Big)-j^4\Big(2+5\bar{C}+4\bar{C}^2\Big)+2k^2\Big(1+\bar{C}\Big)\Big)\Big),
\end{aligned}
\tag{4.18}
$$

$$
\begin{aligned}
T_{vel,den}(k,l) = &j^2\Bigg(j\cosh^3(j)\Big(ik(1+\bar{C})\Big(\bar{C}^2j^2+2\Big)-3\bar{C}\cot(\alpha)\Big)\\
&+j\cosh(j)\Big(\cot(\alpha)\Big(2+3\bar{C}\Big)-ik(1+\bar{C})\Big(j^2\big(\bar{C}^2-2\bar{C}-2\big)-2\Big)\Big)\\
&+\sinh^3(j)\Big(3ikj^2\bar{C}\Big(1+\bar{C}\Big)-\cot(\alpha)\Big(2+\bar{C}^2j^2\Big)\Big)\\
&+\sinh(j)\Big(\cot(\alpha)\Big(j^2\bar{C}-2\Big)+ikj^2\bar{C}(1+\bar{C})\Big(j^2(1+\bar{C})+4\Big)\Big)\Bigg),
\end{aligned}
\tag{4.19}
$$

$$
T_{UB}(k,l) = \frac{T_{UB,num}(k,l)}{T_{vel,den}(k,l)},
\tag{4.20}
$$

$$
\begin{aligned}
T_{VB,num}(k,l) = &kl\Bigg(\sinh(j)\cosh(j)\Big(ik\Big(3\bar{C}^2j^4\big(1+\bar{C}\big)+2j^2\big(2+4\bar{C}+\bar{C}^2\big)-4-4\bar{C}\Big)\\
&\qquad-j^2\bar{C}\cot(\alpha)\Big(j^2\bar{C}^2+\bar{C}+4\Big)\Big)\\
&+\sinh^2(j)\Big(ikj\Big(\bar{C}^3j^4\big(1+\bar{C}\big)+\bar{C}j^2\big(5\bar{C}+4\big)-4\bar{C}\big(1+\bar{C}\big)\Big)\\
&\qquad-j\cot(\alpha)\Big(3j^2\bar{C}^2+\big(2+\bar{C}\big)^2\Big)\Big)\\
&-2\bar{C}^2j^3\cot(\alpha)+2ikj\Big(j^2\Big(5\bar{C}^2+6\bar{C}+2\Big)+2+2\bar{C}\Big)\Bigg),
\end{aligned}
\tag{4.21}
$$

$$
T_{VB}(k,l) = \frac{T_{VB,num}(k,l)}{T_{vel,den}(k,l)},
\tag{4.22}
$$

$$
T_{SC,num}(k,l) = -\bar{C}kj\cosh(j),
\tag{4.23}
$$

$$
T_{SC}(k,l) = \frac{T_{SC,num}(k,l)}{T_{surf,den}(k,l)},
\tag{4.24}
$$

$$
\begin{aligned}
T_{UC,num}(k,l) =& \bar{C}\Bigg(\sinh(j)\cosh(j)\Big(j^2\cot(\alpha)\Big(\bar{C}k^2-2\Big)\\
&+ik\Big(2\bar{C}j^4(1+\bar{C})-j^2\Big(k^2(2+\bar{C})(1+\bar{C})+4\Big)+2k^2\Big)\Big)\\
&+j\sinh^2(j)\Big(\cot(\alpha)\Big(k^2(2+\bar{C})-2j^2\bar{C}\Big)+ik\Big(j^2\big(2-\bar{C}k^2(1+\bar{C})\big)+\bar{C}k^2\Big)\Big)\\
&+2j\Big(j^2\cot(\alpha)+ik\Big(j^4(1+\bar{C})^2+j^2\big(2+\bar{C}-k^2(1+\bar{C})^2\big)-k^2\Big)\Big)\Bigg),
\end{aligned}
\tag{4.25}
$$

$$
T_{UC}(k,l) = \frac{T_{UC,num}(k,l)}{T_{vel,den}(k,l)},
\tag{4.26}
$$

$$
\begin{aligned}
T_{VC,num}(k,l) =& -kl\bar{C}\Bigg(\sinh(j)\cosh(j)\Big(ik\Big(j^2\big(2+\bar{C}\big)\big(1+\bar{C}\big)-2\Big)-j^2\bar{C}\cot(\alpha)\Big)\\
&+\sinh^2(j)\Big(ikj\bar{C}\Big(j^2(1+\bar{C})-1\Big)-\cot(\alpha)\Big(2+\bar{C}\Big)\Big)+2ijk\Big(j^2(1+\bar{C})^2+1\Big)\Bigg),
\end{aligned}
\tag{4.27}
$$

$$
T_{VC}(k,l) = \frac{T_{VC,num}(k,l)}{T_{vel,den}(k,l)}.
\tag{4.28}
$$

Chapter 5

Antarctica

A version of this chapter is being prepared for publication.

Author Contributions

The concept of the paper was developed by HO, RB, DG and AC. HO developed and ran the python code, and carried out the quantitative analysis of the new subglacial topographic map. RB advised on the geomorphological interpretation. HO wrote the main body of the text, but all authors contributed to the development of the main text and associated figures.

5.1 Abstract

The subglacial landscape of Antarctica offers geomorphological insights into the dynamics of ice-sheet flow regimes, informing numerical models projecting future ice-sheet change. Existing maps of subglacial topography interpolate between millions of geophysical-survey measurements, but these measurements still contain large gaps, leading to spatial biases. High-resolution maps of the ice surface offer an alternative spatially-homogeneous basis for recovering subglacial topography. We present here a new map of subglacial topography, produced using Ice Flow Perturbation Analysis, an inverse method which leverages the principle that stress changes associated with ice flow over bedrock obstacles produce ice-surface topography. Our results significantly enrich our understanding of mesoscale landforms across Antarctica, accentuating the details of known features and unmasking many new ones. Additionally, we use the textural properties of the new topography and a small subset of training data to classify the topography by geomorphological characteristics. The new topographic map, accompanied by this updated geomorphological classification, adds considerably to our knowledge of the subglacial geometry of the Antarctic ice sheets, provides important insights into landforms which are influential in ice flow, and has the potential to guide future geophysical surveying.

5.2 Introduction

As global temperatures rise and oceans warm, it has been estimated that the Antarctic ice sheets will contribute between a few centimetres and nearly a metre to sea level rise by 2100 (Ritz et al., 2015; DeConto and Pollard, 2016; Edwards et al., 2019; Seroussi et al., 2020; Edwards et al., 2021). Poor understanding of the processes which occur during glacial retreat and a lack of knowledge about the boundary conditions at the ice-bed interface have been identified by the Intergovernmental Panel on Climate Change (IPCC) as key causes of this wide range of model predictions (Parizek et al., 2013; Sun et al., 2014; Scambos et al., 2017; Koellner et al., 2019; Fox-Kemper et al., 2021).

The Antarctic ice sheets have an average thickness of 2100 m (Morlighem et al., 2020), obscuring the bed which lies beneath them. Limited geological exposure in subaerial mountain ranges and around the margins offers some insights into the properties of the buried bed (Cox et al., 2023), but the majority of what is known about the ice-bed interface comes from geophysical surveys (Jordan et al., 2010; Golynsky et al., 2018; Baranov et al., 2021; Frémand et al., 2023; Aitken et al., 2023). Topographic maps such as Bedmap3 (Frémand et al., 2023) and Bedmachine Antarctica (Morlighem et al., 2020) interpolate between millions of observations from radar and seismic surveys using methods such as kriging (Fretwell et al., 2013), streamline diffusion and mass conservation (Morlighem et al., 2010).

While in relatively small patches these radar and seismic surveys have line spacing as low as 500 m, in many regions the line spacing is 10 or 15 km, and across inland Antarctica is spacing is up to 300 km. This leads to topographic maps which do not achieve the resolution which models require to predict future sea level (Durand et al., 2011; Gladstone et al., 2012; Pattyn et al., 2013; Nias et al., 2016; McCormack et al., 2018; Castleman et al., 2022). In addition, interpolation techniques are heavily influenced by data density, so continent wide metrics from interpolated products are not spatially consistent and have variable uncertainty, meaning that different regions can not easily be compared. Some studies have used statistical interpolation methods (Goff et al., 2014; Graham et al., 2017; Guan et al., 2018; Mackie and Schroeder, 2019; MacKie and Schroeder, 2020) or machine learning techniques such as in-painting (Cai et al., 2023b; Gavriil et al., 2019) or super-resolution (Leong and Horgan, 2020; Cai et al., 2023a) to simulate subglacial topography and fill data gaps. However, these statistical methods struggle to match observational data and have low objective accuracy, meaning that they have not widely been applied.

Modern satellite observations have high spatial resolution and cover the ice surface of the whole of Antarctica. An alternative approach to classical interpolation techniques is to combine these high resolution observations of the ice surface and knowledge of glacial flow to determine bed properties through inverse methods (Van Pelt et al., 2013; Barnes et al., 2021). It is well known that perturbations in the ice-bed interface are transferred to the ice surface by flowing ice (De Rydt et al., 2013; Crozier et al., 2018; Cooper et al., 2019b),

and this relationship between the bed and the surface has been described mathematically by multiple studies (Nye, 1959; Budd, 1970; Reeh, 1987; Gudmundsson, 2003, 2008). Following these studies, we apply an inverse method known as Ice Flow Perturbation Analysis (IFPA), which exploits analytical formulations of perturbation transfer, to produce a new map of basal topography across the interior of Antarctica. We explore the types of topography in this new map, and classify the topography based on geomorphological characteristics, providing new insights into the nature of subglacial landforms across Antarctica.

5.3 Ice Flow Perturbation Analysis methodology

For ice with a constant viscosity in a planar slab aligned in the direction of ice flow, the non-dimensionalised Fourier transforms of perturbations in ice surface elevation, ($\hat{S}$), and velocity, ($\hat{U}$, $\hat{V}$), can be calculated from the non-dimensionalised Fourier transforms of perturbations in bed topography, ($\hat{B}$), and basal slipperiness, ($\hat{C}$):

$$\hat{S}(k,l) = T_{SB}(k,l)\,\hat{B}(k,l) + T_{SC}(k,l)\,\hat{C}(k,l), \tag{5.1}$$

$$\hat{U}(k,l) = T_{UB}(k,l)\,\hat{B}(k,l) + T_{UC}(k,l)\,\hat{C}(k,l), \tag{5.2}$$

$$\hat{V}(k,l) = T_{VB}(k,l)\,\hat{B}(k,l) + T_{VC}(k,l)\,\hat{C}(k,l), \tag{5.3}$$

where T_{SB}, T_{SC}, T_{UB}, T_{UC}, T_{VB}, T_{VC} are wavenumber specific non-dimensional transfer functions which describe the ratio of perturbations in the bed properties and perturbations in the ice surface properties, and which vary with the wavenumbers k and l, angle of slope α, sliding law parameter m, and mean non-dimensional slipperiness $\bar{C}$. The mathematical forms of these transfer functions are given in full in the supplement to Chapter 4, for both full-Stokes flow (Gudmundsson, 2003) (2003 equations) and the shallow-ice-stream approximation (Gudmundsson, 2008) (2008 equations).

Ice Flow Perturbation Analysis (IFPA) uses these transfer functions to calculate the bed topography $b(x,y)$, and bed slipperiness $c(x,y)$ over a patch with coordinates x and y, from the ice surface elevation $s(x,y)$, and ice surface velocities $u(x,y)$ and $v(x,y)$ (Chapter 3 and 4).

5.3.1 For a single isolated patch

For a square grid with dimensions *square_size*, and coordinates x and y, we need ice surface elevation $s(x,y)$ (in metres), ice surface velocities in the x and y direction $u(x,y)$ and $v(x,y)$ respectively (in metres per year), and a mean ice thickness $\bar{h}$ (in metres). To calculate the bed properties using IFPA, these steps are followed (Figure 5.1):

1. **Ice flow direction**
   The mean ice-flow direction is calculated.

2. **Data rotation**
   We then interpolate the ice surface and velocity data onto a grid aligned with the mean ice-flow direction with the specified grid dimension. It is important that the wavenumbers k are aligned to the ice-flow direction, and that the wavenumbers l are normal to the ice-flow direction for the application of the transfer functions. This can theoretically be done by taking k' and l' for the Fourier-transformed data grid, and recalculating k and l with respect to the mean ice-flow direction using trigonometry. However, this introduces edge effects which can not easily be quantified, and we opt instead to interpolate the data onto a rotated grid which is aligned to the ice flow direction, standardising these effects everywhere.

3. **Subtraction of a reference planar slab**
   From the interpolated ice surface elevation and velocity, a reference slab inclined in the direction of ice flow is calculated. This slab has angle of slope α. The sloped surface of the reference slab is subtracted from the elevation data, and the mean ice-velocity is subtracted from $u(x,y)$ and $v(x,y)$, leaving only perturbations from the reference slab.

4. **Non-dimensionalisation**
   Elevations are non-dimensionalised by dividing by the length scaling factor (mean ice thickness, $\bar{h}$). Velocities are non-dimensionalised by dividing by the velocity scaling factor (mean ice velocity).

5. **Fourier transform**
   After the application of a simple tapering function to avoid edge effects over a specified fraction of the grid (*tapering*), the non-dimensionalised ice surface elevation and velocities are Fourier transformed to give $\hat{S}(k,l)$, $\hat{U}(k,l)$ and $\hat{V}(k,l)$.

6. **Computing the Transfer functions**
   The transfer functions T_{sb}, T_{sc}, T_{ub}, T_{uc}, T_{vb} and T_{vc}, are calculated using either the full-Stokes flow (2003) or shallow-ice-stream approximation equations (2008) depending on which is most suitable. For topography which will be applied in a shallow-ice-stream model we recommend the shallow-ice-stream equations. Due to their more complex form, the full-Stokes flow transfer functions take approximately twice as long to compute.

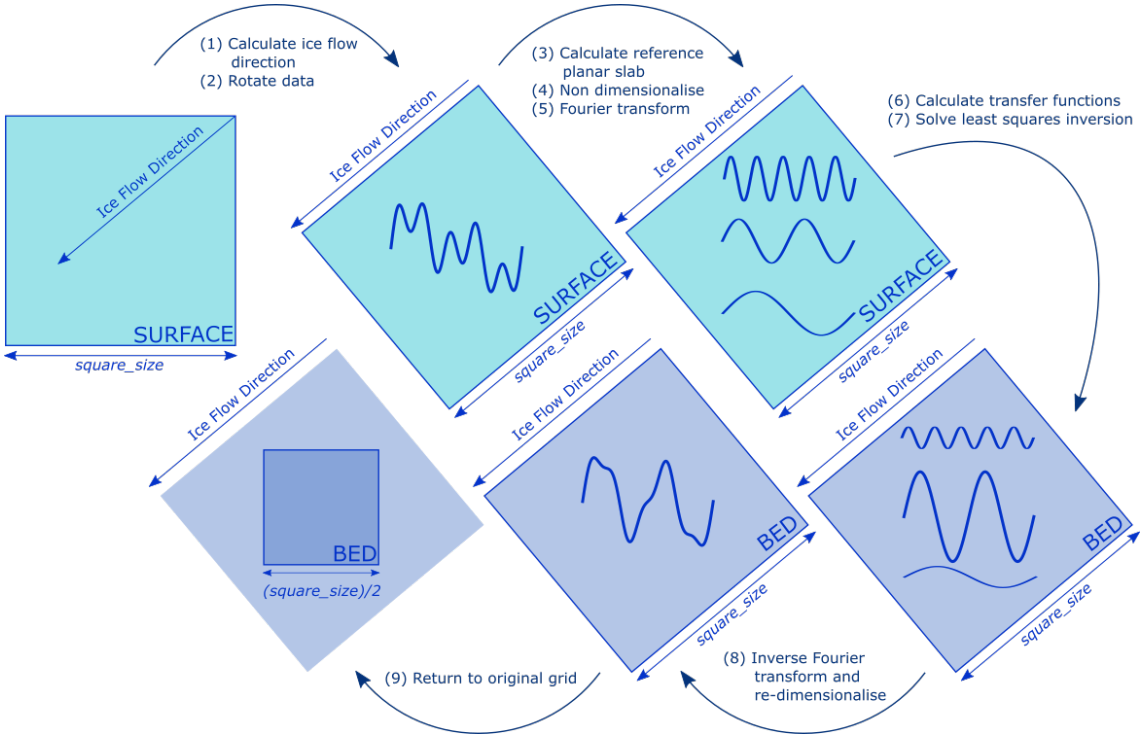

Fig. 5.1 A schematic illustrating the order in which various steps are carried out when Ice Flow Perturbation Analysis is applied to a single patch. Step numbers correspond to the description in Section 5.3.1.

7. **Least squares inversion**
   Equations 5.1, 5.2 and 5.3 can be solved to give $\hat{B}(k,l)$ and $\hat{C}(k,l)$ using a weighted least squares inversion, for each combination of k and l, following the method of Thorsteinsson et al. (2003) and Appendix C of Chapter 3. To balance the relative sizes of the perturbations in velocity and elevation in the least squares equation, we apply a weighting factor er (also referred to as $\sum_S$). To suppress artificial amplification of small wavelengths which fall within the null space of the inversion, we use filtering parameters p and $WavCut$, to reduce small wavelengths. Landforms aligned to ice flow also fall in the null space of the inversion and are removed using the directional parameters, Cut.

8. **Dimensionalisation and adding the reference planar slab**
   The resulting non-dimensionalised topography, $\hat{B}(k,l)$, and slipperiness, $\hat{C}(k,l)$, are inverse fourier transformed, and then re-dimensionalised. Elevations are dimensionalised using the reference length scale (mean ice thickness, $\bar{h}$). Slipperiness is dimensionalised using the reference slipperiness scale ($\bar{c}/\bar{C}$). The mean surface elevation $\bar{s}$ and the slope of the reference planar slab are adding to the dimensionalised topography, and the mean ice thickness, $\bar{h}$, is subtracted.

9. **Results**
   This process calculates the bed topography, $b(x,y)$ (in metres), and bed slipperiness, $c(x,y)$ (in myr^{-1}Pa^{-1}) on the rotated grid. These are re-interpolated back to the original polar stereographic grid, and only the central part of the original grid is used to ensure that the same area is included regardless of the ice flow direction, and that areas smoothed during tapering are also cropped. For $tapering = 0.1$, we use the central 50% of the original grid.

This process can be carried out in python using the function bed_conditions_clean from the package inversion_module_v2.py.

5.3.2 Over larger areas

To produce a smooth data product over larger areas, we run the inversion on multiple overlapping patches, and use a weighted sine function based on proximity to the centre of the patch to combine them. Patch results are given a weighting of 0 at the edges of the patch, and 1 in the centre. In the code for the inversion, the number of overlapping patches used in each region is specified with the parameter n, and the number of adjacent patches to be calculated in the x and y directions is specified with the parameter adj.

This process can be carried out in python using the function terminal_inversion_smooth from the package inversion_module_v2.py. For the map included here, this code took approximately a week to run for the whole of Antarctica, although subsequent improvements mean that it can now be run in around 7 hours.

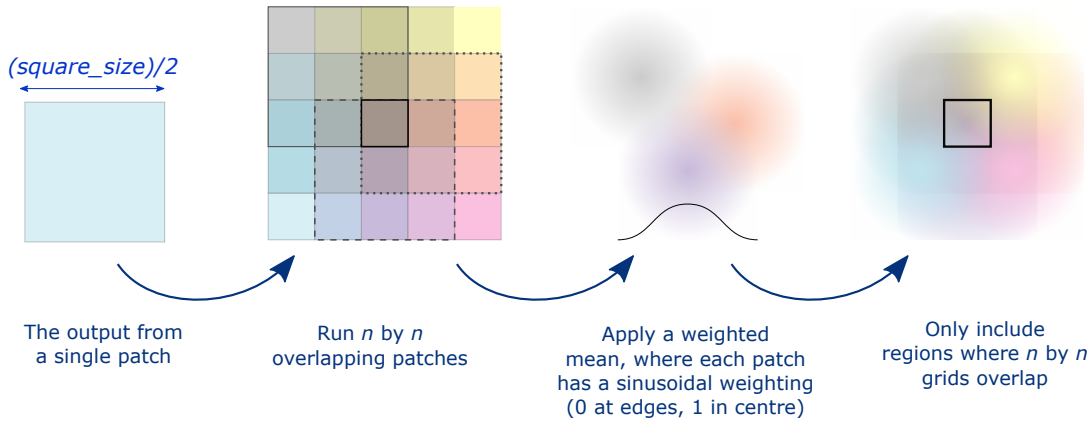

Fig. 5.2 A schematic diagram to illustrate the steps taken when combining multiple overlapping patches to produce a smooth data product over a larger area.

5.3.3 For the whole of Antarctica

For the surface elevation input, we used the Gapless REMA digital elevation model (Dong et al., 2022), which fills voids in the REMA digital elevation model (Howat et al., 2019) by

combining multiple source DEMs, and has a spatial resolution of 100 m. For the surface velocities, we used the ITSLIVE Antarctic ice velocity product (Gardner et al., 2018), which is a composite of velocity measurements made between 1995 and 2016, and has a spatial resolution of 450 m. A list of coordinates was prepared with 50 km spacing in the x and y directions on the polar stereographic grid. Coordinates were saved if they fell within the Antarctic continent, if their 50 km by 50 km region contained no null values, and if they had a mean surface elevation of more than 250 m. Coordinates with a lower mean surface elevation were assumed to be too close to the grounding line, where the physical processes are not captured in the linearised equations used in IFPA. MPI (Message Passing Interface) was used to parallelise the running of the IFPA code over this list of coordinates on the University of Edinburgh linux servers.

The following parameters were used, where an asterisk (*) indicates values chosen because they returned reasonable amplitude features in previous work on Thwaites Glacier (Chapter 3) and Pine Island Glacier (Chapter 4):

- **Tapering parameter*:** $tapering = 0.1$
- **Sliding exponent*:** $m = 1$
- **Filtering parameters*:** $p = -2$, $wavcutB = 1$, $wavcutC = 2$
- **Weighting factor*:** $er = 10^{-3}$
- **Mean non-dimensional slipperiness*:** $\bar{C} = 100$
  Note that slipperiness is not expected to be constant across Antarctica. The effect of varying $\bar{C}$ was explored in Chapter 4.
- **Directional filtering parameters:** $cutB = 10$ and $cutC = 15$
  The angle (in degrees) from the flow direction at which variability in the basal conditions, which falls into the null space of the inversion, is removed.
- **Patch dimensions:** $square\_size = 50000$
- **Number of overlapping grids:** $n = 3$
- **Number of adjacent grids:** $adj = [6,6]$
  Note that a larger value of adj would reduce the grid spacing required in the list of coordinates, and reduce run time by lowering the number of repeat calculations between neighbouring patches. We used a value of 6 to keep memory usage low, as all adjacent patches are kept open simultaneously until the results are saved.
- **Transfer functions:** Full-Stokes flow transfer functions (2003 equations)
- **Mean ice thickness:** $\bar{h}$
  For each patch, we calculate the mean ice thickness values from Bedmachine Antarctica (Morlighem et al., 2020). This is the only information about the ice thickness

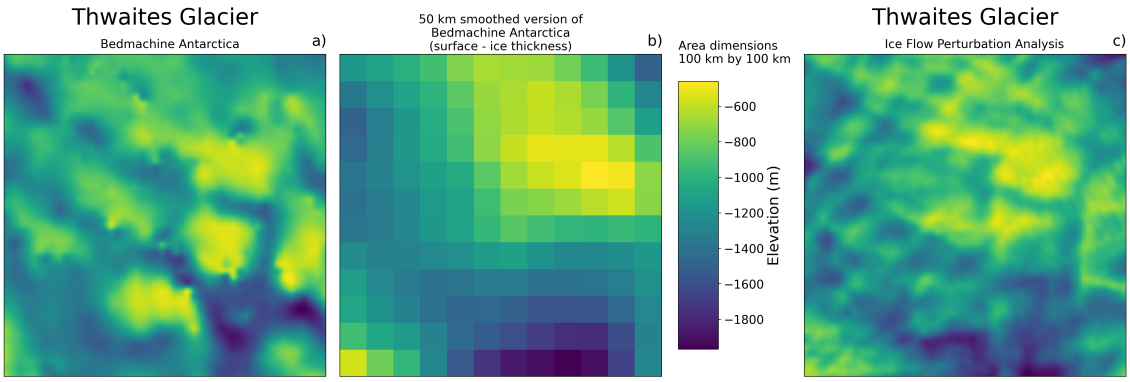

Fig. 5.3 An example of the level of detail provided by the 50 km diameter smoothed ice thickness used in the Ice Flow Perturbation methodology for the Thwaites Glacier region. In the central plot, each individual square pixel is 8.3 km square ($square\_size/2n$).

used, and does not include any mesoscale topographic features in which we are most interested. Figure 5.3 illustrates how little topographic information is provided to the inversion by including the mean ice thickness when the number of overlapping grids $n = 3$, and the patch dimensions $square\_size = 50000$.

A total of 4269 patches of bed topography, each 50 km by 50km, were analysed. This process was carried out in python using the script mpi_inversion.py. As a result of the weighted mean procedure used when applying IFPA over larger areas, these patches could then be smoothly joined together without edge effects to create the map which is presented here. This joining process was carried out in python using the script Stitching.py.

5.4 A new map of Antarctic subglacial topography

We present here the new map of Antarctic subglacial topography produced using the Ice Flow Perturbation Analysis (IFPA) methodology, applied to the Gapless REMA digital elevation model (Howat et al., 2019; Dong et al., 2022), and ice velocities from NASA ITS_LIVE (Gardner et al., 2018) using a 50 km smoothed ice thickness from Bedmachine Antarctica (Morlighem et al., 2020) as baseline topography. IFPA assumes ice flow in an inclined plane, which is not appropriate near the grounding zone around the coast of Antarctica, so we only apply IFPA in interior regions (see Figure 5.5e).

5.4.1 Selected new details in interior regions

The strength of Ice Flow Perturbation Analysis lies in its ability to explore the mesoscale (2-30 km) topographic variability which is transferred to the ice surface (Chapter 4), and we therefore focus our analysis on ways of exploring the novel estimates of mesoscale details. We begin with a selection of regional snapshots which provide an insight into the level of detail which the new map allows us to explore across Antarctica, focusing

on incised valleys (Figure 5.4a-c), lineations in topography which may have a geological or tectonic origin (Figure 5.4d-f), and alpine ridge networks (Figure 5.5a-d). A more comprehensive set of maps (but at a larger scale) are available in the Extended Figures (Section 5.8), and the complete data set is available online.

Incised valleys

In Maud Subglacial Basin in central Dronning Maud Land, we see one of the most significant new features from the IFPA map. A narrow but steep-sided canyon cuts across the basin, running for nearly 400 km and having an average depth of around 50 m and width of around 6 km (Figure 5.4a). This valley is particularly notable due to its length, and its location in a region with almost no radar observations about which very little is known. A subglacial canyon feature has been observed running for over 750 km in north-west Greenland (Bamber et al., 2013b; Keisling et al., 2020), with depths varying from 200 m at the inland end to 800 m at the deepest downstream part. Our Antarctic features appear much shallower and more similar to the inland end of this Greenlandic paleofluvial mega-canyon, although without ice-penetrating radar observations it is difficult to give our features a reliable depth.

We observe another set of similar incised features in Wilhelm II Land (Figure 5.4b). However, while the valley in Maud Subglacial Basin lies within a basin and may represent a significant subglacial drainage channel incising into unconsolidated subglacial sediments, the incisions in Wilhelm II Land appear to cut across more substantial ridges. If these features do indeed have a hydrological origin, they must represent the movement of significant volumes of water. In Greenland, similar channels at Humbolt Glacier have been interpreted as evidence of pre-glacial fluvial activity, potentially connected to large glacial outburst floods (Livingstone et al., 2017; Keisling et al., 2020). Vast water volumes are required to carve these channels, and in Greenland much of this subglacial water flow originates from seasonal surface melt. In the Foundation Ice Stream region of West Antarctica, large subglacial bed channels have been interpreted as evidence for a temperate ice sheet during the Pliocene warm period (Rose et al., 2014). These new features may provide further evidence of past hydrological activity across Antarctica.

However, not all the valley features in the new IFPA map will have fluvial origins. The IFPA map also shows incised valleys in regions of higher elevation, such as at Hercules Dome where several deep valleys cut across the peak of the subglacial topography (Figure 5.4c). These valleys are similar to those imaged nearby with multi-element swath radar (Hoffman et al., 2023), which are thought to be U-shaped valleys from alpine style glaciation, and have been interpreted as initiation zones for ice sheet growth.

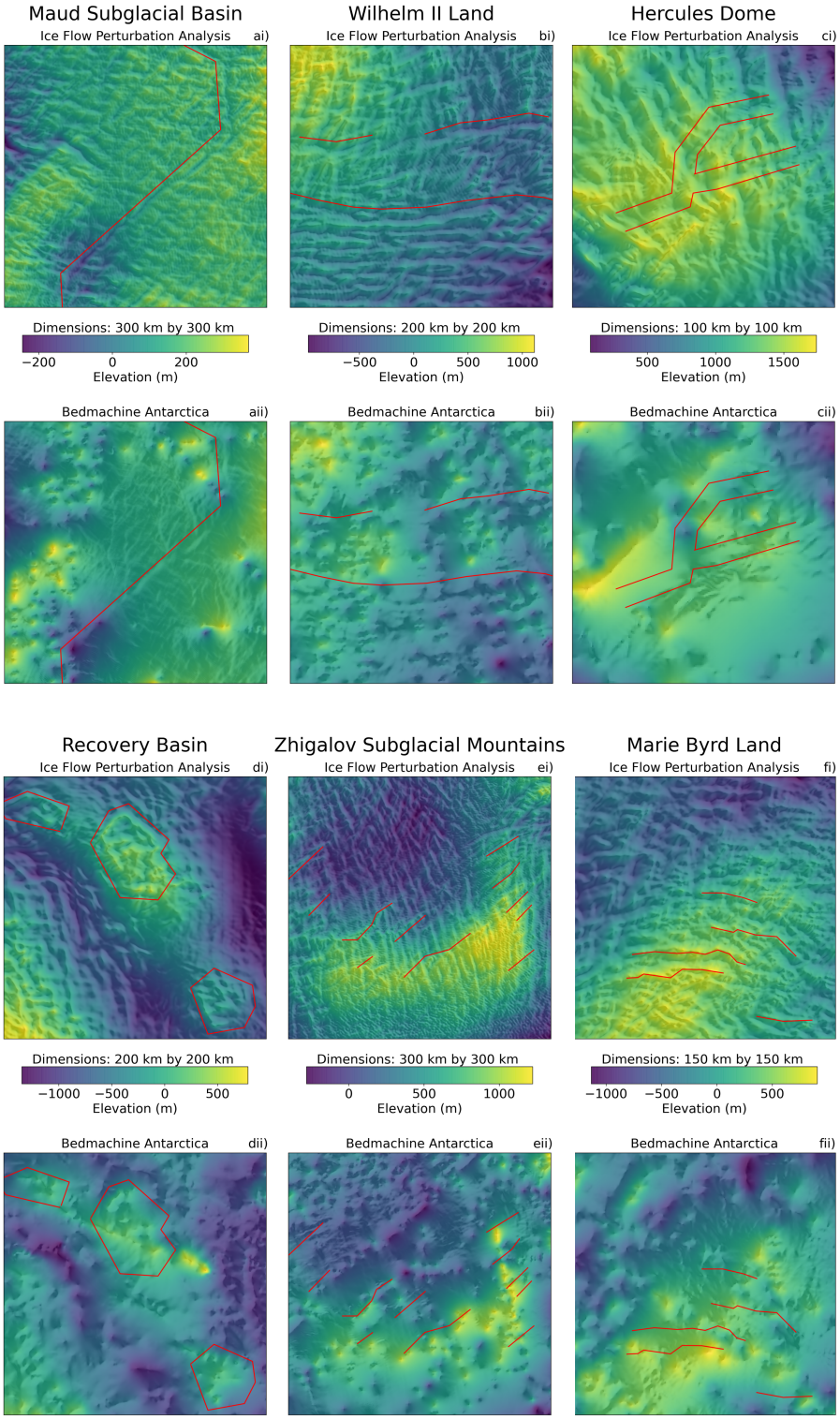

Fig. 5.4 A comparison of the subglacial topography (overlain on a hillshade with azimuth of 315° and altitude of 45°) from i) Ice Flow Perturbation Analysis and ii) Bedmachine Antarctica (Morlighem et al., 2020) for a) Maud Subglacial Basin, b) Wilhelm II Land, c) Hercules Dome, d) Recovery Subglacial Basin, e) Zhigalov Subglacial Mountains and f) central Marie Byrd Land. Note that these patches vary in size from 300 km by 300 km to 100 km by 100 km, as shown above the corresponding colour scale. Their locations are shown in Figure 5.5e. Notable features which are mentioned in the text have been annotated in red.

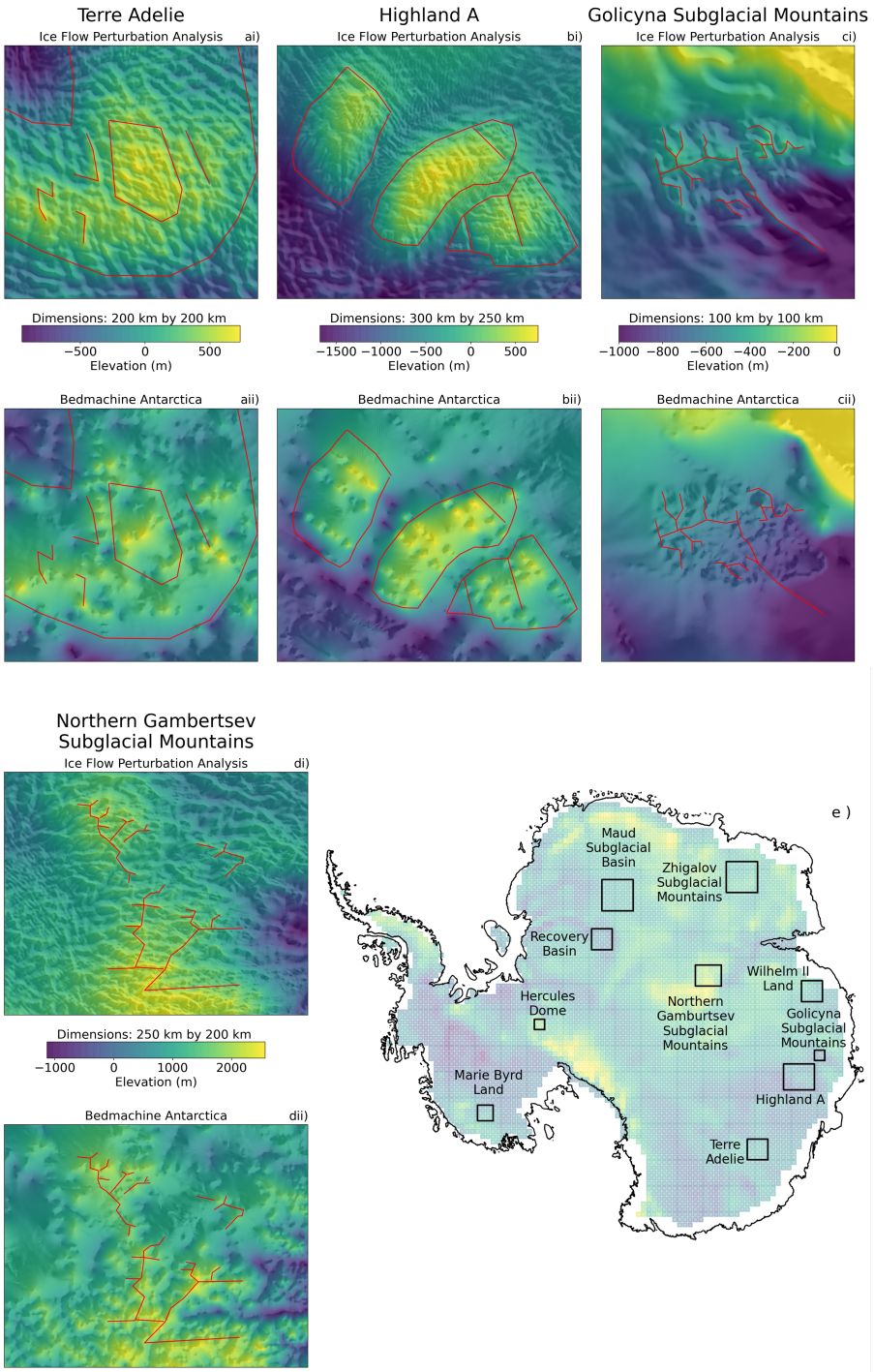

Fig. 5.5 A comparison of the subglacial topography (overlain on a hill-shade with azimuth of 315° and altitude of 45°) from i) Ice Flow Perturbation Analysis and ii) Bedmachine Antarctica (Morlighem et al., 2020) for a) part of Terre Adélie Subglacial Highlands, b) Highland A, c) part of Golicyna Subglacial Highlands, and d) northern Gamburtsev Subglacial Mountains. Note that these patches vary in size from 300 km by 250 km to 100 km by 100 km, as shown above the corresponding colour scale. Their locations are shown in Panel e), which also shows the spatial extent of the IFPA map. Notable features which are mentioned in the text have been annotated in red.

Geological and tectonic lineations

Although IFPA assumes small perturbations to a flow in a linear slab, it also identifies sharp edges in basal topography, as shown for Recovery Subglacial Basin (Figure 5.4d). Radar surveys of the basin have shown that there is a region of raised topography in the centre of the basin (Bell et al., 2007), with a series of subglacial lakes in the lower topography around this region (Humbert et al., 2018; Diez et al., 2019), but have not had high enough resolution to resolve the full extent of the features along the raised topographic ridge. The IFPA map shows a series of hills with sharp edges which have not previously been so well defined. These sharp edges may represent a change in the geology, and have been interpreted from gravity and magnetic surveys to represent sedimentary rocks from a former depositional basin which is no longer preserved (Aitken et al., 2023).

Further topographic evidence for tectonic activity is shown in the IFPA map for the region around Zhigalov Subglacial Mountains in Enderby Land, East Antarctica (Figure 5.4e). The topography in this region displays a strong north-south trend, which aligns with other nearby features in the Queen Fabiola Mountains and the West and Central Ragnhild Troughs. Geological mapping, informed primarily by gravity and magnetic surveys, has interpreted this trend as connected to north-south rifting during the Paleozoic to Mesozoic period (Eisen et al., 2020).

Although the largest updates in the topography from IFPA are in East Antarctica, we also observe novel well-defined features in West Antarctica, despite the relatively higher density of radar survey lines (Frémand et al., 2023). However, in parts of Marie Byrd Land, the gaps between survey lines can be as large as 25 km, leading to artefacts of survey lines in interpolated bed products. The IFPA map for central Marie Byrd Land (Figure 5.4f) shows that the bed topography is dominated by an east-west trend. Again, this trend is likely to have a tectonic origin, connected to extension in the area from the formation of the West Antarctic Rift System during the Cretaceous period (Luyendyk et al., 2003; Winberry and Anandakrishnan, 2004; Ferraccioli et al., 2007).

Alpine topography and ridge networks

In many of the Antarctic subglacial highlands in the IFPA map, we see complex topography with a distinctive texture. In the western Terre Adélie Subglacial Highlands, the IFPA map makes the broad scale shape of the topography much clearer, but also adds significantly more small scale topography to our understanding of the region (Figure 5.5a). We highlight a central topographic block which has some geometric features which resemble alpine valleys, similar to those seen in recent ice-penetrating radar surveying at Highland A (Figure 5.5b). At Highland A these features have been interpreted to be an ancient preserved river landscape (Jamieson et al., 2023), which provides clues as to the age, stability and initiation speed of the Antarctic Ice Sheet.

Several previous works have noted that in subglacial mountain ranges the curvature of the surface topography can be used to identify mountain ridges and valley bottoms (Lea et al., 2023; Jamieson et al., 2023). The new IFPA map illustrates this very nicely in both the eastern Golicyna Subglacial Mountains (Figure 5.5c) and northern Gamburtsev Subglacial Mountains (Figure 5.5d). In this part of Golicyna Subglacial Mountains, a complex ridge network is revealed by the IFPA map, which has not previously been explored in this level of detail. Bedmachine Antarctica v3 does not contain any bed picks in this region, and from the level of detail visible in the ice surface it seems likely that the topography here is not particularly deep, and that the ice thickness may currently be overestimated.

The Gamburtsev Subglacial Mountains were surveyed intensively during the International Polar Year Antarctica's Gamburtsev Province (AGAP) project (Ferraccioli et al., 2011). As Ice Flow Perturbation Analysis can not resolve features smaller than the ice thickness, it does not resolve the full complexity of these subglacial mountain ranges as known from the AGAP surveys. It is possible that application of IFPA on smaller grids aligned with the glacial valleys could be more physically appropriate, but methods such as mass conservation (Morlighem et al., 2010, 2020), which work well in confined troughs and valleys are likely to give better results in regions where ice flow is steered through complex topography. However, similarly to the Golicyna Subglacial Mountains, IFPA identifies the apex of ridges well (Figure 5.5d), and around the margins of the highly surveyed area we see that IFPA extends our understanding of the main ridges, showing ridge networks branching outwards. This is particularly noticeable in the northern part of the Gamburtsev Subglacial Mountains, between Lambert and Mellor glaciers (Figure 5.5d). Semi-automated mapping of changes in surface curvature has previously been applied to look at ridge networks in this regions (Lea et al., 2023), complementing the IFPA topography.

5.4.2 Artefacts from surface elevation and velocity

IFPA assumes that all topography in the ice surface occurs as a result of ice flow over bed perturbations. However, in some regions, surface processes can also create topography. The regular periodic waves of megadunes produced by katabatic winds on the East Antarctic plateau (Frezzotti et al., 2002) are a good example of this, and we see the imprint of these landforms in the IFPA bed topography (Figure 5.6a). Artefacts in the bed can also be produced when there are artefacts in the input data sets. In the South Pole Basin region, the ITS_LIVE velocity product contains many linear features which closely follow lines of latitude, forming curves centered on the pole (Gardner et al., 2018) (Figure 5.6b), and these linear features are also present in the IFPA bed topography. Although these two examples can be detected, and only cover a small proportion of the total mapped region, other surface processes or randomly distributed data artefacts may be present which are harder to identify and remove. As new techniques for processing satellite observations are

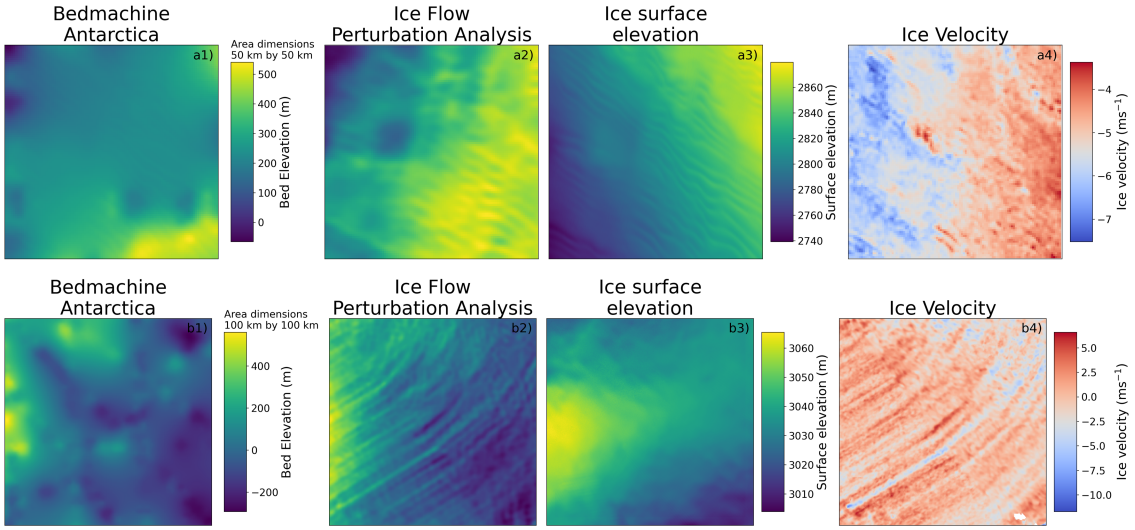

Fig. 5.6 Examples of the way that the subglacial topography produced from Ice Flow Perturbation Analysis can have artefacts produced by a) features in the ice surface which are not produced by ice flow processes, in this case megadunes formed by katabatic winds, and b) artefacts in the surface data, in this case velocity artefacts caused by proximity to the South Pole. Panels show 1) topography from Bedmachine Antarctica (Morlighem et al., 2020), 2) topography from Ice Flow Perturbation Analysis, 3) the ice-surface elevation (Howat et al., 2019; Dong et al., 2022) and 4) the ice-surface velocity in the x direction (Gardner et al., 2018) for these two regions.

developed and become more standardised, gridded velocity products will contain fewer artefacts, so the application of IFPA to future datasets may reveal new features which are currently obscured.

5.5 The bigger picture: Antarctic-wide metrics

5.5.1 Textural and spectral metrics

Although there are many interesting mesoscale details in the Ice Flow Perturbation Analysis map, it also allows us to compare the properties of subglacial topography across Antarctica. To provide a more holistic quantitative analysis of the IFPA topography, we calculated a variety of textural and spectral characteristics for 4629 regions of 50 km by 50 km, using a selection of computer vision techniques. We focus on image properties which can distinguish between different textures, such as peak counting, band-pass filtered topography, and characteristics of the frequency spectrum. Comparative plots for all the metrics including those not shown in the main text are included in the Extended Figures (Section 5.8). We calculate these textural and spectral metrics for both the new IFPA bed topography and also for the bed topography from the Bedmachine Antarctica DEM. These metrics are calculated for 4269 regions, each 50 km by 50 km.

Metrics focused on the elevation distribution are the mean, the standard deviation, the standard deviation with the local mean slope removed, skewness and kurtosis. To characterise the texture, we also calculated the RMS slope and RMS curvature. The Fourier transform of the elevation reveals the spatial frequency spectrum, and we calculated its fractal dimension, and the wavelength and orientation of the strongest power component. Since we expect IFPA to contribute new topography mainly at short wavelengths, we also applied high and low frequency band-pass filters to the topography, and calculated the standard deviation, RMS slope and RMS curvature for the band-pass filtered topography. Another way to look at the new topography at short wavelengths is to count local maxima (or minima), and we counted peaks with amplitudes of 20 m, 50 m, 100 m and 250 m in a 5 km radius. We used the following metrics:

- **Mean elevation**
- **Standard deviation**
- **Standard deviation with the slope removed**
  We calculate the best fit plane to the bed topography DEM, and then subtract this from the DEM. This is a simple way to remove the long wavelength topography, and to see roughness from the short wavelength landforms.
- **Skewness**
  We calculate the unbiased Fisher-Pearson coefficient of skewness for the elevation distribution with the scipy.stats.skew function.
- **Kurtosis**
  We calculate the Fisher kurtosis of the elevation distribution with the scipy.stats.kurtosis function.
- **RMS slope**
  The root mean square of the first derivative of the bed topography. All derivatives were calculated using the np.gradient function.
- **RMS curvature**
  The root mean square of the second derivative.
- **Low and High frequency Standard deviation**
  We use the skimage.filters.difference_of_gaussians function to band-pass filter the bed topography for High and Low wavelengths with $\sigma = 4$, and $\sigma = 80$, respectively. The standard deviation was calculated for each of these band-pass filtered topographies.
- **Low and high frequency RMS slope**
  The root mean square of the first derivative of the band-pass filtered topography.

- **Low and high frequency RMS curvature**
  The root mean square of the second derivative of the band-pass filtered topography.

- **Fractal dimension (> 5km)**
  Fourier fractal dimension is a statistical measure of the level of detail in a surface, with a higher fractal dimension indicating a more complex surface, or rougher subglacial topography. Russ (2013) and Florindo and Bruno (2012) showed that the Fourier fractal dimension of a surface (D_{ff}) can be calculated from the gradient of the line of best fit to the Fourier power spectrum of the topography (β).

$$D_{ff} = \frac{6+\beta}{2} \tag{5.4}$$

  We calculate the Fourier spectrum using the fast Fourier transform following Equation 5.5, with hann windowing to reduce edge effects, in this case only for wavelengths greater than 5 km. The power spectral density is the square of the Fourier transform, corrected for grid spacing and windowing, as in Equation 5.6.

$$\hat{f}(k,l) = \sum_{x=0}^{N_x-1} \sum_{y=0}^{N_y-1} f(x,y)w(x,y) \exp\left(-2\pi i\left(\frac{kx}{N_x} + \frac{ly}{N_y}\right)\right) \tag{5.5}$$

$$k = 0,...,N_x-1, l = 0,...,N_y-1$$

$$PSD(k,l) = \frac{|\,\hat{f}(k,l)\,|^2\,\Delta_x\Delta_y}{\sum_{x=0}^{N_x-1}\sum_{y=0}^{N_y-1} w(x,y)^2} \tag{5.6}$$

  where $w(x,y)$ is a Hann windowing function, k and l are the wavenumbers, and Δ_x and Δ_y are the grid spacings in the x and y directions.

- **Fractal dimension (for wavelengths > ice thickness)**
  The Fourier fractal dimension when only wavelengths greater than the ice thickness are considered, calculated as above.

- **Wavelength of maximum power**
  The Fourier power spectrum is wavelength normalised with comparison to the line of best fit to the Fourier power spectrum, and we take the wavelength with the highest normalised power.

- **Angle of maximum power**
  The orientation (calculated from the corresponding wavenumbers) with the highest normalised power.

- **The number of 20m/50m/100m/250m hills in 5km**
  Using the scipy.ndimage.filters.maximum_filter function, we count the number of grid cells which are the highest cell in their 5 km neighbourhood and are at least 20m/50m/100m/250m higher than their lowest neighbour. This analysis was also

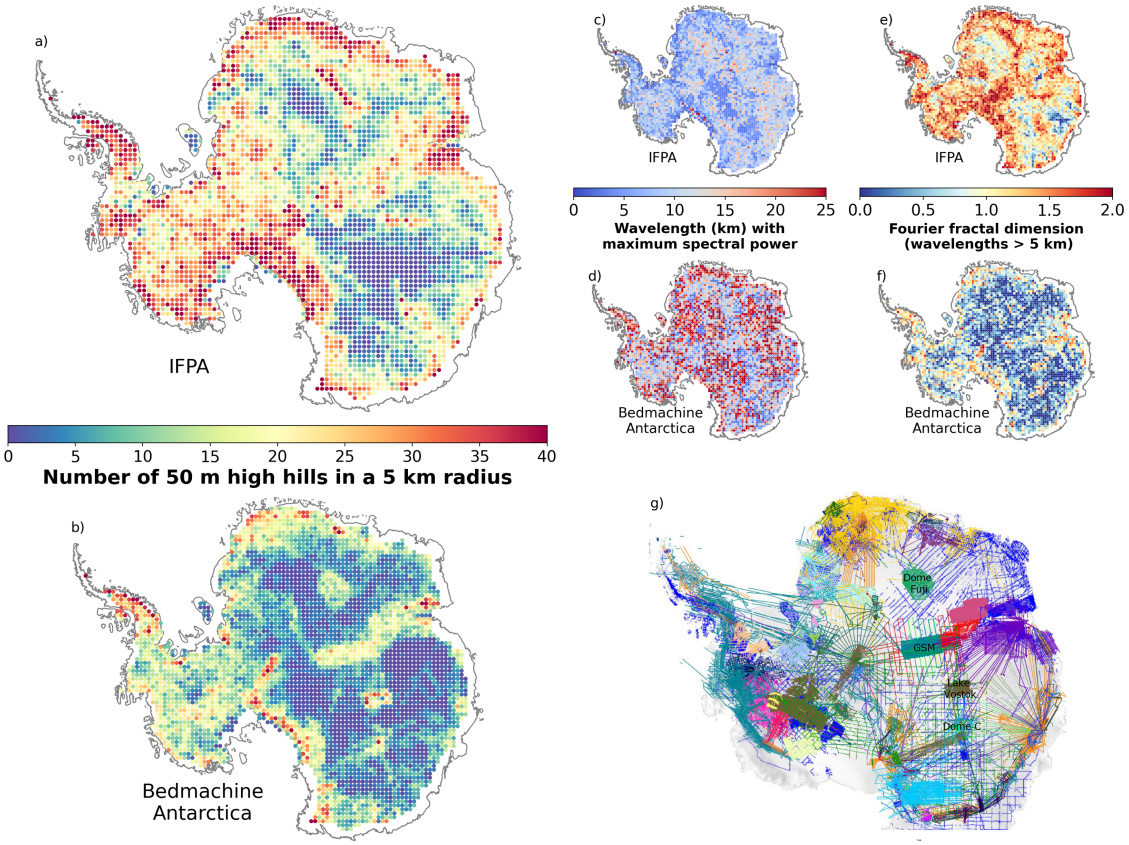

Fig. 5.7 The number of 50 m high hills within a 5 km radius, the wavelength with maximum spectral power (km) and the Fourier fractal dimension for wavelengths greater than 5 km displayed from each 50 km by 50 km patch of subglacial topography from Ice Flow Perturbation Analysis (Panels a), c) and e) respectively), and Bedmachine Antarctica (Panels b), d) and f) respectively). Panel g) shows the distribution of bed picks from geophysical surveys included in Bedmachine Antarctica v3 and is adapted from the Figure 2 of the user guide for MEaSUREs BedMachine Antarctica, Version 3 (Morlighem et al., 2020). Significant radar surveys in East Antarctica have been labelled to contextualise the data density used in Bedmachine Antarctica: Dome Fuji, the AGAP survey in the Gamburtsev Subglacial Mountains (GSM), Lake Vostok and Dome C.

done for minima instead of maxima, but yields almost identical results, so only the maxima are reported here.

These metrics can be calculated in python using the script metrics.py.

5.5.2 Results

Examination of these metrics immediately shows the increased level of detail which is available in the new IFPA topography map across the whole of Antarctica. There is a significant difference between the dominant wavelength of the topography included in the IFPA map (Figure 5.7c) and the Bedmachine Antarctica (Morlighem et al., 2020) map (Figure 5.7d), with a mean dominant wavelength of 8.5 km for IFPA and 14.5 km for Bedmachine Antarctica. When looking at the number of 50 m high hills in a 5 km radius

(Figure 5.7a and 5.7b), the IFPA map contains in total 40886 more of these hills than Bedmachine Antarctica, distributed across most of Antarctica.

In addition, metrics focused on short-wavelength topography, such as the number of 50 m high hills in a 5 km radius, show that Bedmachine Antarctica is strongly influenced by the density of radar surveys. Detailed areas (high hill density) in Bedmachine Antarctica mirror the locations of high density radar surveys over Dome Fuji (Tsutaki et al., 2022), the Gamburtsev Subglacial Mountains (Ferraccioli et al., 2011), Lake Vostok (Popov et al., 2012) and Dome C (Figure 5.7g). In contrast, the pattern of detailed regions for IFPA corresponds with the known topographic distribution, because IFPA is not influenced by the density of radar surveys and provides a spatially relatively unbiased view into the characteristics of Antarctic subglacial topography.

We also consider metrics which focus on the frequency spectrum more broadly, such as Fourier fractal dimension. This is a statistical measure of the complexity of a surface (Russ, 2013; Florindo and Bruno, 2012)), which has implications for the dynamics of ice flow (Hubbard et al., 2000; Schoof, 2002; Hogan et al., 2020). These broader metrics also show patterns in the IFPA map which correspond to the geomorphology. We see higher fractal dimension in the IFPA map (Figure 5.7e) in regions such as the Transantarctic Mountains and the Polar Gap subglacial highlands where we know there is elevated and rougher topography. An exception to this is in the South Pole basin, where high fractal dimension is caused by artefacts in the surface velocity due to proximity to the pole (See Section 5.4.2 and Figure 5.6b). In contrast the fractal dimension for Bedmachine Antarctica (Figure 5.7f) does not seem to show any connection to topography, because broad scale roughness in interpolated products is also controlled by the uneven distribution of ice-penetrating radar observations.

When combined, these metrics and the maps presented in Section 5.4.1 show just how much detail about the subglacial topography of Antarctica can be learnt from the ice surface, and illustrate the step forward we have taken in our understanding of the mesoscale topography beneath Antarctica. The new features in the IFPA map may also provide guidance for geophysical surveys which aim to focus on particular topographic features and regions with variable subglacial roughness.

5.6 Geomorphological mapping of topographic styles

From the maps presented in Section 5.4, it is clear that IFPA reveals heterogeneous styles of topography across Antarctica. We now consider the potential for using the IFPA topography to map different landscape types.

5.6.1 Topographic classification

Much of what is known about the subglacial topography of Antarctica is contextualised with reference to the deglaciated beds of former ice-sheets in North America, Patagonia and Scandinavia (Stroeven and Kleman, 1999; Jamieson et al., 2010; Margold et al., 2015; Sugden and Hall, 2020). Sugden and John (1976) classified exposed Antarctic marginal topography using a process-based geomorphological approach. Following the release of Bedmap2 (Fretwell et al., 2013), this classification was extended to the ice-covered parts of the continent by Jamieson et al. (2014). These previous geomorphological classifications have divided Antarctic topography into 3 categories: alpine glacial erosion, low-relief areal scour, and selective linear erosion. Alpine style landscapes are characterised as containing deep glacial valleys, and sharp peaks, similar to those around the modern Patagonian ice fields (Sugden and John, 1976; Jamieson et al., 2014). Landscapes of areal scour are formed by unconstricted ice flow, leaving smooth, low-relief, bare-rock topography, similar to parts of central northern Canada (Sugden, 1978) and Scotland (Rea and Evans, 1996). Selective linear erosion occurs in regions where there is significant topographic steering of ice flow, and is often concentrated in fast flowing ice streams and glacial troughs, similar to the fjords of the Scandinavian coast (Kessler et al., 2008).

To classify the topography from IFPA, we broadly use the same three categories. However, in visual explorations of the IFPA map, we observe slightly different textures for mountainous terrain containing nunataks where the bed extrudes above the ice surface (aerial alpine), and mountainous terrain which is fully buried beneath the ice (subglacial alpine). For the classification presented here, we separate these into two categories, although in reality there is a continuous spectrum with subaerial and subglacial as two end-members.

Computer vision techniques allow for the identification of different textures in digital images (Trevisani and Rocca, 2015), and for automated image classification. Using selected example regions as a small training data set, we leverage the textural and spectral characteristics described previously to create a classification protocol, and to categorise 4629 regions of Antarctica, each 50 km by 50 km, as either aerial alpine, subglacial alpine, areal scour or ice stream topography. Regions with the distinctive properties of artefacts from undulating dunes in the ice surface are removed. For each of the 5 categories, we identified three 150 km by 150 km regions of relevant topography from across Antarctica (Figure 5.8), giving twenty-seven 50 km by 50 km regions where the textural metrics were calculated. Figure 5.9 shows how these metrics vary for the different topographic styles.

We begin with topographic types with very distinct and identifiable characteristics: areal scour, dunes, and subaerial alpine topography. Areally scoured areas have notably smooth topography, and hence can be identified by low RMS curvature (< 0.025, Fig. 5.9a) and few hills of any prominence (< 15 of 20 m height, Fig. 5.9b), as well as a low RMS slope for the high frequency component of the topography (< 0.07, Fig. 5.9c). Areas with artefacts from dunes in the ice surface are dominated by small-amplitude and

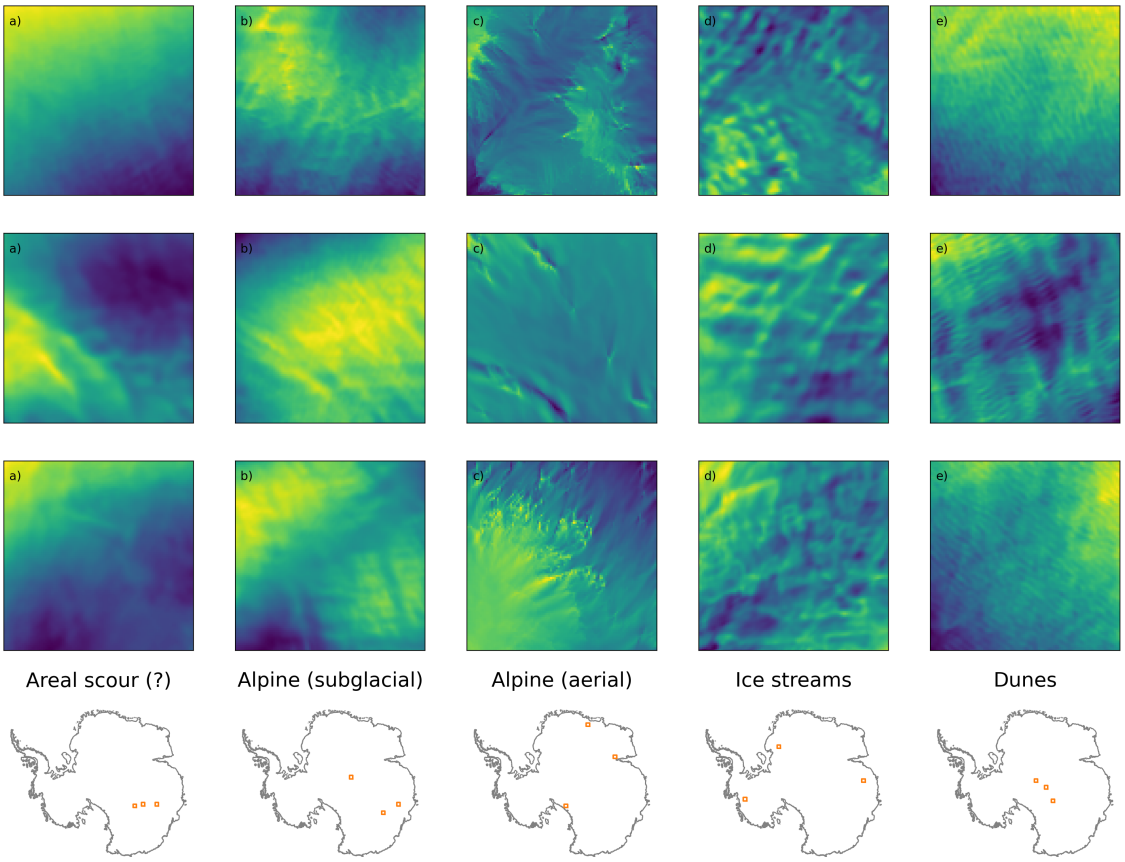

Fig. 5.8 150 km by 150 km topographic patches from IFPA for a) areal scour, b) alpine (subglacial), c) alpine (aerial), d) selective linear erosion in ice streams and e) artefacts caused by dunes in the ice surface. The locations of the chosen topographic patches are shown on the maps at the bottom of each column.

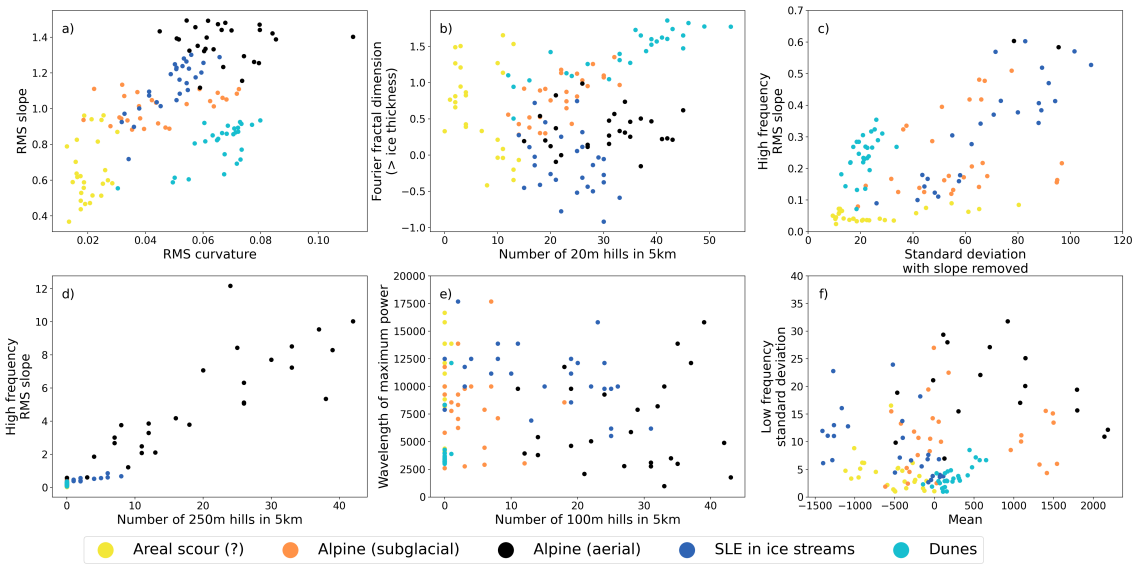

Fig. 5.9 Eleven textural and spectral characteristics plotted for the training data set for five classes of subglacial topography (areal scour in yellow, alpine (subglacial) in orange, alpine (aerial) in black, selective linear erosion (SLE) in ice streams in dark blue and artefacts from dunes in light blue). Note that the axis scales for panel c) have been chosen to show the variability between regions of areal scour and regions with artefacts from dunes, and so most data points for alpine (aerial) fall outside of the chosen region.

high-frequency landforms, with very few 100 m high hills in a 5 km radius (= 0, Fig. 5.9e), and a low dominant wavelength ($<$ 5 km, Fig. 5.9e). Their texture is also distinctive, combining low RMS slope ($<$ 0.9, Fig. 5.9a) and high RMS curvature (RMS slope/RMS curvature $<$ 14.75, Fig. 5.9a). Subaerial alpine topography can be distinguished by high relief, but also by high RMS slope for the high frequency component of the topography ($>$ 2, Fig. 5.9d) and a large number of 250 m high hills in a 5 km radius ($>$ 10, Fig. 5.9d).

Subglacial alpine topography is not as easy to distinguish as subaerial alpine topography, due to the thicker ice reducing the imprint of buried mountains in the ice surface. However, the distinctive branching tendril texture means that these regions can be distinguished from lower topography due to a moderate RMS slope ($<$ 1.1, Fig. 5.9a) and a moderate Fourier fractal dimension ($>$ 0.5, Fig. 5.9b). We also classify high elevation regions ($>$ 1000 m) with high standard deviation at low frequencies ($>$ 19) as subglacial alpine topography. Selective linear erosion topography in ice streams occurs in lower, more eroded regions of the ice sheet where ice is faster flowing, and has a pattern of individual bumps that are not connected by ridges. This results in a high RMS slope ($>$ 1.0, Fig. 5.9a) and low Fourier fractal dimension ($<$ 0.25, Fig. 5.9b). Following Sugden and John (1976) and Jamieson et al. (2014), we classify anything which is not definitely within one of these categories as other selective linear erosion.

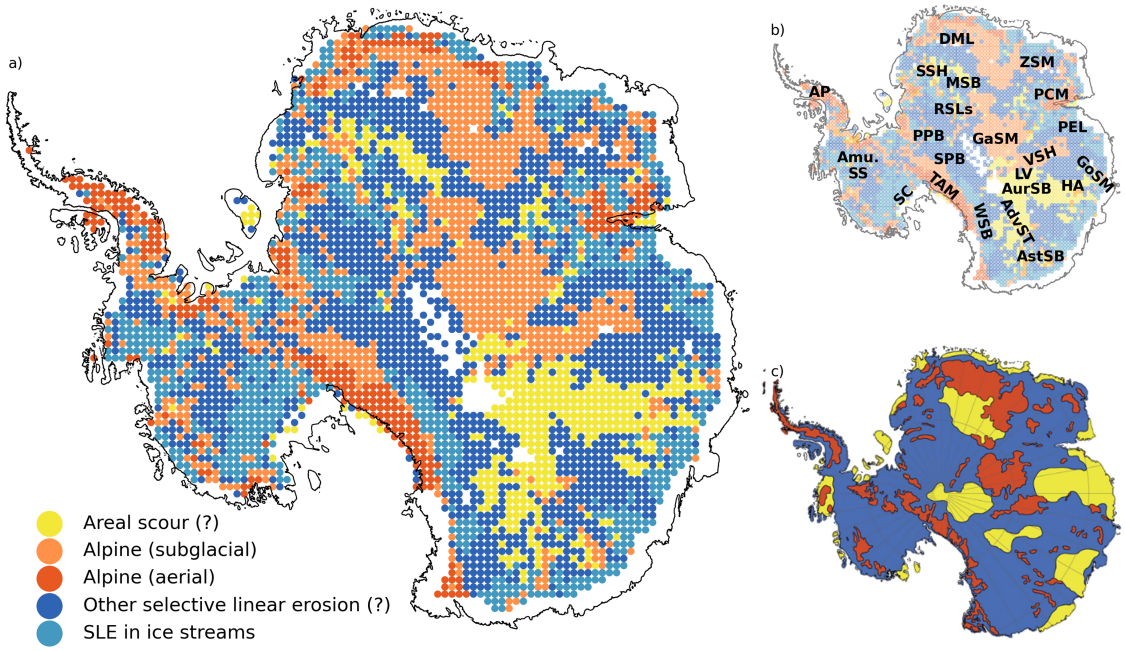

Fig. 5.10 A comparison of a) the new geomorphological classification of Antarctic subglacial topography based on the textural and spectral characteristics of the subglacial topography inverted with Ice Flow Perturbation Analysis, and c) the geomorphological classification from Jamieson et al. (2014) (Adapted from their Figure 8). Regions of areal scour are shown in yellow, alpine (subglacial) in orange, alpine (aerial) in black, selective linear erosion (SLE) in ice streams in light blue and regions of other selective linear erosion in dark blue. Question marks on areal scour (?) and other selective linear erosion (?) indicate topographic classes where the previous names (Sugden and John, 1976; Jamieson et al., 2014) may no longer be the most appropriate. Regions identified as having similar spectral properties to those containing artefacts due to dunes in the ice surface have been removed in the IFPA classification. Panel b) shows the locations of regions mentioned in the text: Adv. ST - Adventure Subglacial Trench, Amu. SS - Amundsen Sea Sector, AP - Antarctic Peninsula, Ast SB - Astrolabe Subglacial Basin, Aur SB - Aurora Subglacial Basin, DML - Dronning Maud Land, GaSM - Gamburtsev Subglacial Mountains, GoSM - Golicyna Subglacial Mountains, HA - Highland A, LV - Lake Vostok, MSB - Maud Subglacial Basin, PCM - Prince Charles Mountains, PEL - Princess Elizabeth Land, PPB - Pensacola-Pole Basin, RSLs - Recovery Subglacial Lakes, SC - Siple Coast, SPB - South Pole Basin, SSH - Slessor Subglacial Highlands, TAM - Transantarctic Mountains, VSH - Vostok Subglacial Highlands, WSB - Wilkes Subglacial Basin, ZSM - Zhigalov Subglacial Mountains.

5.6.2 An updated geomorphological map of Antarctica

This morphometric classification was applied to the IFPA topography across Antarctica and the resultant map is presented in Figure 5.10a, alongside the geomorphological classification from Jamieson et al. (2014) (Figure 5.10c). Despite being derived from a small set of training data (Figure 5.9), the classification returns a pattern that corresponds well what we know of the topography from ice-penetrating radar surveys (Frémand et al., 2023).

In this new geomorphological map, subaerial mountains fringe Antarctica in the Transantarctic Mountains, Antarctic Peninsula, Dronning Maud Land and Prince Charles Mountains. Significant subglacial mountain ranges are seen in Dronning Maud Land, Gamburtsev Subglacial Mountains, and Vostok Subglacial Highlands, but smaller subglacial mountain ranges are also identified in regions such as Highland A, Zhigalov Subglacial Mountains and Slessor Highlands. It is notable that this new classification does not identify any significant new mountain ranges, suggesting that ice-penetrating radar surveys have now covered a large enough proportion of the continent to give a broad brush view of alpine topography. However, there are still significant features and details within those alpine regions which are yet to be resolved, such as parts of Golicyna Subglacial Mountains (Figure 5.5c).

In the Jamieson et al. (2014) map, regions of “areal scour" are mainly concentrated in areas such as Princess Elizabeth Land, central Dronning Maud Land and South Pole Basin where there was almost no ice-penetrating radar at the time of the Bedmap2 release (Fretwell et al., 2013; Pritchard, 2014), leading to flat topography in interpolated products. In contrast, areally scoured topography in the IFPA classification is concentrated in central East Antarctica, primarily within the Aurora Subglacial Basin, but also in small patches in Maud Subglacial Basin, Adventure Subglacial Trench and parts of Wilkes Basin. Given the prevalence in our classification of areally scoured topography within large subglacial basins, we suggest that within the interior of Antarctica, smooth, low-relief topography may actually represent sedimentary infill of basins, rather than the smooth exposed-bedrock surfaces which typify areal scour (Rea and Evans, 1996), and hence refer to this as “areal scour (?)" in the key for all our figures. Previous classifications were based on observations of exposed topography around ice-sheet margins (Sugden and John, 1976; Jamieson et al., 2014), and with increased knowledge in the satellite era this may no longer be the most sensible way to interpret the interior topography of Antarctica.

Perhaps unsurprisingly, we also categorise some significant subglacial lake regions (e.g. Lake Vostok (Popov, 2020), Recovery subglacial lakes (Humbert et al., 2018), Astrolabe subglacial lake (Siegert and Glasser, 1997; Cui et al., 2020a)) as areally scoured topography. As low basal shear stress in subglacial lakes leads to the flattening of topography in the ice above them (Livingstone et al., 2022), the ice surface can not be expected to tell us about the submarine topography of these lakes. Nevertheless, smooth surface topography is often used in remote sensing inventories as a way of identifying potential subglacial lakes (Wright and Siegert, 2012; Livingstone et al., 2022), and isolated smooth regions of IFPA

topography could also be explored as potential subglacial lakes, particularly alongside suitably-located ice-penetrating radar surveys (Napoleoni et al., 2020).

Sugden and John (1976) defined selective linear erosion as topography containing significant incisions into the landscape, such as glacial troughs. However, in the Jamieson et al. (2014) classification shown in Figure 5.10, selective linear erosion simply represents any region which is neither alpine or areally scoured. We therefore split the class into selective linear erosion in ice streams (topography containing significant incisions into the landscape), and other selective linear erosion (everything else). In the geomorphological map, we see selective linear erosion in ice streams primarily around the margins of Antarctica in fast flowing areas like the Siple Coast, Amundsen Sea sector and Pensacola-Pole Basin, but also in the central Wilkes Basin. Although we classify the remaining topography as "other selective linear erosion (?)", this is more likely to represent a range of landscapes which have experienced some glacial erosion but which is not necessarily under topographic control. Further work could utilise the increased level of detail in the IFPA map to look at some of these regions and identify more sub-classes of active subglacial landscape.

During the calculation of the IFPA subglacial topography map, a constant value of the mean non-dimensional slipperiness parameter $\bar{C}$ was applied, as this value reproduces the correct amplitude of topography when applied at Thwaites Glacier (Chapter 3). However, a spatially invariant $\bar{C}$ does not account for geological and geomorphological variability in subglacial conditions across Antarctica, and is likely to cause errors in the amplitude of the topography in many regions. Comparison with data from Pine Island Glacier suggests values of $\bar{C} = 150$ in fast-flowing glacial troughs and $\bar{C} = 50$ in slower-moving highlands (Chapter 4), and this new geomorphological map may help to provide guidance as to how to apply spatially variable values of $\bar{C}$ across Antarctica in further work.

5.7 Conclusions

We apply Ice Flow Perturbation Analysis to satellite remote sensing data sets of the ice surface to produce a new map of subglacial topography beneath the Antarctic Ice Sheet. The IFPA map significantly improves our understanding of known mesoscale features of the subglacial landscape across Antarctica by sharpening their outlines, and also contains numerous new features which have not previously been observed, such as a 400 km long canyon which cuts across Maud Subglacial Basin in Dronning Maud Land, and a complex alpine ridge network in the eastern Golicyna Subglacial Mountains. Quantitative analysis of the new map reveals wider patterns, and we find that the new IFPA map contains more than 40,000 newly defined hills with a 50 m prominence. Metrics summarising short wavelength variability show that the new IFPA map contains topography which, unlike Bedmachine Antarctica, is not biased by the density of radar observations, and which reflects regional trends. We also use a small training data set and a range of textural characteristics to

produce an updated geomorphological classification of Antarctic subglacial topography into regions displaying characteristics of alpine (subaerial and subglacial), sediment-filled basin (previously misclassified as areal scour), and selective linear erosion landscapes. The new IFPA subglacial topography map, accompanied by this updated geomorphological classification, represents an enriched insight into the geometry and geomorphology of the landforms beneath Antarctica, and provides guidance for future geophysical surveying.

5.8 Extended figures

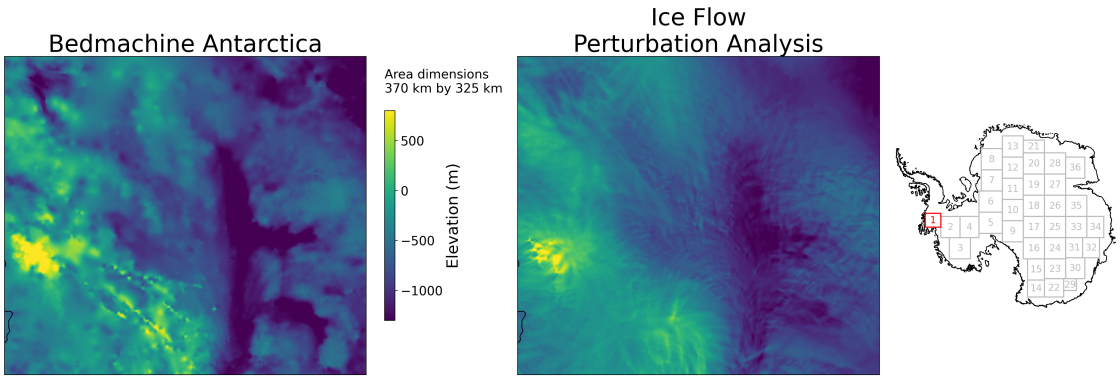

Fig. 5.11 A comparison of the bed topography from Bedmachine Antarctica and Ice Flow Perturbation Analysis for the Pine Island Glacier region of West Antarctica. The dimensions of this region are shown above the colour scale, and the location is shown in the Antarctic overview map.

5.8.1 A more comprehensive selection of topographic comparisons

We present in the main body of the text a selection of bed topography patches with features of interest. For completeness, we include a larger selection of figures here, covering the interior regions of the entire Antarctic continent. These figures cover larger areas than those presented in the main body of the text, and so some of the detail is obscured by the colour scale, but they give a more comprehensive overview of the features detected by Ice Flow Perturbation Analysis.

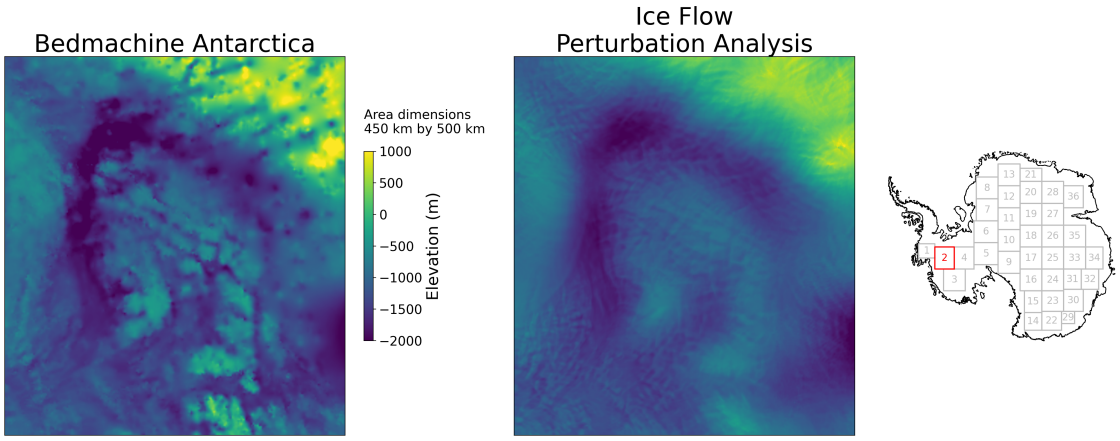

Fig. 5.12 A comparison of the bed topography from Bedmachine Antarctica and Ice Flow Perturbation Analysis for the Thwaites Glacier region of West Antarctica. The dimensions of this region are shown above the colour scale, and the location is shown in the Antarctic overview map.

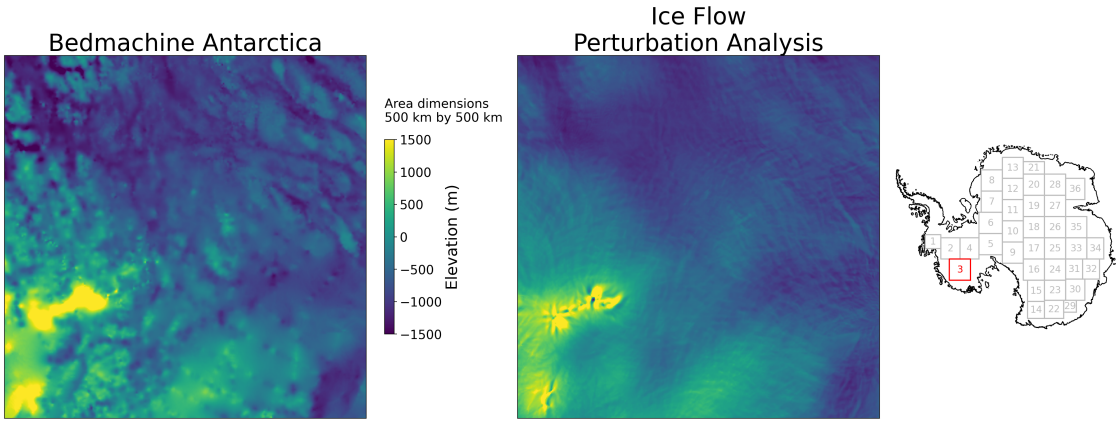

Fig. 5.13 A comparison of the bed topography from Bedmachine Antarctica and Ice Flow Perturbation Analysis for the Marie Byrd Land region of West Antarctica. The dimensions of this region are shown above the colour scale, and the location is shown in the Antarctic overview map.

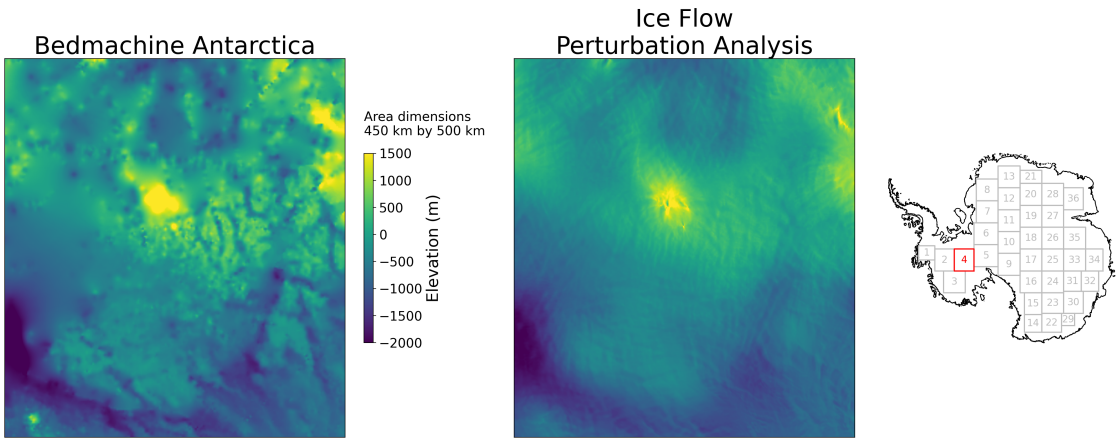

Fig. 5.14 A comparison of the bed topography from Bedmachine Antarctica and Ice Flow Perturbation Analysis for the Whitmore Mountains region. The dimensions of this region are shown above the colour scale, and the location is shown in the Antarctic overview map.

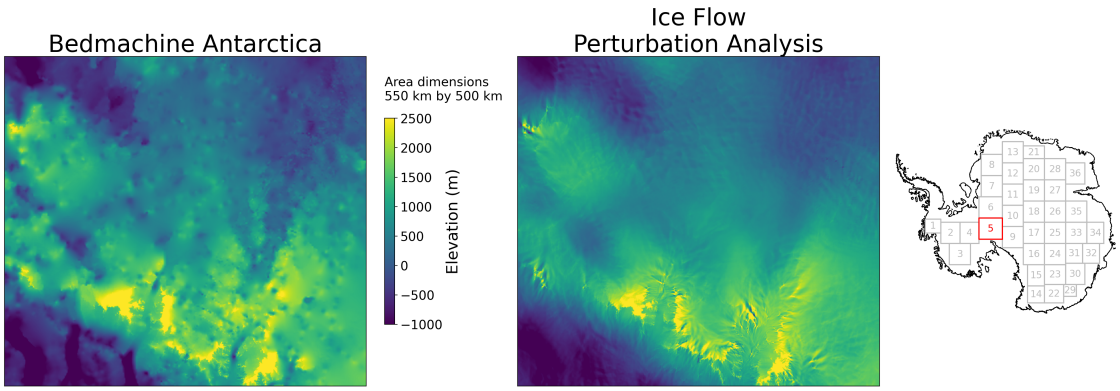

Fig. 5.15 A comparison of the bed topography from Bedmachine Antarctica and Ice Flow Perturbation Analysis for the southern end of the Trans-Antarctic Mountains. The dimensions of this region are shown above the colour scale, and the location is shown in the Antarctic overview map.

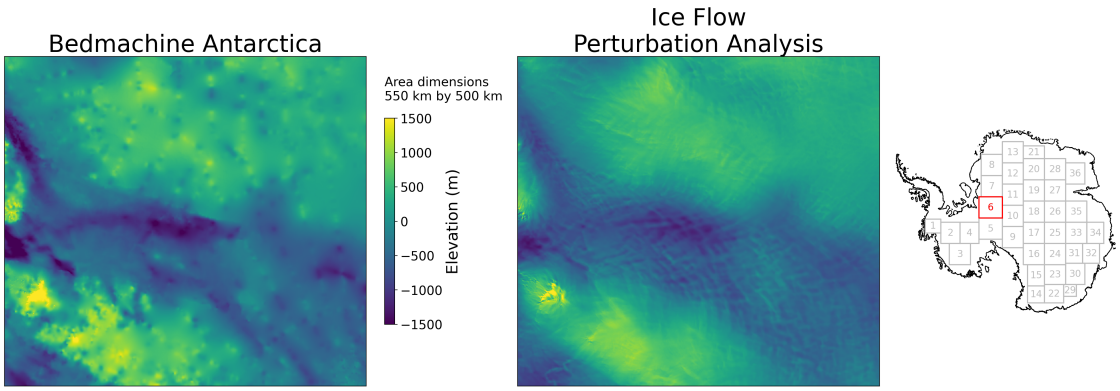

Fig. 5.16 A comparison of the bed topography from Bedmachine Antarctica and Ice Flow Perturbation Analysis for the Pensacola-Pole Basin. The dimensions of this region are shown above the colour scale, and the location is shown in the Antarctic overview map.

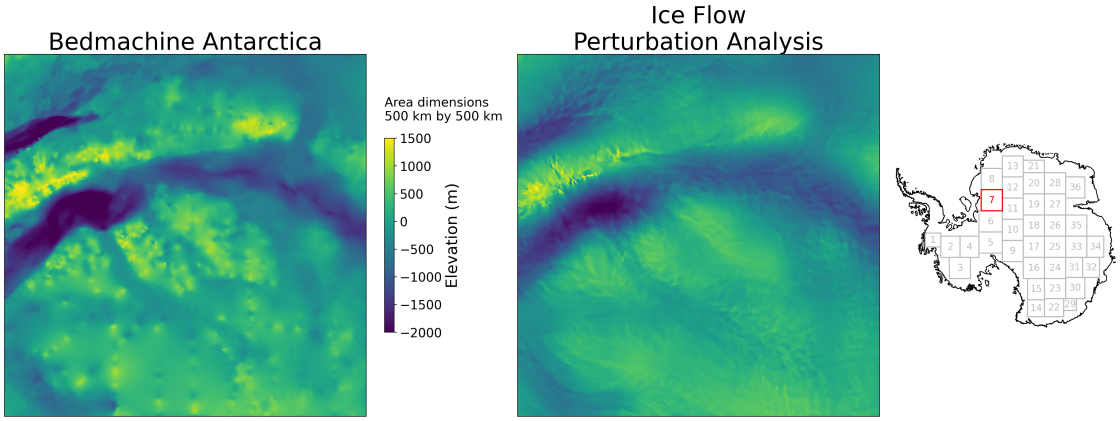

Fig. 5.17 A comparison of the bed topography from Bedmachine Antarctica and Ice Flow Perturbation Analysis for the Polar Gap Subglacial Highlands and Recovery Glacier. The dimensions of this region are shown above the colour scale, and the location is shown in the Antarctic overview map.

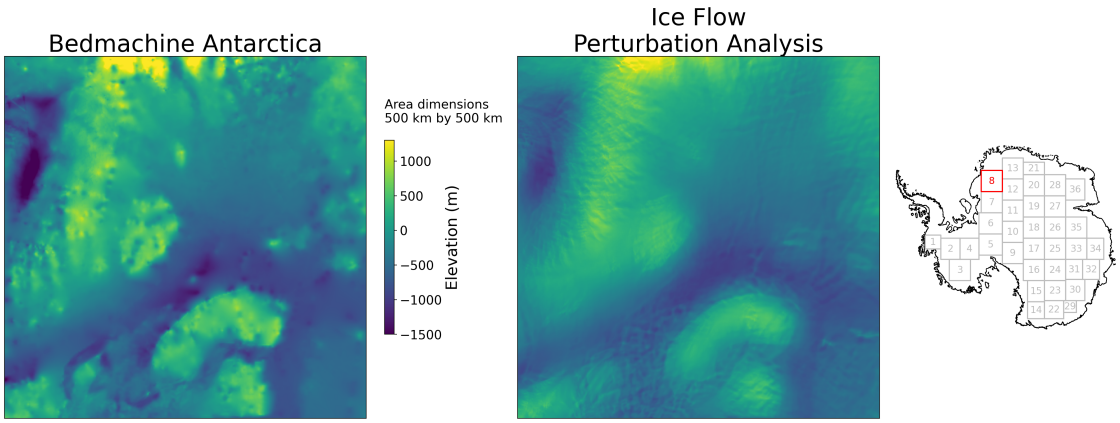

Fig. 5.18 A comparison of the bed topography from Bedmachine Antarctica and Ice Flow Perturbation Analysis for the Slessor Glacier Basin. The dimensions of this region are shown above the colour scale, and the location is shown in the Antarctic overview map.

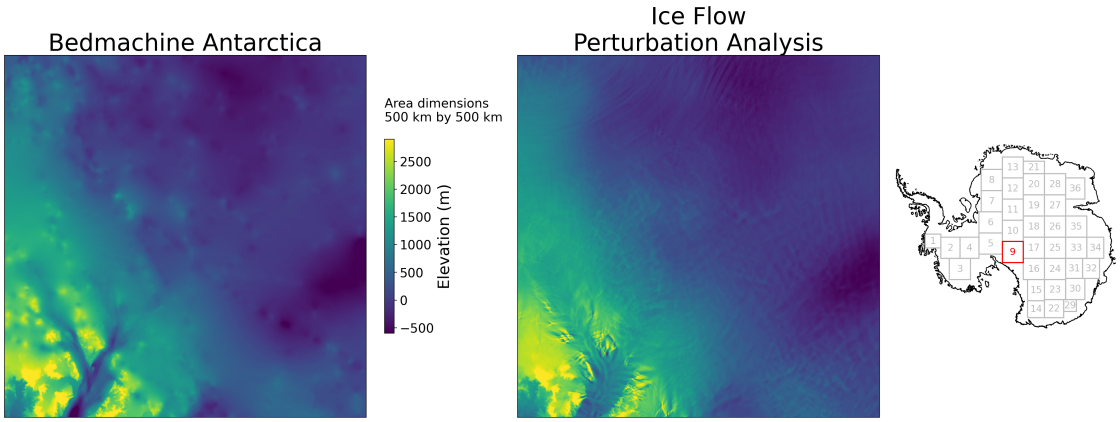

Fig. 5.19 A comparison of the bed topography from Bedmachine Antarctica and Ice Flow Perturbation Analysis for South Pole Basin. The dimensions of this region are shown above the colour scale, and the location is shown in the Antarctic overview map.

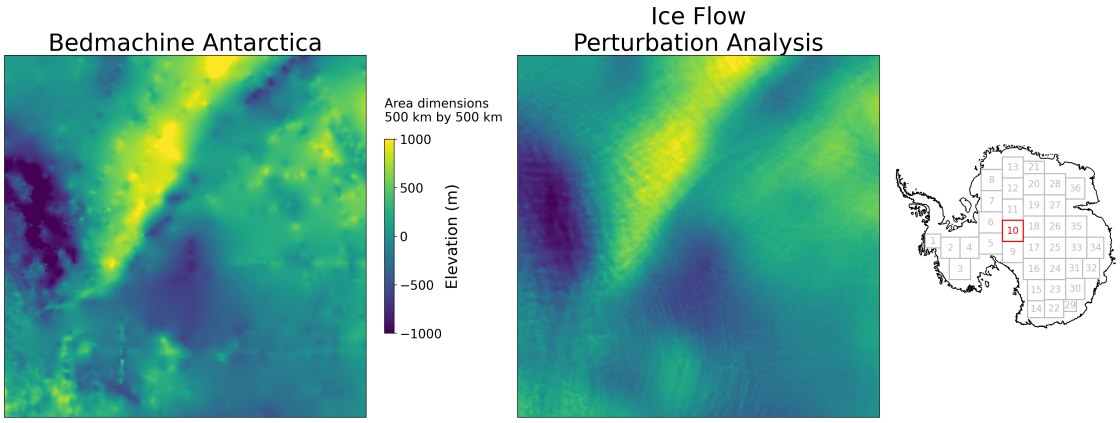

Fig. 5.20 A comparison of the bed topography from Bedmachine Antarctica and Ice Flow Perturbation Analysis for the South Pole Basin and the Recovery Subglacial Highlands. The dimensions of this region are shown above the colour scale, and the location is shown in the Antarctic overview map.

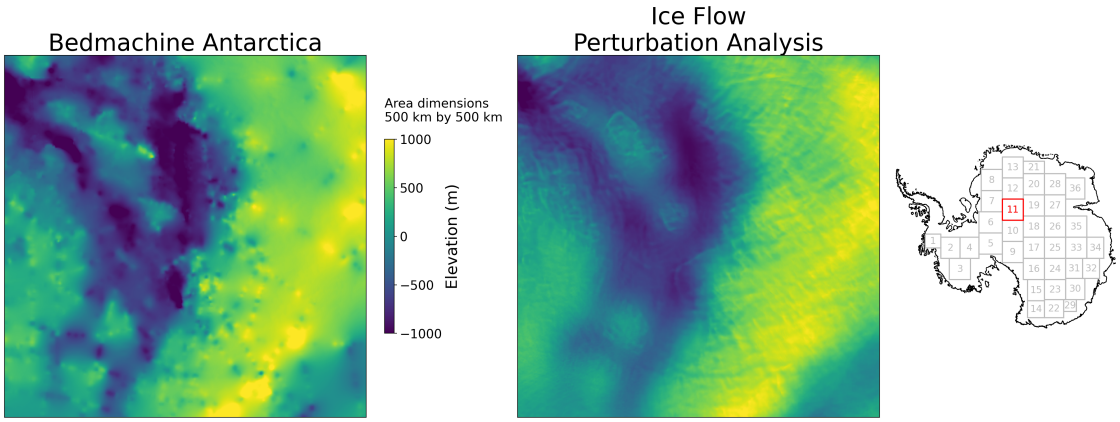

Fig. 5.21 A comparison of the bed topography from Bedmachine Antarctica and Ice Flow Perturbation Analysis for the Recovery Basin in East Antarctica. The dimensions of this region are shown above the colour scale, and the location is shown in the Antarctic overview map.

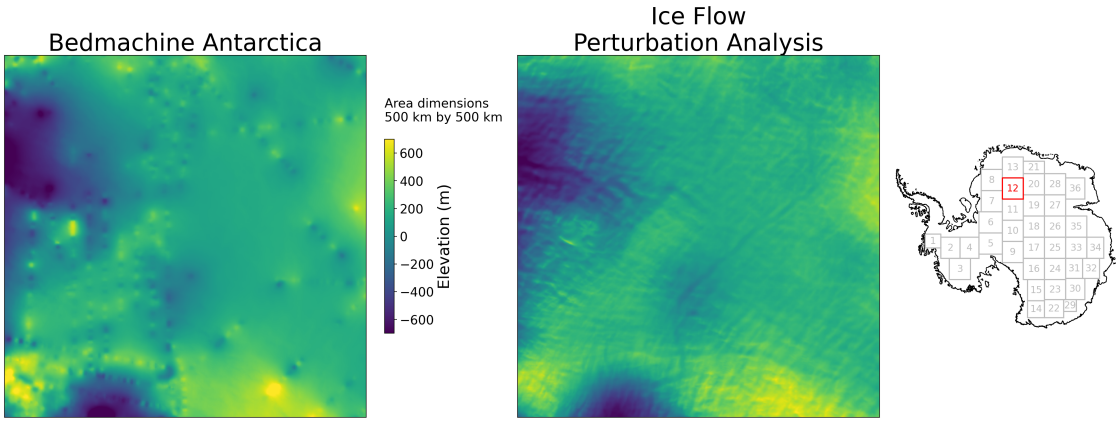

Fig. 5.22 A comparison of the bed topography from Bedmachine Antarctica and Ice Flow Perturbation Analysis for the Maud Subglacial Basin in East Antarctica. The dimensions of this region are shown above the colour scale, and the location is shown in the Antarctic overview map.

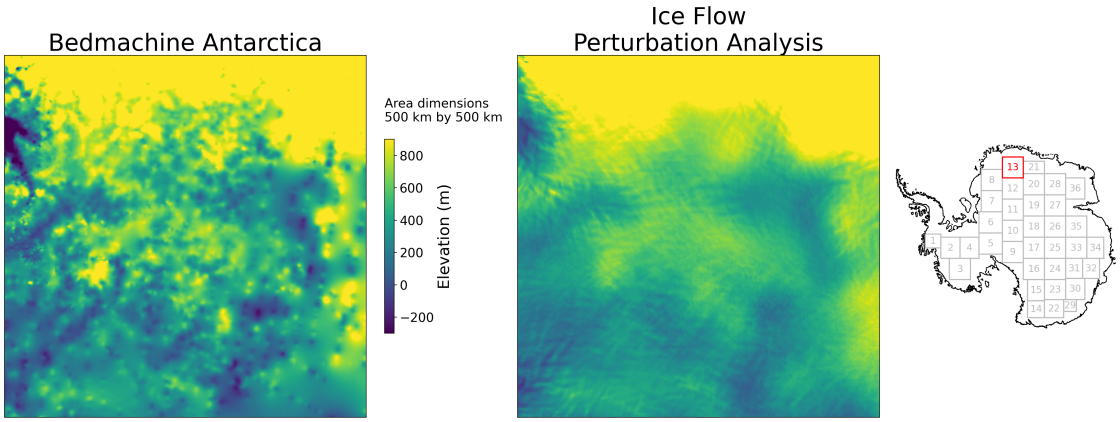

Fig. 5.23 A comparison of the bed topography from Bedmachine Antarctica and Ice Flow Perturbation Analysis for the western part of Donning Maud Land. The dimensions of this region are shown above the colour scale, and the location is shown in the Antarctic overview map.

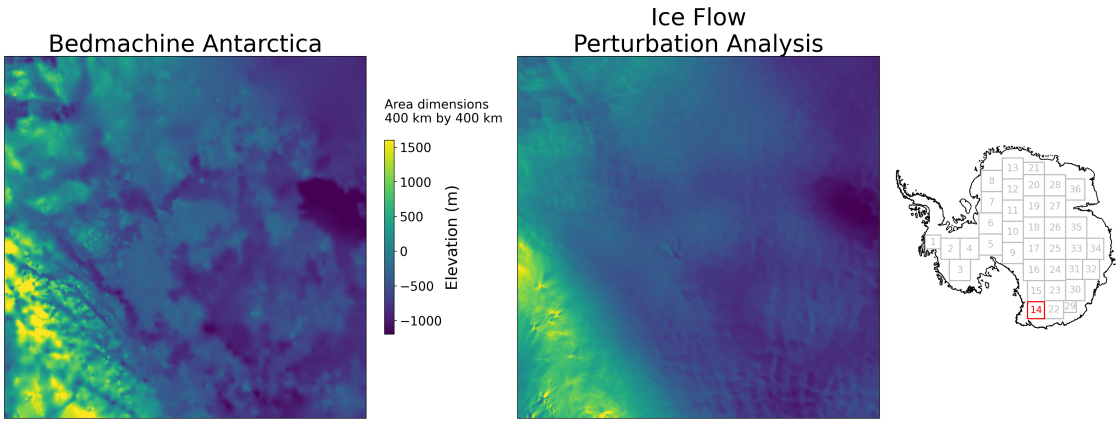

Fig. 5.24 A comparison of the bed topography from Bedmachine Antarctica and Ice Flow Perturbation Analysis for Oates Land in East Antarctica. The dimensions of this region are shown above the colour scale, and the location is shown in the Antarctic overview map.

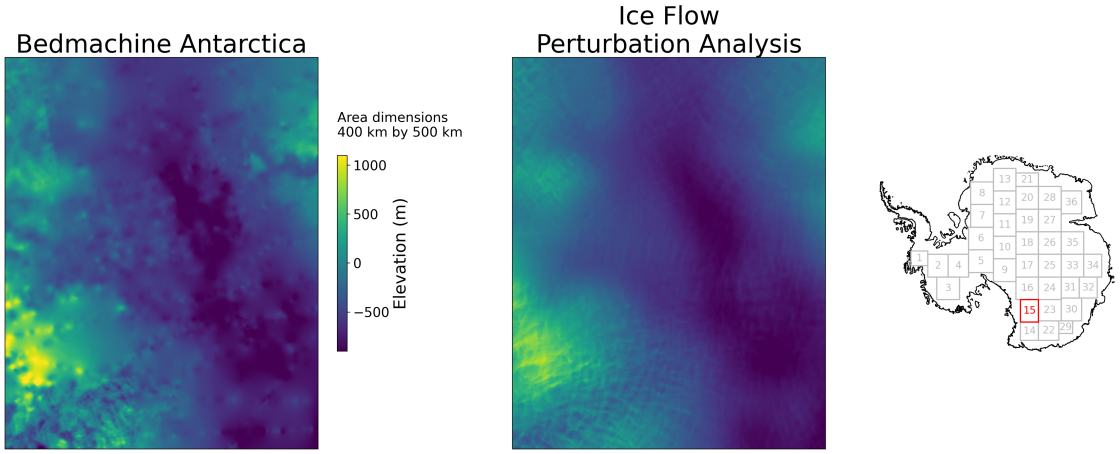

Fig. 5.25 A comparison of the bed topography from Bedmachine Antarctica and Ice Flow Perturbation Analysis for the Wilkes subglacial basin. The dimensions of this region are shown above the colour scale, and the location is shown in the Antarctic overview map.

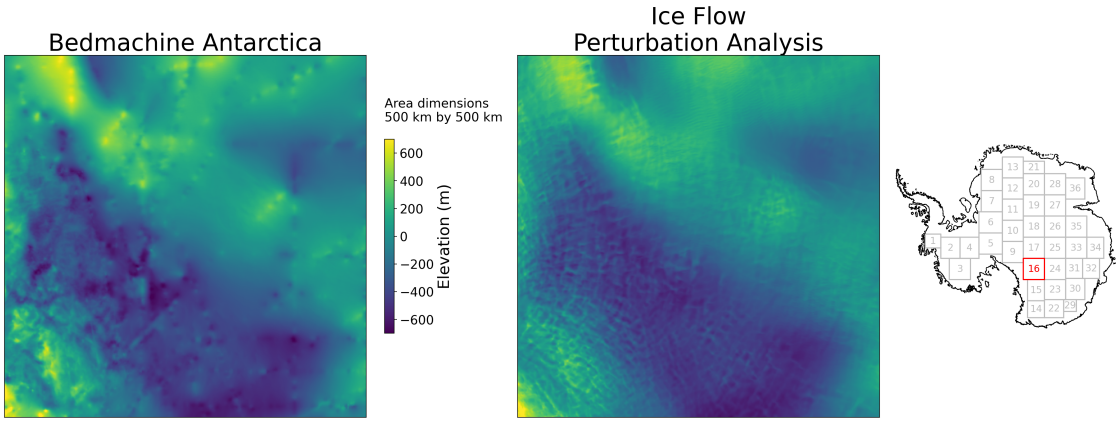

Fig. 5.26 A comparison of the bed topography from Bedmachine Antarctica and Ice Flow Perturbation Analysis for the southern part of the Wilkes subglacial Basin. The dimensions of this region are shown above the colour scale, and the location is shown in the Antarctic overview map.

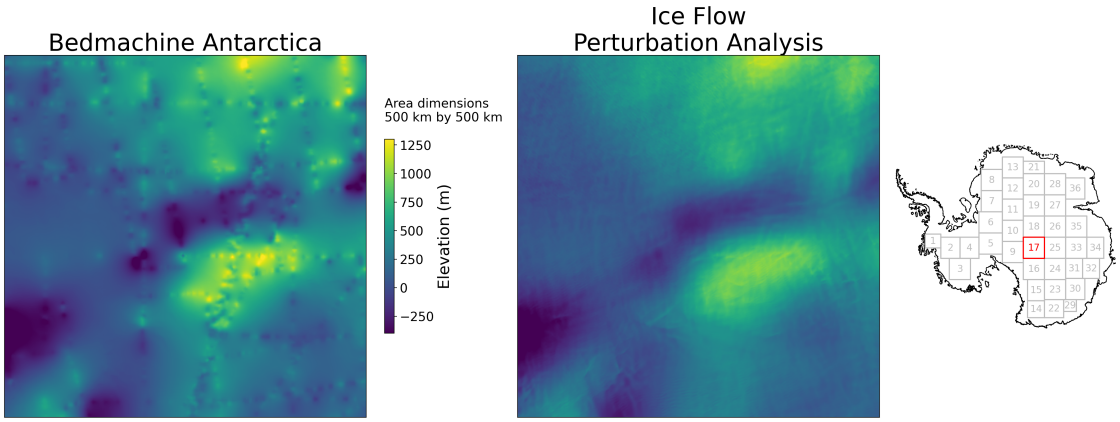

Fig. 5.27 A comparison of the bed topography from Bedmachine Antarctica and Ice Flow Perturbation Analysis for the southern part of the Vostok Subglacial Highlands, and the south eastern part of the Gamburtsev Subglacial Mountains. The dimensions of this region are shown above the colour scale, and the location is shown in the Antarctic overview map.

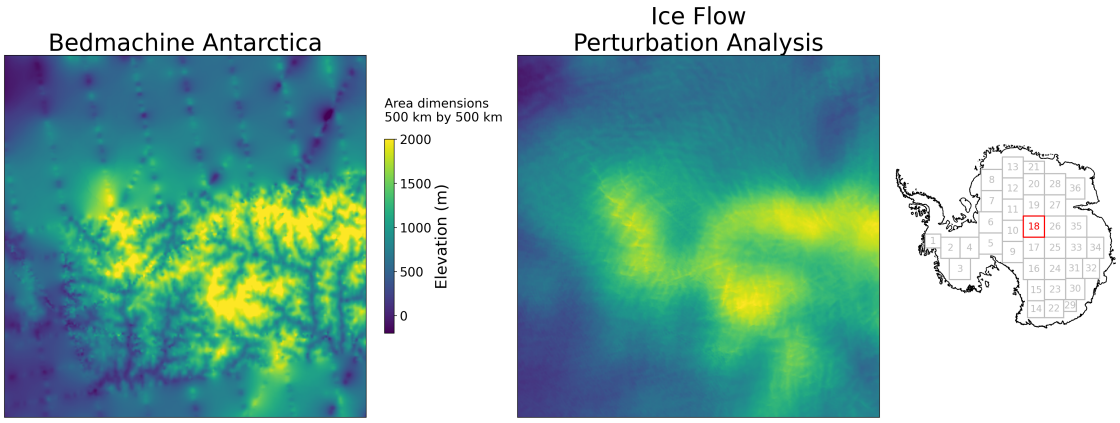

Fig. 5.28 A comparison of the bed topography from Bedmachine Antarctica and Ice Flow Perturbation Analysis for southern part of the Gamburtsev Subglacial Mountains. The dimensions of this region are shown above the colour scale, and the location is shown in the Antarctic overview map.

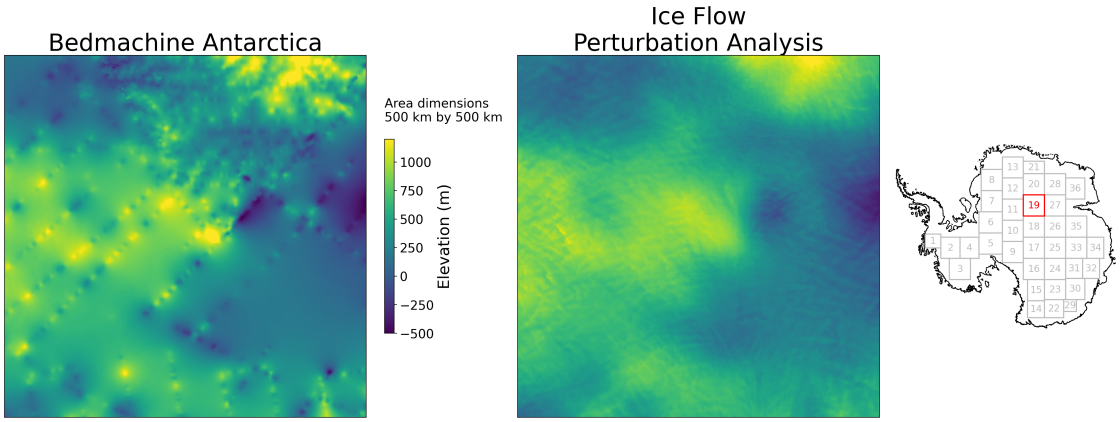

Fig. 5.29 A comparison of the bed topography from Bedmachine Antarctica and Ice Flow Perturbation Analysis for the northern part of the Recovery subglacial highlands and part of Dome Fuji. The dimensions of this region are shown above the colour scale, and the location is shown in the Antarctic overview map.

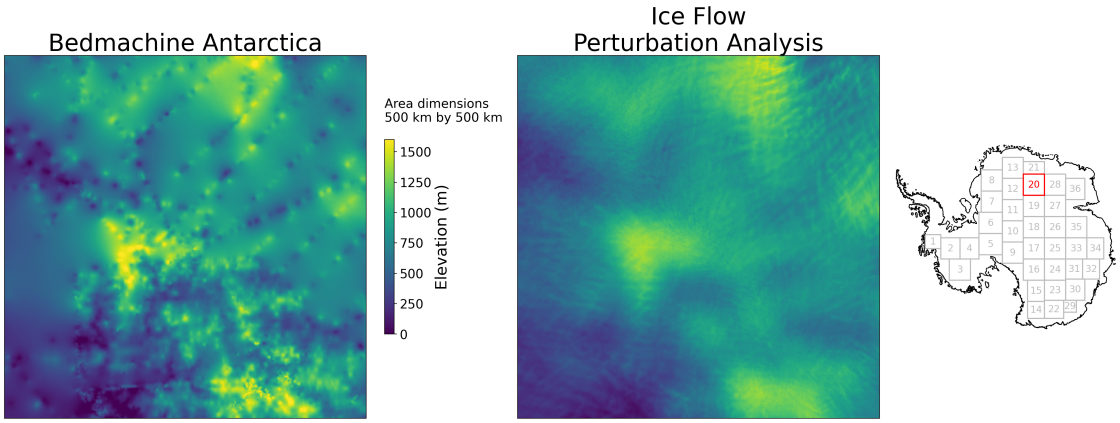

Fig. 5.30 A comparison of the bed topography from Bedmachine Antarctica and Ice Flow Perturbation Analysis for the interior part of Dronning Maud land including Valkyrie Dome. The dimensions of this region are shown above the colour scale, and the location is shown in the Antarctic overview map.

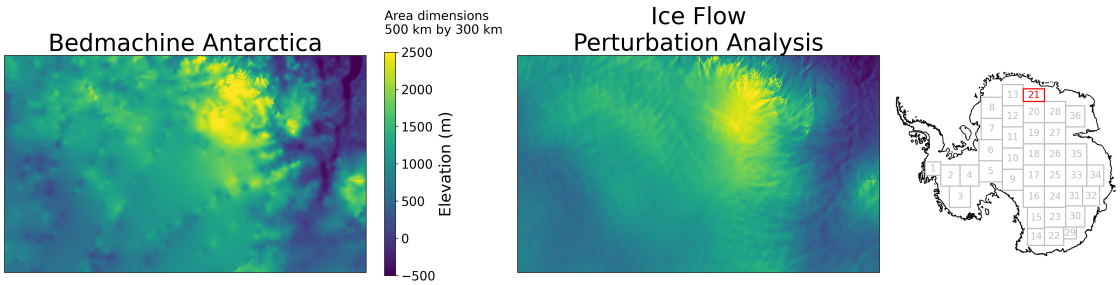

Fig. 5.31 A comparison of the bed topography from Bedmachine Antarctica and Ice Flow Perturbation Analysis for the Sr Rondane mountains in Dronning Maud Land. The dimensions of this region are shown above the colour scale, and the location is shown in the Antarctic overview map.

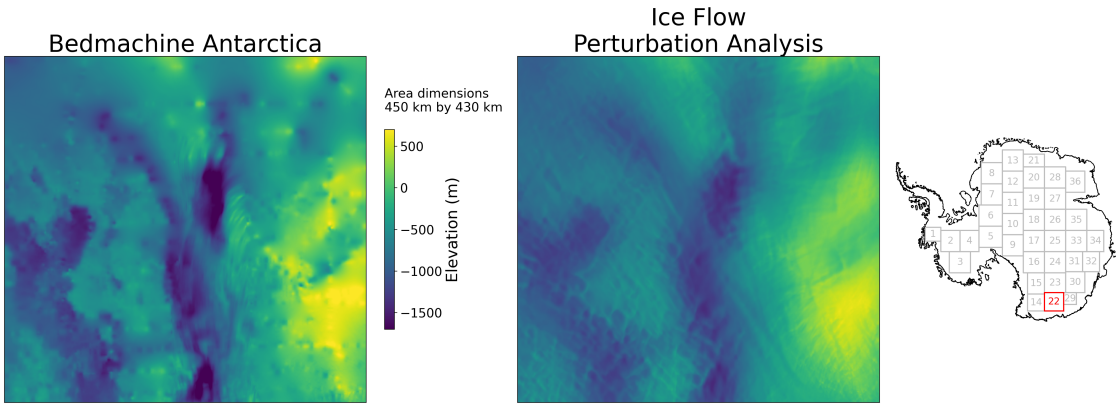

Fig. 5.32 A comparison of the bed topography from Bedmachine Antarctica and Ice Flow Perturbation Analysis for the Southern Cross Subglacial Highlands and Webb Subglacial Trench. The dimensions of this region are shown above the colour scale, and the location is shown in the Antarctic overview map.

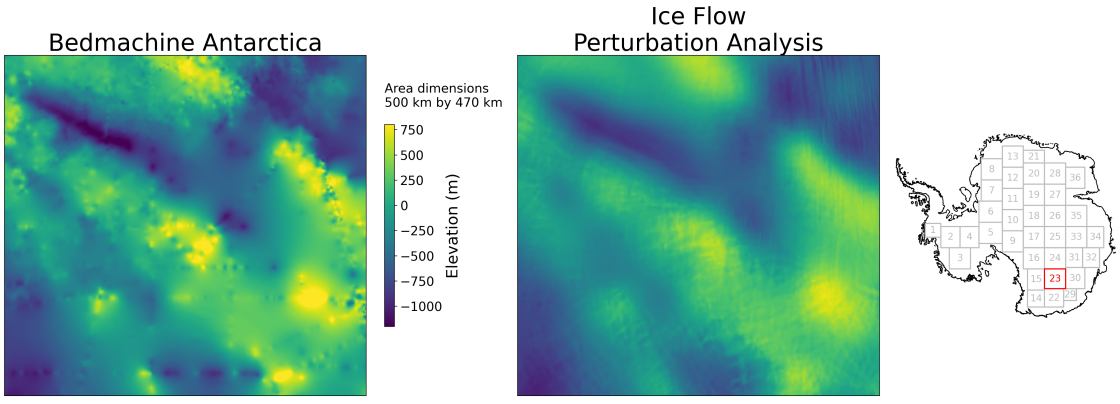

Fig. 5.33 A comparison of the bed topography from Bedmachine Antarctica and Ice Flow Perturbation Analysis for the Resolution Subglacial Highlands. The dimensions of this region are shown above the colour scale, and the location is shown in the Antarctic overview map.

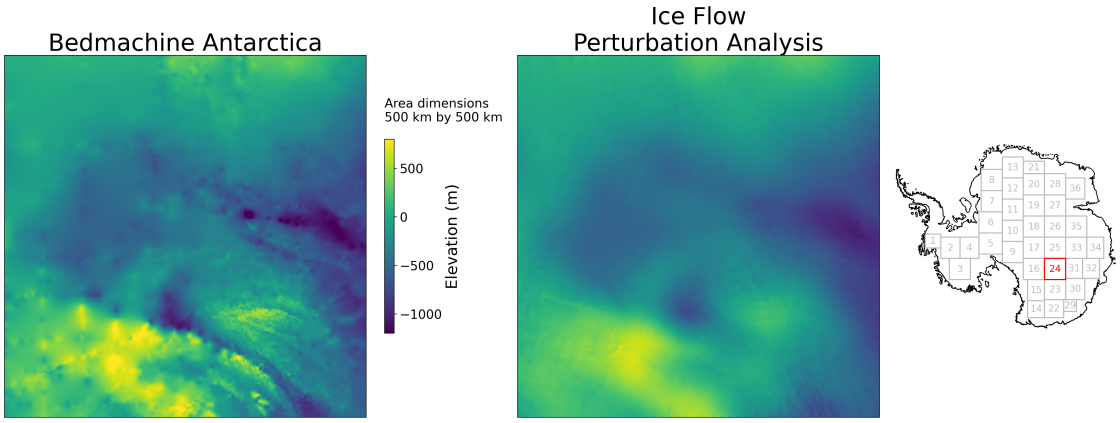

Fig. 5.34 A comparison of the bed topography from Bedmachine Antarctica and Ice Flow Perturbation Analysis for the Peacock Subglacial Trench and Aurora Subglacial Basin. The dimensions of this region are shown above the colour scale, and the location is shown in the Antarctic overview map.

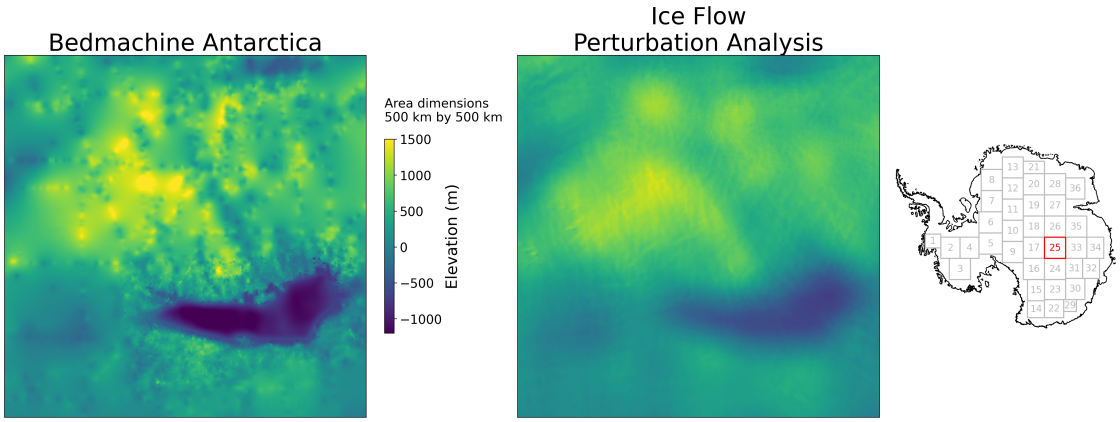

Fig. 5.35 A comparison of the bed topography from Bedmachine Antarctica and Ice Flow Perturbation Analysis for Lake Vostok and the Vostok subglacial highlands. The dimensions of this region are shown above the colour scale, and the location is shown in the Antarctic overview map.

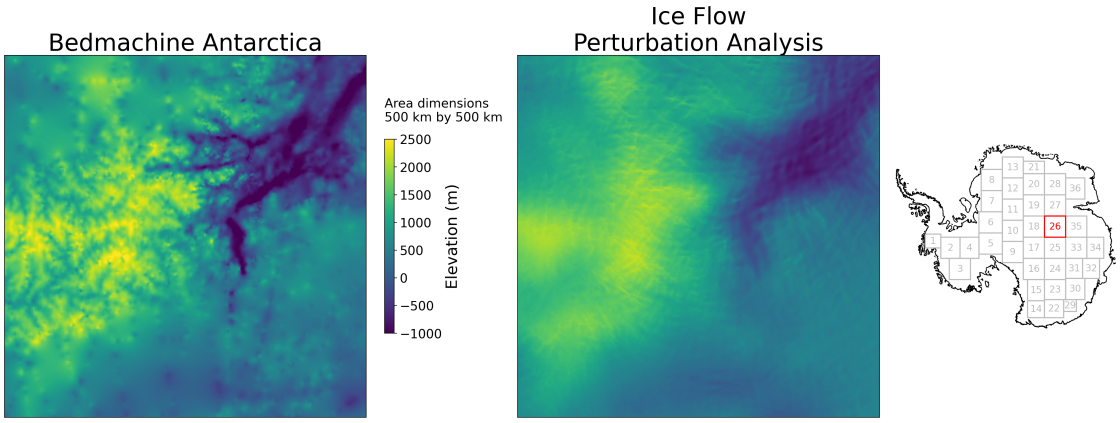

Fig. 5.36 A comparison of the bed topography from Bedmachine Antarctica and Ice Flow Perturbation Analysis for the northern part of the Gamburtsev Subglacial Mountains and the start of the Lambert rift. The dimensions of this region are shown above the colour scale, and the location is shown in the Antarctic overview map.

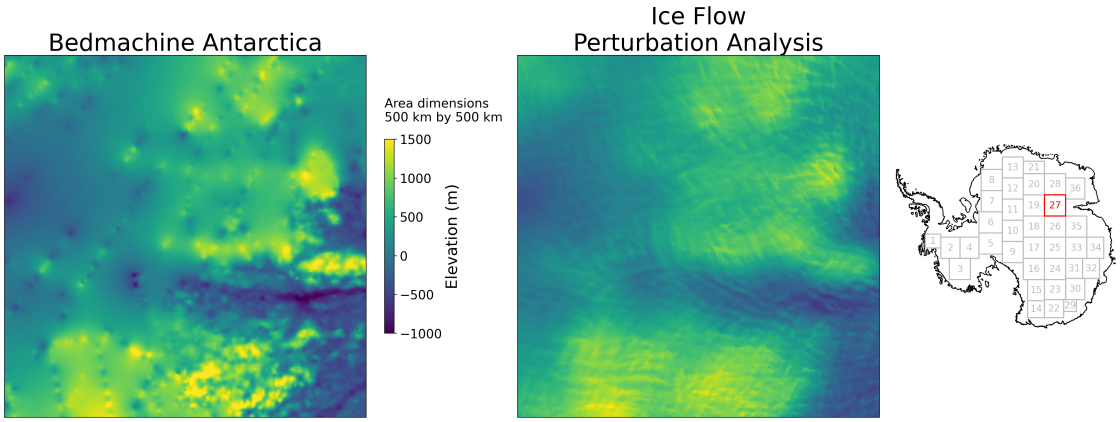

Fig. 5.37 A comparison of the bed topography from Bedmachine Antarctica and Ice Flow Perturbation Analysis for the north western part of the Gambertsev Subglacial Mountains and Mellor Glacier. The dimensions of this region are shown above the colour scale, and the location is shown in the Antarctic overview map.

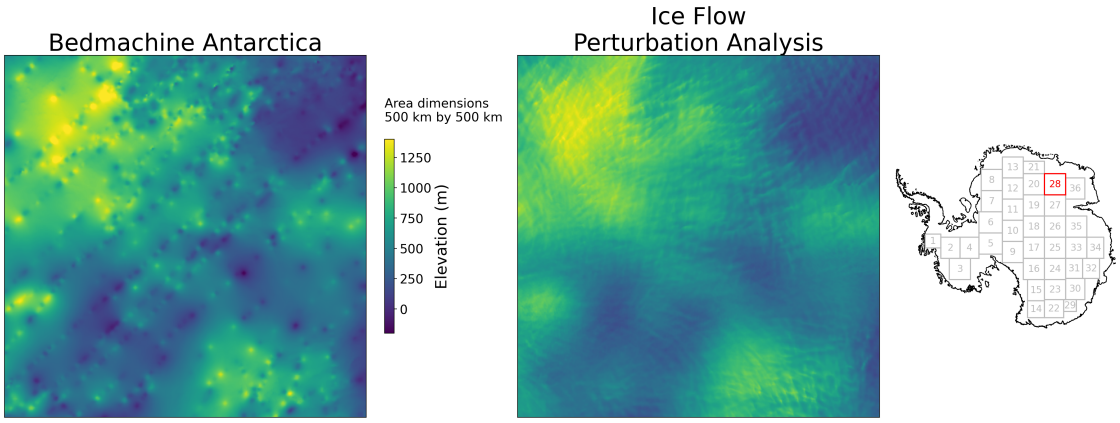

Fig. 5.38 A comparison of the bed topography from Bedmachine Antarctica and Ice Flow Perturbation Analysis for the Serlapova subglacial mountains and the interior part of Enderby land. The dimensions of this region are shown above the colour scale, and the location is shown in the Antarctic overview map.

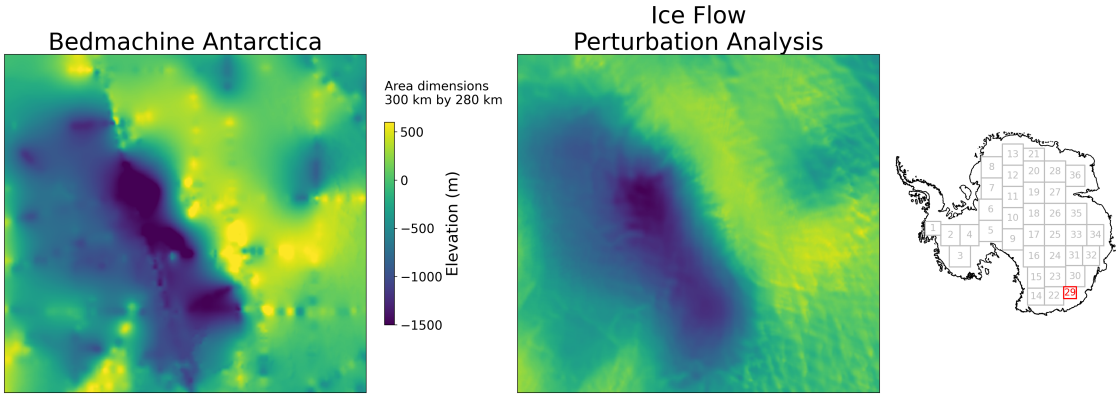

Fig. 5.39 A comparison of the bed topography from Bedmachine Antarctica and Ice Flow Perturbation Analysis for the Astrolabe subglacial basin and the Porpoise subglacial highlands. The dimensions of this region are shown above the colour scale, and the location is shown in the Antarctic overview map.

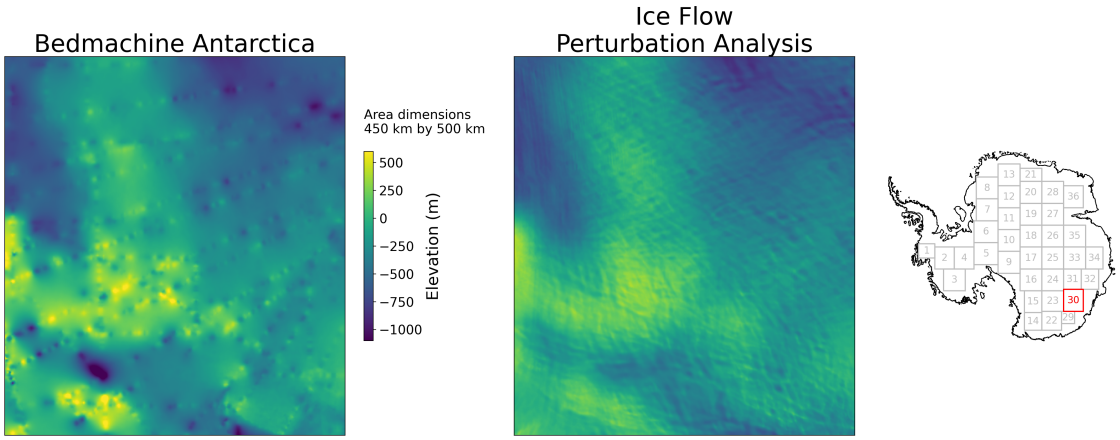

Fig. 5.40 A comparison of the bed topography from Bedmachine Antarctica and Ice Flow Perturbation Analysis for the Terre Adélie subglacial highlands, part of Highland C and part of Sabrina subglacial basin. The dimensions of this region are shown above the colour scale, and the location is shown in the Antarctic overview map.

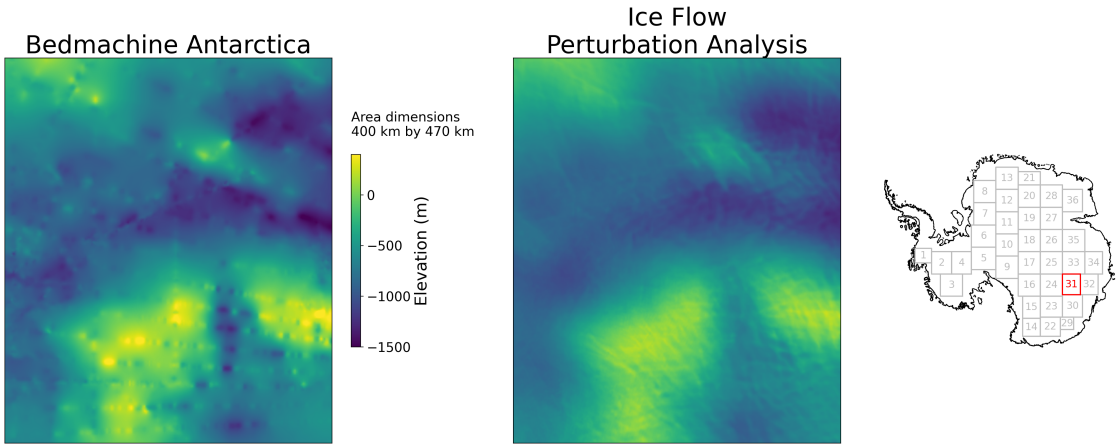

Fig. 5.41 A comparison of the bed topography from Bedmachine Antarctica and Ice Flow Perturbation Analysis for the southern part of Highlands B and C. The dimensions of this region are shown above the colour scale, and the location is shown in the Antarctic overview map.

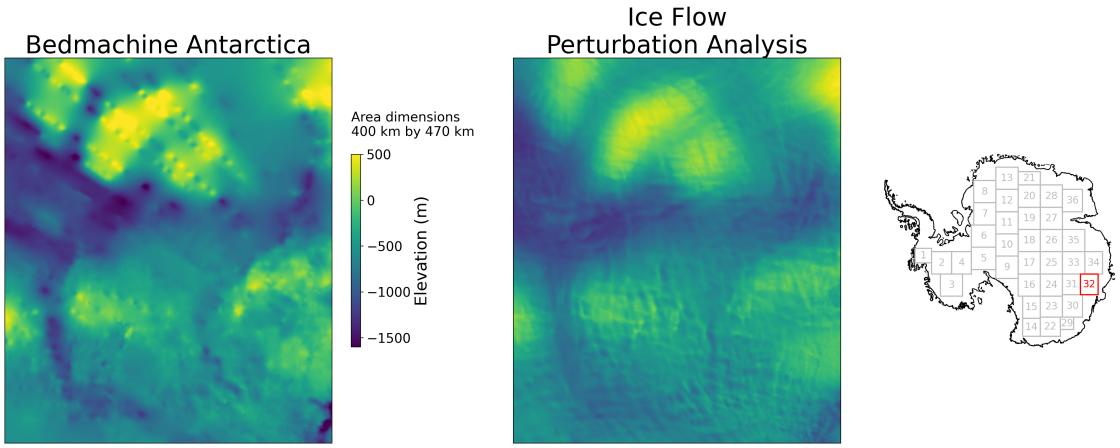

Fig. 5.42 A comparison of the bed topography from Bedmachine Antarctica and Ice Flow Perturbation Analysis for Highland A, and the northern part of Highland B. The dimensions of this region are shown above the colour scale, and the location is shown in the Antarctic overview map.

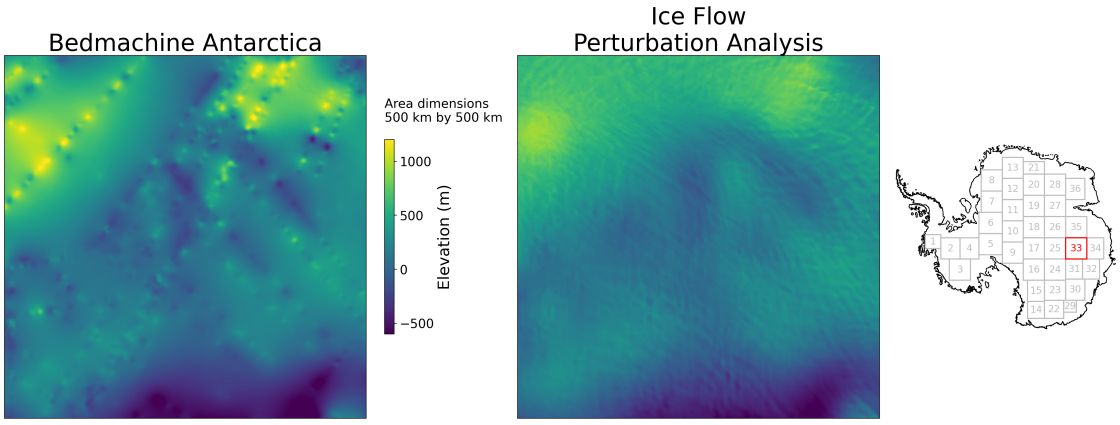

Fig. 5.43 A comparison of the bed topography from Bedmachine Antarctica and Ice Flow Perturbation Analysis for part of Queen Mary land and Wilhelm II land underneath the Korotkevich plateau in East Antarctica. The dimensions of this region are shown above the colour scale, and the location is shown in the Antarctic overview map.

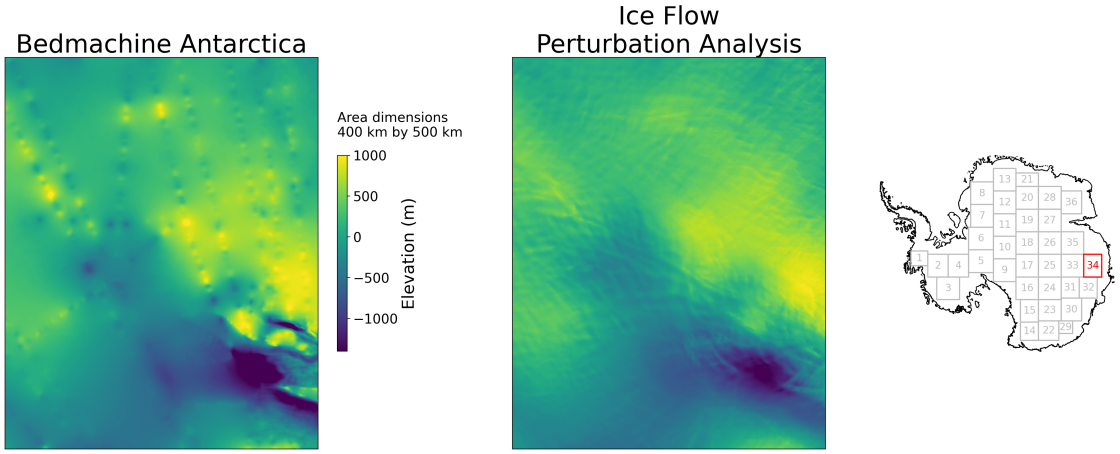

Fig. 5.44 A comparison of the bed topography from Bedmachine Antarctica and Ice Flow Perturbation Analysis for the Golicyna Subglacial Mountains in East Antarctica. The dimensions of this region are shown above the colour scale, and the location is shown in the Antarctic overview map.

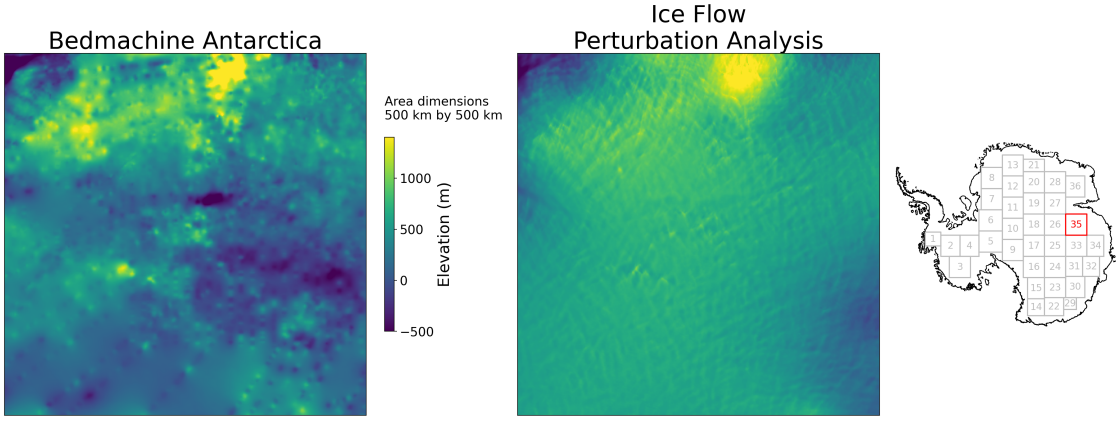

Fig. 5.45 A comparison of the bed topography from Bedmachine Antarctica and Ice Flow Perturbation Analysis for Princess Elizabeth land in East Antarctica. The dimensions of this region are shown above the colour scale, and the location is shown in the Antarctic overview map.

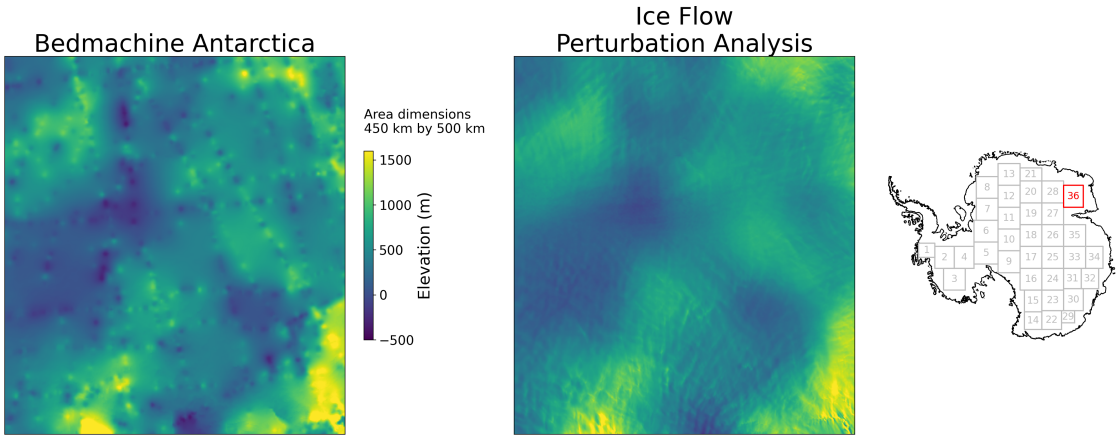

Fig. 5.46 A comparison of the bed topography from Bedmachine Antarctica and Ice Flow Perturbation Analysis for the Zhigalov subglacial mountains and central Kemp Land. The dimensions of this region are shown above the colour scale, and the location is shown in the Antarctic overview map.

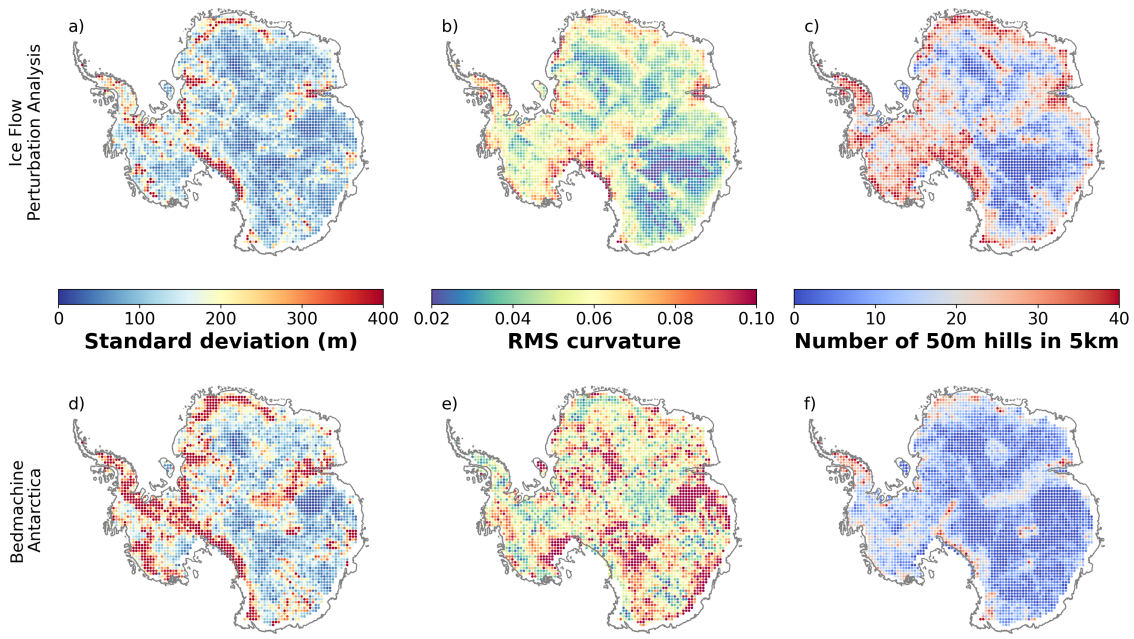

Fig. 5.47 Standard deviation, RMS Curvature and number of 50 m high hills within a 5 km radius dispalyed for 50 km by 50 km patches of subglacial topography from Ice Flow Perturbation Analysis (Panels a, b, and c respectively), and Bedmachine Antarctica (Panels d, e, and f respectively).

5.8.2 A more comprehensive selection of Antarctic wide metrics

We present in the main body of the text plots of number of 50 m high hills in a 5 km radius, wavelength of maximum power, and Fourier fractal dimension, calculated over the 4269 50 km by 50km patches which IFPA has been applied to. For completeness, here we include plots of all the textural metrics calculated.

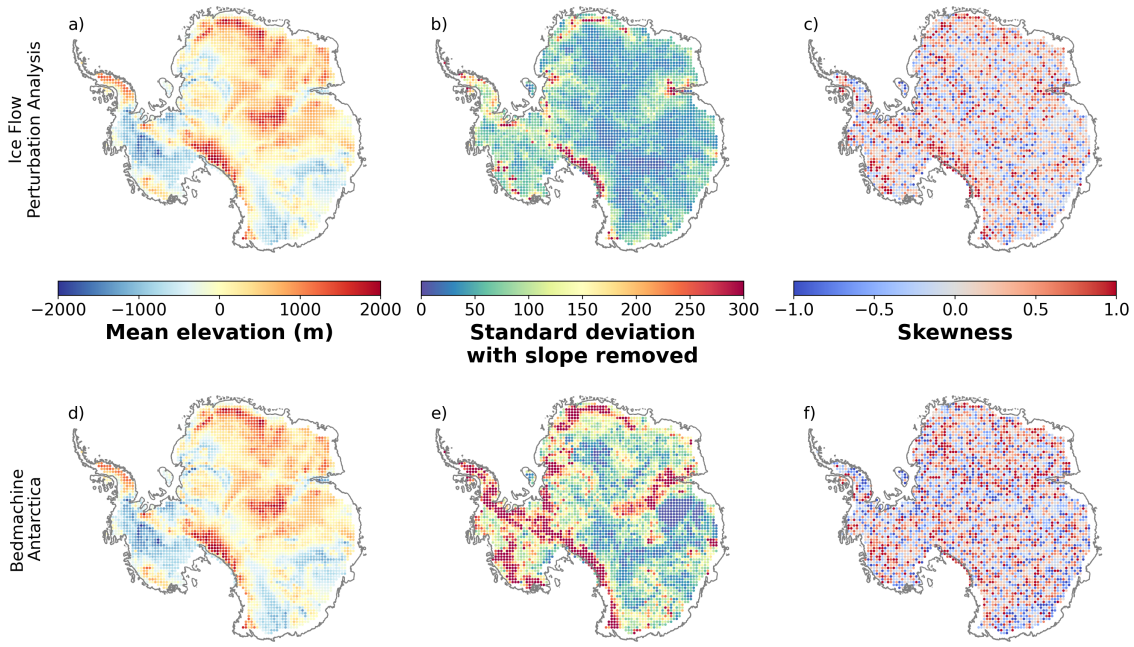

Fig. 5.48 Mean elevation, Standard deviation with the slope removed and skewness for 50 km by 50km patches of bed topography from Ice Flow Perturbation Analysis (a), b) and c) respectively), and Bedmachine Antarctica (d), e) and f) respectively).

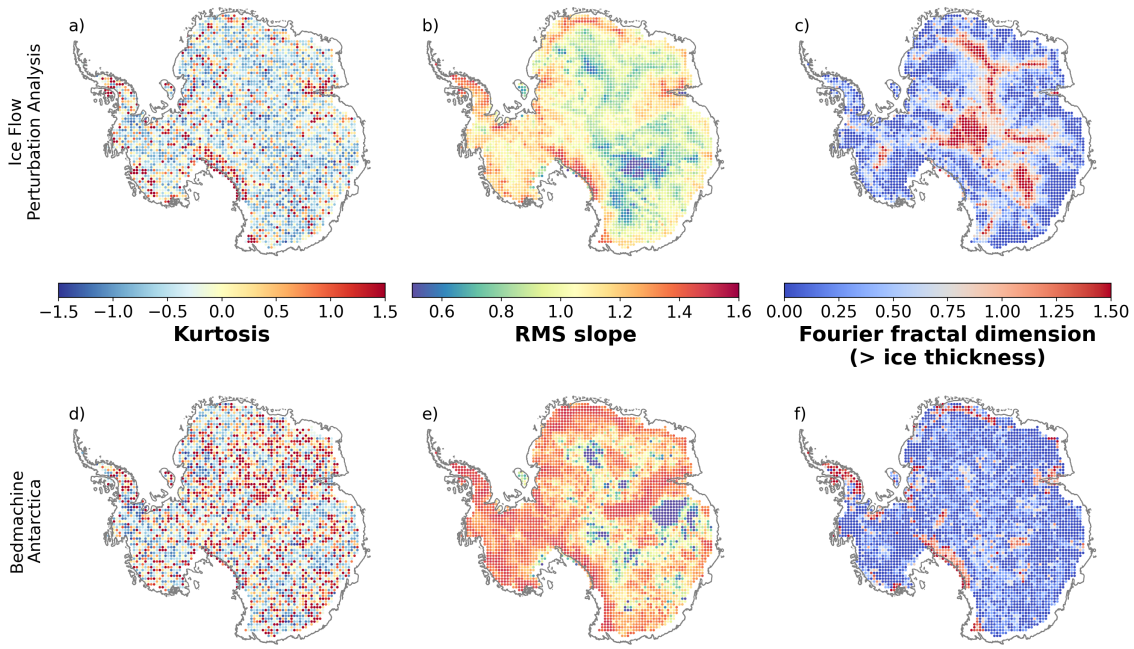

Fig. 5.49 Kurtosis, RMS slope and fractal dimension (wavelengths > ice thickness) for 50 km by 50km patches of bed topography from Ice Flow Perturbation Analysis (a), b) and c) respectively), and Bedmachine Antarctica (d), e) and f) respectively).

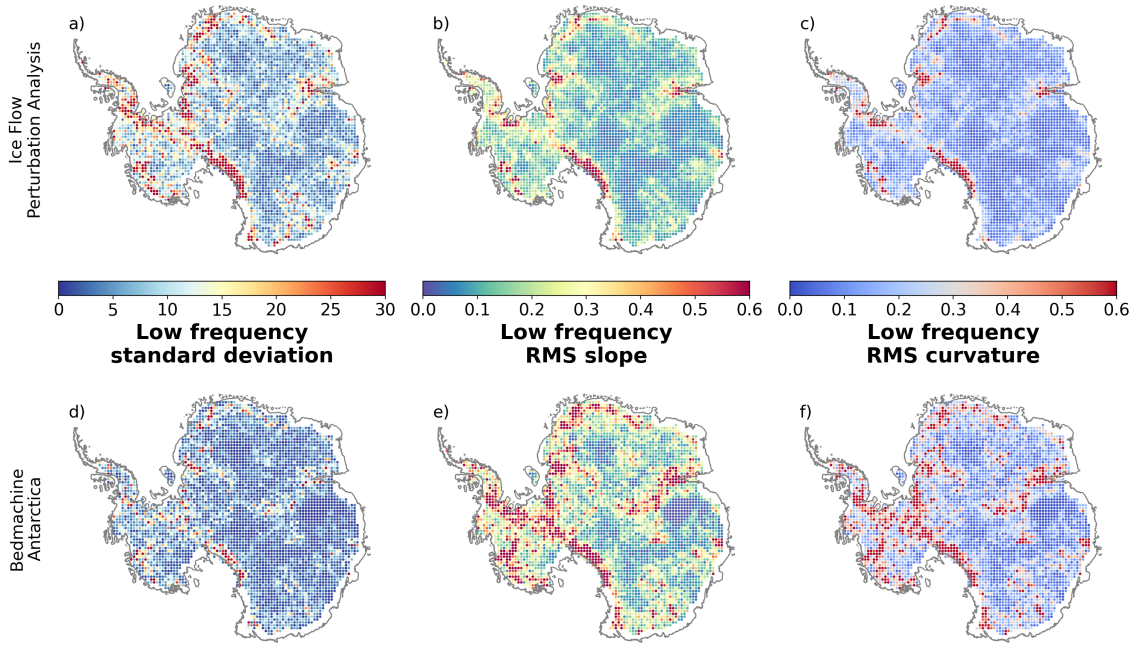

Fig. 5.50 Low frequency standard deviation, RMS slope and RMS curvature for 50 km by 50km patches of bed topography from Ice Flow Perturbation Analysis (a), b) and c) respectively), and Bedmachine Antarctica (d), e) and f) respectively).

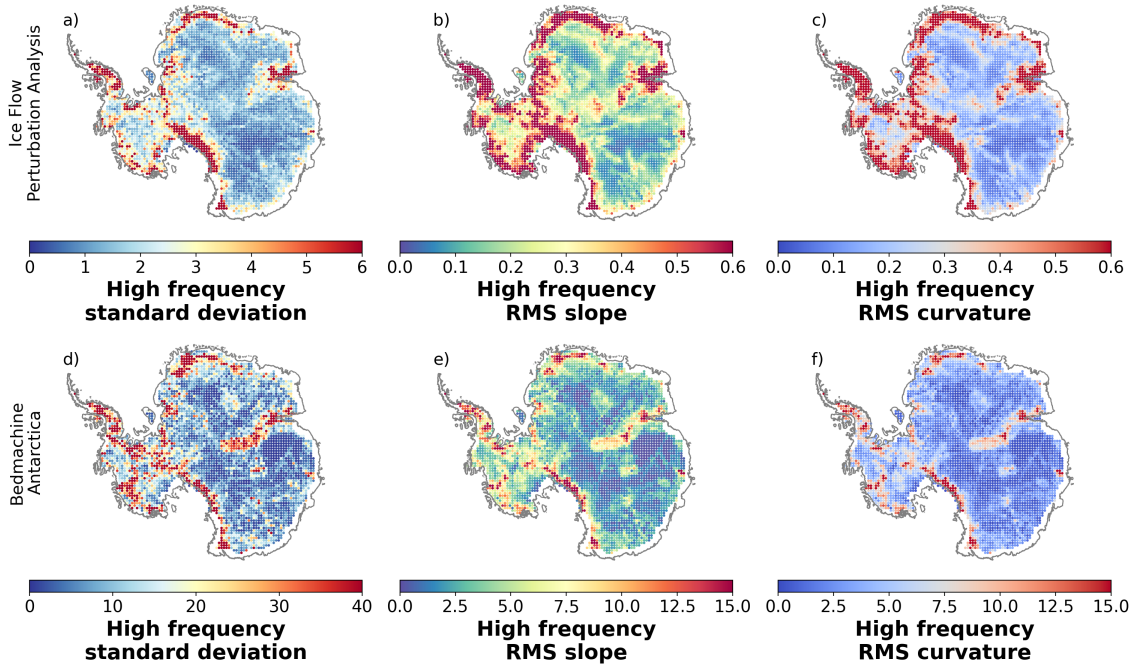

Fig. 5.51 High frequency standard deviation, RMS slope and RMS curvature for 50 km by 50km patches of bed topography from Ice Flow Perturbation Analysis (a), b) and c) respectively), and Bedmachine Antarctica (d), e) and f) respectively). Note that in this figure the Ice Flow Perturbation Analysis metrics are on a different colour scale to the metrics for Bedmachine Antarctica.

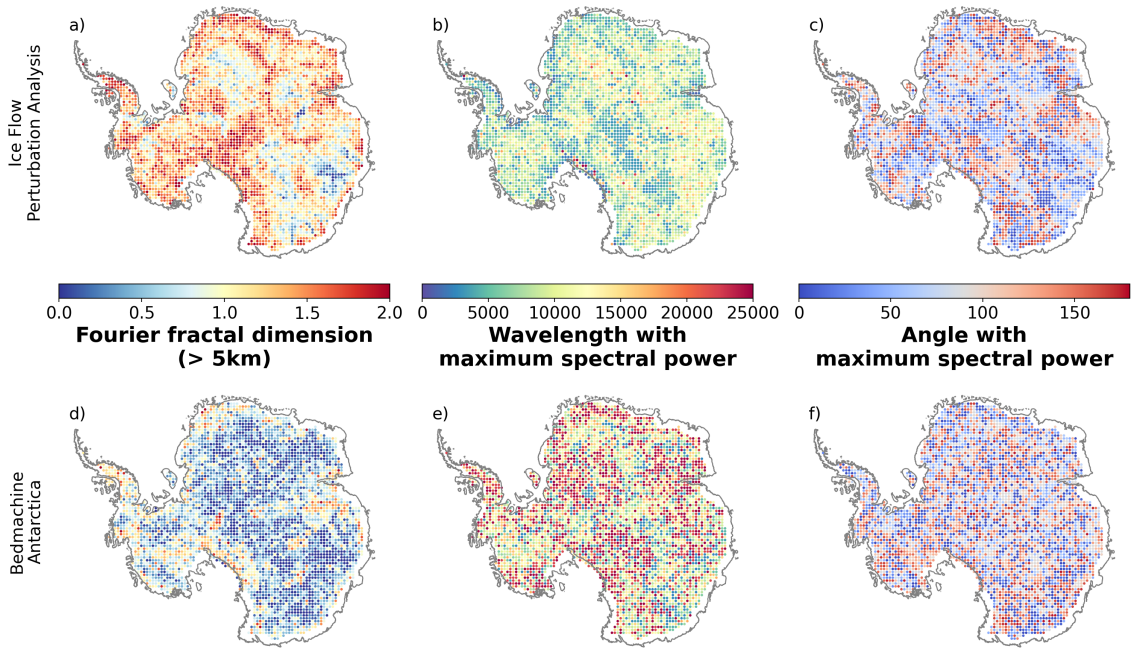

Fig. 5.52 Fractal dimension (wavelengths > 5km), Wavelength with maximum spectral power and angle with maximum spectral power for 50 km by 50km patches of bed topography from Ice Flow Perturbation Analysis (a), b) and c) respectively), and Bedmachine Antarctica (d), e) and f) respectively). Angles are measured anticlockwise relative to the positive x axis.

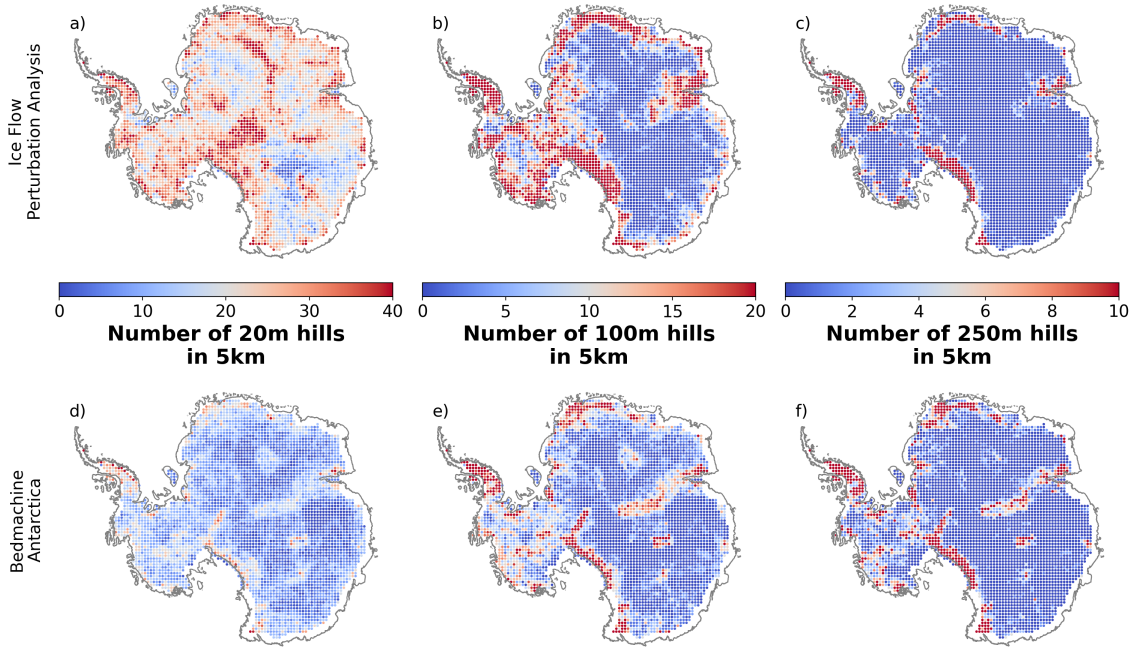

Fig. 5.53 Number of 20 m hills in 5 km, number of 100 m hills in 5 km and number of 200 m hills in 5 km for 50 km by 50 km patches of bed topography from Ice Flow Perturbation Analysis (a), b) and c) respectively), and Bedmachine Antarctica (d), e) and f) respectively).

Chapter 6

Integrated Discussion

In this chapter, I firstly give a brief summary of the findings of Chapters 3, 4 and 5, and explore how each of these chapters builds upon the previous. I present some new ice-penetrating radar data observations, which support the findings of Chapter 4, before a detailed discussion of ways in which this research could be improved in the future and its potential to contribute more widely to glaciological modelling.

6.1 Summary of work

When ice flows over obstacles in the ice-bed interface, this causes stress changes in the ice, which propagate upwards to the ice surface. For sufficiently large obstacles, these stress changes create topography in the ice surface. The work in this thesis explored how landforms in the ice surface can be studied to learn more about obstacles to flow at the ice-bed interface, and developed a methodology for doing this, which I have termed Ice Flow Perturbation Analysis (IFPA).

Chapter 3 used a variety of synthetic tests to explore whether it is possible to learn about the ice-bed interface from the ice surface. I found that, on the condition that subglacial landforms are aligned at greater than 15 degrees to the ice-flow direction, it is possible to resolve landforms with amplitudes greater than $0.005\bar{h}$, and a wavelength greater than $\bar{h}$ where $\bar{h}$ is the average ice thickness. When exploring the influence of errors in ice-surface datasets, I found that random (or spatially uncorrelated) errors normally have a white noise spectrum, and so can be accounted for in Fourier space. After a variety of synthetic tests, I concluded that with idealised data, it should be possible to reconstruct the variability in the bed.

Following on from these synthetic tests, Chapter 3 also assessed the feasibility of reconstructing the variability in the bed from real, non-idealised, noisy data. I used high-resolution swath-radar measurements from the Upper and Lower Thwaites Glacier regions to judge the success of the inverted results (Figure 3.6). I concluded that with suitable values of the model parameters, the method is successful at returning realistic data which

match the swath radar observations, and used these tuned observations to create a map of subglacial topography across the central trunk of Thwaites Glacier (Figure 3.5). Chapter 3 therefore established that the IFPA methodology can take satellite observations of the ice surface and reconstruct real topography observed by ice-penetrating radars.

In Chapter 4 I additionally explored how the IFPA method compares to streamline diffusion, the method used by Bedmachine Antarctica (Morlighem et al., 2020) to interpolate between ice-penetrating radar depth measurements in the interior of Antarctica. I used ice-penetrating radar observations from Pine Island Glacier, which were not included in version 1 of Bedmachine Antarctica (although they have subsequently been included in version 3). Comparison of the subglacial topography from IFPA, streamline diffusion and direct measurements of subglacial topography from ice-penetrating radar showed that IFPA can identify some features which are present in radar observations but which are not identified by streamline diffusion (Figure 4.2). This makes sense, because streamline diffusion uses the ice flow direction to interpolate between linear radar surveys, but not the speed of the ice or the topographic variation. This means that IFPA has the potential to reveal new landforms in areas where high-resolution ice-penetrating radar surveys have not yet been carried out.

In Chapter 4 I also used the radar observations to explore the optimal value for the mean non-dimensional slipperiness parameter, $\bar{C}$ (Figures 4.4 and 4.5). I found that the optimum value of $\bar{C}$ depends on the nature of the ice flow, and suggested values of $\bar{C} = 150$ in fast-flowing tributaries and $\bar{C} = 50$ in slower-moving higher-elevation areas between tributaries.

The IFPA methodology was improved from Chapter 3 to Chapter 4 to allow application of either the full-Stokes transfer functions (Gudmundsson, 2003) or the shallow-ice approximation transfer functions (Gudmundsson, 2008). It was also optimised to allow faster running over large regions by reducing the number of patches which needed to be repeated, and to allow for regions with significant differences between the direction of flow and the input data grid. These developments were made as part of a workflow to facilitate application of IFPA more efficiently across larger regions, and ultimately all of Antarctica, setting up the work presented in Chapter 5. This latest version of the IFPA methodology, which would form the most appropriate basis for future work suggested in Section 6.3, is detailed in Section 5.3.

In Chapter 5, I applied the improved version of the IFPA method to surface data from across the whole of Antarctica, and produced a new map of Antarctic subglacial topography (Section 5.4). This new map revealed new features in the bed across Antarctica in the regions between ice-penetrating radar surveys, and also improved our understanding of the boundaries and geometry of features which have only been partially observed in geophysical surveys (Section 5.4.1). I used quantitative metrics to compare the new subglacial topography to Bedmachine Antarctica v3 (Morlighem et al., 2020). The new topography displays spatial trends which are consistent with known geological variability,

and in contrast to Bedmachine Antarctica, is spatially unbiased, and not influenced by the location of ice-penetrating radar surveys (Figure 5.7).

Mountainous terrain and infilled sedimentary basins manifest distinctively in the new topographic map, as their geomorphology gives them very different landscape textures. I used these geomorphological properties, along with a small sample of training data, to produce a local classification of the type of topography across the new map, expanding previous classifications by Sugden and John (1976) and Jamieson et al. (2014) (Section 5.6). This geomorphological map reflects patterns which are seen in ice-penetrating radar measurements (Frémand et al., 2023).

Overall, this thesis concluded that IFPA can be used to study perturbations in the bed beneath flowing ice over the whole of the Antarctic continent, and that IFPA offers a way forward, in interior regions of Antarctica between widely-spaced radar surveys, to recover more realistic subglacial topographies than are presently provided by the interpolation methods employed by the Bedmap and Bedmachine series. Although satellite based ice-penetrating radar has so far been unsuccessful at imaging subglacial topography (Hall et al., 2008), IFPA demonstrates a path for exploring many aspects of Antarctic subglacial topography from satellite remote sensing products. The new map produced by applying IFPA to the whole of Antarctica contains many interesting new features, and has the potential to be highly useful for guiding future geophysical surveying.

6.2 New radar measurements from Thwaites Glacier

Since Chapter 3 was published, more ice-penetrating radar surveys have been carried out at Thwaites Glacier, West Antarctica, as part of the International Thwaites Glacier Collaboration. I worked for the British Antarctic Survey as a part of a four-person team collecting some of these radar measurements on the 22/23 austral field season at the downstream end of Thwaites Glacier. In this section I briefly discuss the acquisition and analysis of these data and their value in serving as a further check of the IFPA methodology.

The radar-data acquisition at Thwaites Glacier in 2022/23 was part of a major glaciology-oceanography science programme funded primarily by the U.K and U.S. government science agencies between 2017 and 2024, and named the International Thwaites Glacier Collaboration. In the 2022/23 austral field season we collected 41 ice-penetrating radar profiles, each 10 km long, on the downstream part of Thwaites Glacier, with a 500 m spacing between profiles, covering a 20 km by 10 km area, 85 km upstream of the grounding line. We collected these data using the British Antarctic Survey DELORES monopulse radar, which has a central frequency of around 3 MHz. For the data presented in this thesis, I filtered and gained each profile with Sandmeier ReflexW software, and used wavelets of a suitable depth and with the strongest-corrected-echo power to pick the subglacial topography. The full processing and bed-picking workflow followed very closely the methods that are presented in Bingham et al. (2017). As these new ice-penetrating radar

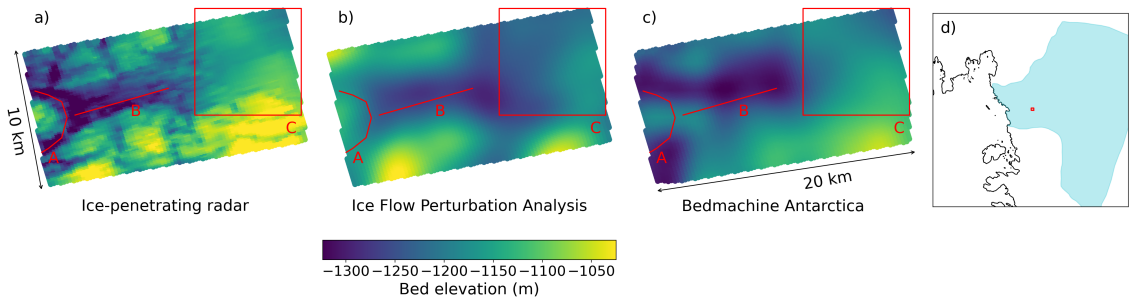

Fig. 6.1 A comparison of the subglacial topography from a) ice-penetrating radar, b) Ice Flow Perturbation Analysis and c) Bedmachine Antarctica (Morlighem et al., 2020) for a small region of the central trunk of Thwaites Glacier (10 km by 20 km), in West Antarctica. The location of this region is shown in red in panel d), with the outline of Thwaites Glacier in light blue. Annotated in red are notable features from the ice-penetrating radar data: A) a deep moat which bifurcates around a large hill, B) a deep valley which runs through the centre of the region, and C) a smooth shallow basin.

measurements have not yet been included in any large radar compilations like Bedmap3 (Frémand et al., 2023) and Bedmachine Antarctica (Morlighem et al., 2020), they provide a further test of the accuracy of the maps of subglacial topography produced using IFPA.

Figure 6.1 shows a comparison between the bed pick from the ice-penetrating radar, and the subglacial topography from IFPA and Bedmachine Antarctica. The key features of the surveyed bed are a deep moat which bifurcates around a large hill (Figure 6.1 A), a deep valley which runs through the centre of the region (Figure 6.1 B), and the smooth shallow basin in the top right corner (Figure 6.1 Box C). All three of these features are also clearly identified in the IFPA subglacial topography, whereas the bifurcation of the valley is not clear in the Bedmachine Antarctica bed. This provides additional support for the conclusion of Chapter 4 that IFPA can identify features which are not picked up by the streamline diffusion interpolation technique, even in areas which are thought to be relatively well surveyed.

There are very few high-resolution, three-dimensional surveys of subglacial topography. Existing examples include Smith and Murray (2009); King et al. (2016); Bingham et al. (2017); Holschuh et al. (2020); Schlegel et al. (2022) and Hoffman et al. (2023). However, numerical modelling shows that landforms like the valley and moat observed in this region of Thwaites Glacier have an influence on the local hydrology (Alley et al., 2021), and their formation has been linked to large volumes of sediment transport. These features may provide insights into the active processes which are occurring beneath ice sheets, and the ability to locate such potentially critical features with IFPA before carrying out fieldwork could increase efficiency and improve the utilisation of resources.

6.3 Limitations and future work

This thesis presents a functional workflow for applying the Ice Flow Perturbation Analysis method, and a new map of subglacial topography across Antarctica which has been produced with it. Here, I discuss some potential applications of the new map, ways in which the IFPA methodology could be improved to tackle some of the current limitations, uses for an updated topography map, and finally other data sets to which the IFPA method could be applied.

6.3.1 Applications of the current IFPA topography map

Despite not being able to capture the correct absolute amplitudes of many subglacial terrains (for reasons already explored in Sections 4.5.2 and 5.6.2), the topography maps produced by IFPA show the locations of many subglacial landforms extremely clearly. In addition, the relative amplitudes of features in regions with similar slipperiness are also likely to be reliable. There are therefore still many useful applications for the current map, even without attempting to correct the amplitudes (see Section 6.3.2 for ways to do this). Chapter 5 discussed what can be learnt from the texture of the topography, ignoring its amplitude, about the geology and geomorphology of the subglacial topography based on the work of Sugden and John (1976) and Jamieson et al. (2014). Here, I explore some other potential uses of the current IFPA topography map.

Ice-penetrating radar survey planning

In order to better understand the future behaviour of the Antarctic ice sheets, we need a more detailed understanding of many processes, and in particular the way in which ice flows over the bed (Parizek et al., 2013; Koellner et al., 2019). Airborne surveys have already given us a good overview of the basal scale topography (Fretwell et al., 2013; Morlighem et al., 2020; Frémand et al., 2023), but smaller landforms are also important for ice flow (Gladstone et al., 2012; Pattyn et al., 2013; McCormack et al., 2018; Castleman et al., 2022) because they influence the distribution of sediments and water at the bed (Holschuh et al., 2020; Alley et al., 2021). Although there are some high-resolution surveys of the subglacial topography underneath Antarctica (Smith and Murray, 2009; King et al., 2016; Bingham et al., 2017; Holschuh et al., 2020; Tsutaki et al., 2022; Hoffman et al., 2023), these only cover a tiny proportion of the continent, and it is difficult to build a picture of the overall bed character from limited snapshots.

The subglacial topography in the IFPA map reveals thousands of new topographic features which have a significant enough influence on ice flow to produce topography on the ice surface. Some of these are large enough in size to need a dedicated survey, but in many cases the landforms found by IFPA may simply guide the location of ice-penetrating

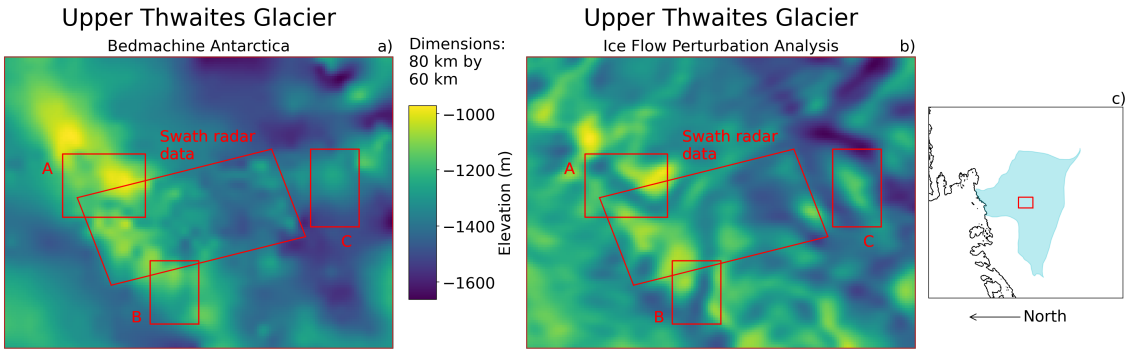

Fig. 6.2 A comparison of the subglacial topography for a) Bedmachine Antarctica and b) Ice Flow Perturbation Analysis for the Upper Thwaites Glacier region in West Antarctica. The largest red rectangle outlines the region which has been surveyed with swath radar (Holschuh et al., 2020), with smaller red rectangles outlining notable features which lie just outside the surveyed region. Boxes A and B show the extension of subglacial channels beyond the surveyed region, and box C shows a crag and tail feature. Panel c) shows the location of the subglacial topographic region presented in panels a) and b).

radar surveys to ensure that they gather the maximum amount of useful information about the subglacial topography.

For example, in the Upper Thwaites Glacier region in West Antarctica, Holschuh et al. (2020) used swath processing of ice-penetrating radar data to produce a detailed map of subglacial topography, which has been included in Bedmachine Antarctica (Figure 6.2a). This map shows many interesting topographic features, including flutes, moats and crags-and-tails (Alley et al., 2021). The IFPA map shows a number of further features which lie just outside the surveyed region, including subglacial valleys (Figure 6.2 Boxes A and B) and another hill (Figure 6.2 Box C) which is likely to be a similar crag-and-tail feature to those at the southern end of the surveyed region (See Figure 3.6 for more details). IFPA is therefore now positioned to be applied as an important tool for future Antarctic geophysical-survey planning, to ensure that surveys target the types of topography that are needed for understanding subglacial processes.

Where is IFPA a poor match to the known topography?

Throughout the work presented in this thesis, I have primarily focussed on regions where the match to existing topography is good, although I have discussed some examples of regions where the IFPA topography is not particularly representative of what is known from ice-penetrating radar surveys (e.g. the example of surface megadunes in central East Antarctica discussed in Section 5.4.2). In this section I focus on the insights that are provided specifically by locations where IFPA and directly measured subglacial topography show a poor match.

In some fast-flowing ice streams, the IFPA map shows sharp ridges which traverse the main trunks of the glaciers. Two examples of this are shown in Figure 6.3a and

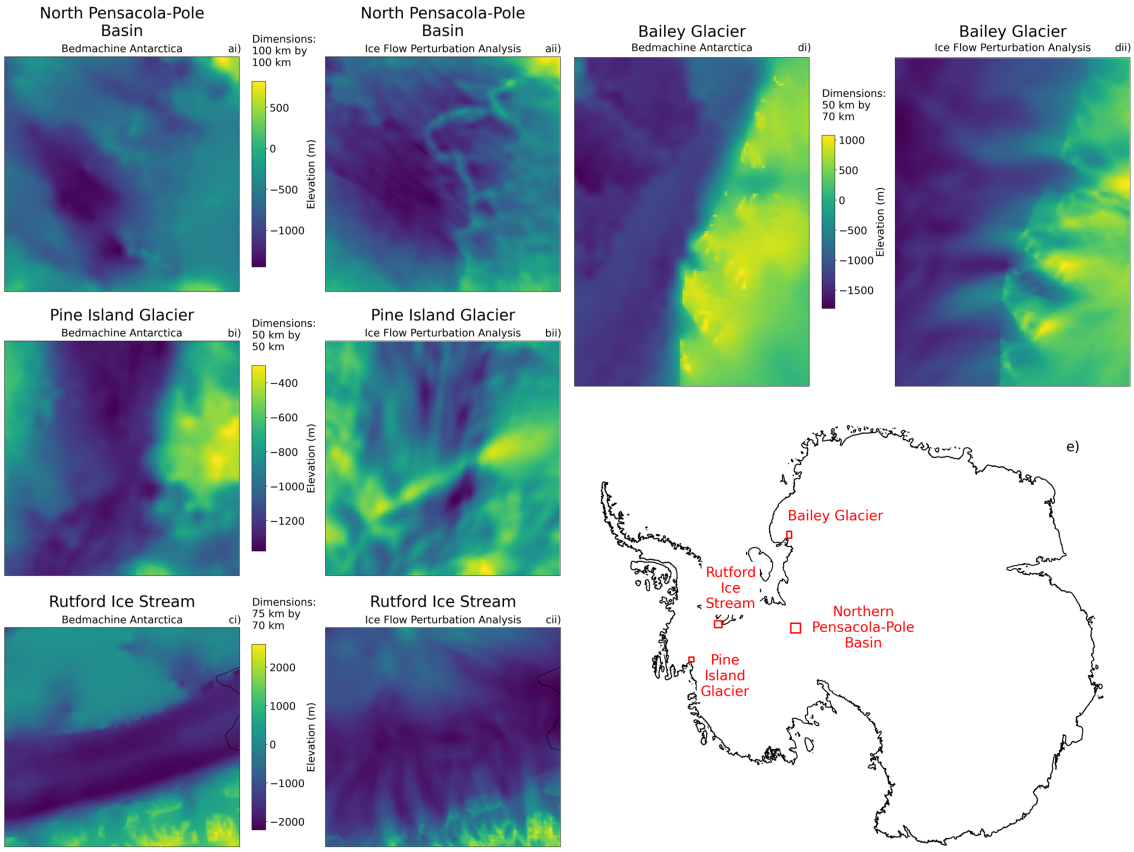

Fig. 6.3 A comparison between subglacial topography from i) Bedmachine Antarctica and ii) Ice Flow Perturbation Analysis for a) the north Pensacola-Pole Basin, b) the main trunk of Pine Island Glacier, c) Rutford Ice Stream and d) Bailey Glacier. Panel e) shows the locations of these regions on an outline map of Antarctica. Panels a) and b) are examples of anomalous ridges which appear across some fast-flowing ice streams in the IFPA topography. Panels c) and d) are examples of anomalous spurs extending from mountainous regions into fast-flowing ice streams in the IFPA topography.

6.3b for north Pensacola-Pole Basin and Pine Island Glacier respectively. We know from geophysical observations on Pine Island Glacier (Vaughan et al., 2006; Jordan and Robinson, 2021) and Pensacola-Pole Basin (Paxman et al., 2019a) that both of these regions are underlain by deformable sediments, which may deform in alignment with the ice-flow direction but are unlikely to form ridges across flow. Ice-penetrating radar measurements (Vaughan et al., 2006) show that the ridge at Pine Island Glacier is an artefact. Instead, the surface landforms which lead to the presence of these subglacial ridges in the IFPA topography must originate elsewhere. One explanation might be that sidewall pressure in narrow troughs leads to changes in the ice flow regime which are not captured by the assumption of ice flow in an inclined plane (Glen, 1958), but which induce ridges or velocity changes in the surface which propagate through IFPA processing.

Another feature which we observe in the IFPA topography is the presence of anomalous spurs extending from mountainous regions into fast-flowing ice streams. Two examples of this are shown in Figure 6.3c) and 6.3d), from Rutford Ice Stream and Bailey Glacier respectively. We know from high-resolution ice-penetrating radar observations (Smith et al., 2007; King et al., 2016; Diez et al., 2018) that Rutford Ice Stream and Bailey Glacier lie in glacial troughs, similar to the U-shaped valleys we see in many deglaciated landscapes. The spurs observed in IFPA must therefore originate elsewhere. The simplest explanation for these is that the assumption of uniform flow in a planar slab does not hold in this region, due to the U-shaped topography and due to the presence of shear margins at the edges of the glacial trough where the ice velocity changes significantly. Significant velocity changes in the shear margins will also invalidate the assumption of small perturbations in the linearisation.

The assumption of a uniform background state which can be approximated by flow in a planar slab is precisely why the IFPA method also does not perform well in regions with mountainous topography such as the Antarctic Peninsula. As discussed in Section 5.4.1, it is possible that the application of IPFA on grids aligned to the glacial valleys which do not include the shear margins could yield improved results. In addition, the application of non-uniform background states, as applied by Ng et al. (2018) to flowlines at Columbia Glacier and Nordenskiöld Glacier, could help to tailor the background state used in IFPA to the local bed geometry. However, methods such as mass conservation (Morlighem et al., 2010, 2020), which works well in confined troughs, are likely to give better results in regions where ice flow is steered through narrow topography. We therefore do not need to rely on IFPA in these regions.

6.3.2 Improving the Antarctic IFPA map for use in ice-sheet modelling

With the parameters currently in use, across much of Antarctica the topography maps produced by IFPA are significantly lower in amplitude than ice-penetrating radar observations show to be the reality, and in many regions the IFPA subglacial topography does not capture the full variability in amplitudes which we know is present. Here, I discuss some

ways to improve the amplitude match between IFPA and ice-penetrating radar topography, as well as some other ways to improve the IFPA methodology.

Improving the amplitude match of IFPA to radar data

Section 5.6.2 showed that the topography maps produced with IFPA do not always match the amplitude of the topography across much of Antarctica when compared to ice-penetrating radar observations. There are likely to be two main causes of this amplitude underestimate. Firstly, the IFPA method requires an average ice thickness for each patch, which leads to some smoothing of the results. Secondly, I used IFPA with a mean non-dimensional slipperiness parameter of $\bar{C} = 100$ everywhere. Since there is considerable variability in topographic character, linked to tectonic structures and geological variability (Clyne et al., 2020; Jordan et al., 2023), we can expect that there is spatial variability in the slipperiness of the ice-bed interface (Barnes et al., 2021). However, there is definitely still value in simple models, and modellers are aware that adding more tunable parameters does not always lead to better results (Wolovick et al., 2023).

In order to better match the observed amplitudes of ice-penetrating radar data, and reflect the variable geological properties of the ice-bed interface, future work using IFPA could apply a variable mean non-dimensional slipperiness parameter, $\bar{C}$, across Antarctica. The simplest way to incorporate this into the existing coding framework for IFPA would be to change $\bar{C}$ from a constant variable which is independent of the location, to being location dependent. This could be done through the introduction of a map of values which have been decided to be suitable, or if there is sufficient evidence of a link between topography and slipperiness (Muto et al., 2019b; Clyne et al., 2020), could be calculated as a function of the pre-known topography.

My work on Pine Island Glacier (Chapter 4) suggests that values of $\bar{C} = 150$ in fast-flowing tributaries and $\bar{C} = 50$ in slower moving regions may be more applicable there, but these values are not necessarily suitable for everywhere in Antarctica. Geological transitions between slippery sediment-covered, water-saturated beds and harder exposed bedrock may be abrupt or gradual, depending on whether the transition is connected to tectonic activity, or sediment transport through ice motion (Muto et al., 2019b; Clyne et al., 2020; Aitken et al., 2023; Jordan et al., 2023). Careful consideration would therefore be required to ensure that the variable values of $\bar{C}$ have some grounding in real world observations. As discussed in Chapter 4, it may also be possible to calculate suitable values of $\bar{C}$ by using the surface velocity field alongside observations of the thermal and mechanic properties of the ice. Inversions which calculate the deformation velocity (Rignot et al., 2011b) may offer an independent constraint on basal slipperiness and ice viscosity, which could reduce some of the trade-offs currently present in the IFPA results.

Another parameter within the IFPA framework which also influences the amplitudes of the topography produced is the weighting parameter, Σ_s. Due to the non-uniqueness of solutions to a least-squares problem when multiplicative factors are applied, this weighting

parameter is applied to control the balance between the sizes of the non-dimensionalised velocities and elevations. This ensures that the least-squares solution for each wavenumber combination represents both the velocities and the elevations. However, increasing Σ_s tends to decrease the amplitude of the topography (Figure 3.14), meaning that varying the magnitude of Σ_s could influence the amplitude of the topography produced by IFPA in a more global manner. Without many more high-resolution grids of topography than currently exist to tune the parameters, it is difficult to decide on the most suitable value of Σ_s.

In this thesis, and the associated published works, I have skirted around the problem of mis-matching amplitudes by stressing the important of the shapes of landforms and the locations of the local mimina and maxima outlined by IFPA. Both $\bar{C}$ and Σ_s influence the amplitude of the landforms in the IFPA topography, but they can not change the locations of those features, and it is important to remember this when interpreting the output. The IFPA map presented in Chapter 5 uses the same values of these parameters across the whole of Antarctica, and there is definite scope for improvement in the map by applying locally tuned parameters.

Integrating IFPA with ice-penetrating radar measurements

One of the great strengths of the IFPA methodology is that it does not require high-density radar observations in the region being studied, and only needs a single ice-thickness estimate for each 50 km by 50 km region. However, because the radar observations are not evenly distributed, this also means that there are regions where the resulting topography is vertically offset from the radar observations. Future iterations of the IFPA methodology could better integrate the existing ice-penetrating radar observations, producing a final topographic product which is more useful for ice-sheet modelling.

The IFPA method requires an estimate of the average ice thickness within each patch, as the transfer of variability from the bed to the ice surface depends on the ice thickness. Currently, this ice-thickness estimate comes from a 50 km smoothed version of Bedmachine Antarctica (Morlighem et al., 2020). However, now that Bedmap3 has been released (Frémand et al., 2023), it may be possible to provide an average ice thickness estimate in each region which comes directly from the ice-penetrating radar measurements, and accounts for their spatial distribution. This could help to reduce the offset between the IFPA topography and some of the radar topography, but is unlikely to eliminate it totally.

By producing different IFPA products with different values of $\bar{C}$ over Pine Island Glacier, we know that varying the parameters in IFPA can influence the amplitude of hills and valleys but not their locations. One possible approach (shown in Figure 6.4) to better fitting the existing radar observations may be to treat the output of IFPA as a flexible sheet with fixed minima and maxima, and effectively stretching or compressing this sheet to fit the radar observations. This could be done by calculating the misfit between the radar observations and the IFPA topography, and interpolating the misfit across the entire

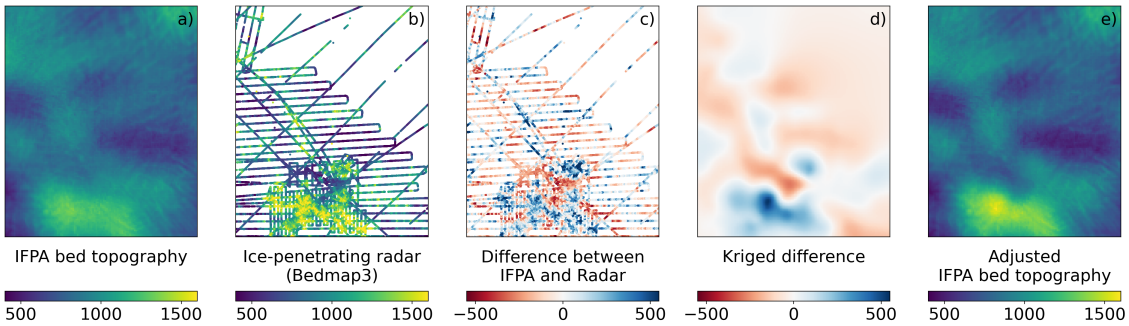

Fig. 6.4 An illustration of a potential methodology for correcting the IFPA data to better match ice-penetrating radar observations at Valkyrie Dome, in East Antarctica. Beginning with a) the IFPA subglacial topography and b) the ice-penetrating radar observations from Bedmap3 (Frémand et al., 2023) for this region, I calculate c) the difference, and use an interpolation algorithm (here ordinary kriging from the pykrige package) to calculate d) a difference field across the region. This can then be added to the IFPA topography to produce e) an adjusted IFPA subglacial topography.

domain, before subtracting the misfit from the IFPA topography. However, depending on the method used for the interpolation, this could introduce new errors into the topography. This approach reduces the misfit to the radar data, but still does not ensure that the known topography is prioritised.

The problem of interpolating between data with variable densities has been considered in depth by ocean-bathymetry mappers (Weatherall et al., 2015; Dorschel et al., 2022), who often use a remove-restore method with stacked continuous curvature splines in tension to account for topographic variability with different levels of detail (Hell and Jakobsson, 2011). A similar approach to this could be utilised while incorporating the ice-penetrating radar into the IFPA map, where the IFPA map is used as the broad scale interpolation layer, but ice-penetrating radar measurements are taken at higher resolutions.

Iterative forward modelling to better match observations

The current implementation of IFPA uses a linearised version of the full-Stokes equations, which does not always necessarily reflect the full range of the topography, and can produce solutions which are not necessarily physically plausible. Iterative forward modelling of the IFPA generated topography to better match the ice-surface velocities and elevations could help to improve the subglacial topography from IFPA.

This could be done by extending the work of Raymond and Gudmundsson (2009), and forward modelling the topography and slipperiness produced from IFPA to produce diagnostic velocities, from which the inverted topography and slipperiness could be iteratively improved.

An iterative modelling process would allow us to move away from the assumption and limitations of near linearity and could also allow us to invert for the mean non-dimensional slipperiness parameter, $\bar{C}$ alongside the variability in slipperiness. In addition to this, an

integral transform method to applying the transfer functions could be used (Ng et al., 2018; Schelpe and Gudmundsson, 2023), which would allow a spatially variable reference state.

Choice of transfer functions

IFPA is a useful technique for studying Antarctic subglacial landforms because there is a mathematical description of how the bed and the surface topography are related for ice flowing under certain conditions. In the current formulation, IFPA can be applied with this mathematical description taking the form of either full-Stokes transfer functions (Gudmundsson, 2003), or the shallow-ice-approximation transfer functions (Gudmundsson, 2008). Full-Stokes conditions use all the components of stress whereas the shallow-ice-approximation ignores longitudinal and transverse stresses as well as vertical stress gradients.

Gudmundsson (2008) showed that the shallow-ice-stream approximation underestimates the amplitude of subglacial topography for wavelengths less than about 10 ice thicknesses. My work on Pine Island Glacier (Chapter 4) shows that there is only a small difference in the results of applying these two different sets of transfer functions to datasets from the Pine Island Glacier region, and that this difference is greatest in faster flowing ice. In agreement with Gudmundsson (2008), I find that the full-Stokes transfer functions produce higher amplitude topography, and hence I use the full-Stokes transfer functions when applying IFPA to the whole of Antarctica (Chapter 5). However, because both versions of the transfer functions presented here are linear forms which ignore second order terms, they might not reflect all of the processes occurring when variability is transferred to the ice surface.

In addition, the transfer functions applied here assume that the viscosity of the ice is constant throughout the ice column (flow law constant $n = 1$), despite observations showing the this is not the case in Antarctica (Millstein et al., 2022) (n is thought to be between 3 and 4). Variability in ice viscosity across the ice column would lead to non-uniform transfer of perturbations from the ice-bed interface to the ice surface. Jóhannesson (1992) and Raymond and Gudmundsson (2005) showed that higher values of n lead to stronger surface expressions of basal features, so assuming $n =$ may lead to an overestimate of the amplitude of the bed topography. This overestimation may be partially mitigated by the choice of the mean non-dimensional slipperiness parameter $\bar{C}$, which already accounts partially for ice viscosity. It is possible that more suitable transfer functions which better represent the variability in ice conditions across the ice column could help to alleviate this. Studying the effect of basal perturbations on englacial stratigraphy may also provide an avenue to understanding the effect of variable ice viscosity on perturbation transfer, as discussed in Chapter 4.

Unfortunately, these transfer functions are almost impossible to test in their 3 dimensional form with current radar-surveys, which do not cover a wide enough area at a sufficiently high resolution, although some studies have evaluated the extent to which basal

topography can explain surface topography along flowlines (Ng et al., 2018; Igneczi et al., 2018; Crozier et al., 2018). However, if a large high-resolution 3D survey were to be made in the future, it could become possible to calculate the transfer functions for real data, and compare those to the linearised versions which have been used here. Potentially only small differences would be seen, but these could have consequences in other parts of Antarctica. Ideally this survey region would be at least 50 km by 50 km, with lower-than-ice-thickness resolution within that, which is beyond the scope of many surveys. But an increasing understanding of swath processing techniques (Paden et al., 2010; Holschuh et al., 2020; Hoffman et al., 2023) means that future surveys could cover much larger areas, and a comparison of the transfer functions may become possible on a 3D dataset.

Errors in the IFPA map

The current version of the IFPA map is not accompanied by a realistic error product. During the calculation process, as detailed in Chapter 5, I take a weighted mean of 9 overlapping patches on which IFPA has been run, and I use this as the topography value for that pixel. At the same time, I calculate a weighted standard deviation of the values from those 9 overlapping patches, and I include this standard deviation as an estimate of the internal variability between different patches. Since IFPA assumes that ice flow can be approximated by an inclined slab, but different patches have different reference slabs, this standard deviation represents the variability in reference slabs. However, it does not represent any of a whole host of other uncertainties.

As discussed in Section 4.5.2, there is significant uncertainty associated with the IFPA subglacial topography product due to the trade-off between topographic amplitude and the mean non-dimensional slipperiness parameter, $\bar{C}$. This is a spatially variable uncertainty, which is greatest at local topographic minima and maxima, and can be explored by running the IFPA model with a range of mean non-dimensional slipperiness parameter values. However, in an improved IFPA product where the amplitudes are constrained by ice-penetrating radar data, this uncertainty should be reduced. Other uncertainties due to parameter value choices may still play a role though, and so it would be important to explore some of these internal uncertainties when producing an IFPA error product. There is also internal error in the IFPA map in regions where the physical processes are not really suitable for the approximation of flow in an inclined slab, which could be accounted for by looking at the slope of the topography and maps of ice thickness.

As well as errors in the IFPA map due to flexibility in the internal processing steps, another key component of error which is not considered in the current calculation of the IFPA map is uncertainty in the input surface datasets. As the analysis in IFPA occurs in Fourier space, I am less concerned about white noise, which has an equal power spectrum across all wavelengths and is relatively easy to identify and remove during processing, and more concerned about Brownian or red noise, which has a more similar power spectrum to topography and is therefore harder to identify. This means that there is not a clear

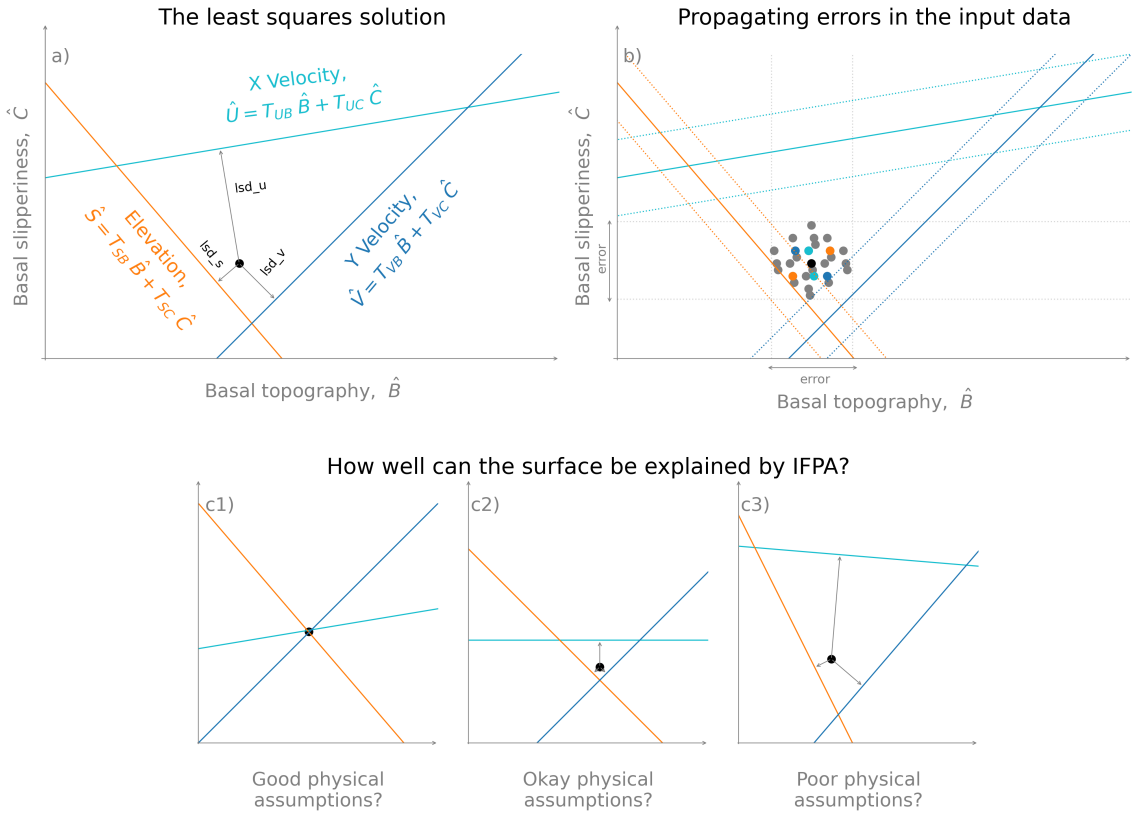

Fig. 6.5 A schematic exploration of different ways to consider errors in the IFPA method through the least squares formulation. a) shows the least squares distances (lsd_s, lsd_u, lsd_v) which are minimised by the least squares solution to calculate $\hat{B}$ and $\hat{C}$. b) shows how errors in the surface data can be propagated to give errors in $\hat{B}$ and $\hat{C}$. c) illustrates how mismatches between the different surface data components can be quantified as a measure of uncertainty from the IFPA equations.

relationship between errors in the ice-surface datasets and in the subglacial topography. In order to calculate the error in the IFPA map caused by errors in the surface data, I therefore propose using a Monte Carlo approach. A set of surface topographies which fall within the error distribution specified should be generated, ideally including some with spatially correlated errors and then the IFPA model will be run for each of these surface datasets. This will generate a range of topographies, from which error bounds can be calculated for the chosen topography. This is likely to be computationally expensive, so may not be practical across all of Antarctica, but some test cases may reveal patterns which can then be applied elsewhere.

Error quantification through the least squares approach

An alternative approach to calculating the errors in the IFPA map is to use the weighted least squares solution (Figure 6.5a). If linear perturbation analysis fully encapsulates all the ice processes then the distances minimised by the least squares solution should be zero (Figure 6.5c1). In regions where the physical assumptions made in the IFPA method are

less representative of the real physics, the sum of the minimised least squares distances will be greater. Additionally, because the least squares analysis is carried out individually for each wavelength, this would allow a quantification of the wavelengths at which other ice processes are occurring. The weighted least squares solution also offers an avenue for propagating errors in the input surface observations to the output bed conditions. Figure 6.5b illustrates the impact that uncertainty in the input surface conditions can have on the minimisation of the least squares distances. However, as the least squares analysis takes place in Fourier space, care would need to be taken when attributing the uncertainty in the surface data to specific wavelengths, and when recombining the uncertainties in the basal components in the spatial domain.

6.3.3 Applications of an improved IFPA topography map

The IFPA topography map presented in Chapter 5 provides an alternative approach to looking at topographic variability across Antarctica in a way which is not reliant on the density of ice-penetrating radar observations. If the problems with the amplitude match to the overlying topography were tackled, this method could produce maps with a variety of uses, including for ice-sheet modelling, and studying basal slipperiness and hydrology across Antarctica.

Modelling future ice-sheet behaviour

Numerical models of future ice-sheet behaviour need high-resolution observations of the subglacial topography to constrain projections of future sea-level rise to levels useful for policy making (Durand et al., 2011; Sun et al., 2014; Seroussi et al., 2017; Nias et al., 2018; Koellner et al., 2019). Since the spacing between radar surveys (Frémand et al., 2023) is much greater than the 1-2 km resolution required by ice-sheet models (McCormack et al., 2018; Castleman et al., 2022), several studies have used the errors in interpolated maps of subglacial topography (Fretwell et al., 2013; Morlighem et al., 2020) to generate statistically plausible beds which can be used in ice-sheet modelling (Sun et al., 2014; MacKie and Schroeder, 2020). However, the errors accompanying some topographic products are likely to be too small. For example, in the region of Thwaites Glacier discussed in Section 6.2 Bedmachine Antarctica has relatively high density observations, and quotes an error ranging between $\pm$30 m (their minimum) and $\pm$40 m depending on the proximity to a survey line. However, as shown in Figure 6.6, the ice-penetrating radar observations do not fall within these error bounds over 73% of this region, suggesting that models which use these observations to generate statistically plausible beds (MacKie and Schroeder, 2020; Leong and Horgan, 2020) may still be underestimating the variability in the topography underneath Antarctica.

It would be valuable to see how much influence an IFPA map which incorporates ice-penetrating radar observations has on numerical simulations of the future behaviour of

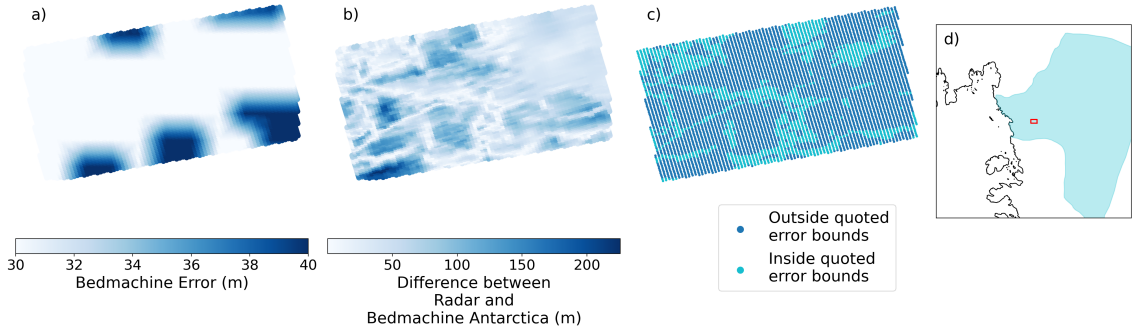

Fig. 6.6 A comparison of a) the quoted error bounds for Bedmachine Antarctica and b) the difference between Bedmachine Antarctica and the ice-penetrating radar observations for a small region in the downstream part of Thwaites Glacier, West Antarctica. Panel c) shows where the ice-penetrating radar values fall within the error bounds of Bedmachine Antarctica, with the location of this region is shown in red in panel d), with the outline of Thwaites Glacier in light blue.

the overlying Antarctic ice sheets. This could be achieved with a few simple runs of this new topography and older topographic maps, or a more complicated set up with a range of possible beds, generated with Monte Carlo simulations. Computationally, it would be sensible to focus on a select few glacier catchments rather than the whole of Antarctica, but if chosen carefully it would be possible to explore a range of different environments to see how much difference this topographic map makes on long term predictions.

Ice-sheet topography around the margins of Antarctica is thought to be the most critical for defining the glaciological response to ocean forcing (Gladstone et al., 2012; Pattyn et al., 2013; Nias et al., 2018), and IFPA is not designed for studying topography in those regions. However, the topography of the interior sectors becomes more important over longer timescales, and interior topography can have significant impacts on the retreat rate, particularly in regions where the basal sliding law is connected to the topographic variability (Parizek et al., 2013; Koellner et al., 2019; Schwans et al., 2023). This may be particularly important in sectors of East Antarctica which are currently thought to be in mass balance but are predicted to see increasing retreat in the future (Stokes et al., 2022), and which have not been the targets of intensive geophysical surveying.

Bed slipperiness

Many ice-sheet models assume fixed topography and invert for the slipperiness (Arthern and Gudmundsson, 2010; Arthern et al., 2015; Kyrke-Smith et al., 2018), although there are some which invert for both together (Pralong and Gudmundsson, 2011; Barnes and Gudmundsson, 2022). The theoretical framework set out by Gudmundsson (2003) and Gudmundsson (2008) shows that variability in subglacial topography and variability in the bed slipperiness should have different, and distinguishable, effects on the ice-surface elevation and velocity. In theory, IFPA should be able to distinguish between changes in the ice-surface stress field caused by topography, and those caused by slipperiness. Due

to the trade-off between the amplitude of basal landforms and the mean non-dimensional slipperiness parameter, $\bar{C}$, I have tended to focus more on the shapes of landforms rather than on their amplitudes, and not put much emphasis on the slipperiness results from the IFPA process. If, however, steps are taken to improve the amplitude of landforms by tuning the model parameters with ice-penetrating radar observations, the slipperiness map produced by IFPA may also be more useful for ice-sheet modelling.

Hydrology

The flow of water beneath ice sheets is controlled by the subglacial hydrological pressure gradient, which depends on both the ice-surface slope and the subglacial topography slope (Shreve, 1972). Ice-surface slope is 10 times as important, but variability in the subglacial topography can be more than 10 times larger than variability in the ice surface, so both can influence water routing pathways. Small changes in either the ice surface or the subglacial topography can influence the hydrological routing beneath the ice sheets, leading to larger phenomena such as piracy-induced stagnation (Anandakrishnan and Alley, 1997; Vaughan et al., 2008). Wright et al. (2008) explored the sensitivity of sub-Antarctic flow paths to changes in the ice surface, concluding that changes in the surface height of just 5 m (or equivalently 50 m in the ice thickness) could have substantial influence on the routing of water through large subglacial lakes in East Antarctica.

Some of the new landforms in the IFPA topography map have amplitudes of more than 50 m, and so could be expected to have an influence on the routing of subglacial water. In particular, small changes along the boundaries of subglacial hydrological catchments could change the direction in which water flows. Wright et al. (2008) discussed the importance of this for understanding water flow through subglacial lakes in the Adventure Trench region of east Antarctica, but the routing of subglacial water is also important through its influence on bed properties (Rémy and Legresy, 2004; Ashmore and Bingham, 2014). It would be informative to apply a hydrological routing algorithm to an amplitude corrected version of the IFPA topography, and to see how much difference this makes to subglacial water routing across Antarctica when compared to other subglacial topography datasets. This could also provide guidance for ice-penetrating radar surveying as to which regions are most important for understanding subglacial water flow paths.

6.3.4 Applying IFPA to other datasets

We can learn a great deal about Antarctic subglacial topography by applying the IFPA method to continent wide datasets. Here I discuss potential applications for a range of different Antarctic datasets, as well as the possibility of applying IFPA in Greenland.

Time variant IFPA topography

When applying IFPA in Antarctica, I have assumed that the ice sheets are in steady state despite knowing that this is not the case, particularly in West Antarctica (Smith et al., 2020; Otosaka et al., 2022). The steady state assumption means that I interpret all surface landforms as the result of current subglacial topography. Most ice-sheet models assume fixed subglacial topography on short term timescales (Barnes and Gudmundsson, 2022), with variations in topography only being considered on long timescales through Glacial Isostatic Adjustment (Adhikari et al., 2014; Larour et al., 2019). However, geophysical observations from Rutford Ice Stream (Smith et al., 2007; King et al., 2009; Smith et al., 2012) show that there is significant sediment movement beneath Antarctic ice streams, and on relatively short timescales.

Although the changes observed at Rutford Ice Stream are too small in their amplitude and width to influence the ice flow enough to have an imprint on the ice surface, it is possible that other places in Antarctica have witnessed larger scale sediment movement which would have an impact on the ice surface. To look at subglacial topography across the whole of Antarctica, I used elevation and velocity products that had been built up from multi-year observations in order to cover the entire continent (Gardner et al., 2018; Howat et al., 2019; Dong et al., 2022). However, to look at variations in topography, it would be necessary to use time-stamped elevation and velocity products with the largest time gap possible. In order to have the correct surface datasets, this analysis would need to be done on a regional rather than continental scale, but could yield insightful results.

In theory, basal topography perturbations and basal slipperiness perturbations have different impacts on the surface elevation and velocity fields, and it is possible to distinguish between the two. However, the work in this thesis shows that due to the lack of knowledge when deciding on the mean non-dimensional slipperiness parameter $\bar{C}$, there is still some trade off in these parameters. When looking at changes occurring between datasets from different years, it would therefore be important to account for the impact of changes in the slipperiness due to changes in basal hydrology or rheology, which are likely to change on much shorter time scales than topography. Ideally, an independent technique for determining $\bar{C}$ could be used to remove this trade off and avoid a situation where changes in the ice surface are falsely attributed solely to changes in the bed topography.

Identifying artefacts

In some regions of the Antarctic-wide IFPA topography map, there are artefacts in the topography produced by features in the ice-surface datasets. Running the analysis again, but with a different set of velocity and elevation products would also allow some of these artefacts to be identified, although not all. Megadunes in the ice surface across much of central East Antarctica (Frezzotti et al., 2002), for example, are real surface features which should be present in all ice-surface elevation products, but which lead to unrealistic

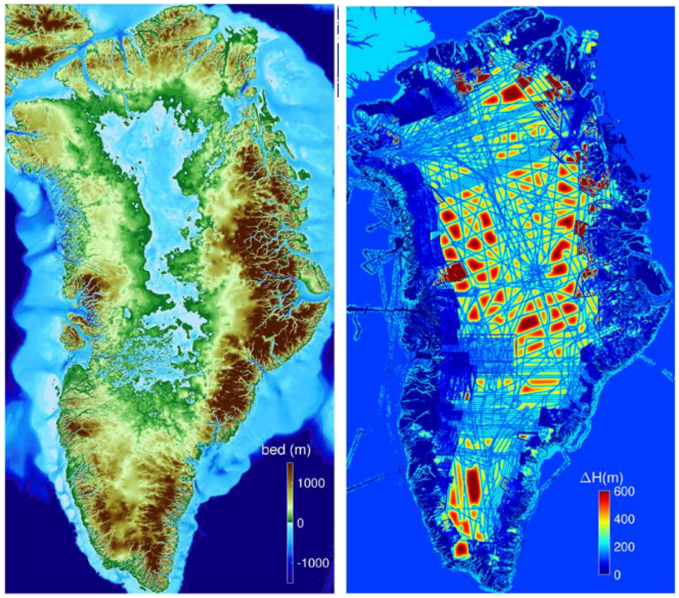

Fig. 6.7 The subglacial topography beneath the Greenland Ice Sheet, and associated error. Figure adapted from the user guide for Bedmachine Greenland v5 (released in 2023, updated from Morlighem et al., 2017).

subglacial topography. However, other artefacts are caused by gaps in satellite tracks or produced during processing of satellite data, and these features could be identified using different surface products.

Greenland

Observations of the thickness of the Greenland Ice Sheet have been made primarily using airborne ice-penetrating radar, leading to the production of several digital elevation models of subglacial topography (Bamber et al., 2013a; Morlighem et al., 2014, 2017). Although there are now a substantial number of ice-penetrating radar observations across Greenland, there are still significant gaps between these observations in the interior parts of Greenland, with survey efforts focussed around the margins and at ice core drilling sites (Paden et al., 2010; Franke et al., 2020).

However, studies comparing subglacial topography from ice-penetrating radar and the ice-surface topography from Arctic DEM (Ekholm et al., 1998; Cooper et al., 2019a) show that, as in Antarctica, the variability at the bed bears a clear resemblance to the variability in the ice surface. These studies have mainly focussed on qualitative assessment of the features in the subglacial topography, but Ng et al. (2018) used a modified version of the same full-Stokes transfer functions applied in IFPA (Gudmundsson, 2003, Chapter 4 to look at topographic variability along flowlines from Nordenskiöld Glacier in western Greenland, concluding that some, but not all, of the surface variability originates from the basal topography. Igneczi et al. (2018) used a similar method to explore how much of the surface relief comes from the subglacial topography.

Given the success of the IFPA methodology in uncovering new topographic landforms in Antarctica, there is significant potential to apply the IFPA methodology to data from the Greenland Ice Sheet. Gaps between ice-penetrating radar surveys can be as large as 75km (Morlighem et al., 2017), and there are likely to be interesting features that have not yet been explored in these regions.

Chapter 7

Conclusions

This thesis aimed to explore ways in which variability in the surface topography of the Antarctic Ice Sheet can help us to learn about the conditions at the ice-bed interface, and in particular the subglacial topography. I had three key research objectives for this thesis (Repeated here from Section 2.6):

- **Thesis Objective 1 (Feasibility):** To assess whether inverse methods based on the spectral properties of modern satellite datasets can be utilised to study the ice-bed interface, through comparison with high-resolution ice-penetrating radar surveys.
- **Thesis Objective 2 (Utility):** To assess whether inverse methods based on the spectral properties of modern satellite datasets perform better than other methods for studying the ice-bed interface in regions without high-resolution ice-penetrating radar surveys.
- **Thesis Objective 3 (Extendibility)** To assess what inverse methods based on the spectral properties of modern satellite datasets can tell us about the ice-bed interface for the whole Antarctic continent, especially in areas with low density of geophysical survey data.

The key research findings are as follows:

Linear perturbation theory can be utilised to study the ice-bed interface

Through a combination of synthetic experiments and application of linear perturbation theory to data from Thwaites Glacier in West Antarctica, this thesis shows that linear perturbation theory can be utilised to study the ice-bed interface. Synthetic experiments showed the range of landforms which can be resolved by this methodology, and also explore the effect of noise in the surface datasets. Application of linear perturbation theory to data from Thwaites Glacier in West Antarctica confirmed that the method works on real as well as synthetic data, and allowed the tuning of several important model parameters to ensure that the best possible results were obtained.

Having established that linear perturbation theory can be utilised to study the ice-bed interface, I improved the methodology to be applied in all areas regardless of the ice flow direction. I named this updated methodology Ice Flow Perturbation Analysis (IFPA).

Ice Flow Perturbation Analysis does perform better than other methods for studying the ice-bed interface in regions without high-resolution radar surveys

High-resolution ice-penetrating radar surveys had been collected at Pine Island Glacier, and were not included in early compilations of radar data used in other subglacial topography maps. These surveys therefore provided the perfect test data for IFPA and streamline diffusion, the method used in Bedmachine Antarctica for interior regions. Comparison of the results of IFPA over Pine Island Glacier revealed that the IFPA topography contains landforms which are not included in interpolated products.

The application of IFPA across Pine Island Glacier highlighted the trade-off between the mean non-dimensional slipperiness parameter and the amplitude of landforms in the IFPA topography, and explored how we can learn about the slipperiness by tuning the topography from IFPA to ice-penetrating radar observations in regions where they exist. I emphasised reducing this trade-off as a key future improvement of the IFPA methodology. However, even in current formulation the shapes and locations of landforms are fixed, and can tell us a lot about the mesoscale variability in subglacial topography beneath the polar ice sheets.

Ice Flow Perturbation Analysis tell us a lot about the ice-bed interface for the whole Antarctic continent

In the final section of this thesis, I applied IFPA across the whole of Antarctica to fill in many of the gaps between ice-penetrating radar surveys for the first time. The resulting map of subglacial topography shows many interesting features, such as an extensive subglacial canyon in Maud Subglacial Basin, expands our knowledge of the extent of several mountain ranges, and includes nearly 40,000 new hills with 50m prominence or greater. It also enhances our understanding of the geometry of many features which had been partially but not fully observed in ice-penetrating radar surveys.

Different types of topography in the IFPA map have very distinctive textures, and I used these to classify the new topography into different geomorphological categories. The new geomorphological map showed that the subglacial topography of Antarctica is much rougher than previously thought in many regions, and also highlights the presence of large sediment-filled basins in East Antarctica.

Future directions

The new IFPA topography map produced in this thesis showcases the potential for using variability in the surface topography of the Antarctic Ice Sheet to learn about subglacial

topography. Future improvements in ice-penetrating radar observations, and in satellite datasets mean that there should be ample opportunities to improve and test subglacial topography maps produced through IFPA. In particular the ability to tune the amplitude of topography with radar observations will make the topography maps significantly more useful for modelling future ice-sheet behaviour and looking at distributions of subglacial sediment and subglacial hydrology, leading to better predictions of sea-level rise, as required by policy makers.

Chapter 8

References

Adhikari, S., Ivins, E. R., Larour, E., Seroussi, H., Morlighem, M., and Nowicki, S. (2014). Future Antarctic bed topography and its implications for ice-sheet dynamics. *Solid Earth*, 5(1):569–584.

Aitken, A. R. A., Li, L., Kulessa, B., Schroeder, D., Jordan, T. A., Whittaker, J. M., Anandakrishnan, S., Dawson, E. J., Wiens, D. A., Eisen, O., and Siegert, M. J. (2023). Antarctic sedimentary basins and their influence on ice-sheet dynamics. *Reviews of Geophysics*, 61(3):e2021RG000767.

Aitken, A. R. A., Young, D., Ferraccioli, F., Betts, P. G., Greenbaum, J. S., Richter, T. G., Roberts, J. L., Blankenship, D. D., and Siegert, M. J. (2014). The subglacial geology of Wilkes Land, East Antarctica. *Geophysical Research Letters*, 41(7):2390–2400.

Alley, R., Holschuh, N., MacAyeal, D., Parizek, B., Zoet, L., Riverman, K., Muto, A., Christianson, K., Clyne, E., Anandakrishnan, S., et al. (2021). Bedforms of Thwaites Glacier, West Antarctica: character and origin. *Journal of Geophysical Research: Earth Surface*, 126(12):e2021JF006339.

An, M., Wiens, D. A., Zhao, Y., Feng, M., Nyblade, A., Kanao, M., Li, Y., Maggi, A., and Lévêque, J.-J. (2015). Temperature, lithosphere-asthenosphere boundary, and heat flux beneath the Antarctic Plate inferred from seismic velocities. *Journal of Geophysical Research: Solid Earth*, 120(12):8720–8742.

Anandakrishnan, S. and Alley, R. B. (1997). Stagnation of Ice Stream C, West Antarctica by water piracy. *Geophysical Research Letters*, 24(3):265–268.

Arnold, E., Leuschen, C., Rodriguez-Morales, F., Li, J., Paden, J., Hale, R., and Keshmiri, S. (2020). CReSIS airborne radars and platforms for ice and snow sounding. *Annals of Glaciology*, 61(81):58–67.

Arthern, R. J. and Gudmundsson, G. H. (2010). Initialization of ice-sheet forecasts viewed as an inverse Robin problem. *Journal of Glaciology*, 56(197):527–533.

Arthern, R. J., Hindmarsh, R. C., and Williams, C. R. (2015). Flow speed within the Antarctic Ice Sheet and its controls inferred from satellite observations. *Journal of Geophysical Research: Earth Surface*, 120(7):1171–1188.

Ashmore, D. W. and Bingham, R. G. (2014). Antarctic subglacial hydrology: current knowledge and future challenges. *Antarctic Science*, 26(6):758–773.

Balise, M. J. and Raymond, C. F. (1985). Transfer of basal sliding variations to the surface of a linearly viscous glacier. *Journal of Glaciology*, 31(109):308–318.

Bamber, J. L., Ferraccioli, F., Joughin, I., Shepherd, T., Rippin, D. M., Siegert, M. J., and Vaughan, D. G. (2006). East Antarctic ice-stream tributary underlain by major sedimentary basin. *Geology*, 34(1):33–36.

Bamber, J. L., Gomez-Dans, J. L., and Griggs, J. A. (2009). A new 1 km digital elevation model of the Antarctic derived from combined satellite radar and laser data - Part 1: Data and methods. *The Cryosphere*, 3(1):101–111.

Bamber, J. L., Griggs, J., Hurkmans, R., Dowdeswell, J., Gogineni, S., Howat, I., Mouginot, J., Paden, J., Palmer, S., Rignot, E., et al. (2013a). A new bed-elevation dataset for Greenland. *The Cryosphere*, 7(2):499–510.

Bamber, J. L., Siegert, M. J., Griggs, J. A., Marshall, S. J., and Spada, G. (2013b). Paleofluvial mega-canyon beneath the central Greenland Ice Sheet. *Science*, 341(6149):997–999.

Baranov, A. and Morelli, A. (2013). The Moho depth map of the Antarctica region. *Tectonophysics*, 609:299–313.

Baranov, A., Morelli, A., and Chuvaev, A. (2021). ANTASed–an updated sediment model for Antarctica. *Frontiers in Earth Science*, 9:722699.

Barnes, J. M., Dias Dos Santos, T., Goldberg, D., Hilmar Gudmundsson, G., Morlighem, M., and De Rydt, J. (2021). The transferability of adjoint inversion products between different ice-flow models. *The Cryosphere*, 15(4):1975–2000.

Barnes, J. M. and Gudmundsson, G. H. (2022). The predictive power of ice-sheet models and the regional sensitivity of ice loss to basal sliding parameterisations: a case study of Pine Island and Thwaites glaciers, West Antarctica. *The Cryosphere*, 16(10):4291–4304.

Begeman, C. B., Tulaczyk, S. M., and Fisher, A. T. (2017). Spatially variable geothermal heat flux in West Antarctica: Evidence and implications. *Geophysical Research Letters*, 44(19):9823–9832.

Bell, R. E., Studinger, M., Shuman, C. A., Fahnestock, M. A., and Joughin, I. (2007). Large subglacial lakes in East Antarctica at the onset of fast-flowing ice streams. *Nature*, 445(7130):904–907.

Bentley, C. R. (1974). Crustal structure of Antarctica. In *Developments in Geotectonics*, volume 8, pages 229–240. Elsevier.

Berliner, L., Jezek, K., Cressie, N., Kim, Y., Lam, C., and van der Veen, C. (2008). Modeling dynamic controls on ice streams: a Bayesian statistical approach. *Journal of Glaciology*, 54(187):705 – 714.

Bingham, R. G. and Siegert, M. J. (2007). Radio-echo sounding over polar ice masses. *Journal of Environmental & Engineering Geophysics*, 12(1):47–62.

Bingham, R. G., Vaughan, D. G., King, E. C., Davies, D., Cornford, S. L., Smith, A. M., Arthern, R. J., Brisbourne, A. M., De Rydt, J., Graham, A. G., Spagnolo, M., Marsh, O. J., and Shean, D. E. (2017). Diverse landscapes beneath Pine Island Glacier influence ice flow. *Nature Communications*, 8:1618.

Brisbourne, A. M., Smith, A. M., Vaughan, D. G., King, E. C., Davies, D., Bingham, R. G., Smith, E. C., Nias, I. J., and Rosier, S. H. R. (2017). Bed conditions of Pine Island Glacier, West Antarctica. *Journal of Geophysical Research: Earth Surface*, 122:419–433.

Brondex, J., Gillet-Chaulet, F., and Gagliardini, O. (2019). Sensitivity of centennial mass loss projections of the Amundsen Basin to the friction law. *The Cryosphere*, 13(1):177–195.

Budd, W. (1970). Ice flow Over bedrock perturbations. *Journal of Glaciology*, 9(55):29–48.

Bueler, E. and Brown, J. (2009). Shallow shelf approximation as a "sliding law" in a thermomechanically coupled ice-sheet model. *Journal of Geophysical Research: Earth Surface*, 114.

Burton-Johnson, A., Dziadek, R., and Martin, C. (2020). Geothermal heat flow in Antarctica: current and future directions. *The Cryosphere*, 14(11):3843–3873.

Cai, Y., Wan, F., Lang, S., Cui, X., and Yao, Z. (2023a). Multi-branch deep neural network for bed topography of Antarctica super-resolution: reasonable integration of multiple remote sensing data. *Remote Sensing*, 15(5):1359.

Cai, Y., Yao, Z., Lang, S., Cui, X., Wan, F., and He, Y. (2023b). Generative elevation inpainting: an efficient completion method for generating high-resolution Antarctic bed topography. *IEEE Transactions on Geoscience and Remote Sensing*.

Carter, S. and Fricker, H. (2012). The supply of subglacial meltwater to the grounding line of the Siple Coast, West Antarctica. *Annals of Glaciology*, 53(60):267–280.

Castleman, B. A., Schlegel, N.-J., Caron, L., Larour, E., and Khazendar, A. (2022). Derivation of bedrock topography measurement requirements for the reduction of uncertainty in ice-sheet model projections of Thwaites Glacier. *The Cryosphere*, 16(3):761–778.

Christoffersen, P., Bougamont, M., Carter, S. P., Fricker, H. A., and Tulaczyk, S. (2014). Significant groundwater contribution to Antarctic ice streams hydrologic budget. *Geophysical Research Letters*, 41(6):2003–2010.

Chu, W. (2022). Groundwater under Antarctica goes deep. *Science*, 376(6593):577–578.

Clark, C. D. (1993). Mega-Scale Glacial Lineations and cross-cutting ice-low landforms. *Earth Surface Processes and Landforms*, 18:1–29.

Clow, G. D., Cuffey, K. M., Waddington, E. D., Clow, G. D., Cuffey, K. M., and Waddington, E. D. (2012). High heat-flow beneath the central portion of the West Antarctic Ice Sheet. *American Geophysical Union, Fall Meeting Abstracts*, 2012:C31A–0577.

Clyne, E. R., Anandakrishnan, S., Muto, A., Alley, R. B., and Voigt, D. E. (2020). Interpretation of topography and bed properties beneath Thwaites Glacier, West Antarctica using seismic reflection methods. *Earth and Planetary Science Letters*, 550:116543.

Colleoni, F., De Santis, L., Siddoway, C. S., Bergamasco, A., Golledge, N. R., Lohmann, G., Passchier, S., and Siegert, M. J. (2018). Spatio-temporal variability of processes across Antarctic ice-bed–ocean interfaces. *Nature Communications*, 9(1):2289.

Cooper, M. A., Jordan, T. M., Schroeder, D. M., Siegert, M. J., Williams, C. N., and Bamber, J. L. (2019a). Subglacial roughness of the Greenland Ice Sheet: relationship with contemporary ice velocity and geology. *The Cryosphere*, 13(11):3093–3115.

Cooper, M. A., Jordan, T. M., Siegert, M. J., and Bamber, J. L. (2019b). Surface Expression of Basal and Englacial Features, Properties, and Processes of the Greenland Ice Sheet. *Geophysical Research Letters*, 46(2):783–793.

Cornford, S. L., Martin, D. F., Graves, D. T., Ranken, D. F., Le Brocq, A. M., Gladstone, R. M., Payne, A. J., Ng, E. G., and Lipscomb, W. H. (2013). Adaptive mesh, finite volume modeling of marine ice sheets. *Journal of Computational Physics*, 232(1):529–549.

Cornford, S. L., Martin, D. F., Payne, A. J., Ng, E. G., Le Brocq, A. M., Gladstone, R. M., Edwards, T. L., Shannon, S. R., Agosta, C., van den Broeke, M. R., Hellmer, H. H., Krinner, G., Ligtenberg, S. R. M., Timmermann, R., and Vaughan, D. G. (2015). Century-scale simulations of the response of the West Antarctic Ice Sheet to a warming climate. *The Cryosphere*, 9(4):1579–1600.

Cornford, S. L., Seroussi, H., Asay-Davis, X. S., Gudmundsson, G. H., Arthern, R., Borstad, C., Christmann, J., Dias dos Santos, T., Feldmann, J., Goldberg, D., et al. (2020). Results of the third marine ice sheet model intercomparison project (MISMIP+). *The Cryosphere*, 14(7):2283–2301.

Cox, S. C., Smith Lyttle, B., Elkind, S., Smith Siddoway, C., Morin, P., Capponi, G., Abu-Alam, T., Ballinger, M., Bamber, L., Kitchener, B., et al. (2023). A continent-wide detailed geological map dataset of Antarctica. *Scientific Data*, 10(1):250.

Craddock, C. (1982). Geologic map of Antarctica. *AAPG Bulletin*, 66(7):962–963.

Crozier, J., Karlstrom, L., and Yang, K. (2018). Basal control of supraglacial meltwater catchments on the Greenland Ice Sheet. *The Cryosphere*, 12(10):3383–3407.

Cui, X., Greenbaum, J. S., Lang, S., Zhao, X., Li, L., Guo, J., and Sun, B. (2020a). The scientific operations of Snow Eagle 601 in Antarctica in the past five austral seasons. *Remote Sensing*, 12(18):2994.

Cui, X., Jeofry, H., Greenbaum, J. S., Guo, J., Li, L., Lindzey, L. E., Habbal, F. A., Wei, W., Young, D. A., Ross, N., et al. (2020b). Bed topography of Princess Elizabeth Land in East Antarctica. *Earth System Science Data*, 12(4):2765–2774.

Dahl-Jensen, D., Morgan, V. I., and Elcheikh, A. (1999). Monte Carlo inverse modelling of the Law Dome (Antarctica) temperature profile. *Annals of Glaciology*, 29:145–150.

Dalziel, I. W. and Elliot, D. H. (1982). West Antarctica: problem child of Gondwanaland. *Tectonics*, 1(1):3–19.

Damiani, T. M., Jordan, T. A., Ferraccioli, F., Young, D. A., and Blankenship, D. D. (2014). Variable crustal thickness beneath Thwaites Glacier revealed from airborne gravimetry, possible implications for geothermal heat flux in West Antarctica. *Earth and Planetary Science Letters*, 407:109–122.

Davies, D., Bingham, R. G., King, E. C., Smith, A. M., Brisbourne, A. M., Spagnolo, M., Graham, A. G., Hogg, A. E., and Vaughan, D. G. (2018). How dynamic are ice-stream beds? *The Cryosphere*, 12(5):1615–1628.

De Boer, B., Dolan, A. M., Bernales, J., Gasson, E., Goelzer, H., Golledge, N. R., Sutter, J., Huybrechts, P., Lohmann, G., Rogozhina, I., et al. (2015). Simulating the Antarctic Ice Sheet in the late-Pliocene warm period: PLISMIP-ANT, an ice-sheet model intercomparison project. *The Cryosphere*, 9(3):881–903.

De Rydt, J., Gudmundsson, G. H., Corr, H. F. J., and Christoffersen, P. (2013). Surface undulations of Antarctic ice streams tightly controlled by bedrock topography. *The Cryosphere*, 7(2):407–417.

De Rydt, J., Reese, R., Paolo, F. S., and Gudmundsson, G. H. (2021). Drivers of Pine Island Glacier speed-up between 1996 and 2016. *The Cryosphere*, 15(1):113–132.

DeConto, R. M. and Pollard, D. (2016). Contribution of Antarctica to past and future sea-level rise. *Nature*, 531(7596):591–597.

Diehl, T. M. (2008). Gravity analyses for the crustal structure and subglacial geology of West Antarctica, particularly beneath Thwaites Glacier. *ProQuest Dissertations Publishing*, 1(3341981).

Diehl, T. M., Holt, J. W., Blankenship, D. D., Young, D. A., Jordan, T. A., and Ferraccioli, F. (2008). First airborne gravity results over the Thwaites Glacier catchment, West Antarctica. *Geochemistry, Geophysics, Geosystems*, 9(1):Q04011.

Diez, A., Matsuoka, K., Ferraccioli, F., Jordan, T. A., Corr, H. F., Kohler, J., Olesen, A. V., and Forsberg, R. (2018). Basal settings control fast ice flow in the Recovery/Slessor/Bailey Region, East Antarctica. *Geophysical Research Letters*, 45(6):2706–2715.

Diez, A., Matsuoka, K., Jordan, T. A., Kohler, J., Ferraccioli, F., Corr, H. F., Olesen, A. V., Forsberg, R., and Casal, T. G. (2019). Patchy lakes and topographic origin for fast flow in the Recovery Glacier system, East Antarctica. *Journal of Geophysical Research: Earth Surface*, 124(2):287–304.

Docquier, D., Pollard, D., and Pattyn, F. (2014). Thwaites Glacier grounding-line retreat: Influence of width and buttressing parameterizations. *Journal of Glaciology*, 60(220):305–313.

Dong, Y., Zhao, J., Li, C., and Liao, M. (2022). Gapless-REMA100: A gapless 100-m reference elevation model of Antarctica with voids filled by multi-source DEMs. *ISPRS Journal of Photogrammetry and Remote Sensing*, 186:70–82.

Dorschel, B., Hehemann, L., Viquerat, S., Warnke, F., Dreutter, S., Tenberge, Y. S., Accettella, D., An, L., Barrios, F., Bazhenova, E., et al. (2022). The international bathymetric chart of the Southern Ocean version 2. *Scientific Data*, 9(1):275.

Dow, C., McCormack, F., Young, D., Greenbaum, J., Roberts, J., and Blankenship, D. (2020). Totten Glacier subglacial hydrology determined from geophysics and modeling. *Earth and Planetary Science Letters*, 531:115961.

Dowdeswell, J. A. and Evans, S. (2004). Investigations of the form and flow of ice sheets and glaciers using radio-echo sounding. *Reports on Progress in Physics*, 67(10):1821–1861.

Drewry, D., Jordan, S., and Jankowski, E. (1982). Measured properties of the Antarctic Ice Sheet: surface configuration, ice thickness, volume and bedrock characteristics. *Annals of Glaciology*, 3:83–91.

Dunham, C. K., O'Donnell, J. P., Stuart, G. W., Brisbourne, A. M., Rost, S., Jordan, T. A., Nyblade, A. A., Wiens, D. A., and Aster, R. C. (2020). A joint inversion of receiver function and Rayleigh wave phase velocity dispersion data to estimate crustal structure in West Antarctica. *Geophysical Journal International*, 223(3):1644–1657.

Durand, G., Gagliardini, O., Favier, L., Zwinger, T., and le Meur, E. (2011). Impact of bedrock description on modeling ice-sheet dynamics. *Geophysical Research Letters*, 38(20):L20501.

Durand, G., Gagliardini, O., Zwinger, T., Le Meur, E., and Hindmarsh, R. C. (2009). Full Stokes modeling of marine ice sheets: influence of the grid size. *Annals of Glaciology*, 50(52):109–114.

Edwards, T. L., Brandon, M. A., Durand, G., Edwards, N. R., Golledge, N. R., Holden, P. B., Nias, I. J., Payne, A. J., Ritz, C., and Wernecke, A. (2019). Revisiting Antarctic ice loss due to marine ice-cliff instability. *Nature*, 566(7742):58–64.

Edwards, T. L., Nowicki, S., Marzeion, B., Hock, R., Goelzer, H., Seroussi, H., Jourdain, N. C., Slater, D. A., Turner, F. E., Smith, C. J., et al. (2021). Projected land ice contributions to twenty-first-century sea level rise. *Nature*, 593(7857):74–82.

Eisen, O., Winter, A., Steinhage, D., Kleiner, T., and Humbert, A. (2020). Basal roughness of the East Antarctic Ice Sheet in relation to flow speed and basal thermal state. *Annals of Glaciology*, 61(81):162–175.

Ekholm, S., Keller, K., Bamber, J. L., and Gogineni, S. P. (1998). Unusual surface morphology from digital elevation models of the Greenland Ice Sheet. *Geophysical Research Letters*, 25(19):3623–3626.

Engelhardt, H. (2004). Ice temperature and high geothermal flux at Siple Dome, West Antarctica, from borehole measurements. *Journal of Glaciology*, 50(169):251–256.

Evans, S. and Robin, G. d. (1966). Glacier depth-sounding from the air. *Nature*, 210(5039):883–885.

Favier, L., Durand, G., Cornford, S. L., Gudmundsson, G. H., Gagliardini, O., Gillet-Chaulet, F., Zwinger, T., Payne, A. J., and Le Brocq, A. M. (2014). Retreat of Pine Island Glacier controlled by marine ice-sheet instability. *Nature Climate Change*, 4(2):117–121.

Ferraccioli, F., Coren, F., Bozzo, E., Zanolla, C., Gandolfi, S., Tabacco, I., and Frezzotti, M. (2001). Rifted (?) crust at the East Antarctic Craton margin: gravity and magnetic interpretation along a traverse across the Wilkes Subglacial Basin region. *Earth and Planetary Science Letters*, 192(3):407–421.

Ferraccioli, F., Finn, C. A., Jordan, T. A., Bell, R. E., Anderson, L. M., and Damaske, D. (2011). East Antarctic rifting triggers uplift of the Gamburtsev Mountains. *Nature*, 479(7373):388–392.

Ferraccioli, F., Jordan, T. A., Vaughan, D. G., Holt, J., James, M., Corr, H., Blankenship, D. D., Fairhead, J. D., and Diehl, T. M. (2007). New aerogeophysical survey targets the extent of the West Antarctic Rift System over Ellsworth Land. *Antarctica: A Keystone in a Changing World–Online Proceedings of the 10th ISAES X, edited by AK Cooper and CR Raymond et al., USGS Open-File*, 1047(113):1–10.

Fisher, A. T., Mankoff, K. D., Tulaczyk, S. M., Tyler, S. W., Foley, N., and Team, W. S. (2015). High geothermal heat flux measured below the West Antarctic Ice Sheet. *Science Advances*, 1(6):e1500093.

Florindo, J. B. and Bruno, O. M. (2012). Fractal descriptors based on Fourier spectrum applied to texture analysis. *Physica A: Statistical Mechanics and its Applications*, 391(20):4909–4922.

Forsberg, R., Olesen, A. V., Ferraccioli, F., Jordan, T. A., Matsuoka, K., Zakrajsek, A., Ghidella, M., and Greenbaum, J. S. (2018). Exploring the Recovery Lakes region and interior Dronning Maud Land, East Antarctica, with airborne gravity, magnetic and radar measurements. *Geological Society, London, Special Publications*, 461(1):23–34.

Fowler, A. (1987). Sliding with cavity formation. *Journal of Glaciology*, 33(115):255–267.

Fox-Kemper, B., Hewitt, H. T., Xiao, C., Aðalgeirsdóttir, G., Drijfhout, S. S., Edwards, T. L., Golledge, N. R., Hemer, M., Kopp, R. E., Krinner, G., Mix, A., Notz, D., Nowicki, S., Nurhati, I. S., Ruiz, L., Sallée, J.-B., Slangen, A. B. A., , and Yu, Y. (2021). Ocean, cryosphere and sea-level change, in: Climate Change 2021: The Physical Science Basis. Contribution of Working Group I to the Sixth Assessment Report of the Intergovernmental Panel on Climate Change. *Sixth Assessment Report of the Intergovernmental Panel on Climate Change*, page 1211–1362.

Franke, S., Jansen, D., Binder, T., Dörr, N., Helm, V., Paden, J., Steinhage, D., and Eisen, O. (2020). Bed topography and subglacial landforms in the onset region of the Northeast Greenland Ice Stream. *Annals of Glaciology*, 61(81):143–153.

Frederick, B. C., Young, D. A., Blankenship, D. D., Richter, T. G., Kempf, S. D., Ferraccioli, F., and Siegert, M. J. (2016). Distribution of subglacial sediments across the Wilkes Subglacial Basin, East Antarctica. *Journal of Geophysical Research: Earth Surface*, 121(4):790–813.

Frémand, A. C., Fretwell, P., Bodart, J. A., Pritchard, H. D., Aitken, A., Bamber, J. L., Bell, R., Bianchi, C., Bingham, R. G., Blankenship, D. D., Casassa, G., Catania, G., Christianson, K., Conway, H., Corr, H. F. J., Cui, X., Damaske, D., Damm, V., Drews, R., Eagles, G., Eisen, O., Eisermann, H., Ferraccioli, F., Field, E., Forsberg, R., Franke, S., Fujita, S., Gim, Y., Goel, V., Gogineni, S. P., Greenbaum, J., Hills, B., Hindmarsh, R. C. A., Hoffman, A. O., Holmlund, P., Holschuh, N., Holt, J. W., Horlings, A. N., Humbert, A., Jacobel, R. W., Jansen, D., Jenkins, A., Jokat, W., Jordan, T., King, E., Kohler, J., Krabill, W., Kusk Gillespie, M., Langley, K., Lee, J., Leitchenkov, G., Leuschen, C., Luyendyk, B., MacGregor, J., MacKie, E., Matsuoka, K., Morlighem, M., Mouginot, J., Nitsche, F. O., Nogi, Y., Nost, O. A., Paden, J., Pattyn, F., Popov, S. V., Rignot, E., Rippin, D. M., Rivera, A., Roberts, J., Ross, N., Ruppel, A., Schroeder, D. M., Siegert, M. J., Smith, A. M., Steinhage, D., Studinger, M., Sun, B., Tabacco, I., Tinto, K., Urbini, S., Vaughan, D., Welch, B. C., Wilson, D. S., Young, D. A., and Zirizzotti, A. (2023). Antarctic Bedmap data: Findable, Accessible, Interoperable, and Reusable (FAIR) sharing of 60 years of ice bed, surface, and thickness data. *Earth System Science Data*, 15(7):2695–2710.

Fretwell, P., Pritchard, H. D., Vaughan, D. G., Bamber, J. L., Barrand, N. E., Bell, R., Bianchi, C., Bingham, R. G., Blankenship, D. D., Casassa, G., Catania, G., Callens, D., Conway, H., Cook, A. J., Corr, H. F., Damaske, D., Damm, V., Ferraccioli, F., Forsberg, R., Fujita, S., Gim, Y., Gogineni, P., Griggs, J. A., Hindmarsh, R. C., Holmlund, P., Holt, J. W., Jacobel, R. W., Jenkins, A., Jokat, W., Jordan, T., King, E. C., Kohler, J., Krabill, W., Riger-Kusk, M., Langley, K. A., Leitchenkov, G., Leuschen, C., Luyendyk, B. P., Matsuoka, K., Mouginot, J., Nitsche, F. O., Nogi, Y., Nost, O. A., Popov, S. V., Rignot, E., Rippin, D. M., Rivera, A., Roberts, J., Ross, N., Siegert, M. J., Smith, A. M., Steinhage, D., Studinger, M., Sun, B., Tinto, B. K., Welch, B. C., Wilson, D., Young, D. A., Xiangbin, C., and Zirizzotti, A. (2013). Bedmap2: Improved ice bed, surface and thickness datasets for Antarctica. *The Cryosphere*, 7(1):375–393.

Frezzotti, M., Gandolfi, S., and Urbini, S. (2002). Snow megadunes in Antarctica: Sedimentary structure and genesis. *Journal of Geophysical Research: Atmospheres*, 34:81–88.

Fricker, H. A., Siegfried, M. R., Carter, S. P., and Scambos, T. A. (2016). A decade of progress in observing and modelling Antarctic subglacial water systems. *Philosophical Transactions of the Royal Society A: Mathematical, Physical and Engineering Sciences*, 374(2059):20140294.

Gagliardini, O., Zwinger, T., Gillet-Chaulet, F., Durand, G., Favier, L., De Fleurian, B., Greve, R., Malinen, M., Martín, C., Råback, P., et al. (2013). Capabilities and performance of Elmer/Ice, a new-generation ice-sheet model. *Geoscientific Model Development*, 6(4):1299–1318.

Gardner, A. S., Moholdt, G., Scambos, T., Fahnstock, M., Ligtenberg, S., van den Broeke, M., and Nilsson, J. (2018). Increased West Antarctic and unchanged East Antarctic ice discharge over the last 7 years. *The Cryosphere*, 12(2):521–547.

Gasson, E., DeConto, R., and Pollard, D. (2015). Antarctic bedrock topography uncertainty and ice sheet stability. *Geophysical Research Letters*, 42(13):5372–5377.

Gavriil, K., Muntingh, G., and Barrowclough, O. J. (2019). Void filling of digital elevation models with deep generative models. *IEEE Geoscience and Remote Sensing Letters*, 16(10):1645–1649.

Gillet-Chaulet, F., Durand, G., Gagliardini, O., Mosbeux, C., Mouginot, J., Rémy, F., and Ritz, C. (2016). Assimilation of surface velocities acquired between 1996 and 2010 to constrain the form of the basal friction law under Pine Island Glacier. *Geophysical Research Letters*, 43(19):10–311.

Gladstone, R. M., Payne, A. J., and Cornford, S. L. (2012). Resolution requirements for grounding-line modelling: sensitivity to basal drag and ice-shelf buttressing. *Annals of Glaciology*, 53(60):97–105.

Glen, J. (1958). Measurement of the slip of a glacier past its side wall. *Journal of Glaciology*, 3(23):188–193.

Goeller, S., Thoma, M., Grosfeld, K., and Miller, H. (2013). A balanced water layer concept for subglacial hydrology in large-scale ice sheet models. *The Cryosphere*, 7(4):1095–1106.

Goff, J. A., Powell, E. M., Young, D. A., and Blankenship, D. D. (2014). Conditional simulation of Thwaites Glacier (Antarctica) bed topography for flow models: Incorporating inhomogeneous statistics and channelized morphology. *Journal of Glaciology*, 60(222):635–646.

Goldberg, D., Holland, D. M., and Schoof, C. (2009). Grounding-line movement and ice-shelf buttressing in marine ice sheets. *Journal of Geophysical Research: Earth Surface*, 114(F4):F04026.

Goldberg, D. N. and Heimbach, P. (2013). Parameter and state estimation with a time-dependent adjoint marine ice-sheet model. *The Cryosphere*, 7(6):1659–1678.

Golledge, N. R., Kowalewski, D. E., Naish, T. R., Levy, R. H., Fogwill, C. J., and Gasson, E. G. (2015). The multi-millennial Antarctic commitment to future sea-level rise. *Nature*, 526(7573):421–425.

Golynsky, A., Ferraccioli, F., Hong, J., Golynsky, D., von Frese, R., Young, D., Blankenship, D., Holt, J., Ivanov, S., Kiselev, A., et al. (2018). New magnetic anomaly map of the Antarctic. *Geophysical Research Letters*, 45(13):6437–6449.

Graham, F. S., Roberts, J. L., Galton-Fenzi, B. K., Young, D., Blankenship, D., and Siegert, M. J. (2017). A high-resolution synthetic bed-elevation grid of the Antarctic continent. *Earth System Science Data*, 9(1):267–279.

Gray, L., Joughin, I., Tulaczyk, S., Spikes, V. B., Bindschadler, R., and Jezek, K. (2005). Evidence for subglacial water transport in the West Antarctic Ice Sheet through three-dimensional satellite radar interferometry. *Geophysical Research Letters*, 32(3):L03501.

Groenewald, P., Moyes, A., Grantham, G., and Krynauw, J. (1995). East Antarctic crustal evolution: geological constraints and modelling in western Dronning Maud Land. *Precambrian Research*, 75(3-4):231–250.

Guan, Y., Haran, M., and Pollard, D. (2018). Inferring ice thickness from a glacier dynamics model and multiple surface data sets. *Environmetrics*, 29(5-6):e2460.

Gudmundsson, G. H. (1999). A three-dimensional numerical model of the confluence area of Unteraargletscher, Bernese Alps, Switzerland. *Journal of Glaciology*, 45(150):219–230.

Gudmundsson, G. H. (2003). Transmission of basal variability to a glacier surface. *Journal of Geophysical Research: Solid Earth*, 108(B5):2253.

Gudmundsson, G. H. (2008). Analytical solutions for the surface response to small amplitude perturbations in boundary data in the shallow-ice-stream approximation. *The Cryosphere*, 2(2):77–93.

Gudmundsson, G. H. (2013). Ice-shelf buttressing and the stability of marine ice sheets. *The Cryosphere*, 7(2):647–655.

Gudmundsson, G. H. and Raymond, M. (2008). On the limit to resolution and information on basal properties obtainable from surface data on ice streams. *The Cryosphere*, 2:167–178.

Gustafson, C. D., Key, K., Siegfried, M. R., Winberry, J. P., Fricker, H. A., Venturelli, R. A., and Michaud, A. B. (2022). A dynamic saline groundwater system mapped beneath an Antarctic ice stream. *Science*, 376(6593):640–644.

Hall, C., Cohen, M., Walker, N., Heliere, F., and Wielders, A. (2008). Radar sounders for Earth and the planets. In *7th European Conference on Synthetic Aperture Radar*, pages 1–4. VDE.

Hell, B. and Jakobsson, M. (2011). Gridding heterogeneous bathymetric data sets with stacked continuous curvature splines in tension. *Marine Geophysical Research*, 32:493–501.

Herzfeld, U. C., Eriksson, M. G., and Holmlund, P. (1993). On the influence of kriging parameters on the cartographic output— a study in mapping subglacial topography. *Mathematical Geology*, 25:881–900.

Hindmarsh, R. (2004). A numerical comparison of approximations to the Stokes equations used in ice-sheet and glacier modeling. *Journal of Geophysical Research: Earth Surface*, 109(F1).

Hoffman, A. O., Christianson, K., Shapero, D., Smith, B. E., and Joughin, I. (2020). Brief communication: Heterogenous thinning and subglacial lake activity on Thwaites Glacier, West Antarctica. *The Cryosphere*, 14(12):4603–4609.

Hoffman, A. O., Holschuh, N., Mueller, M., Paden, J., Muto, A., Ariho, G., Brigham, C., Christian, J. E., Davidge, L., Heitmann, E., et al. (2023). Scars of tectonism promote ice-sheet nucleation from Hercules Dome into West Antarctica. *Nature Geoscience*, 16(11):1005–1013.

Hogan, K., Arnold, N., Larter, R., Kirkham, J., Noormets, R., Ó Cofaigh, C., Golledge, N., and Dowdeswell, J. (2022). Subglacial Water Flow Over an Antarctic Palaeo-Ice Stream Bed. *Journal of Geophysical Research: Earth Surface*, 127(2):e2021JF006442.

Hogan, K., Larter, R., Graham, A. G., Arthern, R., Kirkham, J., Totten Minzoni, R., Jordan, T., Clark, R., Fitzgerald, V., Anderson, J., Hillenbrand, C.-D., Nitsche, F., Simkins, L., Smith, J., Gohl, K., Arndt, J. E., Hong, J., and Wellner, J. (2020). Revealing the former bed of Thwaites Glacier using sea-floor bathymetry. *The Cryosphere*, 14:2883–2908.

Holschuh, N., Christianson, K., Paden, J., Alley, R., and Anandakrishnan, S. (2020). Linking postglacial landscapes to glacier dynamics using swath radar at Thwaites Glacier, Antarctica. *Geology*, 48(3):268–272.

Holt, J. W., Blankenship, D. D., Morse, D. L., Young, D. A., Peters, M. E., Kempf, S. D., Richter, T. G., Vaughan, D. G., and Corr, H. F. J. (2006). New boundary conditions for the West Antarctic Ice Sheet: Subglacial topography of the Thwaites and Smith glacier catchments. *Geophysical Research Letters*, 33(9):L09502.

Hondoh, T., Shoji, H., Watanabe, O., Salamatin, A. N., and Lipenkov, V. Y. (2002). Depth–age and temperature prediction at Dome Fuji station, East Antarctica. *Annals of Glaciology*, 35:384–390.

Howat, I. M., Porter, C., Smith, B. E., Noh, M.-J., and Morin, P. (2019). The Reference Elevation Model of Antarctica. *The Cryosphere*, 13(2):665–674.

Hubbard, B., Siegert, M. J., and McCarroll, D. (2000). Spectral roughness of glaciated bedrock geomorphic surfaces: implications for glacier sliding. *Journal of Geophysical Research: Solid Earth*, 105(B9):21295–21303.

Hübscher, C., Jokat, W., and Miller, H. (1996). Structure and origin of southern Weddell Sea crust: results and implications. *Geological Society, London, Special Publications*, 108(1):201–211.

Hughes, T. J. (1981). The weak underbelly of the West Antarctic Ice Sheet. *Journal of Glaciology*, 27(97):518–525.

Hulbe, C. L. and MacAyeal, D. R. (1999). A new numerical model of coupled inland ice-sheet, ice-stream, and ice-shelf flow and its application to the West Antarctic Ice Sheet. *Journal of Geophysical Research: Solid Earth*, 104:25349–25366.

Humbert, A., Steinhage, D., Helm, V., Beyer, S., and Kleiner, T. (2018). Missing evidence of widespread subglacial lakes at Recovery Glacier, Antarctica. *Journal of Geophysical Research: Earth Surface*, 123(11):2802–2826.

Hutter, K. (2017). *Theoretical Glaciology: Material Science of Ice and the Mechanics of Glaciers and Ice Sheets*, volume 1. Springer.

Huybrechts, P. (1990). A 3-D model for the Antarctic Ice Sheet: a sensitivity study on the glacial-interglacial contrast. *Climate Dynamics*, 5:79–92.

Igneczi, A., Sole, A. J., Livingstone, S. J., Ng, F. S. L., and Yang, K. (2018). Greenland Ice Sheet surface topography and drainage structure controlled by the transfer of basal variability. *Frontiers in Earth Science*, 6:101.

Iken, A. (1981). The effect of the subglacial water pressure on the sliding velocity of a glacier in an idealized numerical model. *Journal of Glaciology*, 27(97):407–421.

IMBIE, T. (2021). Antarctic and Greenland Ice Sheet mass balance 1992–2020 for IPCC AR6 (Version 1.0), UK Polar Data Centre, Natural Environment Research Council, UK Research & Innovation [data set].

Jamieson, S. S., Ross, N., Paxman, G. J., Clubb, F. J., Young, D. A., Yan, S., Greenbaum, J., Blankenship, D. D., and Siegert, M. J. (2023). An ancient river landscape preserved beneath the East Antarctic Ice Sheet. *Nature Communications*, 14(1):6507.

Jamieson, S. S., Stokes, C. R., Ross, N., Rippin, D. M., Bingham, R. G., Wilson, D. S., Margold, M., and Bentley, M. J. (2014). The glacial geomorphology of the Antarctic ice-sheet bed. *Antarctic Science*, 26(6):724–741.

Jamieson, S. S., Sugden, D. E., and Hulton, N. R. (2010). The evolution of the subglacial landscape of Antarctica. *Earth and Planetary Science Letters*, 293(1-2):1–27.

Jóhannesson, T. (1992). *Landscape of temperate ice caps*. University of Washington.

Jordan, T., Martin, C., Ferraccioli, F., Matsuoka, K., Corr, H., Forsberg, R., Olesen, A., and Siegert, M. (2018). Anomalously high geothermal flux near the South Pole. *Scientific Reports*, 8(1):16785.

Jordan, T. and Robinson, C. (2021). Bed, surface-elevation and ice-thickness measurements derived from radar data acquired during the Thwaites Glacier airborne survey (2019/2020) (Version 1.0) [Data set]. *NERC EDS UK Polar Data Centre*.

Jordan, T. A., Ferraccioli, F., Vaughan, D. G., Holt, J. W., Corr, H., Blankenship, D. D., and Diehl, T. M. (2010). Aerogravity evidence for major crustal thinning under the Pine Island Glacier region (West Antarctica). *Bulletin of the Geological Society of America*, 122(5-6):714–726.

Jordan, T. A., Thompson, S., Kulessa, B., and Ferraccioli, F. (2023). Geological sketch map and implications for ice flow of Thwaites Glacier, West Antarctica, from integrated aerogeophysical observations. *Science Advances*, 9(22):eadf2639.

Joughin, I., Smith, B. E., and Holland, D. M. (2010). Sensitivity of 21st century sea level to ocean-induced thinning of Pine Island Glacier, Antarctica. *Geophysical Research Letters*, 37(20):L20502.

Joughin, I., Smith, B. E., and Medley, B. (2014). Marine ice-sheet collapse potentially under way for the Thwaites Glacier Basin, West Antarctica. *Science*, 344(6185):735–8.

Joughin, I., Tulaczyk, S., Bamber, J. L., Blankenship, D., Holt, J. W., Scambos, T., and Vaughan, D. G. (2009). Basal conditions for Pine Island and Thwaites glaciers, West Antarctica, determined using satellite and airborne data. *Journal of Glaciology*, 55(190):245–257.

Joughin, I., Tulaczyk, S., MacAyeal, D. R., and Engelhardt, H. (2004). Melting and freezing beneath the Ross Ice Streams, Antarctica. *Journal of Glaciology*, 50(168):96–108.

Kanao, M., Fujiwara, A., Miyamachi, H., Toda, S., Ito, K., Tomura, M., Ikawa, T., et al. (2011). Reflection imaging of the crust and the lithospheric mantle in the Lützow-Holm complex, Eastern Dronning Maud Land, Antarctica, derived from the SEAL transects. *Tectonophysics*, 508(1-4):73–84.

Karlsson, N. B., Binder, T., Eagles, G., Helm, V., Pattyn, F., van Liefferinge, B., and Eisen, O. (2018). Glaciological characteristics in the Dome Fuji region and new assessment for "Oldest Ice". *The Cryosphere*, 12(7):2413–2424.

Kazmierczak, E., Sun, S., Coulon, V., and Pattyn, F. (2022). Subglacial hydrology modulates basal sliding response of the Antarctic ice sheet to climate forcing. *The Cryosphere*, 16(10):4537–4552.

Keisling, B. A., Nielsen, L. T., Hvidberg, C. S., Nuterman, R., and DeConto, R. M. (2020). Pliocene–Pleistocene megafloods as a mechanism for Greenlandic megacanyon formation. *Geology*, 48(7):737–741.

Kessler, M. A., Anderson, R. S., and Briner, J. P. (2008). Fjord insertion into continental margins driven by topographic steering of ice. *Nature Geoscience*, 1(6):365–369.

Killingbeck, S. F., Dow, C. F., and Unsworth, M. J. (2022). A quantitative method for deriving salinity of subglacial water using ground-based transient electromagnetics. *Journal of Glaciology*, 68(268):319–336.

King, E. (2011). Ice stream or not? Radio-echo sounding of Carlson Inlet, West Antarctica. *The Cryosphere*, 5(4):907–916.

King, E. C., Hindmarsh, R. C., and Stokes, C. R. (2009). Formation of mega-scale glacial lineations observed beneath a West Antarctic ice stream. *Nature Geoscience*, 2(8):585–588.

King, E. C., Pritchard, H. D., and Smith, A. M. (2016). Subglacial landforms beneath Rutford Ice Stream, Antarctica: detailed bed topography from ice-penetrating radar. *Earth System Science Data*, 8(1):151–158.

Kirkham, J. D., Hogan, K. A., Larter, R. D., Arnold, N. S., Nitsche, F. O., Golledge, N. R., and Dowdeswell, J. A. (2019). Past water flow beneath Pine Island and Thwaites glaciers, West Antarctica. *The Cryosphere*, 13(7):1959–1981.

Kirkham, J. D., Hogan, K. A., Larter, R. D., Arnold, N. S., Nitsche, F. O., Kuhn, G., Gohl, K., Anderson, J. B., and Dowdeswell, J. A. (2020). Morphometry of bedrock meltwater channels on Antarctic inner continental shelves: Implications for channel development and subglacial hydrology. *Geomorphology*, 370:107369.

Koellner, S., Parizek, B. R., Alley, R. B., Muto, A., and Holschuh, N. (2019). The impact of spatially-variable basal properties on outlet glacier flow. *Earth and Planetary Science Letters*, 515:200–208.

Kufner, S., Brisbourne, A., Smith, A., Hudson, T., Murray, T., Schlegel, R., Kendall, J., Anandakrishnan, S., and Lee, I. (2021). Not all icequakes are created equal: Basal icequakes suggest diverse bed deformation mechanisms at Rutford Ice Stream, West Antarctica. *Journal of Geophysical Research: Earth Surface*, 126(3):2020JF006001.

Kyrke-Smith, T., Gudmundsson, G., and Farrell, P. (2018). Relevance of detail in basal topography for basal slipperiness inversions: a case study on Pine Island Glacier, Antarctica. *Frontiers in Earth Science*, 6:33.

Kyrke-Smith, T. M., Gudmundsson, G. H., and Farrell, P. E. (2017). Can seismic observations of bed conditions on ice streams help constrain parameters in ice-flow models? *Journal of Geophysical Research: Earth Surface*, 122(11):2269–2282.

Laird, C. M., Blake, W. A., Matsuoka, K., Conway, H., Allen, C. T., Leuschen, C. J., and Gogineni, S. (2009). Deep ice stratigraphy and basal conditions in central West Antarctica revealed by coherent radar. *IEEE Geoscience and Remote Sensing Letters*, 7(2):246–250.

Larour, E., Seroussi, H., Adhikari, S., Ivins, E., Caron, L., Morlighem, M., and Schlegel, N. (2019). Slowdown in Antarctic mass loss from solid Earth and sea-level feedbacks. *Science*, 364(6444):eaav7908.

Larour, E., Seroussi, H., Morlighem, M., and Rignot, E. (2012). Continental scale, high order, high spatial resolution, ice sheet modeling using the Ice Sheet System Model (ISSM). *Journal of Geophysical Research: Earth Surface*, 117:F01022.

Larter, R. D., Hogan, K. A., Hillenbrand, C.-D., Smith, J. A., Batchelor, C. L., Cartigny, M., Tate, A. J., Kirkham, J. D., Roseby, Z. A., Kuhn, G., et al. (2019). Subglacial hydrological control on flow of an Antarctic Peninsula palaeo-ice stream. *The Cryosphere*, 13(6):1583–1596.

Le Brocq, A. M., Payne, A. J., and Vieli, A. (2010). An improved Antarctic dataset for high resolution numerical ice-sheet models (ALBMAP v1). *Earth System Science Data*, 2(2):247–260.

Le Meur, E., Gagliardini, O., Zwinger, T., and Ruokolainen, J. (2004). Glacier flow modelling: A comparison of the Shallow Ice Approximation and the full-Stokes solution.

Lea, E. J., Jamieson, S. S., and Bentley, M. J. (2023). Alpine topography of the Gamburtsev Subglacial Mountains, Antarctica, mapped from ice-sheet surface morphology. *The Cryosphere Discussions*, 2023:1–28.

Leguy, G., Asay-Davis, X., and Lipscomb, W. (2014). Parameterization of basal friction near grounding lines in a one-dimensional ice-sheet model. *The Cryosphere*, 8(4):1239–1259.

Leitchenkov, G. L. and Kudryavtzev, G. (2000). Structure and origin of the Earth´ s crust in the Weddell Sea Embayment (beneath the front of the Filchner and Ronne Ice Shelves) from deep seismic sounding data. *Polarforschung*, 67(3):143–154.

Leong, W. J. and Horgan, H. J. (2020). DeepBedMap: A deep neural network for resolving the bed topography of Antarctica. *The Cryosphere*, 14(11):3687–3705.

Lepp, A., Simkins, L., Anderson, J., Clark, R., Wellner, J., Hillenbrand, C., Smith, J., Lehrmann, A., Totten, R., Larter, R., and Hogan, K. (2022). Sedimentary signatures of persistent subglacial meltwater drainage from Thwaites Glacier, Antarctica. *Frontiers in Earth Science*, 10(1):863200.

Lipscomb, W. H., Price, S. F., Hoffman, M. J., Leguy, G. R., Bennett, A. R., Bradley, S. L., Evans, K. J., Fyke, J. G., Kennedy, J. H., Perego, M., et al. (2019). Description and evaluation of the community ice-sheet model (CISM) v2. 1. *Geoscientific Model Development*, 12(1):387–424.

Livingstone, S. J., Chu, W., Ely, J. C., and Kingslake, J. (2017). Paleofluvial and subglacial channel networks beneath Humboldt Glacier, Greenland. *Geology*, 45(6):551–554.

Livingstone, S. J., Li, Y., Rutishauser, A., Sanderson, R. J., Winter, K., Mikucki, J. A., Björnsson, H., Bowling, J. S., Chu, W., Dow, C. F., et al. (2022). Subglacial lakes and their changing role in a warming climate. *Nature Reviews Earth & Environment*, 3(2):106–124.

Lliboutry, L. (1968). General theory of subglacial cavitation and sliding of temperate glaciers. *Journal of Glaciology*, 7(49):21–58.

Loose, B., Naveira Garabato, A. C., Schlosser, P., Jenkins, W. J., Vaughan, D., and Heywood, K. J. (2018). Evidence of an active volcanic heat source beneath the Pine Island Glacier. *Nature Communications*, 9(1):2431.

Luyendyk, B. P., Wilson, D. S., and Siddoway, C. S. (2003). Eastern margin of the Ross Sea Rift in western Marie Byrd Land, Antarctica: Crustal structure and tectonic development. *Geochemistry, Geophysics, Geosystems*, 4(10):1090.

Lythe, M., Vaughan, D., Lambrecht, A., Miller, H., Nixdorf, U., Oerter, H., Steinhage, D., Huybrechts, P., et al. (2001). BEDMAP: A new ice thickness and subglacial topographic model of Antarctica. *Journal of Geophysical Research: Solid Earth*, 106(B6):11335–11351.

MacAyeal, D. R. (1989). Large-scale ice flow over a viscous basal sediment: theory and application to Ice Stream B, Antarctica. *Journal of Geophysical Research*, 94(134):4071–4087.

MacGregor, J. A., Boisvert, L. N., Medley, B., Petty, A. A., Harbeck, J. P., Bell, R. E., Blair, J. B., Blanchard-Wrigglesworth, E., Buckley, E. M., Christoffersen, M. S., et al. (2021). The scientific legacy of NASA's Operation IceBridge.

Mackie, E. and Schroeder, D. (2019). Paleo observations used to geostatistically simulate the subglacial geology of Thwaites Glacier. In *AGU Fall Meeting Abstracts*, pages C51A–03.

MacKie, E., Schroeder, D., Caers, J., Siegfried, M., and Scheidt, C. (2020). Antarctic topographic realizations and geostatistical modeling used to map subglacial lakes. *Journal of Geophysical Research: Earth Surface*, 125(3):e2019JF005420.

MacKie, E. J. and Schroeder, D. M. (2020). Geostatistically simulating subglacial topography with synthetic training data. In *IGARSS 2020-2020 IEEE International Geoscience and Remote Sensing Symposium*, pages 2991–2994.

MacKie, E. J., Schroeder, D. M., Zuo, C., Yin, Z., and Caers, J. (2021). Stochastic modeling of subglacial topography exposes uncertainty in water routing at Jakobshavn Glacier. *Journal of Glaciology*, 67(261):75–83.

Malczyk, G., Gourmelen, N., Goldberg, D., Wuite, J., and Nagler, T. (2020). Repeat subglacial lake drainage and filling beneath Thwaites Glacier. *Geophysical Research Letters*, 47(23):e2020GL089658.

Margold, M., Stokes, C. R., and Clark, C. D. (2015). Ice streams in the Laurentide Ice Sheet: Identification, characteristics and comparison to modern ice sheets. *Earth-Science Reviews*, 143:117–146.

Martos, Y. M., Catalán, M., Jordan, T. A., Golynsky, A., Golynsky, D., Eagles, G., and Vaughan, D. G. (2017). Heat flux distribution of Antarctica unveiled. *Geophysical Research Letters*, 44(22):11–417.

McCormack, F., Galton-Fenzi, B., Seroussi, H., and Roberts, J. (2018). The impact of bed elevation resolution on Thwaites Glacier ice dynamics. *Twenty-Fifth Annual WAIS Workshop*.

Mercer, J. H. (1978). West Antarctic Ice Sheet and CO2 greenhouse effect: a threat of disaster. *Nature*, 271(5643):321–325.

Millan, R., Rignot, E., Bernier, V., Morlighem, M., and Dutrieux, P. (2017). Bathymetry of the Amundsen Sea Embayment sector of West Antarctica from Operation IceBridge gravity and other data. *Geophysical Research Letters*, 44(3):1360–1368.

Millstein, J. D., Minchew, B. M., and Pegler, S. S. (2022). Ice viscosity is more sensitive to stress than commonly assumed. *Communications Earth & Environment*, 3(1):57.

Montagnat, M., Azuma, N., Dahl-Jensen, D., Eichler, J., Fujita, S., Gillet-Chaulet, F., Kipfstuhl, S., Samyn, D., Svensson, A., and Weikusat, I. (2014). Fabric along the NEEM ice core, Greenland, and its comparison with GRIP and NGRIP ice cores. *The Cryosphere*, 8(4):1129–1138.

Mony, L., Roberts, J. L., and Halpin, J. A. (2020). Inferring geothermal heat flux from an ice-borehole temperature profile at Law Dome, East Antarctica. *Journal of Glaciology*, 66(257):509–519.

Morlighem, M., Rignot, E., Binder, T., Blankenship, D., Drews, R., Eagles, G., Eisen, O., Ferraccioli, F., Forsberg, R., Fretwell, P., Goel, V., Greenbaum, J. S., Gudmundsson, H., Guo, J., Helm, V., Hofstede, C., Howat, I., Humbert, A., Jokat, W., Karlsson, N. B., Lee, W. S., Matsuoka, K., Millan, R., Mouginot, J., Paden, J., Pattyn, F., Roberts, J., Rosier, S., Ruppel, A., Seroussi, H., Smith, E. C., Steinhage, D., Sun, B., Broeke, M. R. v. d., Ommen, T. D. v., Wessem, M. v., and Young, D. A. (2020). Deep glacial troughs and stabilizing ridges unveiled beneath the margins of the Antarctic ice sheet. *Nature Geoscience*, 13(2):132–137.

Morlighem, M., Rignot, E., Mouginot, J., Seroussi, H., and Larour, E. (2014). Deeply incised submarine glacial valleys beneath the Greenland ice sheet. *Nature Geoscience*, 7(6):418–422.

Morlighem, M., Rignot, E., Seroussi, H., Larour, E., Ben Dhia, H., and Aubry, D. (2010). Spatial patterns of basal drag inferred using control methods from a full-Stokes and simpler models for Pine Island Glacier, West Antarctica. *Geophysical Research Letters*, 37(14).

Morlighem, M., Rignot, E., Seroussi, H., Larour, E., Ben Dhia, H., and Aubry, D. (2011). A mass conservation approach for mapping glacier ice thickness. *Geophysical Research Letters*, 38(19):L19503.

Morlighem, M., Williams, C. N., Rignot, E., An, L., Arndt, J. E., Bamber, J. L., Catania, G., Chauché, N., Dowdeswell, J. A., Dorschel, B., et al. (2017). BedMachine v3: Complete bed topography and ocean bathymetry mapping of Greenland from multi-beam echo sounding combined with mass conservation. *Geophysical Research Letters*, 44(21):11051–11061.

Muto, A., Alley, R. B., Parizek, B. R., and Anandakrishnan, S. (2019a). Bed-type variability and till (dis)continuity beneath Thwaites Glacier, West Antarctica. *Annals of Glaciology*, 60(80):82–90.

Muto, A., Anandakrishnan, S., Alley, R. B., Horgan, H. J., Parizek, B. R., Koellner, S., Christianson, K., and Holschuh, N. (2019b). Relating bed character and subglacial morphology using seismic data from Thwaites Glacier, West Antarctica. *Earth and Planetary Science Letters*, 507:199–206.

Muto, A., Peters, L. E., Gohl, K., Sasgen, I., Alley, R. B., Anandakrishnan, S., and Riverman, K. L. (2016). Subglacial bathymetry and sediment distribution beneath Pine Island Glacier Ice Shelf modeled using aerogravity and in situ geophysical data: New results. *Earth and Planetary Science Letters*, 433:63–75.

Napoleoni, F., Jamieson, S. S., Ross, N., Bentley, M. J., Rivera, A., Smith, A. M., Siegert, M. J., Paxman, G. J., Gacitúa, G., Uribe, J. A., et al. (2020). Subglacial lakes and hydrology across the Ellsworth Subglacial Highlands, West Antarctica. *The Cryosphere*, 14(12):4507–4524.

Ng, F. S. L., Igneczi, A., Sole, A. J., and Livingstone, S. J. (2018). Response of surface topography to basal variability along glacial flowlines. *Journal of Geophysical Research: Earth Surface*, 123(10):2319–2340.

Nias, I. J., Cornford, S. L., and Payne, A. J. (2016). Contrasting the modelled sensitivity of the Amundsen Sea Embayment ice streams. *Journal of Glaciology*, 62(233):552–562.

Nias, I. J., Cornford, S. L., and Payne, A. J. (2018). New mass-conserving bedrock topography for Pine Island Glacier impacts simulated decadal rates of mass loss. *Geophysical Research Letters*, 45(7):3173–3181.

Nitsche, F. O., Gohl, K., Larter, R. D., Hillenbrand, C. D., Kuhn, G., Smith, J. A., Jacobs, S., Anderson, J. B., and Jakobsson, M. (2013). Paleo ice flow and subglacial meltwater dynamics in Pine Island Bay, West Antarctica. *The Cryosphere*, 7(1):249–262.

Nowicki, S., Bindschadler, R. A., Abe-Ouchi, A., Aschwanden, A., Bueler, E., Choi, H., Fastook, J., Granzow, G., Greve, R., Gutowski, G., et al. (2013). Insights into spatial sensitivities of ice-mass response to environmental change from the SeaRISE ice-sheet modeling project I: Antarctica. *Journal of Geophysical Research: Earth Surface*, 118(2):1002–1024.

Nye, J. F. (1959). The motion of ice sheets and glaciers. *Journal of Glaciology*, 3(26):493–507.

Ockenden, H., Bingham, R. G., Curtis, A., and Goldberg, D. (2022). Inverting ice-surface elevation and velocity for bed topography and slipperiness beneath Thwaites Glacier. *The Cryosphere*, 16(9):3867–3887.

Ockenden, H., Bingham, R. G., Curtis, A., and Goldberg, D. (2023). Ice-Flow Perturbation Analysis: a method to estimate ice-sheet bed topography and conditions from surface datasets. *Journal of Glaciology*, pages 1–10.

Oerlemans, J. (1982). A model of the Antarctic Ice Sheet. *Nature*, 297(5867):550–553.

Oppenheimer, M., Glavovic, B., Hinkel, J., van de Wal, R., Magnan, A., Abd-Elgawad, A., Cai, R., Cifuentes-Jara, M., DeConto, R., Ghosh, T., et al. (2019). The ocean and cryosphere in a changing climate. *The Intergovernmental Panel on Climate Change*.

Oswald, G. and Robin, G. d. (1973). Lakes beneath the Antarctic Ice Sheet. *Nature*, 245(5423):251–254.

Otosaka, I. N., Shepherd, A., Ivins, E. R., Schlegel, N.-J., Amory, C., van den Broeke, M., Horwath, M., Joughin, I., King, M., Krinner, G., et al. (2022). Mass balance of the Greenland and Antarctic ice sheets from 1992 to 2020. *Earth System Science Data*, 15(4):1597–1616.

Paden, J., Akins, T., Dunson, D., Allen, C., and Gogineni, P. (2010). Ice-sheet bed 3-D tomography. *Journal of Glaciology*, 56(195):3–11.

Parizek, B. R., Christianson, K., Anandakrishnan, S., Alley, R. B., Walker, R. T., Edwards, R. A., Wolfe, D. S., Bertini, G. T., Rinehart, S. K., Bindschadler, R. A., and Nowicki, S. M. (2013). Dynamic (in)stability of Thwaites Glacier, West Antarctica. *Journal of Geophysical Research: Earth Surface*, 118(2):638–655.

Pattyn, F. (1996). Numerical modelling of a fast-flowing outlet glacier: experiments with different basal conditions. *Annals of Glaciology*, 23:237–246.

Pattyn, F. (2003). A new three-dimensional higher-order thermomechanical ice sheet model: Basic sensitivity, ice stream development, and ice flow across subglacial lakes. *Journal of Geophysical Research: Solid Earth*, 108(B8):2382.

Pattyn, F., Perichon, L., Durand, G., Favier, L., Gagliardini, O., Hindmarsh, R. C., Zwinger, T., Albrecht, T., Cornford, S., Docquier, D., et al. (2013). Grounding-line migration in plan-view marine ice-sheet models: results of the ice2sea MISMIP3d intercomparison. *Journal of Glaciology*, 59(215):410–422.

Pattyn, F., Schoof, C., Perichon, L., Hindmarsh, R., Bueler, E., De Fleurian, B., Durand, G., Gagliardini, O., Gladstone, R., Goldberg, D., et al. (2012). Results of the marine ice-sheet model intercomparison project, MISMIP. *The Cryosphere*, 6:573–588.

Paxman, G. J., Gasson, E. G., Jamieson, S. S., Bentley, M. J., and Ferraccioli, F. (2020). Long-term increase in Antarctic Ice Sheet vulnerability driven by bed-topography evolution. *Geophysical Research Letters*, 47(20):e2020GL090003.

Paxman, G. J., Jamieson, S. S., Ferraccioli, F., Jordan, T. A., Bentley, M. J., Ross, N., Forsberg, R., Matsuoka, K., Steinhage, D., Eagles, G., et al. (2019a). Subglacial geology and geomorphology of the Pensacola-Pole Basin, East Antarctica. *Geochemistry, Geophysics, Geosystems*, 20(6):2786–2807.

Paxman, G. J., Jamieson, S. S., Hochmuth, K., Gohl, K., Bentley, M. J., Leitchenkov, G., and Ferraccioli, F. (2019b). Reconstructions of Antarctic topography since the Eocene–Oligocene boundary. *Palaeogeography, Palaeoclimatology, Palaeoecology*, 535:109346.

Pegler, S. S. (2018). Suppression of marine ice-sheet instability. *Journal of Fluid Mechanics*, 857:648–680.

Pollard, D. and DeConto, R. (2012). A simple inverse method for the distribution of basal-sliding coefficients under ice sheets, applied to Antarctica. *The Cryosphere*, 6(5):953–971.

Pollard, D. and DeConto, R. M. (2009). Modelling West Antarctic Ice Sheet growth and collapse through the past five million years. *Nature*, 458(7236):329–332.

Popov, S. (2020). Fifty-five years of Russian radio-echo sounding investigations in Antarctica. *Annals of Glaciology*, 61(81):14–24.

Popov, S., Masolov, V., Lukin, V., and Popkov, A. (2012). Russian seismic, radio and seismological investigations of subglacial Lake Vostok. *Ice and Snow*, 4(120):31–38.

Pralong, M. and Gudmundsson, G. H. (2011). Bayesian estimation of basal conditions on Rutford Ice Stream, West Antarctica, from surface data. *Journal of Glaciology*, 57(202):315–324.

Pritchard, H. D. (2014). Bedgap: where next for Antarctic subglacial mapping? *Antarctic Science*, 26(6):742–757.

Purucker, M. (2013). Geothermal heat flux data set based on low resolution observations collected by the CHAMP satellite between 2000 and 2010, and produced from the MF-6 model following the technique described in Fox Maule et al.(2005).

Quiquet, A., Dumas, C., Ritz, C., Peyaud, V., and Roche, D. M. (2018). The GRISLI ice sheet model (version 2.0): calibration and validation for multi-millennial changes of the Antarctic Ice Sheet. *Geoscientific Model Development*, 11(12):5003–5025.

Raymond, M. J. and Gudmundsson, G. H. (2005). On the relationship between surface and basal properties on glaciers, ice sheets, and ice streams. *Journal of Geophysical Research*, 110(B8):B08411.

Raymond, M. J. and Gudmundsson, G. H. (2009). Estimating basal properties of ice streams from surface measurements: A non-linear Bayesian inverse approach applied to synthetic data. *The Cryosphere*, 3(2):265–278.

Rea, B. R. and Evans, D. J. (1996). Landscapes of areal scouring in NW Scotland. *Scottish Geographical Magazine*, 112(1):47–50.

Reeh, N. (1987). Steady-state three-dimensional ice flow over an undulating base: first-order theory with linear ice rheology. *Journal of Glaciology*, 33(114):177–185.

Rémy, F. and Legresy, B. (2004). Subglacial hydrological networks in Antarctica and their impact on ice flow. *Annals of Glaciology*, 39:67–72.

Rignot, E., Mouginot, J., Morlighem, M., Seroussi, H., and Scheuchl, B. (2014). Widespread, rapid grounding-line retreat of Pine Island, Thwaites, Smith, and Kohler glaciers, West Antarctica, from 1992 to 2011. *Geophysical Research Letters*, 41(10):3502–3509.

Rignot, E., Mouginot, J., and Scheuchl, B. (2011a). Ice flow of the Antarctic Ice Sheet. *Science*, 333(6048):1427–1430.

Rignot, E., Mouginot, J., and Scheuchl, B. (2011b). Ice flow of the Antarctic ice sheet. *Science*, 333(6048):1427–1430.

Rignot, E., Mouginot, J., Scheuchl, B., van den Broeke, M., van Wessem, M. J., and Morlighem, M. (2019). Four decades of Antarctic Ice Sheet mass balance from 1979-2017. *Proceedings of the National Academy of Sciences of the United States of America*, 116(4):1095–1103.

Ritz, C., Edwards, T. L., Durand, G., Payne, A. J., Peyaud, V., and Hindmarsh, R. C. (2015). Potential sea-level rise from Antarctic ice-sheet instability constrained by observations. *Nature*, 528(7580):115–118.

Robin, G. d. (1958). *Seismic shooting and related investigations*. Norsk Polarinstitut.

Robin, G. d., Evans, S., and Bailey, J. T. (1969). Interpretation of radio-echo sounding in polar ice sheets. *Philosophical Transactions of the Royal Society of London. Series A, Mathematical and Physical Sciences*, 265(1166):437–505.

Rose, K. C., Ross, N., Bingham, R. G., Corr, H. F., Ferraccioli, F., Jordan, T. A., Le Brocq, A. M., Rippin, D. M., and Siegert, M. J. (2014). A temperate former West Antarctic Ice Sheet suggested by an extensive zone of subglacial meltwater channels. *Geology*, 42(11):971–974.

Russ, J. C. (2013). Fractal surfaces. In *Fractal surfaces*. Springer Science & Business Media.

Sandiford, M. and McLaren, S. (2002). Tectonic feedback and the ordering of heat producing elements within the continental lithosphere. *Earth and Planetary Science Letters*, 204(1-2):133–150.

Scambos, T., Bell, R., Alley, R., Anandakrishnan, S., Bromwich, D., Brunt, K., Christianson, K., Creyts, T., Das, S., DeConto, R., Dutrieux, P., Fricker, H., Holland, D., MacGregor, J., Medley, B., Nicolas, J., Pollard, D., Siegfried, M., Smith, A., Steig, E., Trusel, L., Vaughan, D., and Yager, P. (2017). How much, how fast?: A science review and outlook for research on the instability of Antarctica's Thwaites Glacier in the 21st century. *Global and Planetary Change*, 153:16–34.

Scambos, T. A., Berthier, E., and Shuman, C. A. (2011). The triggering of subglacial lake drainage during rapid glacier drawdown: Crane Glacier, Antarctic Peninsula. *Annals of Glaciology*, 52(59):74–82.

Scheinert, M., Ferraccioli, F., Schwabe, J., Bell, R., Studinger, M., Damaske, D., Jokat, W., Aleshkova, N., Jordan, T., Leitchenkov, G., et al. (2016). New Antarctic gravity anomaly grid for enhanced geodetic and geophysical studies in Antarctica. *Geophysical Research Letters*, 43(2):600–610.

Schelpe, C. A. and Gudmundsson, G. H. (2023). Incorporating Horizontal Density Variations Into Large-Scale Modeling of Ice Masses. *Journal of Geophysical Research: Earth Surface*, 128(2):e2022JF006744.

Schlegel, R., Murray, T., Smith, A. M., Brisbourne, A. M., Booth, A. D., King, E. C., and Clark, R. A. (2022). Radar-derived subglacial properties and landforms beneath Rutford Ice Stream, West Antarctica. *Journal of Geophysical Research: Earth Surface*, 127(1):e2021JF006349.

Schoof, C. (2002). Basal perturbations under ice streams: form drag and surface expression. *Journal of Glaciology*, 48(162):407–416.

Schoof, C. (2005). The effect of cavitation on glacier sliding. *Proceedings of the Royal Society A: Mathematical, Physical and Engineering Sciences*, 461(2055):609–627.

Schoof, C. (2007). Ice sheet grounding line dynamics: Steady states, stability, and hysteresis. *Journal of Geophysical Research: Earth Surface*, 112(3):1–19.

Schroeder, D., Blankenship, D., Young, D., and Quartini, E. (2014a). Evidence for elevated and spatially variable geothermal flux beneath the West Antarctic Ice Sheet. *Proceedings of the National Academy of Sciences of the United States of America*, 111(25):9070–2.

Schroeder, D. M., Bingham, R. G., Blankenship, D. D., Christianson, K., Eisen, O., Flowers, G. E., Karlsson, N. B., Koutnik, M. R., Paden, J. D., and Siegert, M. J. (2020). Five decades of radioglaciology. *Annals of Glaciology*, 61(81):1–13.

Schroeder, D. M., Blankenship, D. D., Raney, R. K., and Grima, C. (2014b). Estimating subglacial water geometry Using radar bed-echo specularity: application to Thwaites Glacier, West Antarctica. *IEEE Geoscience and Remote Sensing Letters*, 12(3):443–447.

Schroeder, D. M., Blankenship, D. D., and Young, D. A. (2013). Evidence for a water system transition beneath Thwaites Glacier, West Antarctica. *Proceedings of the National Academy of Sciences of the United States of America*, 110(30):12225–8.

Schwans, E., Parizek, B. R., Alley, R. B., Anandakrishnan, S., and Morlighem, M. M. (2023). Model insights into bed control on retreat of Thwaites Glacier, West Antarctica. *Journal of Glaciology*, pages 1–19.

Sergienko, O. V. (2022). No general stability conditions for marine ice-sheet grounding lines in the presence of feedbacks. *Nature Communications*, 13(1):2265.

Seroussi, H., Dhia, H. B., Morlighem, M., Larour, E., Rignot, E., and Aubry, D. (2012). Coupling ice flow models of varying orders of complexity with the Tiling method. *Journal of Glaciology*, 58(210):776–786.

Seroussi, H., Nakayama, Y., Larour, E., Menemenlis, D., Morlighem, M., Rignot, E., and Khazendar, A. (2017). Continued retreat of Thwaites Glacier, West Antarctica, controlled by bed topography and ocean circulation. *Geophysical Research Letters*, 44(12):6191–6199.

Seroussi, H., Nowicki, S., Payne, A. J., Goelzer, H., Lipscomb, W. H., Abe Ouchi, A., Agosta, C., Albrecht, T., Asay-Davis, X., Barthel, A., et al. (2020). ISMIP6 Antarctica: a multi-model ensemble of the Antarctic ice sheet evolution over the 21 st century. *The Cryosphere Discussions*, 2020:1–54.

Shen, W., Wiens, D. A., Anandakrishnan, S., Aster, R. C., Gerstoft, P., Bromirski, P. D., Hansen, S. E., Dalziel, I. W., Heeszel, D. S., Huerta, A. D., et al. (2018). The crust and upper mantle structure of central and West Antarctica from Bayesian inversion of Rayleigh wave and receiver functions. *Journal of Geophysical Research: Solid Earth*, 123(9):7824–7849.

Shen, W., Wiens, D. A., Lloyd, A. J., and Nyblade, A. A. (2020). A geothermal heat flux map of Antarctica empirically constrained by seismic structure. *Geophysical Research Letters*, 47(14):e2020GL086955.

Shepherd, A., Gilbert, L., Muir, A. S., Konrad, H., McMillan, M., Slater, T., Briggs, K. H., Sundal, A. V., Hogg, A. E., and Engdahl, M. E. (2019). Trends in Antarctic Ice Sheet elevation and mass. *Geophysical Research Letters*, 46(14):8174–8183.

Shepherd, A., Ivins, E. R., Geruo, A., Barletta, V. R., Bentley, M. J., Bettadpur, S., Briggs, K. H., Bromwich, D. H., Forsberg, R., Galin, N., Horwath, M., Jacobs, S., Joughin, I., King, M. A., Lenaerts, J. T. M., Li, J., Ligtenberg, S. R. M., Luckman, A., Luthcke, S. B., McMillan, M., Meister, R., Milne, G., Mouginot, J., Muir, A., Nicolas, J. P., Paden, J., Payne, A. J., Pritchard, H., Rignot, E., Rott, H., Sørensen, L. S., Scambos, T. A., Scheuchl, B., Schrama, E. J. O., Smith, B., Sundal, A. V., van Angelen, J. H., van der Berg, W. J., van den Broeke, M. R., Vaughan, D. G., Velicogna, I., Wahr, J., Whitehouse, P. L., Wingham, D. J., Yi, D., Young, D., and Zwally, H. J. (2012). A reconciled estimate of ice-sheet mass balance. *Science*, 338(6111):1183–1189.

Shepherd, T., Bamber, J., and Ferraccioli, F. (2006). Subglacial geology in Coats Land, East Antarctica, revealed by airborne magnetics and radar sounding. *Earth and Planetary Science Letters*, 244(1-2):323–335.

Shreve, R. (1972). Movement of water in glaciers. *Journal of Glaciology*, 11(62):205–214.

Siegert, M. J. and Glasser, N. F. (1997). Convergent flow of ice within the Astrolabe Subglacial Basin, Terre Adélie, East Antarctica: an hypothesis derived from nummerical modelling experiments. *Polar Research*, 16(1):63–72.

Siegert, M. J., Kulessa, B., Bougamont, M., Christoffersen, P., Key, K., Andersen, K. R., Booth, A. D., and Smith, A. M. (2018). Antarctic subglacial groundwater: a concept paper on its measurement and potential influence on ice flow. *Geological Society, London, Special Publications*, 461(1):197–213.

Siegert, M. J., Taylor, J., and Payne, A. J. (2005). Spectral roughness of subglacial topography and implications for former ice-sheet dynamics in East Antarctica. *Global and Planetary Change*, 45(1-3):249–263.

Siegfried, M. and Fricker, H. (2021). Illuminating active subglacial lake processes with ICESat-2 laser altimetry. *Geophysical Research Letters*, 48(14):e2020GL091089.

Simkins, L. M., Greenwood, S. L., Winsborrow, M. C., Bjarnadóttir, L. R., and Lepp, A. P. (2023). Advances in understanding subglacial meltwater drainage from past ice sheets. *Annals of Glaciology*, pages 1–5.

Smith, A. M., Bentley, C. R., Bingham, R. G., and Jordan, T. A. (2012). Rapid subglacial erosion beneath Pine Island Glacier, West Antarctica. *Geophysical Research Letters*, 39:L12501.

Smith, A. M., Jordan, T. A., Ferraccioli, F., and Bingham, R. G. (2013). Influence of subglacial conditions on icestream dynamics: Seismic and potential field data from Pine Island Glacier, West Antarctica. *Journal of Geophysical Research: Solid Earth*, 118:1471–1482.

Smith, A. M. and Murray, T. (2009). Bedform topography and basal conditions beneath a fast-flowing West Antarctic ice stream. *Quaternary Science Reviews*, 28(7-8):584–596.

Smith, A. M., Murray, T., Nicholls, K. W., Makinson, K., Adalgeirsdóttir, G., Behar, A. E., and Vaughan, D. G. (2007). Rapid erosion, drumlin formation, and changing hydrology beneath an Antarctic ice stream. *Geology*, 35(2):127–130.

Smith, B., Fricker, H. A., Gardner, A. S., Medley, B., Nilsson, J., Paolo, F. S., Holschuh, N., Adusumilli, S., Brunt, K., Csatho, B., et al. (2020). Pervasive ice-sheet mass loss reflects competing ocean and atmosphere processes. *Science*, 368(6496):1239–1242.

Smith, B. E., Fricker, H. A., Joughin, I. R., and Tulaczyk, S. (2009). An inventory of active subglacial lakes in Antarctica detected by ICESat (2003–2008). *Journal of Glaciology*, 55(192):573–595.

Smith, B. E., Gourmelen, N., Huth, A., and Joughin, I. (2017). Connected subglacial lake drainage beneath Thwaites Glacier, West Antarctica. *The Cryosphere*, 11(1):451–467.

Smith, E. C., Smith, A. M., White, R. S., Brisbourne, A. M., and Pritchard, H. D. (2015). Mapping the ice-bed interface characteristics of Rutford Ice Stream, West Antarctica, using microseismicity. *Journal of Geophysical Research: Earth Surface*, 120(9):1881–1894.

Stearns, L. A., Smith, B. E., and Hamilton, G. S. (2008). Increased flow speed on a large East Antarctic outlet glacier caused by subglacial floods. *Nature Geoscience*, 1(12):827–831.

Stokes, C. R., Abram, N. J., Bentley, M. J., Edwards, T. L., England, M. H., Foppert, A., Jamieson, S. S., Jones, R. S., King, M. A., Lenaerts, J. T., et al. (2022). Response of the East Antarctic Ice Sheet to past and future climate change. *Nature*, 608(7922):275–286.

Stroeven, A. P. and Kleman, J. (1999). Age of Sirius Group on Mount Feather, McMurdo Dry Valleys, Antarctica, based on glaciological inferences from the overridden mountain range of Scandinavia. *Global and Planetary Change*, 23(1-4):231–247.

Sugden, D. (1978). Glacial erosion by the Laurentide Ice Sheet. *Journal of Glaciology*, 20(83):367–391.

Sugden, D. and Hall, A. (2020). Antarctic blue-ice moraines: Analogue for Northern Hemisphere ice sheets? *Quaternary Science Reviews*, 249:106620.

Sugden, D. E., Bentley, M. J., and Ó Cofaigh, C. (2006). Geological and geomorphological insights into Antarctic Ice Sheet evolution. *Philosophical Transactions of the Royal Society A: Mathematical, Physical and Engineering Sciences*, 364(1844):1607–1625.

Sugden, D. E. and John, B. S. (1976). Glaciers and landscape: a geomorphological approach. *Edward Arnold London*.

Sun, S., Cornford, S. L., Liu, Y., and Moore, J. C. (2014). Dynamic response of Antarctic ice shelves to bedrock uncertainty. *The Cryosphere*, 8(4):1561–1576.

Sun, S., Pattyn, F., Simon, E. G., Albrecht, T., Cornford, S., Calov, R., Dumas, C., Gillet-Chaulet, F., Goelzer, H., Golledge, N. R., et al. (2020). Antarctic ice sheet response to sudden and sustained ice-shelf collapse (ABUMIP). *Journal of Glaciology*, 66(260):891–904.

Thorsteinsson, T., Raymond, C., Gudmundsson, G., Bindschadler, R., Vornberger, P., and Joughin, I. (2003). Bed topography and lubrication inferred from surface measurements on fast-flowing ice streams. *Journal of Glaciology*, 49(167):481–490.

Timmermann, R., Wang, Q., and Hellmer, H. (2012). Ice-shelf basal melting in a global finite-element sea-ice/ice-shelf/ocean model. *Annals of Glaciology*, 53(60):303–314.

Trevisani, S. and Rocca, M. (2015). MAD: robust image texture analysis for applications in high resolution geomorphometry. *Computers & Geosciences*, 81:78–92.

Tsutaki, S., Fujita, S., Kawamura, K., Abe-Ouchi, A., Fukui, K., Motoyama, H., Hoshina, Y., Nakazawa, F., Obase, T., Ohno, H., et al. (2022). High-resolution subglacial topography around Dome Fuji, Antarctica, based on ground-based radar surveys over 30 years. *The Cryosphere*, 16(7):2967–2983.

Tulaczyk, S., Kamb, W. B., and Engelhardt, H. F. (2000a). Basal mechanics of Ice Stream B, West Antarctica: 1. Till mechanics. *Journal of Geophysical Research: Solid Earth*, 105(B1):463–481.

Tulaczyk, S., Kamb, W. B., and Engelhardt, H. F. (2000b). Basal mechanics of Ice Stream B, West Antarctica: 2. Undrained plastic-bed model. *Journal of Geophysical Research: Solid Earth*, 105(B1):483–494.

Turner, J., Orr, A., Gudmundsson, G. H., Jenkins, A., Bingham, R. G., Hillenbrand, C.-D., and Bracegirdle, T. J. (2017). Atmosphere-ocean-ice interactions in the Amundsen Sea Embayment, West Antarctica. *Reviews of Geophysics*, 55(1):235–276.

Van Pelt, W., Oerlemans, J., Reijmer, C., Pettersson, R., Pohjola, V. A., Isaksson, E., and Divine, D. (2013). An iterative inverse method to estimate basal topography and initialize ice-flow models. *The Cryosphere*, 7(3):987–1006.

Vaughan, D. G., Corr, H. F., Ferraccioli, F., Frearson, N., O'Hare, A., Mach, D., Holt, J. W., Blankenship, D. D., Morse, D. L., and Young, D. A. (2006). New boundary conditions for the West Antarctic Ice Sheet: Subglacial topography beneath Pine Island Glacier. *Geophysical Research Letters*, 33:L09501.

Vaughan, D. G., Corr, H. F., Smith, A. M., Pritchard, H. D., and Shepherd, A. (2008). Flow-switching and water piracy between Rutford Ice Stream and Carlson Inlet, West Antarctica. *Journal of Glaciology*, 54(184):41–48.

Wannamaker, P. E., Stodt, J. A., Pellerin, L., Olsen, S. L., and Hall, D. B. (2004). Structure and thermal regime beneath the South Pole region, East Antarctica, from magnetotelluric measurements. *Geophysical Journal International*, 157(1):36–54.

Weatherall, P., Marks, K. M., Jakobsson, M., Schmitt, T., Tani, S., Arndt, J. E., Rovere, M., Chayes, D., Ferrini, V., and Wigley, R. (2015). A new digital bathymetric model of the world's oceans. *Earth and Space Science*, 2(8):331–345.

Weertman, J. (1957). On the sliding of glaciers. *Journal of glaciology*, 3(21):33–38.

Weertman, J. (1974). Stability of the junction of an ice sheet and an ice shelf. *Journal of Glaciology*, 13(67):3–11.

Whillans, I. M. and Johnsen, S. J. (1983). Longitudinal variations in glacial flow: theory and test Using data from the Byrd Station strain network, Antarctica. *Journal of Glaciology*, 29(101):78–97.

Winberry, J. P. and Anandakrishnan, S. (2004). Crustal structure of the West Antarctic Rift System and Marie Byrd Land Hotspot. *Geology*, 32(11):977–980.

Wingham, D. J., Siegert, M. J., Shepherd, A., and Muir, A. S. (2006). Rapid discharge connects Antarctic subglacial lakes. *Nature*, 440(7087):1033–1036.

Wolovick, M., Humbert, A., Kleiner, T., and Rückamp, M. (2023). Regularization and L-curves in ice-sheet inverse models: a case study in the Filchner–Ronne catchment. *The Cryosphere*, 17(12):5027–5060.

Woodard, J., Zoet, L., Iverson, N. R., and Helanow, C. (2021). Variations in hard-bedded topography beneath glaciers. *Journal of Geophysical Research: Earth Surface*, 126(9):e2021JF006326.

Wörner, G. (1999). Lithospheric dynamics and mantle sources of alkaline magmatism of the Cenozoic West Antarctic Rift System. *Global and Planetary Change*, 23(1-4):61–77.

Wright, A. and Siegert, M. (2012). A fourth inventory of Antarctic subglacial lakes. *Antarctic Science*, 24(6):659–664.

Wright, A., Siegert, M., Le Brocq, A., and Gore, D. (2008). High sensitivity of subglacial hydrological pathways in Antarctica to small ice-sheet changes. *Geophysical Research Letters*, 35(17):L17504.

Wright, A. and Siegert, M. J. (2011). The identification and physiographical setting of Antarctic subglacial lakes: an update based on recent discoveries. *Geophysical Monograph Series*, 192:9–26.

Yan, S., Blankenship, D. D., Greenbaum, J. S., Young, D. A., Li, L., Rutishauser, A., Guo, J., Roberts, J. L., van Ommen, T. D., Siegert, M. J., et al. (2022). A newly discovered subglacial lake in East Antarctica likely hosts a valuable sedimentary record of ice and climate change. *Geology*, 50(8):949–953.

Yin, Z., Zuo, C., MacKie, E. J., and Caers, J. (2022). Mapping high-resolution basal topography of West Antarctica from radar data using non-stationary multiple-point geostatistics (MPS-BedMappingV1). *Geoscientific Model Development*, 15(4):1477–1497.

Young, D. A., Roberts, J. L., Ritz, C., Frezzotti, M., Quartini, E., Cavitte, M. G., Tozer, C. R., Steinhage, D., Urbini, S., Corr, H. F., et al. (2017). High-resolution boundary conditions of an old-ice target near Dome C, Antarctica. *The Cryosphere*, 11(4):1897–1911.

Young, D. A., Schroeder, D., Blankenship, D., Kempf, S. D., and Quartini, E. (2016). The distribution of basal water between Antarctic subglacial lakes from radar sounding. *Philosophical Transactions of the Royal Society A: Mathematical, Physical and Engineering Sciences*, 374(2059):20140297.

Yu, H., Rignot, E., Seroussi, H., and Morlighem, M. (2018). Retreat of Thwaites Glacier, West Antarctica, over the next 100 years using various ice-flow models, ice-shelf melt scenarios and basal-friction laws. *The Cryosphere*, 12(12):3861–3876.

Zoet, L. K. and Iverson, N. R. (2020). A slip law for glaciers on deformable beds. *Science*, 368(6486):76–78.